

FLOW AND COMBUSTION IN DISC AND PENT-ROOF SI ENGINES

By:

Ahmad E. M. A. Murad

BSc, MSc

Submitted in accordance with the requirements for the degree of
Doctor of Philosophy

**The University of Leeds
School of Mechanical Engineering**

January 2006

The candidate confirms that the work submitted is his own and appropriate credit has been given where reference has been made to the work of others.

This copy has been supplied on the understanding that it is copyright material and that no quotation from the thesis may be published without proper acknowledgement.

Abstract

Reported in this thesis is a study of combustion in a disc-shaped combustion chamber spark ignition engine, and in-cylinder flow and combustion in an idealised pent-roof spark ignition engine. Both engines were skip fired, to remove residuals and ensure a well-defined in-cylinder fuel-air mixture. Other important parameters were also controlled, e.g. inlet temperature, inlet pressure, air mass flow, mixture strength, engine speed and spark timing.

With the disc-shaped spark ignition engine, a shadowgraph technique was used to study early flame development. Simultaneous natural light and shadowgraph imaging techniques were adopted to validate the later use of the former method for monitoring flame propagation in the pent-roof engine. The disc-shaped engine flame images were processed to yield mean flame radius, flame centroid and to describe flame 'circularity'. Good agreement was obtained between flame radii obtained from natural light and shadowgraph images. No correlation was found between early flame development, centroid displacement, flame 'shape' and the rate of combustion as defined by the crank angle at which peak pressure was attained.

The pent-roof engine was 'mapped' to determine optimum conditions, prior to flow and flame studies on the same engine. Flow was analysed using laser doppler and particle tracking velocimetry techniques. Mean and rms velocities were obtained. Observed flow patterns at the two engine speeds tested (750 and 1500 rpm) differed and were not as expected for the simplified geometry. Similar trends in rms velocity were observed at all locations tested, with similar magnitudes at all points and in all directions tested during the critical combustion period. Simultaneous top and side natural light flame images were generated using two high-speed digital cameras; in-cylinder pressure was also recorded. The top and side images were analysed in terms of top and side successive flame positions and top and side mean flame radius. Centroid displacements, from side flame views, were also determined. No correlation was found between initial flame developments and later flame development viewed from the side.

Acknowledgements

I would like to express my sincere thanks to my supervisor, Professor Chris Sheppard, for his supervision, guidance and encouragement throughout the period of this research. This thesis could not have been written without his valuable comments and the extra time spent correcting chapters. I would also like to thank sincerely Dr. Rob Woolley for his advice, help in preparing the laser and interesting discussions.

I would also like to take this opportunity to thank all of my colleagues in the combustion group at Leeds for their friendship and support, especially Waleed Alrefae for his assistance in the laboratory work.

I am also very grateful to technicians John Groves, Brian Leach, Mark Batchelor, and Jonathan Stephenson for their assistance in the laboratory. In addition, I would like to thank Pat Richardson for her help with university procedures and administration especially on first arrival at Leeds. I wish her all the best in her life after retirement.

I wish to thank the head of the cultural affairs office of the Kuwaiti Embassy, Dr. Bader Al-Dihani and all of the staff working with him for their supervision and continuous help and support. Also, my thanks to the Public Authority for Applied Education and Training for their scholarship, which enabled me to pursue my studies at Leeds University.

Finally, I dedicate this work as a memorial to my mother who spent all her life for her family. My deepest thanks to my father for all his love and support. My deepest gratitude to my wife who has suffered from bone deficiency, but whom nevertheless, tolerated all that pain and looked after our six children. Her support, kindness and sacrifices are all appreciated. Also, special thanks go to my six lovely children.

Contents

Abstract	i
Acknowledgements	ii
Table of Contents	iii
Nomenclature	vii
Chapter One	1
Introduction	1
1.1 Background	1
1.2 The Current Study	3
1.2 Thesis Outline	4
Chapter Two	6
In-cylinder Flow, Turbulence and Combustion	6
2.1 Introduction	6
2.2 Characterisation of Turbulence	7
2.2.1 RMS Turbulent Velocity	8
2.2.2 Integral Length and Time Scales	10
2.3 Bulk Air Motion	13
2.3.1 Axial Swirl	13
2.3.2 Tumble	14
2.4 Engine Combustion	16
2.4.1 Ignition and Early Flame Development	16
2.4.2 Turbulent Flame Propagation	18
2.5 Cyclic Variation	20
2.5.1 Background	20
2.5.2 Cyclic Variation Quantification	22
2.6 Closure	23
Chapter Three	27
Experimental Engine and Instrumentation	27
3.1 Introduction	27
3.2 LUPOE1-D Engine	28

3.3	Modified Petter (LUPOE2-P) Engine	30
3.3.1	Engine Barrel and Assembly	31
3.3.2	Cylinder Head Arrangements	31
3.3.3	Engine Lubrication	32
3.3.4	Modifications	33
3.3.5	TDC Setting	33
3.4	Air and Fuel Supply System	34
3.4.1	Air Supply System	34
3.4.2	Fuel Supply System	34
3.5	Ignition System	35
3.6	Pressure Measurement	35
3.7	Crank Angle Position Measurement	37
3.8	Data Acquisition System	37
3.9	Experimental Procedure	37
	Chapter Four	54
	Flame Visualisation and Flow and Turbulence Characterisation	54
4.1	Introduction	54
4.2	Flame Visualisation (LUPOE1-D)	54
4.2.1	Natural Light Imaging	55
4.2.2	Shadowgraph Technique	55
4.2.3	Simultaneous Natural Light and Shadowgraph Techniques	56
4.3	Flame Visualisation (LUPOE2-P)	57
4.4	Flow and Turbulence Characterisation (LUPOE2-P)	58
4.4.1	Laser Doppler Velocimetry (LDV)	58
4.4.2	Particle Tracking Velocimetry (PTV)	62
	Chapter Five	74
	Processing and Data Analysis	74
5.1	Introduction	74
5.2	In-Cylinder Pressure Data	74
5.2.1	In-Cylinder Pressure Data Processing	74
5.3	Film Data	75

5.3.1 Film Data Processing	76
5.4 Laser Doppler Velocimetry (LDV)-LUPOE2-P Engine	77
5.5 Particle Tracking Velocimetry (PTV)-LUPOE2-P Engine	79
5.5.1 PTV Analysis	79
Chapter Six	87
LUPOE2-P Preliminary Engine Mapping	87
6.1 Introduction	87
6.2 Dynamic Pressure Transducers	88
6.3 Spark Plug Ground Electrode Orientation	90
6.4 Effect of Skip Firing	91
6.5 Effect of Engine Speed	91
6.6 Effect of Equivalence Ratio	92
6.7 Effect of Inlet/Head Temperature	93
6.8 Effect of Air Mass Flow	93
Chapter Seven	102
Experimental Results and Discussion	102
7.1 Introduction	102
7.2 Flame Study (LUPOE1-D)	103
7.2.1 Simultaneous Natural Light and Shadowgraph Study	103
7.2.2 Early Flame Development	104
7.3 Flow Investigation (LUPOE2-P)	108
7.3.1 PTV Flow Investigation	108
7.3.2 LDV Study	110
7.4 Flame Study (LUPOE2-P Engine)	117
7.4.1 Reference Condition	118
7.4.2 Effect of Ignition Timing	121
7.4.3 Effect of Equivalence Ratio	122
7.4.4 Effect of Engine Speed	124
7.4.5 Comparison of Middle Cycles at Various Engine Speeds	126
Chapter Eight	184
Summary, Concluding Discussion and Recommendations for Future Work	184

8.1	Summary	184
8.2	Concluding Discussion	188
8.2.1	In-cylinder Flow and Turbulence	188
8.2.2	Effect of Flow and Turbulence on Combustion	193
8.2.3	Modelling Database	195
8.3	Recommendations for Future Work	197
	References	203
	Appendices A and B	219

Nomenclature

A	-	Constant
c_p	$\text{kJ kg}^{-1} \text{K}^{-1}$	Specific heat capacity (constant pressure)
D	$\text{m}^2 \text{s}^{-1}$	Thermal diffusivity
H	mm	Clearance height
K	-	Karlovitz stretch factor
k	$\text{kW m}^{-1} \text{K}^{-1}$	Thermal conductivity
L	mm	Integral length scale
Le	-	Lewis number
Ma	-	Markstein number
N	-	Number of data points
P	bar	Pressure
P_{\max}	bar	Cylinder peak pressure
\bar{P}_{\max}	bar	Average peak pressure
P_f	mm	Flame perimeter
P_e	mm	Perimeter of equivalent circle
R_L	-	Reynolds number defined by integral length scale
R_x	-	Integral of autocorrelation coefficient
Re	-	Reynolds number
R_s	-	Swirl ratio
R_T	-	Tumble ratio
\bar{S}_p	m s^{-1}	Mean piston speed
\bar{u}	m s^{-1}	Mean velocity
U	m s^{-1}	Instantaneous local fluid velocity
u_l	m s^{-1}	Laminar burning velocity
u_t	m s^{-1}	Turbulent burning velocity
u_{te}	m s^{-1}	Turbulent burning (entrainment) velocity

u_{tr}	m s^{-1}	Turbulent burning (reacting) velocity
u'	m s^{-1}	Root mean square (rms) turbulent velocity
u'_k	m s^{-1}	Effective 'rms' turbulent velocity

Greek symbols

α	$\text{m}^2 \text{s}^{-1}$	Thermal diffusivity
δ_l	mm	Laminar flame thickness
ε	$\text{m}^2 \text{s}^{-3}$	Turbulent kinetic energy dissipation rate
η	mm	Kolmogorov length scale
θ	-	Crank angle
$\theta_{p_{\max}}$	-	Crank angle position of peak pressure
λ	mm	Taylor microscale
ν	$\text{m}^2 \text{s}^{-1}$	Kinematic viscosity
ρ	kg m^{-3}	Density
$\sigma_{p_{\max}}$	bar	Peak pressure variance
τ_L	s	Integral time scale
τ_η	s	Kolmogorov time scale
τ_λ	s	Taylor time scale
ω	rad s^{-1}	Angular velocity
ϕ	-	Equivalence ratio by mass

Subscripts, superscripts and notation

° Degrees

Abbreviations

ADC	Analogue to Digital Converter
aTDC	After Top Dead Centre
B/W	Black/white
BDC	Bottom Dead Centre
BS	Back Scatter
BSA	Burst Spectrum Analyser
bTDC	Before Top Dead Centre
CA/c.a.	Crank Angle
CO	Carbon Monoxide
COV	Coefficient of Variation
CO ₂	Carbon Dioxide
DC	Direct Current
EGR	Exhaust Gas Re-circulation
EPC	Exhaust Port Closure
EPO	Exhaust Port Opening
FID	Flame Ionisation Detector
FPS	Frames per Second
FS	Forward Scatter
FSD	Full-Scale Deflection
GDI	Gasoline Direct Injection
HC	Hydrocarbons
HWA	Hot-Wire Anemometry
IC	Internal Combustion
IMEP	Indicated Mean Effective Pressure
LDV	Laser Doppler Velocimetry
LUPOE	Leeds University Ported Optical Engine
LUPOE1-D	LUPOE1 Disc-Shaped Version
LUPOE2-P	LUPOE2 Pent-Roof Version
MBT	Maximum Brake Torque

MPG	Mile per gallon
NO _x	Oxides of Nitrogen
PC	Personal Computer
PCV	Positive Crank Case Ventilation
PM	Photo-Multiplier
PPR	Pulses per Revolution
PSD	Power Spectrum Density
PIV	Particle Image Velocimetry
PTV	Particle Tracking Velocimetry
RMS/rms	Root Mean Square
RPM	Revolutions per Minute
SF	Shape Factor
SFR	Skip Firing Ratio
TDC	Top Dead Centre
TLC	Top Land Crevice
1D	One-dimension
2D	Two-dimension
3D	Three-dimension

Chapter 1

Introduction

1.1 Background

As the 21st century begins, in the automobile industry there are a number of quite different technologies competing for a chance to reduce automotive emission problems. Among the possible solutions are hybrid electric vehicles (Motavalli, 2000). These vehicles have a high efficiency and low fuel consumption. However, they are limited by the performance of their batteries, which are expensive, heavy and do not last many cycles of charging and discharging. On the other hand, the continuing use of automotive engines involves the risk of increasing air pollution and global warming due to their rapidly increasing numbers, despite impressive advances in output for individual cars. Despite its problems, the internal combustion (IC) engine remains the most practical power source available for transportation.

Many improvements have been the result of imposition of legislation on automotive emissions and fuel consumption. In the USA, automotive manufacturers, in cooperation with the federal government, began researching the causes and effects of vehicle emissions in the early 1960s. They determined that there were three main sources of emissions: exhaust emissions (HC-hydrocarbons, CO-carbon monoxide and NO_x-oxides of nitrogen), crankcase vapours (HC) and fuel evaporation (HC). Similarly, there are concerns over CO₂-carbon dioxide emissions from automotive exhaust, as these contribute to global warming. These emitted gases cause a number of health-related and environmental concerns. Moreover, there are concerns over limited fuel reserves, as demands for energy increase along with the current increase in oil prices.

The installation of emission-control systems to reduce automotive emissions was first adopted in California in 1961. These included removal of blow-by gases from the crankcase with a positive crankcase ventilation (PCV) system; use of an air pump, to provide the air necessary for the oxidising process inside the catalytic converter; introduction of the three-way catalytic converter to reduce the exhaust emissions of HC,

CO and NO_x. Some engines also used exhaust gas re-circulation (EGR) to reduce NO_x emissions. Late in 2004, California became the first state to approve a regulation for reducing CO₂ emissions from vehicle exhausts by using four-way converters (Halderman et al., 2005). However, the effective operation of the catalyst required a stoichiometric mixture. Further development introduced sophisticated technologies, such as automotive sensors (inlet air, coolant temperature, oxygen, etc.), which helped in reducing automotive emissions and improving fuel economy.

An alternative solution to reduce exhaust emissions and improve fuel economy, and hence engine efficiency, can be achieved by using lean burn engines. However, such engines tend to run roughly, due to misfire and incomplete combustion, with slow burning associated with fall in engine power and increased cyclic variation. To compensate for these effects, it is necessary to introduce faster burning. This can be achieved by increasing the in-cylinder turbulence, which enhances turbulent burning velocity. One way to improve turbulence is by introducing bulk flow (axial swirl, tumble) in the cylinder. Tumble flow has been found to accelerate the combustion process and improve engine performance in engines equipped with 'pent' head chambers. Furthermore, fast burn engines have also the advantage of tolerating EGR, which can result in higher efficiency and lower NO_x values. However, excessive turbulence can cause partial or complete flame quenching (Bradley et al., 1992).

Significant improvements in engine efficiency can also be achieved by increasing the effective compression ratio by use of a turbocharger. However, such improvements are limited by the occurrence of knock. Adopting high compression ratio engines with fast burning technology might result in a reliable combustion of lean mixtures without the tendency of knock (Lumley, 1999) and, consequently, lead to reduced fuel consumption, improved thermal efficiency and reduced exhaust emissions. Therefore, to achieve this target, fundamental research studies to understand the interaction between in-cylinder flow and combustion inside the spark ignition engine are required. Due to their complexity, only limited tests (e.g. pressure and emissions data) can be conducted in real production engines. Hence, more detailed in-cylinder flow investigations and turbulent flame propagation studies, using research engines, are vital.

The use of single cylinder research optical engines can help in visualisation and understanding of in-cylinder flow and turbulent flame propagation. It also helps in enabling close control of engine running parameters, such as mixture strength, temperature, inlet pressure and in eliminating residual gases from previous firing cycles by running the engine in skip firing mode (to be explained later in Chapter 3), or adding simulated EGR to the engine over a range of engine operating conditions (Smallbone, 2004). Flow characterisation can be achieved by using flow investigation techniques (Laser Doppler Velocimetry (LDV), Particle Tracking Velocimetry (PTV) and Particle Image Velocimetry (PIV)). Turbulent flame propagation monitoring can be achieved using natural light photography, schlieren or shadowgraph imaging techniques. The two latter techniques are preferable at the very early stages of flame kernel development, due to inadequate light emission from the flame kernels and interference from the spark.

1.2 The Current Study

Successive workers at Leeds (Hicks, 1994; Lee, 1995; Atashkari, 1997; Abdi Aghdam, 2003) have employed variants of the ported optical engines described in Chapter 3 in studies of the fundamentals of turbulent flame development and propagation, as well as to provide validation for a thermodynamic cycle model which attempts to extend Leeds turbulent 'bomb' derived turbulent burning velocity correlations to engine applications (Bradley et al., 1988; Merdjani and Sheppard, 1993). These engines have invariably adopted a cylindrical 'disc' shaped combustion space with full overhead optical access to the combustion space. For this engine, a considerable library of flow, turbulence, in-cylinder pressure and flame propagation rate data has been established (employing laser Doppler anemometry (Atashkari, 1997), particle tracking velocimetry (Cairns, 2001), natural light ciné photography (Abdi Aghdam, 2003), schlieren/shadowgraph ciné photography (Cairns, 2001), single and multiple laser sheet Mie imaging techniques (Hicks, 1994; Lee, 1995) as well as conventional pressure transducer methods (Lee, 1995) for a wide range of conditions. The engines have also been used extensively in auto-ignition/knock studies (König and Sheppard, 1990; König, 1993; Pan, 1994; Pan and Sheppard; 1994 Smallbone, 2004).

The current work was stimulated by Leeds' contribution to the EU sponsored Gasoline Engine Turbocharging (GET) cluster of projects in (GET-CO₂; GET-Drive; GET-Engine) undertaken in association with Renault, VW, PSA motor manufacturers, the turbocharger company Garrett and the consulting engineering company Ricardo. The Leeds effort was directed to integrating their combustion auto-ignition and knock model 'LUSIE' (Leeds University Spark Ignition Engine) into Ricardo's 'WAVE' commercial engine simulation code, with appropriate experimental validation, for application to highly turbocharged downsized multi-cylinder engines.

The purposes of the work reported in this thesis were to add further data to fill a gap in the existing database on the critical initial flame development period and then extend the model validation database to an idealised pent-roof geometry engine of exceptional optical access. This engine's cylinder head geometry and 9.2:1 compression ratio were selected to mimic those of a 1.4 litre VW engine used in the GET project by the VW company and fellow Leeds research student (Wu, 2006). As reported in later chapters, the current author had no involvement with the parallel modelling work, which is reported elsewhere (GET-CO₂ final report; Abdi Aghdam, 2003; Smallbone, 2004).

1.3 Thesis Outline

The work reported in this thesis has been concerned with flame imaging of the early stages of flame development using a 'disc' head engine (LUPOE1-D). This involved using shadowgraph imaging of the early stages of flame development. Simultaneous natural light and shadowgraph imaging techniques on the same engine were adopted for comparative studies, to assess the applications of the simpler technique for engines of less generous optical access and to validate information gathered by previous workers at Leeds University using natural light ciné photography. It has also concerned fundamental study of in-cylinder flow and 3-D turbulent flame imaging in a 'pent' head research spark ignition engine (LUPOE2-P), an idealisation of the commonly adopted 4-valve pent-roof geometries of most current engine manufacturers.

In Chapter 2, a literature review covering the in-cylinder flow, turbulence and combustion of spark ignition engines is presented. Descriptions of the experimental equipment, and instrumentation associated with it, for the two research engines adopted

in the study (LUPOE1-D and LUPOE2-P), are reported in Chapter 3. Set out in Chapter 4 is a brief review of the experimental techniques and associated imaging equipment adopted for flame visualisation, flow and turbulence characterisation inside the engine cylinders. This is followed in Chapter 5 by descriptions of the adopted pressure and flame imaging analysis, and of the flame and flow image processing and analysis techniques employed in this study. In Chapter 6, preliminary pressure-crank angle measurements collected to find the optimum conditions for LUPOE2-P (engine mapping) are reported. Subsequently, in Chapter 7, the imaging and analysis results of the currently reported studies are presented for both engines. Finally the major findings of this research are summarised and discussed, together with recommendations for future work, in Chapter 8.

Chapter 2

In-cylinder Flow, Turbulence and Combustion

2.1 Introduction

The purpose of this chapter is to provide general background for the study presented later in this thesis rather than to provide an in-depth review or literature search; these are available elsewhere (Heywood, 1988; Weaving, 1990). A concern over emission of 'greenhouse effect' gases such as CO₂ from automotive exhausts, which contribute to global warming, and limited hydrocarbon fuel reserves in an era of rapid global economic growth motivates the quest for engines of higher thermal efficiency and fuel economy (mpg). The requirements to do this, while maintaining low noxious emissions, have intensified efforts to develop lean burn concepts.

However, lower combustion temperatures associated with lean burn lead to decreased laminar burning velocity (u_l) and hence decreased turbulent burning velocity (u_t) and slow flame propagation. This in turn leads to long combustion duration and lower thermal efficiency. It can also result in partial or total quench, misfire, increase in cyclic variation and increase in pollutant emissions. To compensate for these effects, it is necessary to introduce faster burning (Lumley, 1999).

Faster burn can be achieved by reducing flame travel. This can be influenced by spark plug location, combustion chamber geometry, or using twin spark plugs (per cylinder) (Li et al., 2004). It can also be promoted by increasing in-cylinder turbulence, which enhances turbulent burning velocity (Arcoumanis et al., 1994). Turbulent flow is irregular both in space and time, and random in three dimensions; its definition is problematic because of unsteadiness and cyclic fluctuation of the 'mean' flow, as discussed later in Section 2.2.

The required small-scale turbulence during the combustion period can be achieved towards the end of the compression stroke by decay of organised bulk motions such as

swirl or tumble (Gosman et al., 1985). However, excessive turbulence can lead to increased heat transfer, misfire and excessive cyclic variation.

One of the first hot-wire anemometry (HWA) experimental studies of in-cylinder turbulence was conducted by Semenov (1963). He showed that, by eliminating the intake and exhaust strokes, turbulence was significantly reduced. He therefore reasoned that the intake stroke was responsible for the initial generation of the turbulent flow-field. The production and modification of this initial flow-field has since been the subject of many studies, some of which are referenced below.

The recent development of laser-based techniques for the measurement of velocity throughout the engine cycle, usually under motoring conditions, has allowed detailed mapping of the flow and improved understanding of the in-cylinder fluid mechanics. A number of workers have used Laser Doppler Velocimetry (LDV) to characterise in-cylinder flow and turbulence on the basis of ensemble averaged data under motoring (Arcoumanis et al., 1994) and firing conditions (Hall, 1987; Miles et al., 1994). Some studies have used Particle Tracking Velocimetry (PTV), which involves manually tracking relatively sparse and individual particles present in the laser sheet (Kent and Trigui, 1994). Most recently, other researchers have employed Particle Image Velocimetry (PIV), using small particles densely to seed the in-cylinder gases (Ghandhi et al., 1992; Towers et al., 1996; Baby et al., 2002).

In the following sections, characterisation of turbulence and bulk air motion are discussed, before moving on to consider turbulent engine combustion and cyclic variation.

2.2 Characterisation of Turbulence

Since turbulent flow is irregular and random, statistical methods are invariably adopted to define it. The quantities normally used are mean velocity, fluctuating velocity about the mean, and a number of length and time scales (Heywood, 1988).

The instantaneous local fluid velocity, U at a point, may be defined as the sum of the mean velocity (\bar{u}) and a temporally fluctuating component $u(t)$ (Heywood, 1988):

$$U(t) = \bar{u} + u(t) \quad (2.1)$$

2.2.1 RMS Turbulent Velocity

The strength of the fluctuating velocity component $u(t)$ is defined by its root-mean-square value (rms) u' , often loosely termed the turbulence intensity (more correctly, turbulence intensity is defined as u' / \bar{u}). The root mean square turbulent velocity (u') is determined from the instantaneous fluctuation velocity (u) about the mean velocity as:

$$u' = \lim_{t \rightarrow \infty} \left[\frac{1}{t} \int_{t_0}^{t_0+t} (U^2 - \bar{u}^2) dt \right]^{0.5} \quad (2.2)$$

In engines, velocity measurements at a point have traditionally been made using the Laser Doppler Velocimetry (LDV) technique, e.g. Section 4.4.1 of this thesis. This method is usually able to generate few instantaneous measurements of velocity in a given crank angle interval ('window') in an individual cycle. In determining u' for this crank angle window, it is usual therefore to 'ensemble average' over a large number of engine cycles (Heywood, 1988):

$$\bar{U}_{EA}(\theta) = \frac{1}{N_c} \sum_{i=1}^{N_c} U(\theta, i) \quad (2.3)$$

where N is the total number of engine cycles for which data are available, $U(\theta, i)$ is the difference between the mean velocity at crank angle θ in cycle i and $\bar{U}_{EA}(\theta)$. However, because of cyclic variation, Section 2.5; in-cylinder flow patterns have been noted to vary from cycle to cycle (Heywood, 1988; Ozdor et al., 1994).

In an attempt to mitigate the effects of such variation in mean flows on the calculated values of u' (which may otherwise be over-estimated), various methods of separating cyclic variation in mean velocity and estimating 'true' rms turbulent velocity have been advanced. One method involves low-pass filtering to estimate the mean velocity in each engine cycle. The rms deviation involves low-pass filtering to estimate the mean velocity in each engine cycle. The rms deviation of the instantaneous velocities from the mean velocities in that cycle are then computed over all cycles (Liou and Santavicca, 1983; Whitelaw and Xu, 1995; Xu, 1995); this is termed velocity-filtering-based analysis. Another technique depends on evaluation of non-stationary autocorrelation functions of the fluctuations about the ensemble-averaged velocity (Glover, 1986; Fansler and French, 1988). An alternative approach is to employ 'conditional sampling' to identify groups of engine cycles of similar behaviour, which can then be further analysed using ensemble-averaging. Conditional sampling techniques have proved useful in resolving the relationship between flow characteristics before ignition near the spark plug, or in the unburned region ahead of the propagating flame, with combustion parameters during individual engine cycles (Swords et al., 1982; Witze et al., 1984; Witze and Martin, 1986; Plee et al., 1987; Whitelaw and Xu, 1993). Some combustion parameters adopted for conditional sampling include peak pressure, flame speed and flame arrival time. In the current study, only conventional ensemble averaging has been employed; this should be considered to be the case in all other works referred to in this thesis, unless otherwise stated.

For a 'disc-shaped' chamber engine, it has been shown that there is an approximately linear relationship between turbulent intensity at TDC and mean piston speed \bar{S}_p (Bopp et al., 1986; Hall and Bracco, 1987). At Leeds University, Atashkari (1997) conducted LDV measurements in the LUPOE1-D engine (described in Chapter 3, Section 3.2) used in the currently reported study. From measurements conducted at different engine speeds, he observed a linear correlation between turbulent intensity at TDC and mean piston speed, as shown in Figure 2.1.

Newman (1993) showed, for a pent-roof chamber and a compression ratio of 10.5, the turbulent intensity was about half mean piston speed for measurements taken near the

spark plug. Arcoumanis et al. (1994) and Gosman (1986) reported turbulent intensity values as high as 1.0-1.2 times the mean piston speed.

The findings of many researchers have supported the supposition of a near-linear relationship between u' and mean piston speed, as shown in Figure 2.2 (Bopp et al., 1986). Although near-linear relationships have generally been obtained for a given location in the cylinder and specific engine geometry, the slopes of u' versus mean piston speed differed.

2.2.2 Integral Length and Time Scales

The size of 'eddies' within a turbulent flow have usually been characterised by one or more turbulent length and time scales. Generally, three length and time scales have been adopted: integral length (L) and time (τ_L) scales, Kolmogorov length (η) and time (τ_η) scales and Taylor length (λ) and time (τ_λ) scales.

The integral length scale (L) is used to characterise the larger scales of turbulence (although much larger eddies than the value of L may exist in the cylinder). The largest eddies in the flow are limited in size by the system boundaries. The integral length scale is defined as the integral of the autocorrelation coefficient (R_x) of the fluctuating velocity at two adjacent points with respect to the variable distance (x) between the points (Heywood, 1988):

$$L = \int_0^{\infty} R_x dx \quad (2.4)$$

$$R_x = \frac{1}{N-1} \sum_{i=1}^N \frac{u(x_0)u(x_0+x)}{u'(x_0)u'(x_0+x)} \quad (2.5)$$

where N is the number of data points. A variation of the spatial velocity autocorrelation coefficient (R_x) with distance is shown diagrammatically in Figure 2.3. Since applying spatial autocorrelation in an engine can be difficult, integral length scale has often been determined from the integral time scale τ_L .

The integral time scale of turbulence is defined via an autocorrelation between two velocities at a fixed point in space, but separated in time (Heywood, 1988):

$$\tau_L = \int_0^{\infty} R_t dt \quad (2.6)$$

$$R_t = \frac{1}{N-1} \sum_{i=1}^N \frac{u(t_0)u(t_0+t)}{u'(t_0)u'(t_0+t)} \quad (2.7)$$

In a flow-field where a mean flow exists, the length scale can be deduced (Tabaczynski, 1976):

$$L = \bar{u} \tau_L \quad (2.8)$$

However, flow in some engines may show near-zero mean velocities. In 1986, Fraser and co-workers employed two-point LDV measurements in a disc-shaped ported engine. They concluded that the integral length scale (L) was proportional to instantaneous clearance height (H), with a proportionality of 0.2 at TDC, as illustrated in Figure 2.4.

Shear forces between large scales eddies and walls cause them to break down into smaller and smaller scales (Heywood, 1988). The Kolmogorov length scale (η) provides a measure of the size of the smallest eddies, where viscous shear stresses act at a molecular level to dissipate turbulent kinetic energy into heat (Tennekes and Lumley, 1972):

$$\eta = \left(\frac{\nu^3}{\varepsilon} \right)^{\frac{1}{4}} \quad (2.9)$$

The corresponding Kolmogorov time scale (τ_η) is given by:

$$\tau_\eta = \left(\frac{\nu}{\varepsilon} \right)^{\frac{1}{2}} \quad (2.10)$$

where ν is the kinematic viscosity and ε is the energy dissipation rate per unit mass. Hence, “the smallest scales of turbulence depend only on the viscosity of the fluid and the dissipation of kinetic energy from the large scales” (Weaving, 1990).

An intermediate length scale, the Taylor length scale (λ), may also be defined by relating the mean fluctuating strain rate (or velocity gradient) to the rms turbulent velocity (Heywood, 1988):

$$\frac{\partial u}{\partial x} \approx \frac{u'}{\lambda} \quad (2.11)$$

The Taylor length scale (λ) and the Taylor time scale (τ_λ) are related by the mean flow velocity as:

$$\lambda = \bar{u} \tau_\lambda \quad (2.12)$$

For isotropic (rms velocities at different directions are equal – e.g. $u' = v' = w'$) and homogeneous (rms velocities at different locations are equal) turbulence, Heywood (1988) stated the following expression for the Taylor length scale:

$$\lambda = \sqrt{\frac{15}{A}} R_L^{-0.5} \quad (2.13)$$

where A is a constant of order unity and R_L is the turbulent Reynolds number. Although turbulence can be characterised by these three scales, there is of course a complete spectrum of eddy sizes from the largest the container can hold, down to the very smallest.

2.3 Bulk Air Motion

As mentioned in Section 2.1, turbulence generation is a function of the bulk flows (axial swirl, tumble) occurring within the engine cylinder.

2.3.1 Axial Swirl

Axial swirl is defined as the rotational component whose axis is parallel to the cylinder axis. The intensity of the imposed swirl can be quantified by a 'swirl ratio' R_s (Heywood, 1988):

$$R_s = \frac{\omega_s}{\omega_n} \quad (2.14)$$

where ω_n is the angular speed of the rotating crankshaft and ω_s is the angular speed of a solid body swirl. The latter is generally measured by swirl meter or by laser velocimetry techniques.

Intake-generated swirl is a particularly important aspect of the air motion in many types of both diesel and gasoline engines. In ported engines, inclining the inlet pipes in the radial direction may generate swirl. In four-stroke engines, swirl may be produced by the induction system, e.g. helical or tangential inlet ports, shrouded valves and valve deactivation (Heywood, 1988). Swirl flow has an important effect on engine combustion. With increase of swirl ratio, burn duration has been shown to decrease and the maximum value of burn rate to increase (Hamamoto et al., 1987). High swirl has been shown to affect combustion-related performance favourably in terms of the maximum cylinder peak pressure and flame growth rate, regardless of ignition position and engine speed (Seong-Soo et al., 1995).

Changing the orientation of a shroud on the intake valve of a research engine, Witze et al. (1981) showed that the fastest burning and the least cyclic variation were associated with the highest swirl condition. Other investigators, Hill and Zhang (1994), have concluded that the introduction of swirl reduced cyclic variation and attributed this to a more repeatable flow than achieved under undirected inlet conditions. Some workers

have suggested that R_s is independent of engine speed (Hill and Zhang, 1994; Seong-Soo et al., 1995), while others have shown an increase (Hall and Bracco, 1987; Saxena and Rask, 1987) or decrease (Liou et al., 1983) in R_s with increase in engine speed. “Although the observations of these workers were derived from LDV measurements at a limited number of locations, there is agreement that the swirl ratio is dependent upon the inlet geometry and breathing of the engine” (Cairns, 2001).

In summary, reports of the influence of axial swirl (in the absence of tumble) on in-cylinder turbulence are contradictory. Both Atashkari (1997) and Hall and Bracco (1987) employed LDV measurements in ported, disc-shaped research engines, and noted the presence of swirl increased the in-cylinder turbulence intensity. However, both Atashkari (1997) and Saxena and Rask (1987) concluded that increasing the swirl ratio beyond certain levels did not further increase the turbulence intensity.

2.3.2 Tumble

In recent years, engine design has moved towards ‘pent roof’ geometry, designed principally to accommodate multiple valves in order to maximise valve area and volumetric efficiency. Such designs have the added advantage of facilitating central ignition, with reduced flame travel and increased burn rate. For such engines, ‘tumble’ flow has been found to accelerate the combustion process and improve engine performance. Tumble is defined as a rotational air motion around an axis perpendicular to the cylinder axis. A tumble ratio (R_T) may be defined:

$$R_T = \frac{\omega_T}{\omega_n} \quad (2.15)$$

where ω_T is the angular momentum of the tumbling motion. A tumble ratio is relatively difficult to define, as the axis of the tumbling vortex changes significantly during compression. Consequently, a reference axis through the centre of mass is often quoted. In the literature, values of R_T of up to 1.7 have been reported (Chapman et al., 1991).

The strength of tumble is governed by the design of the inlets and by the chamber and piston geometry (Kuwahara et al., 1994). The effect of the pent-roof combustion chamber on flow and combustion seems to depend on the details of its geometry. Workers at the Rover Group found that changing the angle of inclination of the head surfaces had a dramatic effect on the flame front area and, as a result, on the burning rate (Herron, 2001).

Tumble motion, as a means of generating turbulence in the cylinder, has been used more often than swirl, because it is simpler to generate than swirl in a four-valve-per-cylinder gasoline engine (Urushihara et al., 1996). Moreover, tumble motion has been shown to generate greater turbulence in the combustion chamber than swirl (Urushihara et al., 1995; Witze et al., 1983).

It has been suggested that four-valve cylinder heads (with their pent-roof geometries and central ignition) can allow survival of the tumbling vortex even after TDC of compression, with associated higher turbulence levels and enhanced burning rates relative to conventional two-valve cylinder heads with disc-type chambers and equipped with directed or helical ports (Arcoumanis et al., 1991). In-cylinder flow measurements (carried out using LDV on a single cylinder four-valve, pent-roof chamber engine of compression ratio of 10.5) confirmed a correlation between stronger tumble during induction and higher convective velocity and turbulence levels near the spark gap at the time of ignition; this resulted in faster combustion rates and more stable combustion under lean mixture conditions (Arcoumanis et al., 1994).

In an experimental study, with a single-cylinder four-valve transparent engine of 8.5 compression ratio, using forward and back scatter LDV techniques, Kang et al. (1996) observed that with tumble flow persisting during the compression stroke, the turbulence intensity at the end of compression was twice that without tumble. Due to the stronger tumbling motion, the release of turbulent kinetic energy was greater during its breakdown and occurred later in compression (Arcoumanis et al., 1990; Rui-Lin et al., 1996). Urushihara et al. (1995) showed that reduction in combustion duration associated with increased tumble flow did not reduce the cyclic variation compared with swirl flow. However, Hu et al. (1992) showed reduced cyclic variation and higher combustion rate for all cases tested with a high tumble inlet configuration. Similarly, Li

et al. (2004) showed that introducing strong tumble flow significantly reduced cyclic variations.

2.4 Engine Combustion

The combustion process in a spark ignition engine can be considered in three phases: (1) ignition and early flame development, (2) propagation of the flame across the combustion chamber and (3) flame termination (Heywood, 1988).

2.4.1 Ignition and Early Flame Development

“The ignition system must provide sufficient voltage across the spark plug electrodes to set up the discharge and supply sufficient energy to the discharge to ignite the combustible mixture adjacent to the plug electrodes under all operating conditions” (Heywood, 1988). The ignition process influences the overall performance of spark ignition engines (Loye and Bracco, 1987). In these engines, many aspects control the mechanism of transferring electrical energy from an ignition system into the mixture in the spark gap. “The major parameters of these are inputs of electrical energy, combustion energy release and heat transfer” (Jeonghoon et al., 2000). A more detailed study of the principles and basic properties of spark ignition is available elsewhere, in the seminal work of Maly (1984).

Early flame development can be affected by spark plug ground electrode orientation, flame attachment and detachment from the electrode, physical properties of the mixture and local in-cylinder flow.

Spark plug ground electrode orientation has been known to influence engine performance (Burgett et al., 1972; Pischinger and Heywood, 1990). The effect can be attributed to changes in the flow field in the vicinity of the spark plug electrodes, electrical spark energy loss to the electrodes and heat transfer between the flame kernel and the electrodes. Early flame development in a spark ignition engine accounts for a large portion of the complete combustion period and also directly affects the performance of late combustion (Seong-Soo et al., 1995; Witze et al., 1990).

In analysing flame development, Hacoheh et al. (1992) showed that if the flame is convected towards the electrodes, then the contact area of the flame with the electrodes is increased. This leads to unfavourable conditions for flame development. However, when the flame is convected away (detached) from the electrodes, the contact area is small and successful ignition is more likely to occur. Pajot et al. (2000) concluded that the largest flames are found relatively far from the electrodes, due to reduced heat exchange with the electrodes. Therefore, reducing the contact area between the flame kernel and the spark plug leads to a faster flame kernel development (Herweg et al., 1990). However, other researchers (Witze et al., 1981) showed that the fastest burn was achieved with high swirl and when the flame remained attached to the spark plug. They noticed that flame detachment from the spark plug could occur early in the burn, midway, or not at all. However, they suggested that these results should be treated with caution when trying to relate them with production engine performance.

It is well known that the physical properties of the mixture and the local flow field at the spark plug affect the initial flame kernel and subsequent flame development (Petrovic, 1982; Swords et al., 1982; Tagalian and Heywood, 1986). The contact area variation between the flame and electrodes due to flame kernel elongation is influenced by changes in the flow field (Herweg et al., 1988; Pischinger and Heywood, 1990). The early flame propagation speed is known to be increased with turbulence intensity of the in-cylinder mixture (Loye and Bracco, 1987). The flame kernel can be convected away from the spark gap, the direction and extent of motion varying cycle by cycle. The surface of the growing flame becomes increasingly distorted with time by the turbulent flow. Both larger scale structures that persist for some time, and smaller scale wrinkling or distortion are apparent (Gatowski and Heywood, 1984).

Loye and Bracco (1987) showed that as engine speed increased, the shape, size and location of the initial kernel became less repeatable, and that the kernel flame front became more convoluted. Some kernels had a fairly continuous flame front, while others had a much more discontinuous appearance. The apparent discontinuity of the flame front could easily have been caused by a highly convoluted, but contiguous flame front in the direction normal to the measuring plane.

2.4.2 Turbulent Flame Propagation

In the spark-ignition engine, there is usually a sufficiently long period for turbulence to mix the fuel and oxidiser down to a molecular level before a spark initiates combustion. The deposition of energy from the spark generates a flame kernel that grows first by laminar and then by turbulent flame propagation. In consequence, both laminar and turbulent burning velocities are important parameters of a combustible mixture.

The laminar burning velocity u_l can be defined as the velocity, relative and normal to the flame-front, with which unburned gas is entrained into a flat, planar front, and is transformed to products under laminar flow conditions (Heywood, 1988). Laminar burning velocities at pressures and temperatures typical of unburned mixtures in an engine are often measured in spherical closed vessels by propagating a laminar flame radially outwards from the vessel centre. The laminar burning velocity is determined from analysis of successive images of flame-front position, usually established using high-speed cine schlieren photography (Bradley et al., 1998).

Gillespie et al. (2000) defined two turbulent burning velocities; one a turbulent entrainment velocity (u_{te}), based on mass rate of entrainment of fresh unburned gas into the flame, the other a turbulent burning (reacting) velocity (u_{tr}), based on rate of mass reaction. The parameter u_{te} is usually determined on the basis of schlieren photography; u_{tr} is usually derived from analysis of pressure records or laser sheet experiments. In the literature, there is confusion between u_{te} and u_{tr} , with turbulent burning velocity labeled u_t in each case. Bradley et al. (2003) have recently shown how the two different parameters can be related to one another.

Under turbulent condition, the flame front is assumed to entrain and then burn the mixture at a rate governed by the rms burning velocity and the local laminar burning velocity (Stone, 1999). Much experimental work has shown the positive effects of the rms turbulent velocity on turbulent burning velocity (Bradley et al., 1988; Hynes, 1986). As previously discussed in Section 2.2, u' at TDC is generally found to be

approximately proportional to the mean piston speed $\overline{S_p}$. It follows, therefore, that u_t should also increase with $\overline{S_p}$.

Andrews et al. (1975) suggested that the ratio of turbulent to laminar burning velocity (u_t/u_l) is proportional to the ratio of the turbulence intensity to the laminar burning velocity (u'/u_l). Bradley et al. (1992) have correlated turbulent burning velocity with turbulence parameters on the basis of 1650 experimental values generated at Leeds University and elsewhere. At Leeds, data were obtained using a fan-stirred explosion bomb to produce controlled isotropic turbulence. Since the bulk of the experiments adopted schlieren photography, the values of u_t are likely to approximate u_{te} rather than u_{tr} , in each case. The correlations suggested that:

$$\frac{u_t}{u_l} = f\left(\frac{u'_k}{u_l}, K, Le(\text{or } Ma)\right) \quad (2.16)$$

where the ratio of u_t/u_l represents the increase in burning velocity due to the presence of turbulence, u'_k is an 'effective' turbulence intensity (obtained from the Power Spectral Density (PSD) from frequencies corresponding to the Kolmogorov scales to that corresponding to the size of the kernel at any instant (Abdel-Gayed et al., 1987)); K is the Karlovitz flame stretch factor (a ratio of chemical (δ_l/u_l) to eddy lifetime (λ/u'), where δ_l is the laminar flame thickness and λ the Taylor microscale); Le is the Lewis number (the thermal diffusivity divided by the diffusion coefficient of the deficient reactant, D ; thus $Le = k/\rho c_p D$, where k is the thermal conductivity, ρ is the density and c_p is specific heat at the constant pressure). The Lewis number was adopted in place of Markstein number, Ma , (a direct measure of the effect of stretch rate on burning velocity (Bradley et al, (1992)) due to insufficiency of Ma data for generating a correlation.

Bradley et al. (1988) discussed the limiting effects of turbulence enhancement in spark ignition engines. When a flame grows, u'_k increases due to the wider spectrum of turbulence scales available to wrinkle the flame surface; as a result, u_t also increases.

However, as u'_k increases, so does the strain rate and the tendency to quench, as shown in Figure 2.5. Further flame growth leads to a large temperature rise and an increase in u_l . This reduces the Karlovitz flame stretch factor K , and quenching becomes less likely. Thus, flame quenching is most likely to occur in the early stages of flame development, when both the temperature and laminar burning velocity are relatively low. This is particularly true for lean mixtures (low u_l) at high turbulence levels (e.g. high engine speeds), since such conditions lead to high values of K .

A number of alternative expressions exist in the literature (some experimentally, others theoretically-based) (Lipatnikov and Chomiak, 2002). Zimont (1979) developed a turbulent combustion model, leading to the following expression:

$$u_{t,0} = Au'^{3/4} u_l^{1/2} \alpha^{-1/4} L^{1/4} \quad (2.17)$$

where $u_{t,0}$ is the developed turbulent burning velocity, A is a constant, u' is root mean square (rms) turbulent velocity, u_l laminar burning velocity, α thermal diffusivity and L integral length scale. To date, this has proved to be the most successful of the available expressions for u_t in modelling the LUPOE1-D engine (Abdi Aghdam, 2003).

2.5 Cyclic Variation

The existence of cyclic combustion variation in spark-ignited, internal combustion engines has long been recognised; its minimisation is one of the many factors to be considered in the design and control of such engines.

2.5.1 Background

During the early stage of combustion, the flame kernel is small; however, it is then displaced from the spark plug region by large-scale flows in a random way, which has significant effect on the subsequent flame propagation. This can lead to cyclic variation in combustion development. Controlling cycle-to-cycle variation, such that all cycles burn in a similar way, would provide an improvement in fuel economy and exhaust

emission levels (Heywood, 1988). It is believed that if cyclic variation could be eliminated, there would be an increase in power output for the same fuel consumption for weak mixtures. Moreover, cyclic variation in combustion leads to differing amounts of work being produced in each cycle. This leads to fluctuations in the engine speed (Stone et al., 1996).

Many researchers have analysed cyclic variation and improved insight into it, but it is still not completely resolved. Unfortunately, there is little agreement between the researchers who have investigated this problem. Various engine configurations have been used, with both liquid and gaseous fuels, which have complicated the interpretation of the results. Cyclic variation has commonly been attributed to three main factors (Bade Shrestha et al., 2001; Heywood, 1988; Gatowski et al., 1984; Reuss, 2000):

- Variation in the in-cylinder flow (turbulence intensity, turbulence length scales).
- Variation in in-cylinder mixture composition.
- Variation in mixing between air, fuel, and inert gases.

Changes in the in-cylinder motion can result in variation in rms turbulent velocity, u' , and mean flow velocity in the vicinity of the spark gap, which affects the initial flame development and promotes cycle-by-cycle variation. The varying flow at the plug can also have a significant effect on the mixture composition in the vicinity of the spark plug at the time of the spark discharge, and so affects the early stage of flame development. Stone et al. (1996) concluded that bodily displacement of the flame kernel during the early stages of combustion has a major role in the origination of cyclic variation in combustion. In a simulation exercise, Holmstrom and Denbratt (1996) similarly showed that random movement of the flame kernel has a significant effect on the cyclic variation. Variation in the growth rate and the location of the flame kernel very early in the combustion process were considered to influence significantly the cyclic variation in the later combustion development (Hall, 1989; Ozdor et al., 1994).

In their literature review, Ozdor et al. (1994) stated that the shorter the combustion stages (especially in the initial flame kernel development stage), the less was the cyclic

variation. Other researchers, Glover et al. (1988), claimed that cyclic variation was mostly attributable to instability in the position of the axis of the tumbling vortex from one cycle to the next. Petrovic (1982) found that improvement of mixture homogeneity has the greatest effect on the decrease of flame initiation variation and on the reduction of its period. Other researchers, Lee and Foster (1995), stated that the effect of mixture concentration variation in the vicinity of the spark plug gap on the cyclic combustion variation was not significant in a homogeneous mixture preparation for any equivalence ratio. Comparing successive flame ‘contours’ of the fastest lean-condition cycles with those of flames recorded for stoichiometric conditions, Aleiferis et al. (2004) showed both to have similar contour characteristics. It was suggested that the fastest lean flames on a cycle-by-cycle basis might have been richer than the average in the vicinity of the spark plug at ignition.

2.5.2 Cyclic Variation Quantification

A number of parameters to quantify cycle-by-cycle variation have been adopted. Pressure-related parameters, for example, in-cylinder peak pressure (maximum pressure) P_{\max} , and the crank angle at which it occurs $\theta_{p_{\max}}$, have been widely used for characterising cyclic variation (Heywood, 1988). The peak pressure P_{\max} exhibits the largest relative cycle-by-cycle variation at maximum brake torque (MBT) timing (Ozdor et al., 1994). However, they claimed that the crank angle at which the peak pressure occurs ($\theta_{p_{\max}}$) is the most suitable indicator for cyclic variation in the initial flame kernel development stage. One important measure of cyclic variability, derived from pressure data, is the coefficient of variation in indicated mean effective pressure. This is defined as standard deviation in IMEP (σ_{IMEP}) divided by the mean IMEP (\overline{IMEP}) and is usually expressed as a percentage (Heywood, 1988):

$$COV_{IMEP} = \frac{\sigma_{IMEP}}{\overline{IMEP}} \quad (2.18)$$

It can also be defined in terms of peak pressure (maximum pressure). The coefficient of variation of peak pressure is:

$$COV_{p_{\max}} = \frac{\sigma_{p_{\max}}}{p_{\max}} \quad (2.19)$$

2.6 Closure

As clearly stated in Section 2.1 (Introduction), the purpose of this chapter has been to provide a general background for the experimental study reported in later chapters. In-depth reviews of in-cylinder flow, turbulence, combustion and cyclic variation are available elsewhere (Heywood, 1988; Weaving, 1990; Ozdor et al., 1994).

The following chapters are concerned with description of the equipment and methods adopted in the current study, prior to presentation of the results and conclusions of the work.

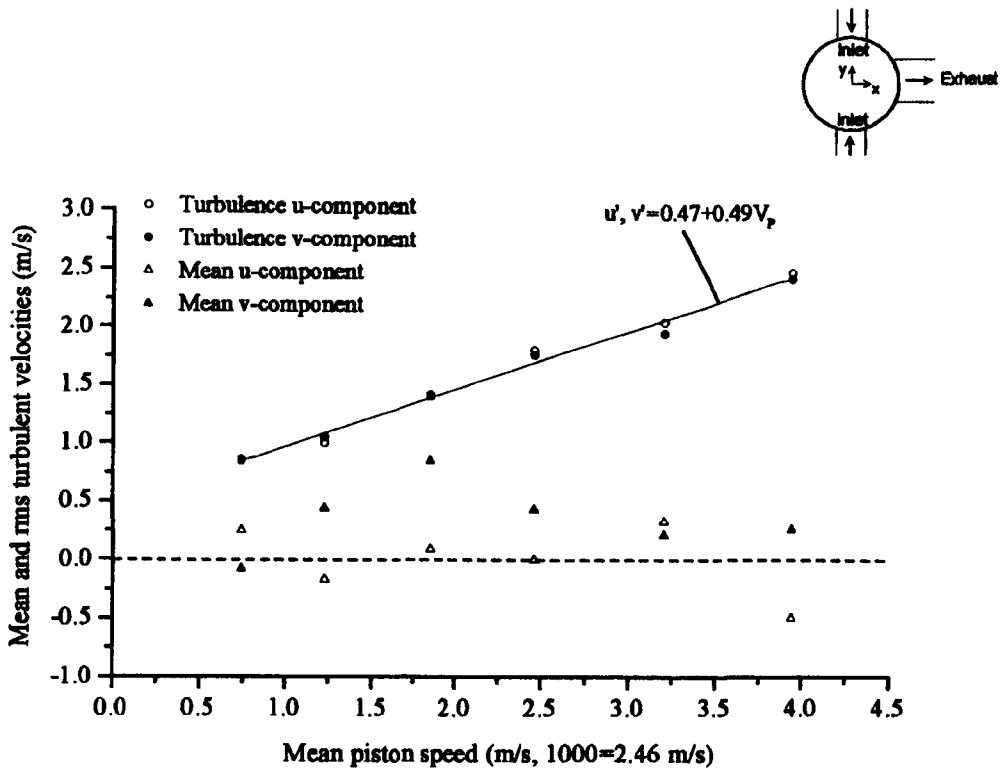


Figure 2.1: Mean and *rms* turbulent velocities in centre of the chamber at TDC versus mean piston speed for LUPOE1-D engine (Atashkari, 1997).

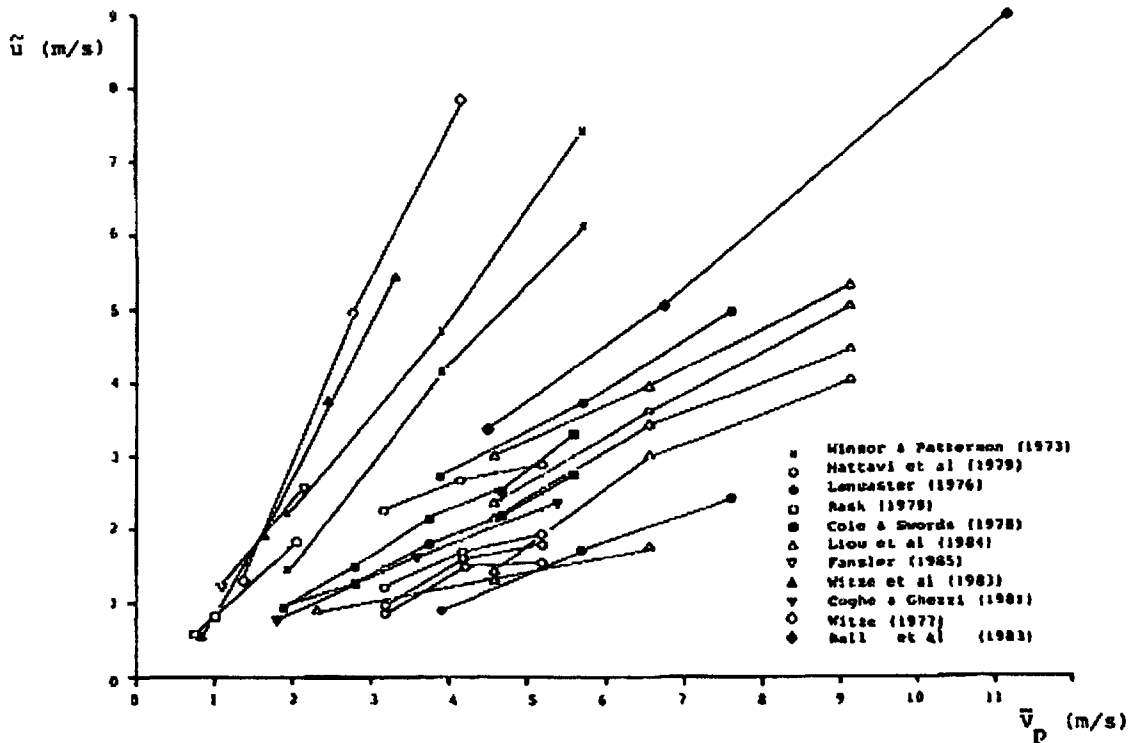


Figure 2.2: Variation of TDC turbulence with mean piston speed: previous investigations (Bopp et al., 1986).

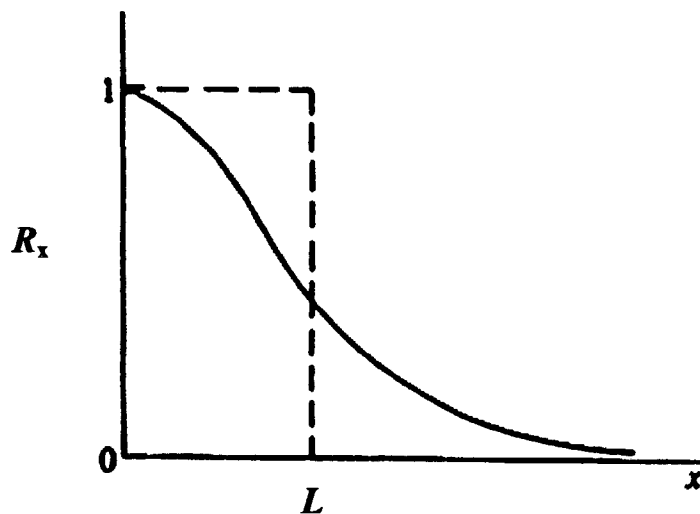


Figure 2.3 Variation of spatial velocity autocorrelation coefficient R_x with distance defining integral length scale (L).

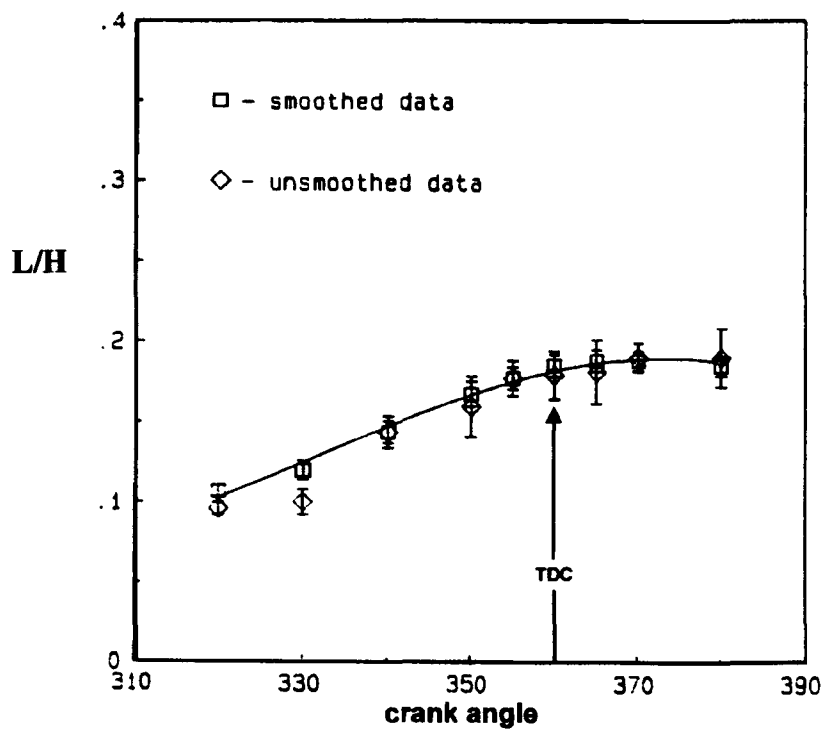


Figure 2.4: Ratio of integral length scale to instantaneous clearance height (L/H) versus crank angle for smoothed and unsmoothed data (Fraser et al., 1986).

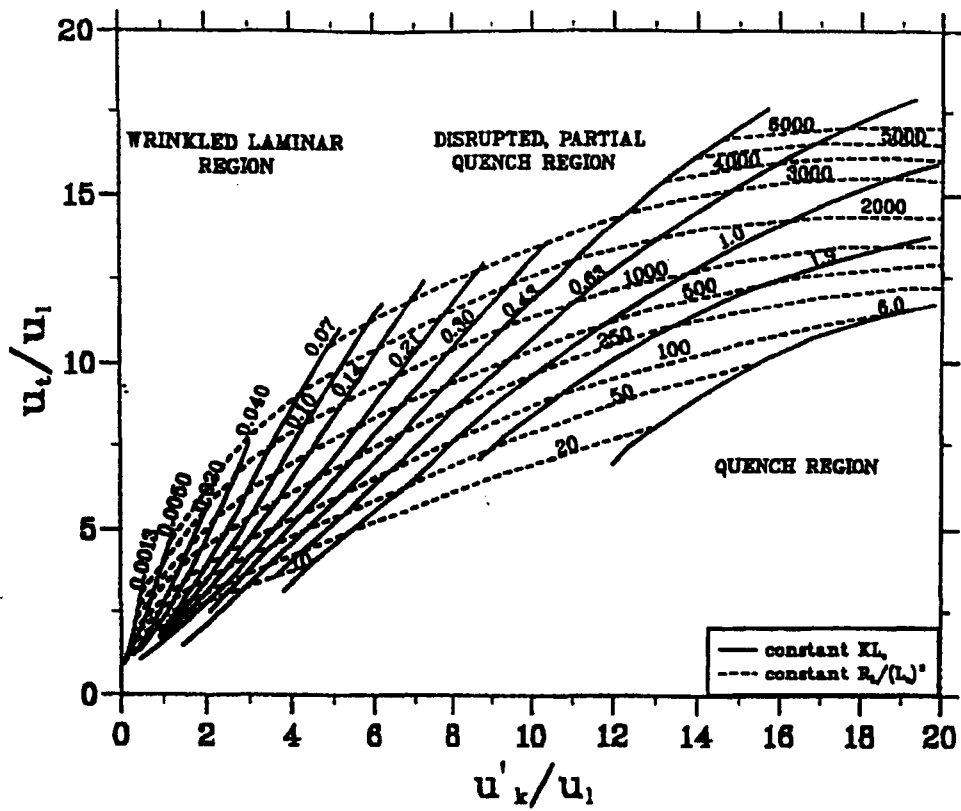


Figure 2.5: Leeds burning velocity correlation for u_t/u_1 against u'_k/u_1 (Bradley et al., 1992).

Chapter 3

Experimental Engine and Instrumentation

3.1 Introduction

Described in this chapter are the two experimental engines, together with the associated equipment and instrumentation, used in the current study. The first engine, designated LUPOE1 (Leeds University Ported Optical Engine Version 1), was based on a JLO L372, ported single cylinder, two-stroke engine (König, 1993). This engine was modified by Hicks (1994) to enable single and multiple laser sheet flame imaging. Further modifications were carried out by Lee (1995) to enable the introduction of axial swirl into the flow. Further studies using the engine and derivatives have been performed by Buran (1998), Gillespie (1998), Cairns (2001), Abdi Aghdam (2003) and Smallbone (2004). Since no new modifications to the engine were introduced in the current study, this engine is only briefly described in Section 3.2; very detailed descriptions are given in the work of Lee (1995) as well as in the other these mentioned above.

The second engine was based upon the more substantial base of a Lister-Petter-PH1; this was heavily modified and designated LUPOE2. The revised engine adopted the same bore diameter as LUPOE1, with which cylinder heads were interchangeable, but with its longer stroke, it was possible to achieve higher effective compression ratios for a given clearance volume. In the work described in this thesis, LUPOE1 was always fitted with the 'disc' (cylindrical combustion space) cylinder head used by earlier workers (i.e. LUPOE1-D) and LUPOE2 with the 'pent' cylinder head described in Section 3.3 (i.e. LUPOE2-P). The specifications of the engines are set out in Table 3.1.

	LUPOE1-D	LUPOE2- P
Bore (mm)	80	80
Stroke (mm)	74	110
Effective Stroke (mm)	52	84
Effective bore/stroke ratio	1.54	0.95
Swept Volume (cc)	372	553
Effective Swept Volume (cc)	266.4	422.2
Clearance Volume (cc)	42.7	51.4
Nominal Volumetric Compression Ratio	7.2:1	9.2:1
Con-rod length (mm)	148	232
Crank throw (mm)	37	55
Exhaust port open/close	108.5° a/bTDC	115.4° a/bTDC
Inlet port open/close	115.7° a/bTDC	120° a/bTDC

Table 3.1 Engine Specifications for LUPOE1-D and LUPOE2-P Engines

3.2 LUPOE1-D Engine

The LUPOE1-D engine used during the current study was a ported, single cylinder engine, with a disc-shaped optical combustion chamber to enable full access for flame imaging. Essentially, just the crankcase, crankshaft and piston of the JLO engine were retained. This crankcase was fitted with a purpose designed and manufactured spheroidal graphite casting with a honed bore. The casting was machined to accepted twin inlets and exhaust pipe connecting to the ports, with flanges to connect to the crankcase and cylinder head, Figure 3.1. To minimise engine speed variations, Hicks (1994), fitted a new flywheel (of a greater mass and inertia than that the original).

The cylinder head, Figure 3.2 was designed for maximum overhead optical access as well as near complete optical access to the clearance height via two side windows, Figure 3.1. The disc shaped optical cylinder head comprised two main parts; an upper 'top hat' section and a lower 'flat' section. The 'top hat' section of the cylinder head was bolted to the lower 'flat' section, which had cavities into which two quartz inserts for laser sheet access and exit were bonded with a silicone based adhesive. A quartz window, which gave optical access to the complete cylinder bore, was fixed into the annular 'top hat' section and secured by a separate metal ring. To allow versatility in

cylinder head design, the cylinder was designed such that the piston at TDC would protrude from the top flange by 12 mm. A seal between the cylinder head arrangement and the top flange of the cylinder was accomplished by means of a Viton 'O' ring. Accurate location of the cylinder head was achieved via two diametrically opposed dowel pins secured in the top of the flange.

A purpose-built spark plug was adopted, as shown in Figure 3.2, to maximise the optical access to the combustion chamber. In some experiments, for better visualisation of early flame development, the spark plug was modified so that the electrodes were clearly visible, as shown in Figure 3.3.

The original JLO pistons were machined flat and fitted with 6 mm thick silver-surfaced mirror when back-reflection shadowgraph film techniques and simultaneous natural light and shadowgraph studies were made. This modification to the piston resulted in a slightly lowered calculated effective compression ratio of 7.2. However, the piston was usually fitted with a disc (instead of a mirror) bonded to the piston crown, machined flat and painted matt black to minimise laser flare when not using shadowgraph film techniques.

Pressurised air-fuel mixture entered the cylinder through two opposed inlet ports and was expelled through an exhaust port at 90° to the inlets (Figure 3.5). To improve scavenging, the radial inlet ports were inclined vertically to an angle of 20° . Lee (1995) fitted a simple brass venturi carburettor to each inlet pipe, together with three electrical 'band' heaters ($2 \times 250\text{W}$ and $1 \times 125\text{W}$) on each inlet line to ensure complete fuel evaporation (Figure 3.6). The top flange of the cylinder barrel was similarly heated to maintain the cylinder at a constant operating condition.

The engine was operated in 'skip fire' mode, to ensure that no residual was left from the previous firing cycle. Skip firing involved a number of motoring cycles (without combustion) between each firing cycle. For example, in the case of a skip fire ratio of five, the engine was fired every fifth cycle, with four motoring cycles in between, as shown in Figure 3.4.

Thermocouples were fitted to the barrel (at three different heights) to measure cylinder wall temperature. Two thermocouples were fitted at the end of each inlet to measure inlet temperature. One thermocouple was fitted on the lower part of the head to measure head temperature. The engine was connected to a DC dynamometer, which could also be used to motor the engine.

To avoid excessive oil fouling of the cylinder head windows, every day before conducting any experiment, a small amount of oil (about 50 ml) was fed into the crankcase through the breather hole. The engine was rotated by hand a few revolutions so that all the moving parts were lubricated. Then the oil was drained out and just a small amount was left in the crankcase to enable the crank assembly to splash the cylinder wall with oil during its motion. However, leakage of mixture into the crankcase caused a pressure build up, augmented by the piston motion during the expansion stroke, within the crankcase assembly. This forced lubricating oil up past the piston rings into the combustion chamber and out past the crankcase seals. To minimise these effects, a Citroën 2CV one-way oil filter/breather valve was installed, via a flexible hose, between a 30 mm diameter hole drilled in the crankcase wall and the exhaust. This arrangement generated a partial vacuum in the crankcase and led to much improved flame image quality (Hicks, 1994; Lee, 1995).

3.3 Modified Petter (LUPOE2-P) Engine

This engine had a longer stroke than that of LUPOE1-D, allowing increased compression ratio for a given clearance volume. The configuration of LUPOE2-P used predominantly in the currently reported study had a compression ratio of 9.2:1 when fitted with the idealised pent-roof cylinder head described later; it was also operated under skip firing condition.

The bore diameter was changed from its original 87.3 mm, to 80 mm, the same as that of the LUPOE1-D engine, so that cylinder heads could be interchangeable. To accommodate the head windows, the spark plug position was slightly offset (by 1.8 mm) from the centre of the bore, as shown in Figure 3.7. Pressurised air entered the cylinder through one inlet port, inclined vertically to an angle of 40° , as shown in Figure 3.8. Early tests showed that the heaters attached to the long inlet pipe were not

sufficient to vaporise the fuel completely and, as a result, the engine mis-fired and incomplete combustion occurred. Therefore, additional heaters were added to the inlet port to ensure mixture vaporisation. Temperatures were recorded by two thermocouples. One thermocouple was fitted at the end of the inlet port, as shown in Figure 3.8, and the other was fitted at the top part of the top collar, as shown in Figure 3.10(c).

3.3.1 Engine Barrel and Assembly

The exhaust system was modified, with multiple small ports in place of the large ports in the cylinder barrel, as shown in Figure 3.9, and connected to two exhaust manifolds. This was intended to improve engine breathing and control of flow in the cylinder. It allowed 'diffusion' of exhaust into an annulus (prior to removal via the two exhaust pipes) to prevent the strong exhaust flow through the single exhaust port experienced with LUPOE1-D (as observed by Cairns, 2001), the latter having created bulk flows in the cylinder which affected the subsequent cycle.

The inlet tube was inclined at a vertical angle (40°) to assist scavenging and promote 'tumble' motion in the cylinder. The barrel comprised four main parts: mounting flange, exhaust collar, top collar, and liner, which are shown in Figure 3.10.

The ported breathing design and the change in bore diameter required a new modified piston with a longer skirt, as shown in Figure 3.11. The top land crevice height of the piston above the top ring was 13 mm. This was to allow for possible mirror attachment for shadowgraph photography, whilst maintaining adequate strength to retain the piston rings. This influenced the amount of mass lost to the exhaust early in the compression process. To allow ready adoption of alternative designs of piston crown, a two-piece piston was adopted, as shown in Figure 3.12. An assembly diagram for the LUPOE2-P barrel is shown in Figure 3.13.

3.3.2 Cylinder Head Arrangements

Pent-roof cylinder heads, 'metal' and 'optical' versions, were used in the current reported study, as shown in Figures 3.14 and 3.15, respectively. The pent angle was inclined on a vertical angle of 21° . The metal version was used initially for finding the

optimum conditions of the engine at different operating conditions (engine mapping). This was to save the less robust optical version from the possibility of damage. The metal head was fitted with two flush-mounted pressure transducers; one, water-cooled, to the top and the other to the side of the chamber. Once the optimum conditions had been determined, only the optical version was used. This was equipped with two top and two side windows for flow studies and flame imaging. The view of the underside, showing the extent of the windows, is illustrated in Figure 3.16(b). Flow studies, employing LDV, were conducted using the top and the side windows of the optical version. Simultaneous top and side natural light flame images and pressure data were also collected using the optical version. Due to the limited space in the top part of the optical version, two side flush-mounted transducers were used, as shown in Figure 3.15. Another barrel and head, made of Perspex, was additionally made and used in the study for cold flow studies by PTV, as shown in Figure 3.17.

3.3.3 Engine Lubrication

The LUPOE2-P required a continuous supply of oil to lubricate the crankshaft and 'little end' journal bearings. The original engine's oil pump was used to supply pressurised oil to these bearings. This created a problem for the new, ported, engine. When dismantling the cylinder head after running the engine, large amounts of oil were observed in the cylinder. A small modification was carried out, installing an oil trap in the lower part of the barrel to minimise oil splashing into the combustion chamber, as shown in Figure 3.18.

3.3.4 Modifications

The design of the new engine (LUPOE2-P) was such that changes could be effected by minor modifications to the cylinder head, liner, exhaust collar or piston crown, as shown in Table 3.2.

	Remarks
Swept Volume	Can be changed by modified liner
Effective Swept Volume	Can be changed by modified liner
Clearance Volume	Can be changed by different heads or different piston crown shapes
Nominal Volumetric Compression Ratio	Can be altered by different heads, liners or piston crown shapes
Exhaust port open/close	Can be affected by liner design
Inlet port open/close	Can be affected by liner design

Table 3.2 Engine Geometry for LUPOE2-P

3.3.5 TDC Setting

Before serious experiments could be conducted using the LUPOE2-P engine, it was vitally important to set the top dead centre (TDC) position correctly, for the subsequent analysis of cylinder pressure data. Three methods were adopted to do this. First, with the cylinder head removed, a dial indicator attached to the top part of the cylinder barrel was used to assess the topmost position of the piston crown. By rotating the flywheel of the engine by hand, the dial indicator detected the highest position (TDC) of the piston. The disadvantage of this method related to piston pin offset at TDC. A second method involved noting the crank angle for peak pressure on a non-firing trace; this had to occur slightly before TDC (Douglas et al., 1997). The second method proved a useful way of confirming the first method (Figure 3.19). Later, a third method was adopted; this involved setting the TDC position by using a proximity meter, as shown in Figure 3.20. With the engine run at low speed, this detected the highest position of the piston crown in a cycle. The shaft encoder output signals and proximity meter readings suggested good agreement for TDC position, as shown in Figure 3.21.

3.4 Air and Fuel Supply Systems

Throughout the experiments, controlled air and fuel supply systems were used. The fresh charge was blown into the engine cylinder under pressure (Section 3.4.1). Under firing conditions, the fuel was introduced via carburettors, fitted to each inlet pipe.

3.4.1 Air Supply System

The air supply for both engines used in the present study was from the laboratory's compressed air line. A Norgen pressure regulator was installed in-line to regulate the delivery pressure to 4 bar (gauge) and the air was filtered to remove any oil and water vapour contamination. The air system was split and delivered to the hoses feeding the inlet lines.

Brooks 5812N Thermal Mass Flow Meters were installed to monitor the airflow rate. The meters were calibrated by the manufacturer at a standard condition (1.013 bar and 0°C) for a full-scale deflection (FSD) flow rate of 400 litres/min, equivalent to 8.6 g/s. A Brooks 5875 display unit was connected to the meters. The unit consists of four channels; two channels were selected, one for each inlet hose. The air then passed through in-line 5-litre reservoirs (air surge tanks) employed to damp air fluctuations resulting from the reciprocating piston motion, before feeding the inlet manifolds (two in the case of LUPOE1-D and one in the case of LUPOE2-P).

3.4.2 Fuel Supply System

The fuel used in the current study was iso-octane (2-2-4 trimethylpentane). The fuel was stored in a one-litre tank, from which the fuel was supplied to an electric fuel pump via a fuel filter. A pressure regulator controlled the delivery pressure of the fuel. The fuel supply was divided downstream of the pressure regulator and flowed via two separate Platoon rotameters. Both rotameters were capable of measuring fuel flow rates between 2 and 25 cm³/min to the two fuel nozzles. The original nozzles used in the LUPOE1-D engine were calibrated by Lee (1995), and the new nozzles used in the LUPOE2-P engine were calibrated during the present study by the current author. Lee (1995) conducted a series of experiments to verify the calculated in-cylinder equivalence ratio,

using a rapid acting sampling ('snatch') valve. The method involved extracting a small sample of gas from the engine's exhaust manifold, which was then passed to a hydrocarbon analyser having a flame ionisation detector (FID) for on-line analysis. In the detector, a small amount of sample gas was burnt in a polarised hydrogen flame located between negative and positive electrodes. As the hydrocarbon in the sample burned, ions were formed at the electrodes. The resulting ions formed caused a current to flow, which was related to the concentration of hydrocarbon in the sample. For the current study, the snatch valve and hydrocarbon analyser were not available and so it was not possible to verify the set equivalence ratio for LUPOE2-P in the same fashion. However, since the configuration of the air and fuel entering supply systems used in current work were identical to those used by Lee, the mixture was assumed correct. The combined fuel-air system is shown in Figure 3.22. A similar fuel-air system diagram for LUPOE1-D is available elsewhere (Abdi Aghdam, 2003).

3.5 Ignition System

The ignition system used for both LUPOE1-D and LUPOE2-P engines comprised a Lucas contact-less electronic ignition unit, a standard Lucas ignition coil, and a 12-volt battery. A purpose-built spark plug was used to maximise the optical access to the combustion chamber (Buran, 1998; Lee, 1995). The control unit for the ignition system counted shaft encoder pulses and triggered the spark at the required crank angle set by the user.

3.6 Pressure Measurement

Cylinder pressure was measured using piezoelectric pressure transducers. This type of transducer contains a quartz crystal, one end of which is exposed through a diaphragm to the cylinder pressure; as the cylinder pressure increases, the crystal is compressed and generates an electric charge, which is proportional to the pressure. However, piezoelectric pressure transducers have a number of disadvantages. They monitor gauge (not absolute) pressure, experience sensitivity to thermal shock, long and short-term drift, and sensitivity to temperature, so that the output has to be referenced at the beginning of each cycle to an absolute pressure (Burnt and Pond, 1997; Douglas et al., 1997; Higuma et al., 1999; Rosseel et al., 1999).

When running the LUPOE1-D engine, an absolute pressure transducer, Kistler Type 4045 A50 (with the range of 0-50 bars), was placed in the cylinder wall just above the exhaust port (108.5° a/bTDC), so that it was protected from combustion pressure and temperature by the piston but was uncovered at later stages of expansion. In the case of the LUPOE2-P engine, when using the above absolute transducer, a non-linear error was experienced. Since it was not possible to obtain an immediate replacement, another available absolute transducer, Kistler Type 4045 A5, was adopted, but this had a range of only 0-5 bar, and it was not possible to use this in firing tests. The engine was therefore motored at different operating conditions similar to those of the firing tests (equivalence ratios, engine speeds, temperatures and air mass flow). The absolute pressure at a given point (80° a/bTDC) from the motoring tests was then used to reference the pressure recorded by the gauge pressure transducer at the corresponding crank angle in later firing tests.

The piezoelectric pressure transducers used in this study for the LUPOE1-D optical head and LUPOE2-P metal head were both water-cooled to minimise the effect of thermal shock. The pressure transducer was selected for its ability to measure a rapidly changing pressure in the range of 0-250 bar. In the LUPOE1-D engine, a Kistler Type 601A pressure transducer was used. Due to the limited space available with the disc-shaped combustion chamber, a 3 mm diameter v-shaped channel was drilled immediately below the pressure transducer mounting position to allow a flow of water to provide some cooling of the pressure transducer (Gillespie, 1998).

In the LUPOE2-P engine, a Kistler Type 601A pressure transducer was installed in the top of the metal pent-shaped cylinder head. It was fitted in a special adapter for water-cooling. A non-water-cooled Kistler Type 601A pressure transducer was fitted in the side. Illustration of both transducers is shown in Figure 3.14. Due to limited space in the optical version, two non-water-cooled Kistler Type 601A pressure transducers were fitted to the sides of the head, as shown in Figure 3.15.

The signals generated by the piezoelectric transducers were transmitted via Kistler Type 5011 charge amplifiers to the computer data acquisition system. The piezoresistive absolute pressure transducers were similarly connected via a Kistler Type 4601A amplifier.

3.7 Crank Angle Position Measurement

Hohner Type 3202 and 3702 shaft encoders were used in conjunction with the LUPOE1-D and LUPOE2-P engines, respectively. In each case, shaft encoders were coupled to the free end of the crankshaft. Both encoders generated 1800 pulses per revolution (PPR), i.e. pulses were generated at 0.2° crank angle increment. The shaft encoders also generated an additional reference signal per revolution for TDC and BDC (bottom dead centre) alignment purposes.

3.8 Data Acquisition System

The analogue pressure pulses from both dynamic and absolute pressure transducers, along with the shaft encoder pulses, were then converted to digital format using an on-line Microlink 4000 analogue to digital converter (ADC). Two channels were used to record these pulses: one was used to record the absolute pressure pulses, the second to record the dynamic pressure, TDC, BDC, spark ignition and shaft encoder pulses. Each channel was capable of data acquisition at up to 1 Msamples/sec with 12 analogue bits (4096 levels), and had a maximum storage capacity of 128 ksamples. Each analogue channel also had four digital inputs, each with one bit accuracy (giving a total of 16 bits).

The pressure signals were sampled mostly with a 200 KHz sampling rate. The start of sampling was controlled by the engine control unit, based upon identifying the BDC of the next firing cycle before starting sampling. The engine control and data acquisition system is shown in Figure 3.23.

3.9 Experimental Procedure

Prior to each experiment, all heaters were switched on with the engine air supply blowing continuously, with the piston at the BDC position. This method ensured a constant and uniform temperature prior to any test recorded. The warm-up period was essential to ensure complete evaporation of the fuel in the mixture entering the cylinder through the inlet manifolds. The charge amplifiers and the Brooks thermal mass flow meter were turned on. The air supply main valve was opened and the air pressure

regulated to 4 bar. Then, the engine was motored by the dynamometer at low engine speed, whilst the air supply was set for both inlet lines. Then, the fuel pump was switched on and the rotameters set to achieve the required test equivalence ratio, using their calibrated values. This procedure was important to minimise the time when setting the fuel and air entering the cylinder during the actual tests.

Before the actual experiments were carried out, the valve controlling the water supply to the cooled piezoelectric pressure transducer was turned on when using the water-cooled transducer. The WAVECAP software used in the data acquisition system was activated to capture and store pressure and shaft encoder signals. The ignition timing, skip firing and the engine speed were then adjusted to meet test requirements. The spark was initiated after a few firing cycles (4 firing cycles), the WAVECAP software was run, and data were saved following actuation of a manual trigger. The temperatures of inlet mixtures and cylinder head were recorded after the trigger.

Following this review of the experimental engine and instrumentation, the next chapter is concerned with techniques used for flame visualisation and flow and turbulence characterisation in the present study.

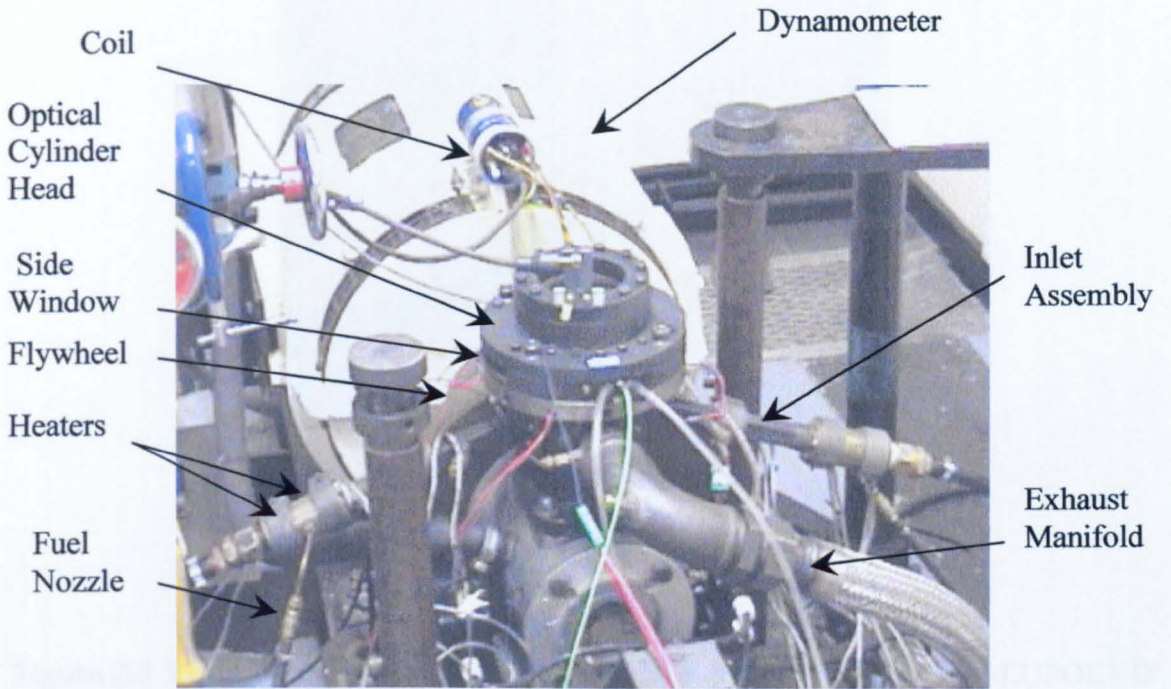


Figure 3.1 LUPOE1-D engine.

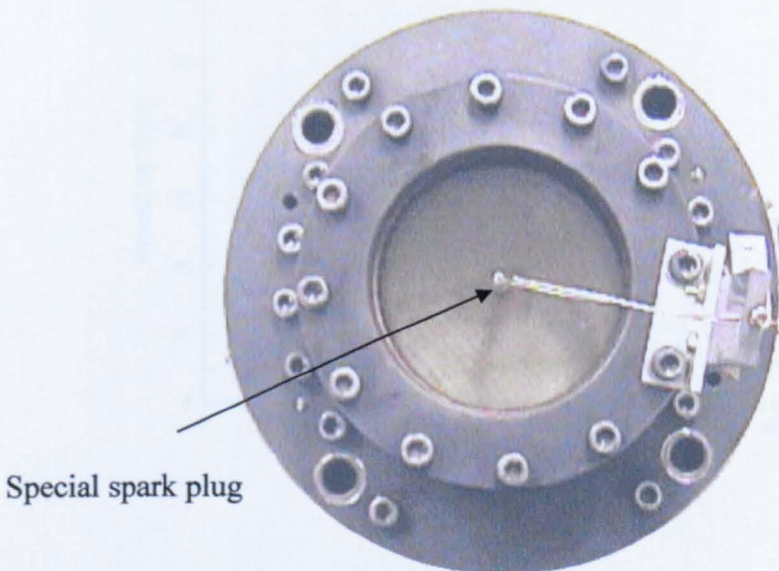


Figure 3.2 Top-view of disc-shaped head for LUPOE1-D, showing purpose-built spark plug for optimum optical access.

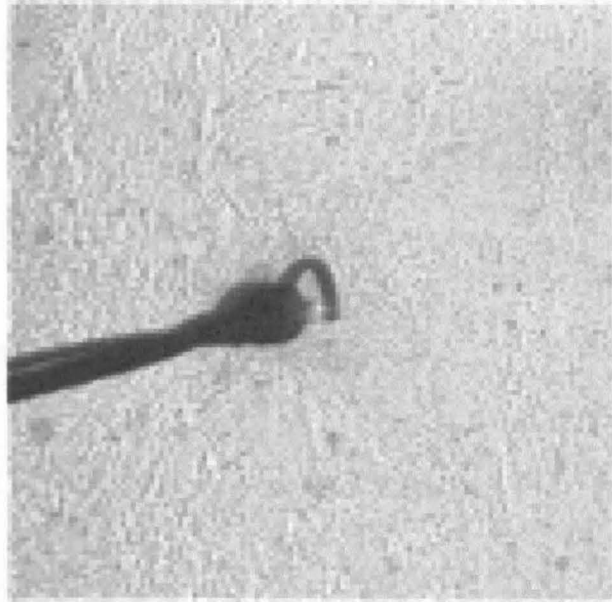


Figure 3.3 Revised spark plug used for observation of spark discharge in LUPOE1-D (note 3mm offset from chamber axis).

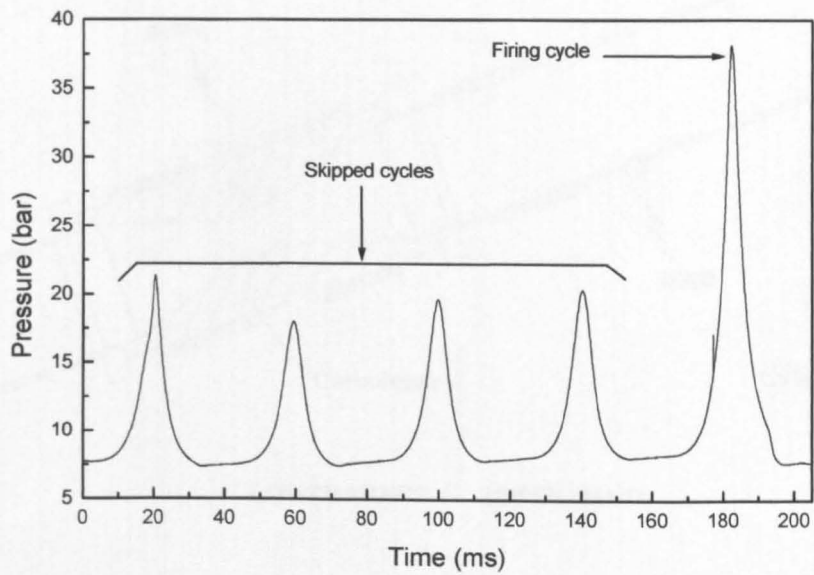


Figure 3.4 Typical pressure record for LUPOE1-D engine running in skip firing mode.

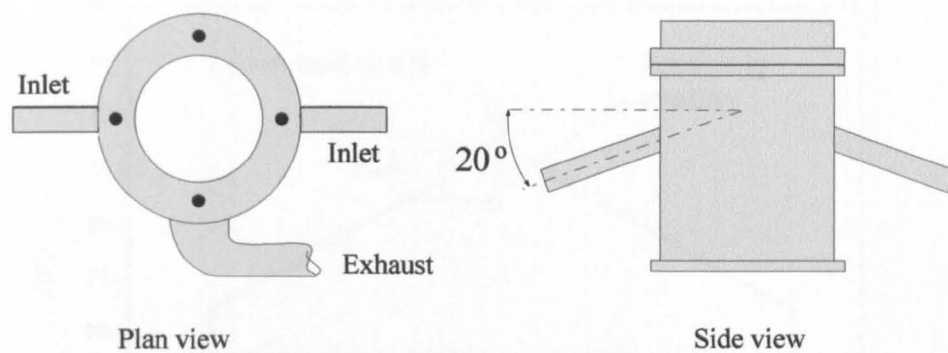


Figure 3.5: LUPOE1-D inlet/exhaust arrangement (Cairns, 2001).

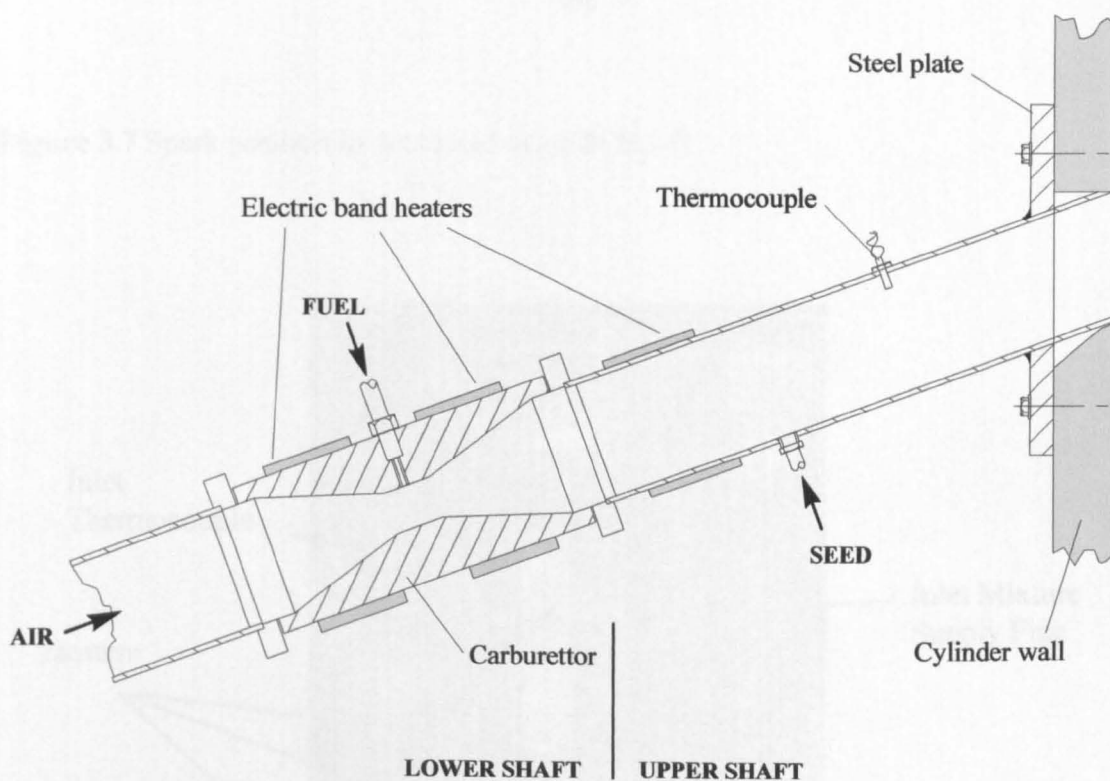


Figure 3.6: Inlet pipe assembly (Cairns, 2001).

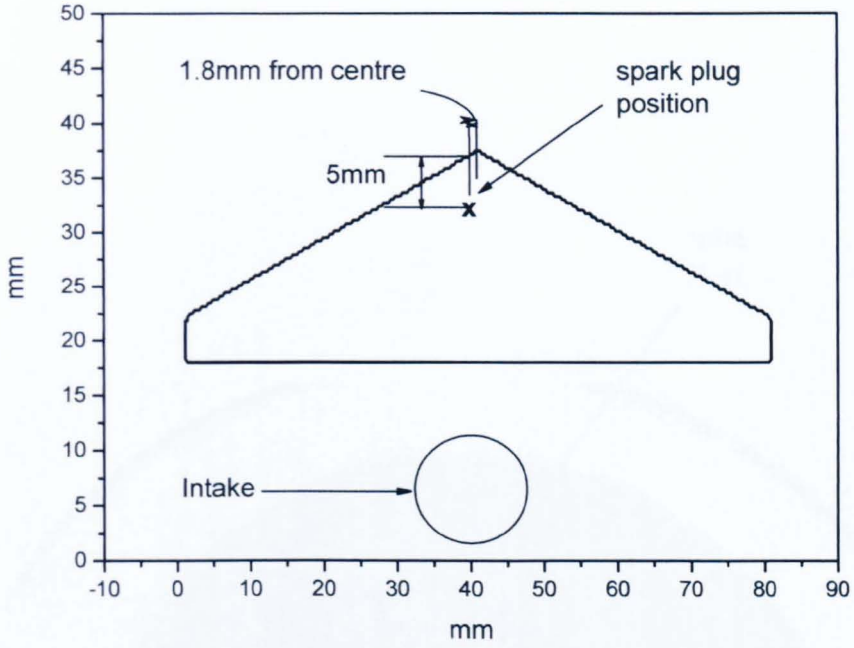


Figure 3.7 Spark position in pent head of LUPOE2-P.

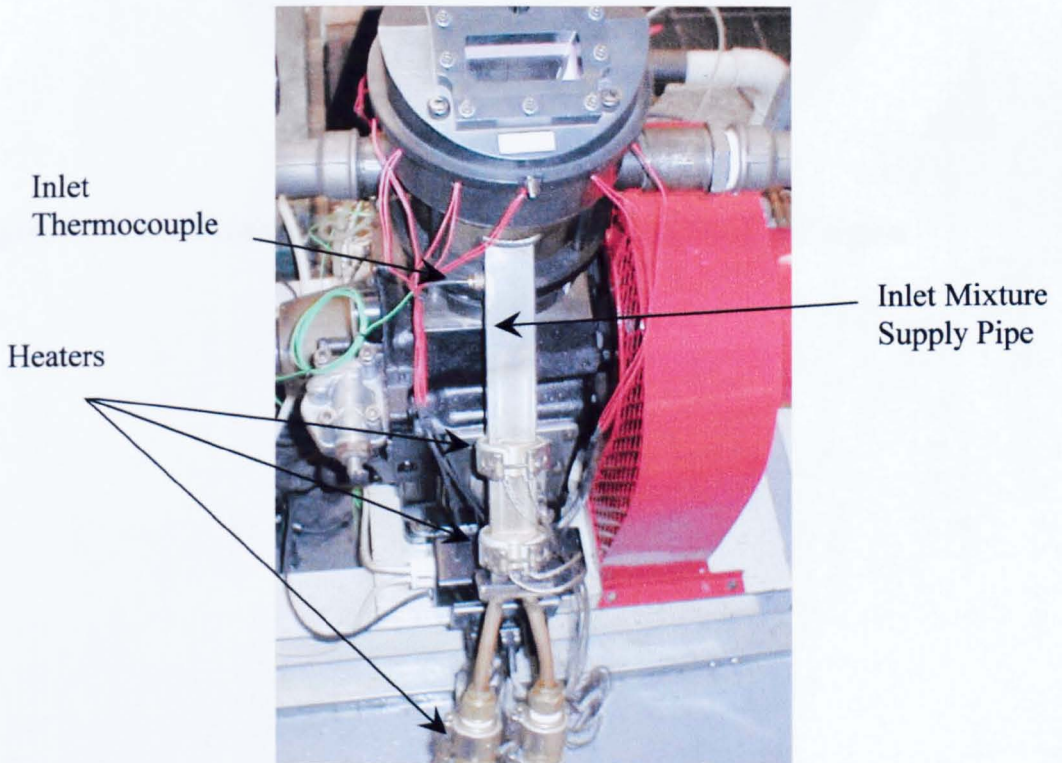


Figure 3.8 Intake supply (pipe inclined a 40° to vertical)-LUPOE2-P.

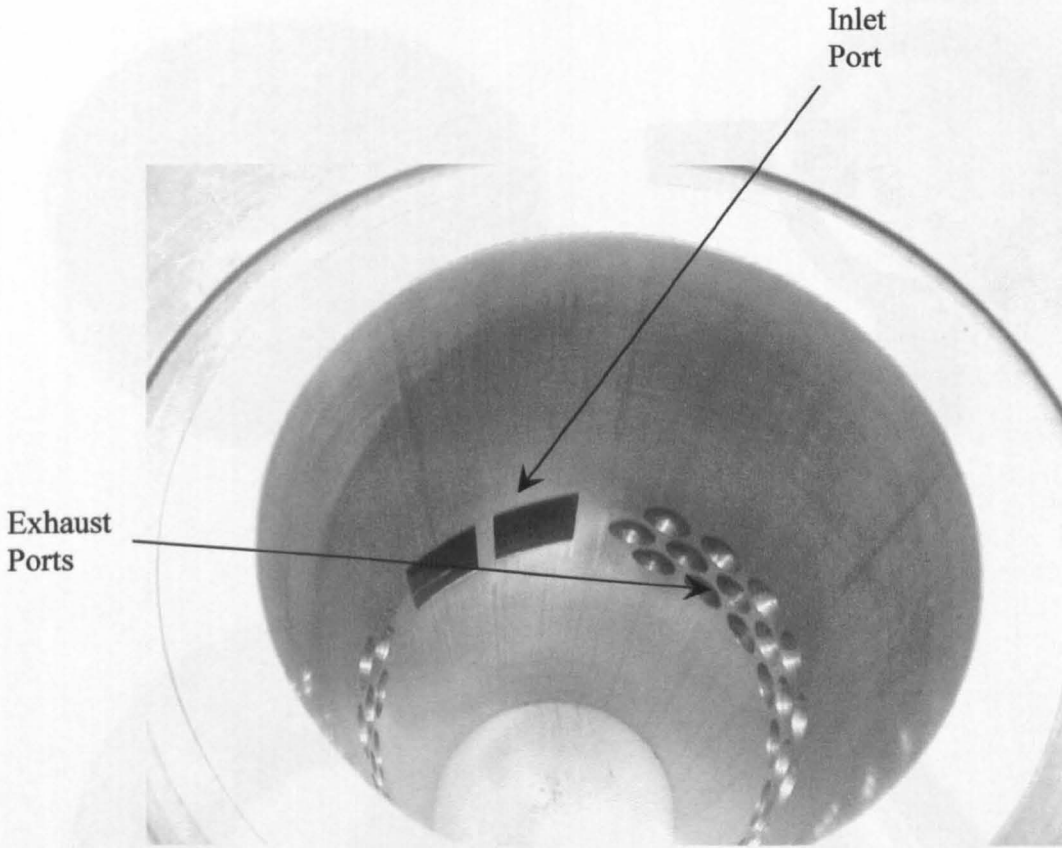


Figure 3.9 Liner showing distributed exhaust ports in LUPOE2-P engine.

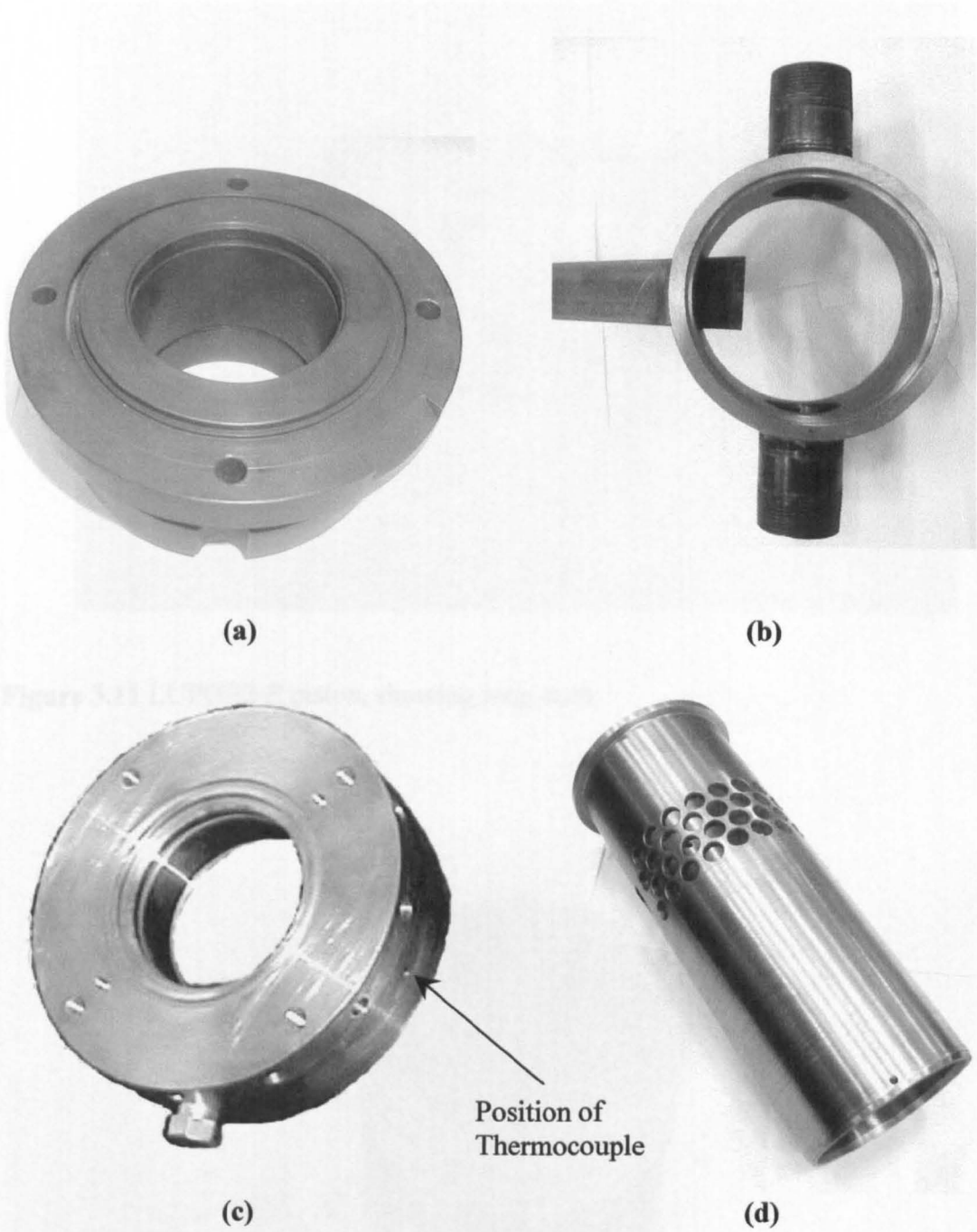


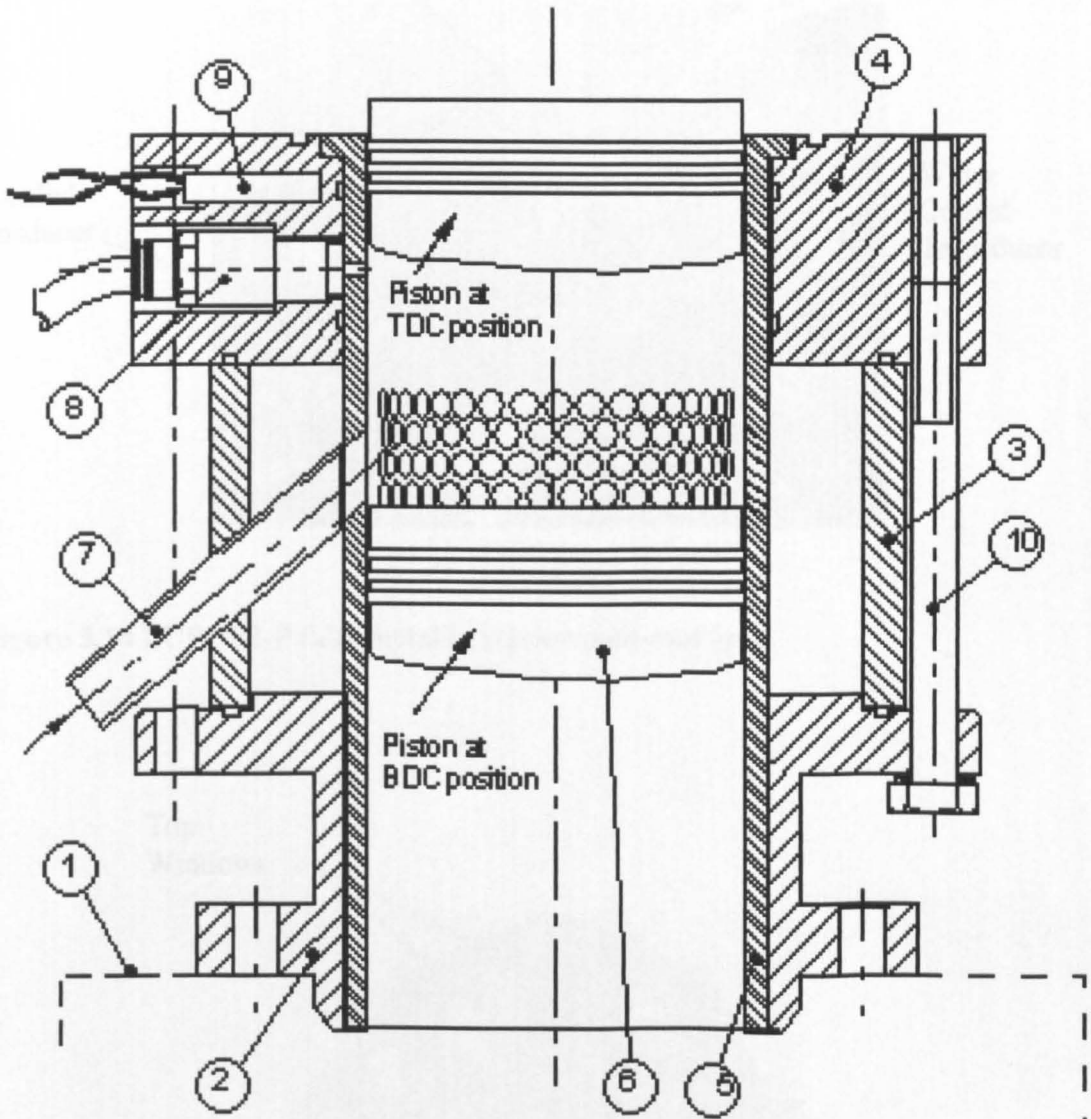
Figure 3.10: (a) mounting flange, (b) exhaust collar with inlet and exhaust tubes, (c) top collar and (d) liner (Abdi Aghdam, 2003).



Figure 3.11 LUPOE2-P piston, showing long skirt.



Figure 3.12 LUPOE2-P two-piece piston.



- | | |
|--------------------|------------------------|
| 1. Crankcase | 6. Piston |
| 2. Mounting flange | 7. Inlet tube |
| 3. Exhaust collar | 8. Absolute transducer |
| 4. Top collar | 9. Cartridge heater |
| 5. Liner | 10. Connecting bolt |

Figure 3.13: Barrel assembly for LUPOE2-P engine (Abdi Aghdam, 2003).

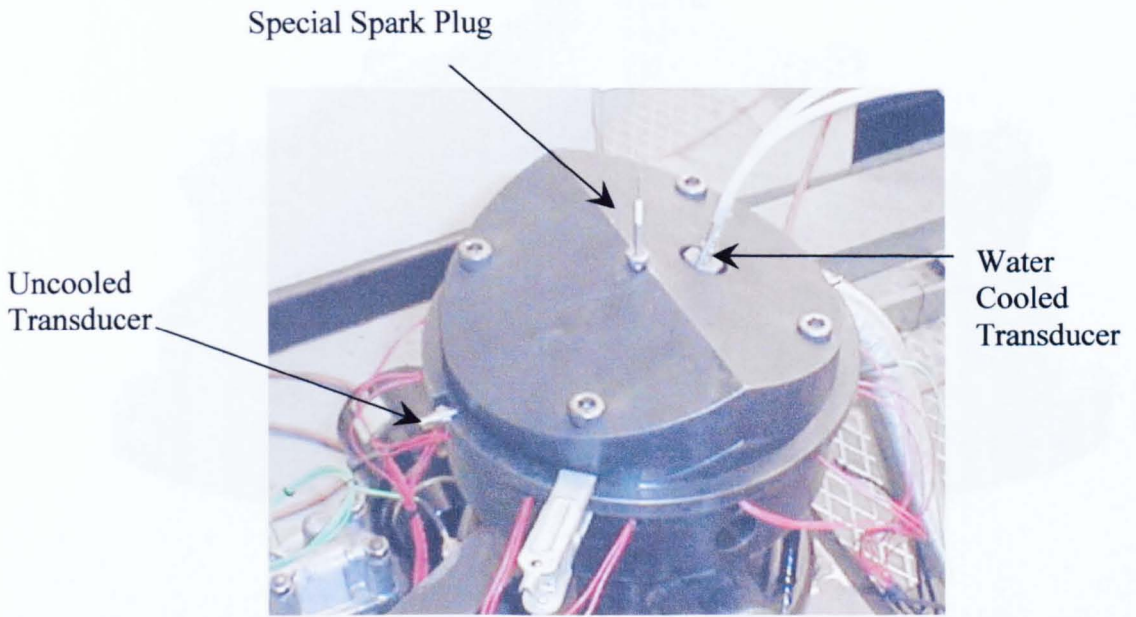


Figure 3.14 LUPOE2-P fully metallic version pent-roof head.

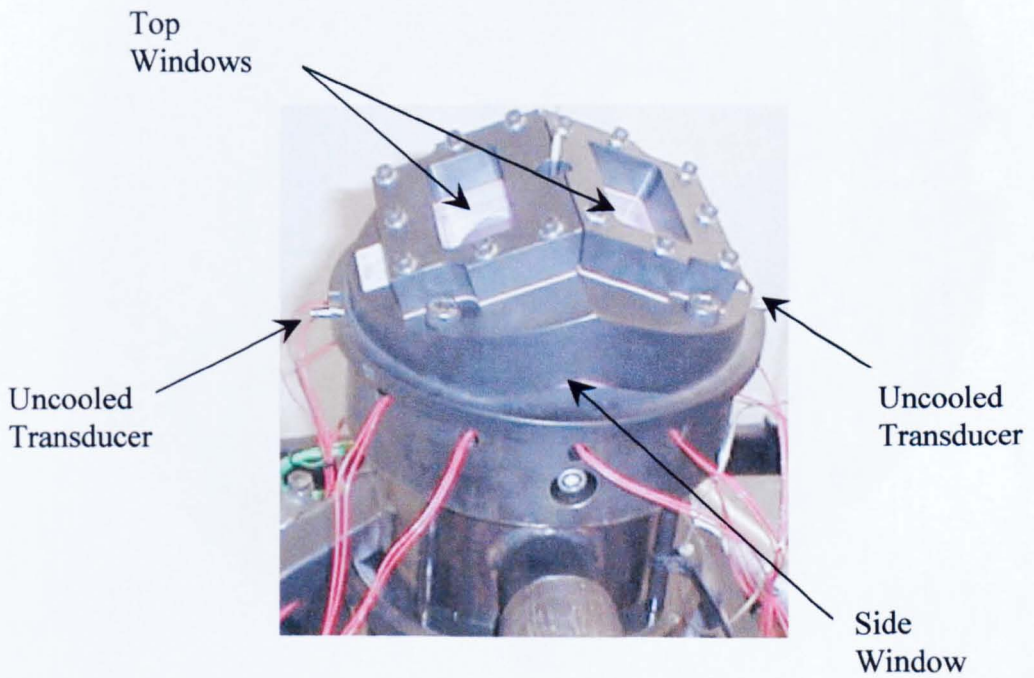


Figure 3.15 LUPOE2-P optical pent-roof head.



(a)



(b)

Figure 3.16 LUPOE2-P optical pent-roof head, (a) side view (b) underside showing extent of window.

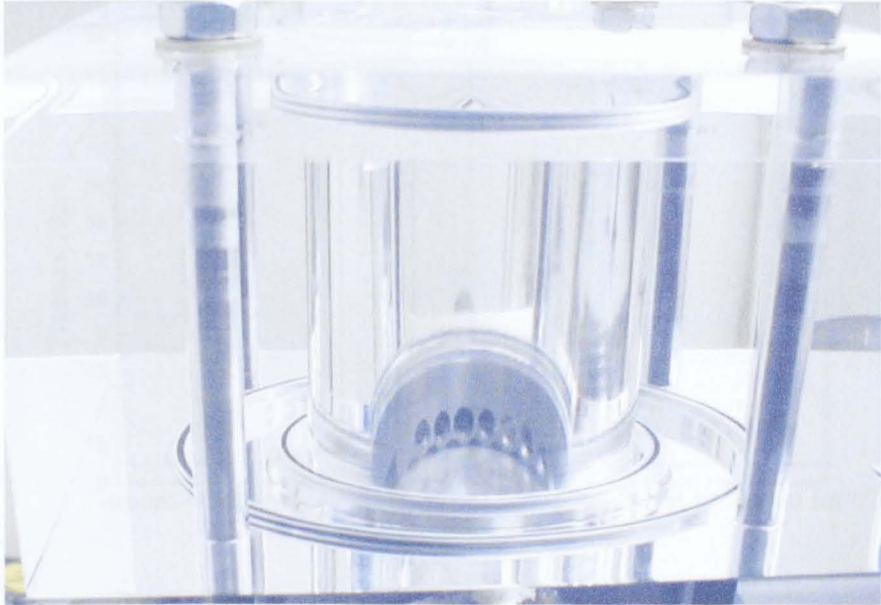


Figure 3.17 LUPOE2-P Perspex barrel and head (with piston close to BDC).

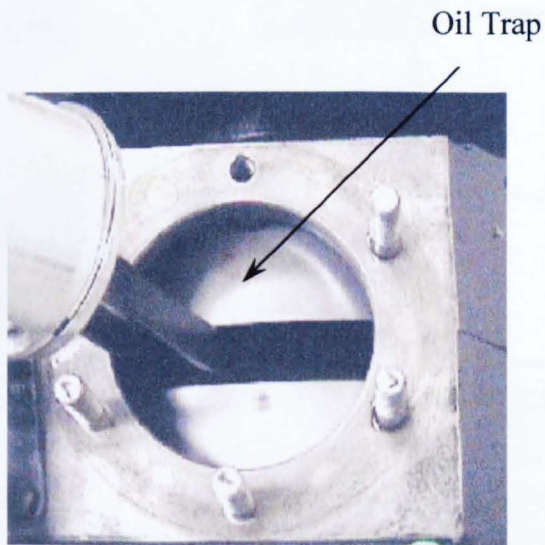


Figure 3.18 LUPOE2-P oil trap.

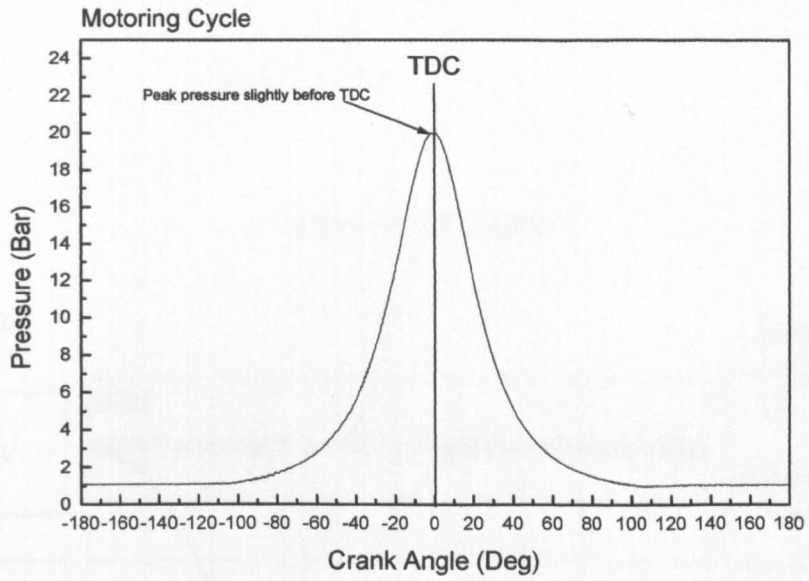


Figure 3.19 LUPOE2-P motoring trace.

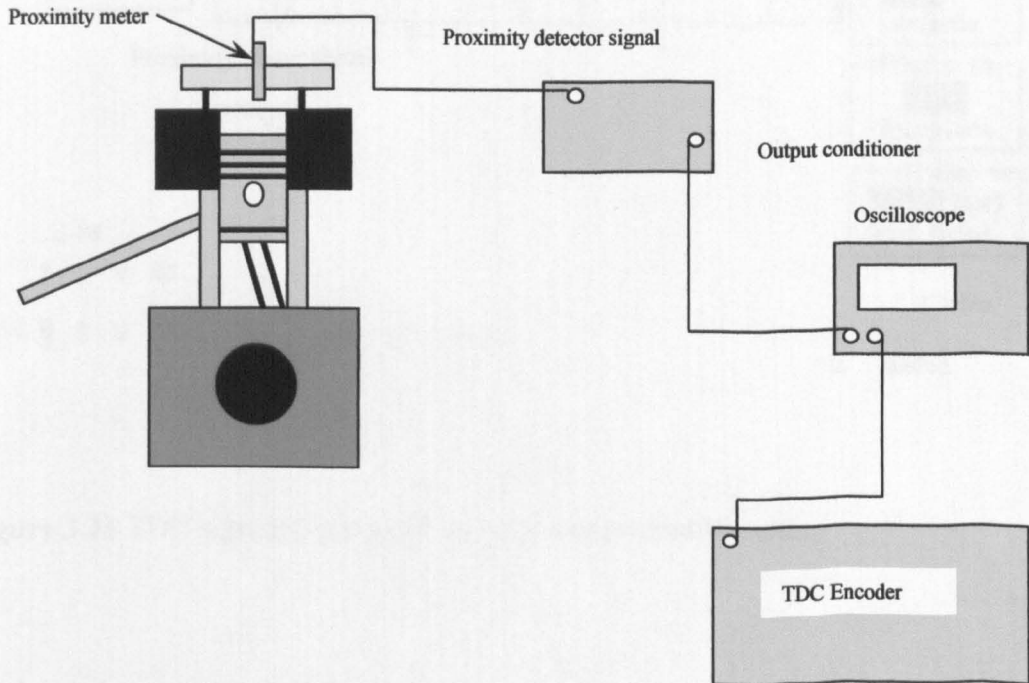


Figure 3.20 Schematic of TDC detection using proximity meter.

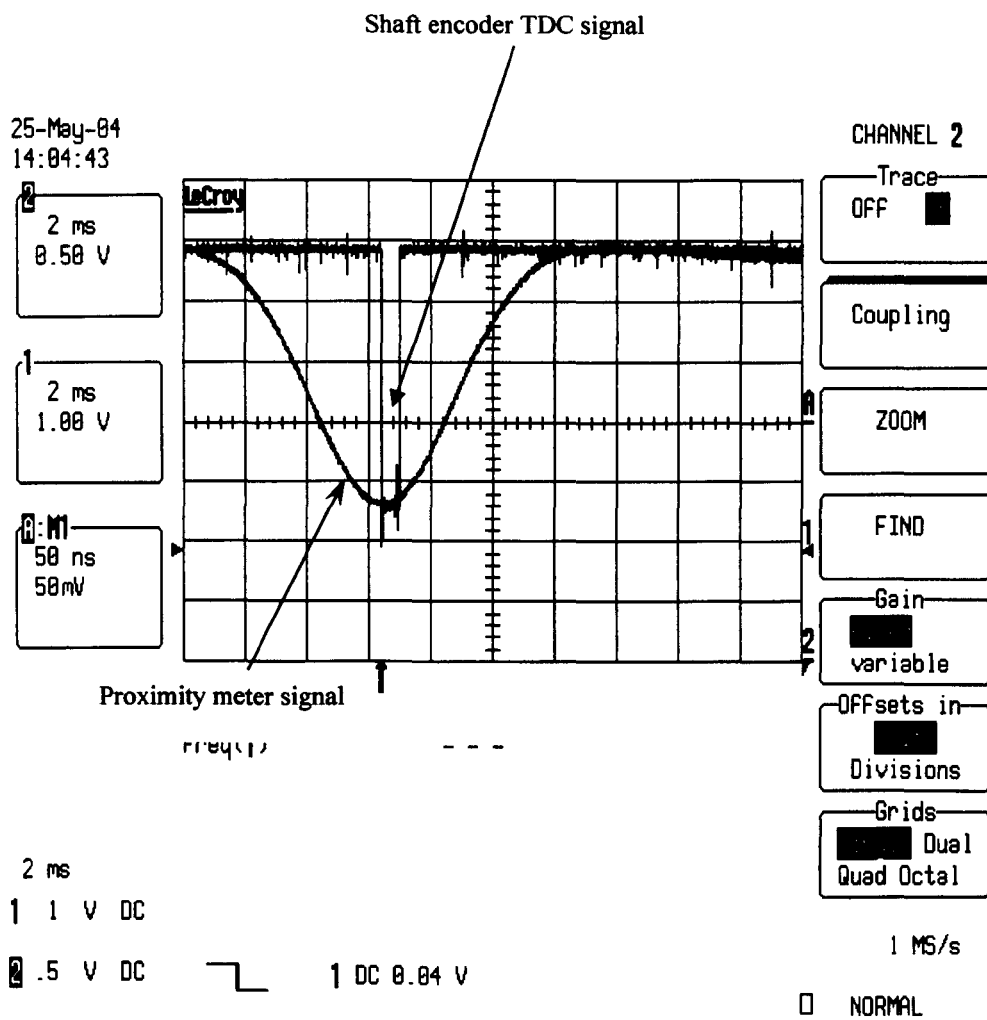


Figure 3.21 TDC signals from shaft encoder and proximity meter.

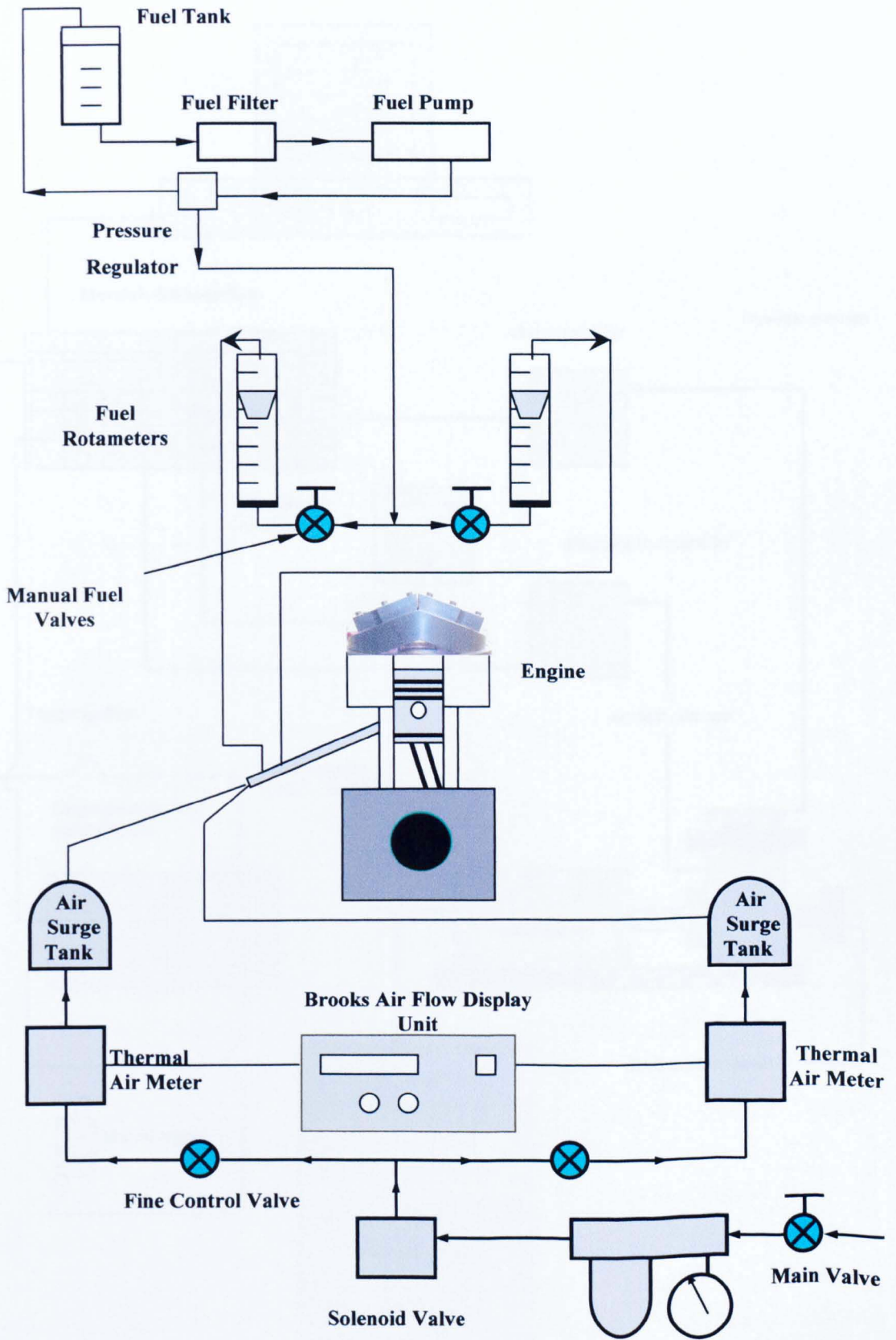


Figure 3.22 Schematic of fuel-air supply and control systems.

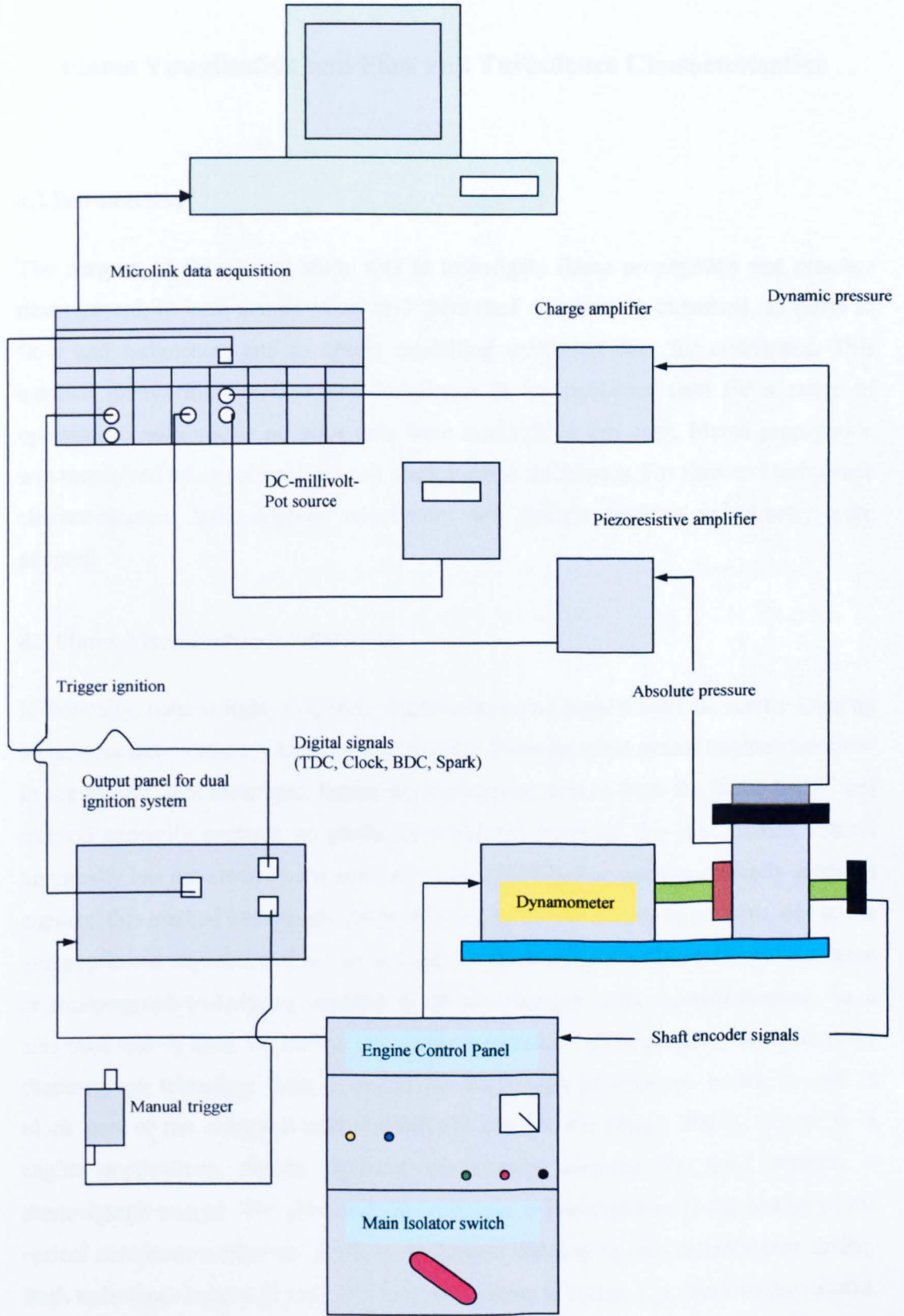


Figure 3.23 Schematic of engine control and data acquisition system.

Chapter 4

Flame Visualisation and Flow and Turbulence Characterisation

4.1 Introduction

The purpose of the current study was to investigate flame propagation and pressure development, in both simple ‘disc’ and ‘pent-roof’ combustion chambers, to relate to flow and turbulence, and to obtain modelling validation data for colleagues. This entailed monitoring the flow and turbulence in the pent-roof case for a range of operating conditions, as no prior data were available in this case. Flame propagation was monitored using natural light and shadowgraph techniques. For flow and turbulence characterisation, laser doppler velocimetry and particle tracking velocimetry were adopted.

4.2 Flame Visualisation (LUPOE1-D)

Historically, natural light, schlieren, shadowgraph and laser sheet Mie scatter imaging techniques have variously been used to monitor flame progress across engine chambers. In the natural light technique, luminosity for imaging comes from the flame itself. This method generally presents no particular problems; however, for lean flames, natural luminosity has not always been adequate (Lewis, 1987). For suitably optically accessed engines, this method has the advantage of being relatively simple to perform, due to the uncomplicated experimental set-up and ease of processing to a binary image. Schlieren or shadowgraph techniques, sensitive to density changes in the imaged medium, have also been widely used. In general, the schlieren technique gives greater contrast than the shadowgraph technique. This is due to the knife-edge or aperture, which is used to block part of the refracted light through the test section (Zhao, 2001). However, in engine applications, density gradients are usually adequate for good contrast in shadowgraph images. The shadowgraph technique is less sensitive to the quality of the optical components than the schlieren technique, leading to considerable cost saving. Both techniques require the use of a mirrored piston, to reflect light back to the camera, unless optical access through both sides of the combustion space is available. The

schlieren method is more sensitive to the inevitable rocking of the mirrored piston surface relative to the knife-edge. This rendered the schlieren technique difficult in the currently reported study, so that natural light and shadowgraph imaging (sometimes simultaneous) were preferred.

4.2.1 Natural Light Imaging

Natural light imaging is relatively easy to perform and involves relatively little data processing time. It was adopted for the LUPOE1-D engine, taking advantage of the excellent full-bore optical access of the disc-shaped combustion chamber, described in Section 3.2. The natural light flame chemiluminescence was captured using the high-speed digital Phantom V4.1 camera. The framing rate for the camera was set to 3700 fps, with an exposure time of 21 μ sec. For visualisation of the entire bore, at this framing rate, the available image size was 256 by 256 pixels. Both Abdi Aghdam (2003) and Smallbone (2004) had previously conducted extensive natural light imaging using LUPOE1-D at a number of engine operating conditions. The current study encompassed both natural light and shadowgraph imaging, sometimes simultaneously, as described later in Section 4.2.3.

4.2.2 Shadowgraph Technique

A shadowgraph technique requires a light source and optical lens to generate a parallel beam of light, which is guided into the combustion chamber. The technique relies on density gradients in the combustion zone to change refractive index and generate an image on screen. Due to the substantial difference between burned and unburned gas densities, the entrainment flame front can be derived from the image. With only (full-bore) overhead optical access, a mirror is needed on the piston crown to reflect light from the chamber. Any piston crown surface rocking motion may displace the image on the screen (Zhao, 2001). The optical set-up of a shadowgraph system is similar to that of schlieren, with the exception that (in the latter method) a knife-edge or aperture is used to block part of the refracted light passing straight through the test section, as discussed above.

The shadowgraph technique was adopted in the LUPOE1-D engine for investigation of early flame development, which was not clear in natural light images due to low light levels and interference from the spark. A high-speed digital Phantom V4.1 camera, 32000 fps maximum framing rate, was adopted. The framing rate was generally set to 11200 fps, with an exposure time of 10 μsec . At this framing rate, the image size available was only 128 by 128 pixels; hence, for good spatial resolution, only the 40 mm diameter central region of the chamber was imaged.

The light from a 12V halogen lamp was passed through a plano-convex lens, where the light beam was focused into the pinhole. The beam was then expanded to 150 mm diameter before passing through a plano-convex lens of 1000 mm focal length; this larger lens was used to form a parallel circular cross-section beam of light with neutral density. This light was then reflected by a 220 mm square silver-surfaced mirror above the engine at an angle of 45° , before passing through the cylinder head window onto the circular silver surfaced mirror bonded to the top of the piston. The light passing back through regions of varying density (and refractive index) at the flame front was refracted and subsequently reflected back to the receiving optics/camera, as shown in Figure 4.1. It was necessary to slightly misalign the input and receiving optics (by $\sim 0.3^\circ$), imaging of a grid placed on the piston crown showed that the resulting image distortion was negligible.

4.2.3 Simultaneous Natural Light and Shadowgraph Techniques

Simultaneous natural light and shadowgraph imaging were also undertaken, for comparative purposes. Beyond the point in flame development where there was adequate luminosity for natural light imaging, the mean flame radii obtained from the two sets of images proved surprisingly similar, giving confidence in the adoption of natural light filming for the later LUPOE2-P experiments, where the optical access requirements for shadowgraph images could not be met.

The same basic set-up used for study of early flame development, Section 4.2.2, was employed, but for the natural light flame images; natural light from chemiluminescent flames was picked up from the 220 mm square mirror at the top of the engine and directed via a 25 mm silver-surfaced mirror to the high-speed digital Phantom V4.1

camera, Figure 4.2. The framing rate for the camera was set to 3700 fps, with an exposure time of 21 μ sec. For visualisation of the entire bore, at this framing rate, the available image size was 256 by 256 pixels, as mentioned above in Section 4.2.1. For shadowgraph flame images, a Hitachi 16HM high-speed ciné camera, which had a maximum framing rate of 10,000 frames per second, was used (as only one digital high-speed camera was available at the time of undertaking these experiments). The set-up for the simultaneous imaging is shown in Figure 4.2.

4.3 Flame Visualisation (LUPOE2-P)

The pent-roof geometry clearly precluded adoption of schlieren or shadowgraph photography. However, the earlier work with the 'disc' chamber had demonstrated (with electronic high-speed cameras) that image definition with a natural light technique was almost as good. Use of natural light imaging also readily allowed a degree of 3D information, using more than one camera. For studies of 3D flame propagation in the pent-roof (LUPOE2-P) engine, simultaneous top and side natural light film imaging was employed, using the optical head version of LUPOE2-P. This involved using two separate Phantom high-speed cameras for top and side flame images. The framing rate for the side camera was set to 7100 fps with an exposure time of 30 μ sec. At this framing rate, the available image size was 256 by 128 pixels. The framing rate for the top camera was set to 3550 fps with an exposure time of 30 μ sec; however, this was achieved with a software setting of 3560 fps. At this framing rate, the available image size was 256 by 256 pixels.

The top two windows were inclined at an angle of 21° to the horizontal. Rather than using a separate camera for imaging each window, four sets of reflecting mirrors were used, so that images from the two inclined windows could be recorded with a single camera, as shown in Figure 4.3. The arrangement involving two high-speed cameras, for simultaneous top and side flame imaging, is shown in Figure 4.4.

The metal retaining clamps of the two overhead windows, as shown in Figure 4.5, precluded imaging the very earliest stages of flame development via the top high-speed camera. The side camera was able to capture the full flame development from initiation (Figure 4.6).

4.4 Flow and Turbulence Characterisation (LUPOE2-P)

For LUPOE2-P flow and turbulence characterisation, both the optical engine variant used in the imaging described above and the perspex variant (Section 3.3.2) giving full access to the cylinder barrel, were used. Both forward and backscatter LDV methods were adopted for point measurements in various places within the combustion space; the measurements made were supported by whole field PTV flow studies carried out using the perspex variant of the engine.

4.4.1 Laser Doppler Velocimetry (LDV)

Light scattering has proved to be one of the most powerful techniques for probing the properties of particulate systems. The technique of using the Doppler shift of laser light to determine velocities was first demonstrated in 1964 by Yeh and Cummins, who observed the shift of light scattered from particles carried in a water flow. Measurements of flow velocities in gases soon followed (Drain, 1980). Laser Doppler velocimetry is generally considered to be the most suitable technique for point measurements of turbulent fluid velocity. In the LDV technique, it is the velocity of small particles embedded in the flow, not that of the flow itself, that is measured (Stevenson, 1976); hence, determination of flow velocity directly depends on the ability of these particles to follow faithfully the fluid flow.

The principle upon which the LDA technique is based is the Doppler effect, where an apparent change in the observed frequency of a wave is a result of relative motion between the source (moving object) and the (stationary) observer. The light source is provided by a laser, which produces a high intensity, continuous, monochromatic, spatially precise beam of light which is first split into two beams which are then made to cross. When the laser beams, at same frequencies cross, they produce stationary fringes (a pattern of bright and dark stripes). As such, it is not possible to infer the direction of the flow since a particle moving through the interference fringes in one direction would produce the same Doppler frequency as one moving in the opposite direction. In order to resolve this problem, two coherent laser beams that have slightly different frequencies are crossed. This is accomplished by applying a frequency shift to one of the beams (utilising a Bragg cell). Such an arrangement produces a moving

system of fringes, which is formed in the intersection volume. Small particles suspended in the fluid act as moving receivers and transmitters of light waves, which scatter the oncoming laser radiation. Movement of a particle in one direction lowers the frequency difference, and, in the opposite direction, raises it. The scattered light is received by a photodetector (Drain, 1980), which converts it into an electrical signal. Since both Doppler shifted waves are scattered from a particle onto the detector, the resulting frequency difference can be readily determined. The particle velocity can be calculated from the frequency shift of the scattered light. The resulting frequency difference is given by:

$$\Delta f = \frac{2v}{\frac{1}{2}(\lambda_1 + \lambda_2)} \cos \beta \sin \alpha + (f_{s1} - f_{s2}) \quad (4.1)$$

where $v \cos \beta$ is the component of velocity normal to the direction of the intersection of the two beams, λ_1 and λ_2 are the wavelengths of the incident beams, f_{s1} and f_{s2} are the frequencies of the incident beams and α is the angle between the beams.

The intensity of light scattered onto the detector rises and falls at a rate directly proportional to the velocity of the particles (Durst et al., 1976). The instantaneous velocities were measured and then the rms velocities calculated from an array of instantaneous measurements by the Dantec BSA software. By translating the position probe volume, the velocity could be measured at different points within the cylinder.

A Spectra Physics Stabilite Model 2017-04S argon ion laser was used in the currently reported study. It had a broadband rear mirror in the laser cavity, allowing a multi-line laser, with wavelengths in the range of 457.9-514.5 nm. For LDV measurement purposes, the multi-line laser was separated into its single wavelength components, and each component was divided into two beams. This was done with a Dantec 60x40 transmitting box, which is an integrated Bragg cell (beam shifter) and colour separator unit. The multi-line laser beam was first diffracted to its zero and first-order components by 40MHZ frequency shifting through the Bragg cell. These were then separated into three wavelengths by a prism in the colour separator unit, and directed to vertical outputs on the top of the transmitter box. These outputs allowed mounting of Dantec 60x24 manipulators for positioning and angling beam pairs into optical fibres. In the

currently reported study, only the longest wavelength, 514.5 nm (green), was applied. This allowed measurement of one velocity component (1-D LDV). For this configuration, both the zero and first-order green beams were transmitted from the manipulators to the distributor box at the rear end of the transmitter box into separate fibres. A 40 m long integrated LDV optical fibre link was used to transport the two beams from the distributor box to a Dantec 60x10 probe, with 38 mm beam separation. A 160 mm focal length lens was mounted in the front of the probe to focus the two beams and form a measurement volume at their crossing (Jakubik, 2002).

Two methods of light reception were applied, forward and back scatter (FS and BS). In FS, light was received by optics on the opposite side of the measurement volume, i.e. received light direction was forward relative to the beam propagation. However, in BS, light was received by the same lens used to focus the laser beams; i.e. the direction of received light was backward relative to the beam propagation.

For both configurations (FS and BS), a TSI Model 9162 photo-multiplier was used to convert the scattered light to electrical signals. In the case of FS, the scattered light was transferred directly from the receiving optics to the photo-multiplier, which was mounted on the top of the receiving optics, as shown in Figure 4.7. However, in the case of BS, the scattered light was transmitted to the distributor box by the fibre link, then to the photo-multiplier by a separate fibre, as shown in Figure 4.8.

The received signals (both methods, FS and BS) were analysed using a Dantec BSA (Burst Spectrum Analyser) F70. The processor was connected to a PC and controlled by BSA flow software supplied with the processor by Dantec.

Experiments for the pent-roof shaped engine (LUPOE2-P) were conducted with the engine motored over a range of engine speeds (750, 1000, 1500 and 1900 rpm). Both FS and BS techniques were employed at different times, as discussed above, to measure in-cylinder velocities at a number of different locations within the chamber. Forward scattering is characterised by its strong signal to noise ratio, but it requires at least two optical accesses to the engine, as illustrated in Figure 4.7. Though it has a lower signal to noise ratio, backward scattering is necessary when only one optical access is available (Figure 4.8). Two orthogonal velocity components were generally measured

(not simultaneously, since only single component measurement was possible with the available equipment).

The LDV technique is an absolute velocity measurement method, requiring no calibration. Under optimal conditions (good seeding, well defined geometry, etc.) the accuracy of LDV, when compared with other available techniques, is exceptionally good. The accuracy of the LDV technique is dependent on the concentration of the seeding within the flow (Lading, 1994). In this respect, the flow within the reciprocating engine involves more problems than almost any other type of enclosed flow because the seeding concentration will vary throughout the cycle of the engine, due to the movement of the piston. Seeding particles must be added to the flow to provide sufficient scattering sources. If the particles are too large, they will not follow the flow; resulting in an inaccurate representation of the fluid velocity. If the particles are too small, they will not scatter sufficient light to provide the signal-to-noise necessary to minimize measurement uncertainty in the signal processing electronics. For all these reasons, the selection of the seeding material and the particle size requires careful consideration. At Leeds University, Jakubík (2002) explored the use of silicon oil droplets and olive oil droplets. The former was found to result in a poor validation rates, whereas the latter gave acceptable signal strength. Olive oil was used in the current study and found to yield superior data quality.

The air flow rate to the engine was set at 6.89 g/sec (equivalent to 80% of the 400L/min full scale reading of the available air flow meter (Section 3.4.1)) and seeded with olive oil. A small portion of air (3 % of the 80% of the air flow-rate in the case of forward scatter (FS), and 10% of the 80% in the case of backscatter (BS)) from the main fuel and air supply tower was fed to a SCITEC LS-10 liquid seed generator. The seeding generator worked by injecting air into a fluid (olive oil) at near sonic velocity through a number of Laskin nozzles. Each nozzle produced micro-bubbles with micro-droplets inside. These bubbles reached the free oil surface and burst, releasing the micro-droplets. Internal baffles were used to remove unwanted large droplets that could be produced by the splash when a bubble bursts (Oxford Lasers, 2005). This mixture of air and micro-droplets was then directly taken from the cylindrical reservoir (3% in the case of FS, and 10% in the case of BS) to the engine ports and blended back into the main air supply (77% of air flow-rate in case of FS, and 70% in the case of BS, which

was fed from the main fuel and air supply tower, this gave a total of 80% of the 400L/min for each case (FS and BS configurations)), as shown in Figure 4.9. Full details of the LDV system, setting and preparation are described elsewhere (Jakubik, 2002).

The diameters of the generated droplets were in the range 0.5 to 5 μm depending on the operating conditions (pressure drop across nozzles, height of liquid level in reservoir), and applied liquid properties.

In LDV, the uncertainty in both the mean and rms velocities can be reduced by increasing the number of individual tests and achieving high LDV data rates. In the current study, several tests were carried out for each position measured and at each engine speed tested, until the data rate proved satisfactory (~ 12000 Hz for forward scatter (FS) and about 1000-2000 Hz for backscatter (BS) configurations). Measuring uncertainty with LDV can also result from relative motion of the LDV probe and the combustion chamber. For a fixed LDV probe position, such relative motion can arise from engine vibration. The vibration associated with engine speed variation was minimised by the large and heavy flywheel attached to the engine.

The measurement points and directions adopted when using the FS and BS configurations are set out in Chapter 7 (Section 7.3.2). General specifications are tabulated in Appendix A.

4.4.2 Particle Tracking Velocimetry (PTV)

Although LDV velocity data were able to provide much useful insight into the in-cylinder flow, in addition to the required rms velocity fluctuation data, it proved hard to interpret the complex and unsteady flow from the restricted number of positions and directions accessible in the pent-roof chamber. Whole field measurement techniques have been developed to overcome such problems. Whole field measurements are most usually undertaken using particle image velocimetry (PIV) techniques (Calendini et al., 2000; Eric, 1997; Fujimoto, 2002), which have made rapid progress in recent years. No such system was available to the study at the time the currently reported work was

conducted. Hence an alternative particle tracking velocimetry (PTV) was used to characterise the complex in-cylinder flows.

In particle tracking velocimetry (PTV), particles are introduced into the flow and subjected to intense stroboscopic illumination, so that their successive positions can be recorded photographically. In PTV, individual particles or group of particles are identified and matched between exposures, so that their displacement, and hence velocity, may be measured (Neußer et al., 1995).

In summary, when applied under optimal seeding conditions, PTV allows the tracking of individual and relatively large particles (which follow the large-scale turbulent structures) to resolve the in-cylinder flow development throughout relatively long periods of individual engine cycles (Adrian, 1986). This has the advantage of enabling video presentation of data and animations, in addition to vector plotting.

In the currently reported study, a planar laser sheet Particle Tracking Velocimetry (PTV) technique based on the Mie scattering principle was developed to visualise the in-cylinder flow under motoring conditions at two engine speeds (750 rpm and 1500 rpm). An Oxford Lasers Model LS20-50 copper vapour laser was used as the light source for the 2-D imaging experiments, using the Perspex cylinder barrel and head version of the LUPOE2-P engine shown in Chapter 3 (Section 3.3.2). The experimental process involved seeding the mixture entering the engine cylinder with relatively sparse and large particles (typically $< 70\mu\text{m}$); these particles passed through the laser sheet, scattering light towards a camera positioned normal to the plane of illumination. More details of the laser system used in the currently reported study are available elsewhere (Cairns, 2001; Gillespie, 1998).

The 2-D imaging technique required the laser light to be formed into a thin sheet which was then passed through the scattering medium. The apparatus utilised during the experiments is shown schematically in Figure 4.10. Upon exit from the laser head, the 25 mm laser beam was aligned to the desired height, using five 45° dichroic mirrors. A 1000 mm focal length; spherical convex lens focused the beam to the centre of the bore; a 500 mm plano-convex cylindrical lens then formed the light into a thin sheet passing through the centre of one of the top windows. It was necessary to keep the sheet

thickness as thin as possible, estimated to be 250 μm (Woolley, 2005). The laser sheet was positioned in the vertical plane, in the centre of the window opposite to the inlet. The central plane was chosen to allow an element of comparison of the data with LDV measurements (shown later in Chapter 7) taken in the same position.

The air flow rate was set at 6.89 g/sec (80% of the maximum 400 L/min for the meter) and seeded with white pepper (size < 70 μm). A high-speed digital Phantom V4.1 camera was used in the currently reported study, with a framing rate of 2000 fps and a laser frequency of 10 KHZ. At this framing rate, the available image size was 512 by 256 pixels. The particle tracks were to an accuracy of ± 1 pixel ($\pm 80\mu\text{m}$). This error corresponded to a maximum velocity error of $\pm 0.12\text{m/s}$ in calculation of particle velocities.

The LDV technique is insensitive to the properties of the gas under investigation and requires no calibration; it is the more accurate of the two velocity techniques adopted. However, this method yields ensemble averaged rather than cyclically resolved velocity. The whole flow field PTV technique helped to uncover intermittent flow patterns masked in the LDV measurements.

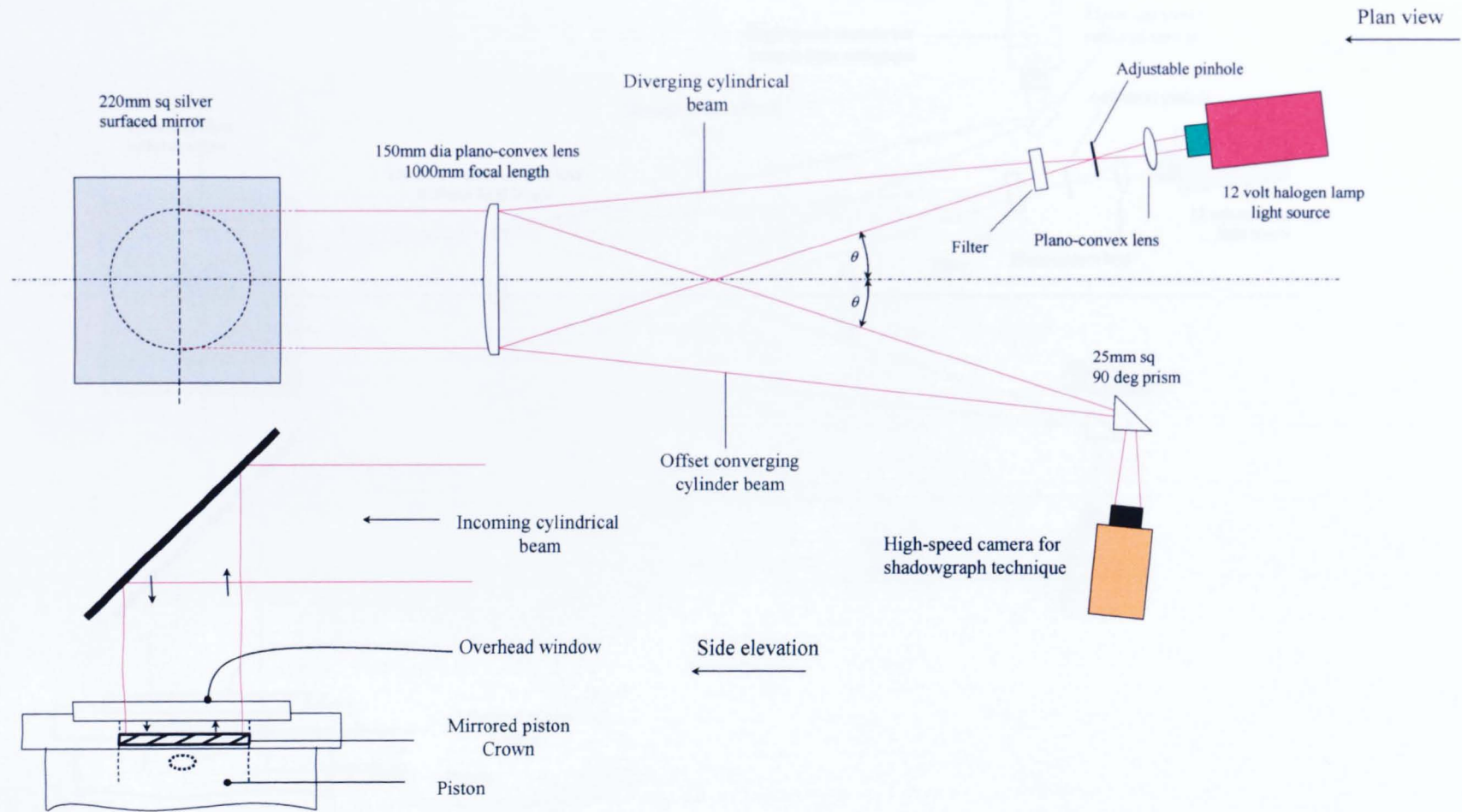


Figure 4.1 Diagrammatic representation of arrangement for imaging (LUPOE1-D), offset angles of incoming beam and return optics are exaggerated for clarity (actual angle $\sim 0.3^\circ$, the small offsets between the 150 mm plano-convex lens and the piston crown mirror are ignored in the diagram, for clarity).

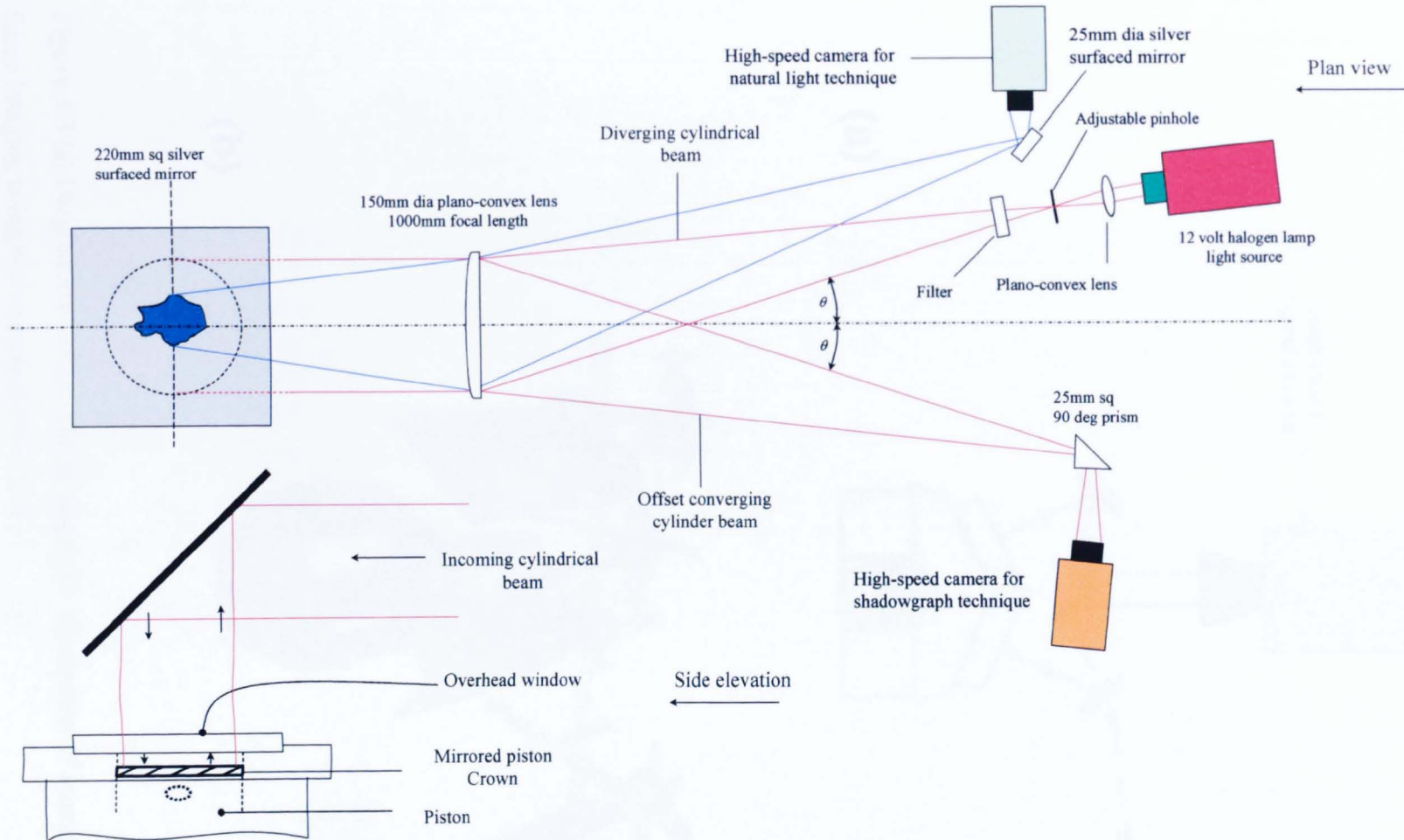


Figure 4.2 Set-up for simultaneous shadowgraph and natural light imaging (LUPOE1-D), offset angles of shadowgraph incoming beam and return optics are exaggerated for clarity (actual offset angle $\sim 0.3^\circ$). Similarly the offset viewing angle for natural light imaging was $\sim 0.6^\circ$. As in Figure 4.1, light offset angles between the 150 mm plano-convex lens and the piston crown mirror are neglected in the diagram for clarity.

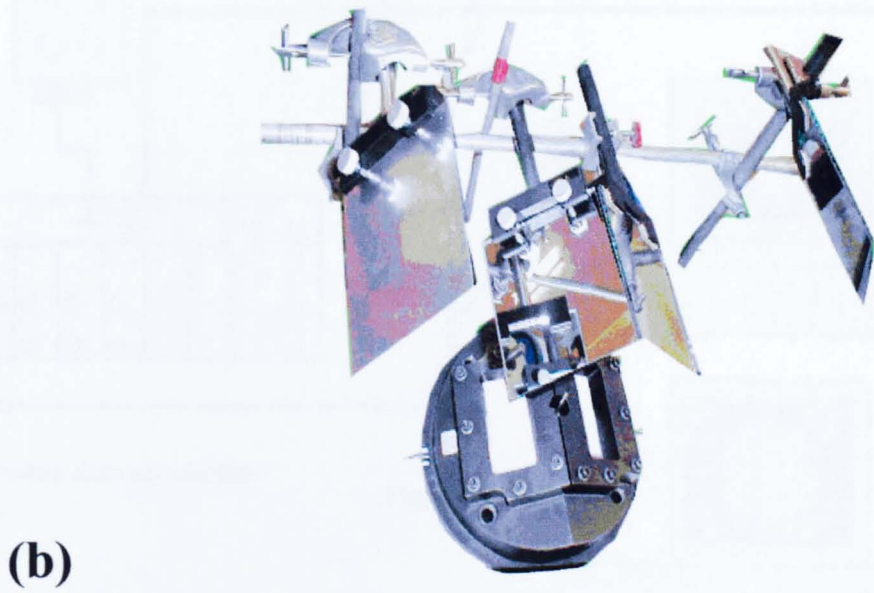
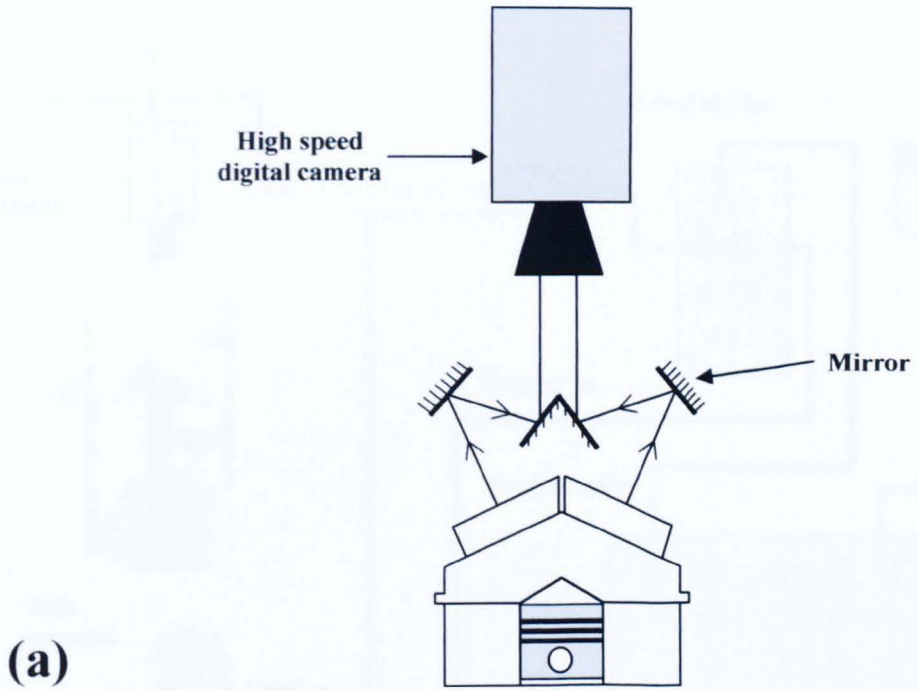


Figure 4.3 (a) Diagrammatical and (b) photographic illustration of mirror set-up for top flame imaging using one camera (LUPOE2-P).

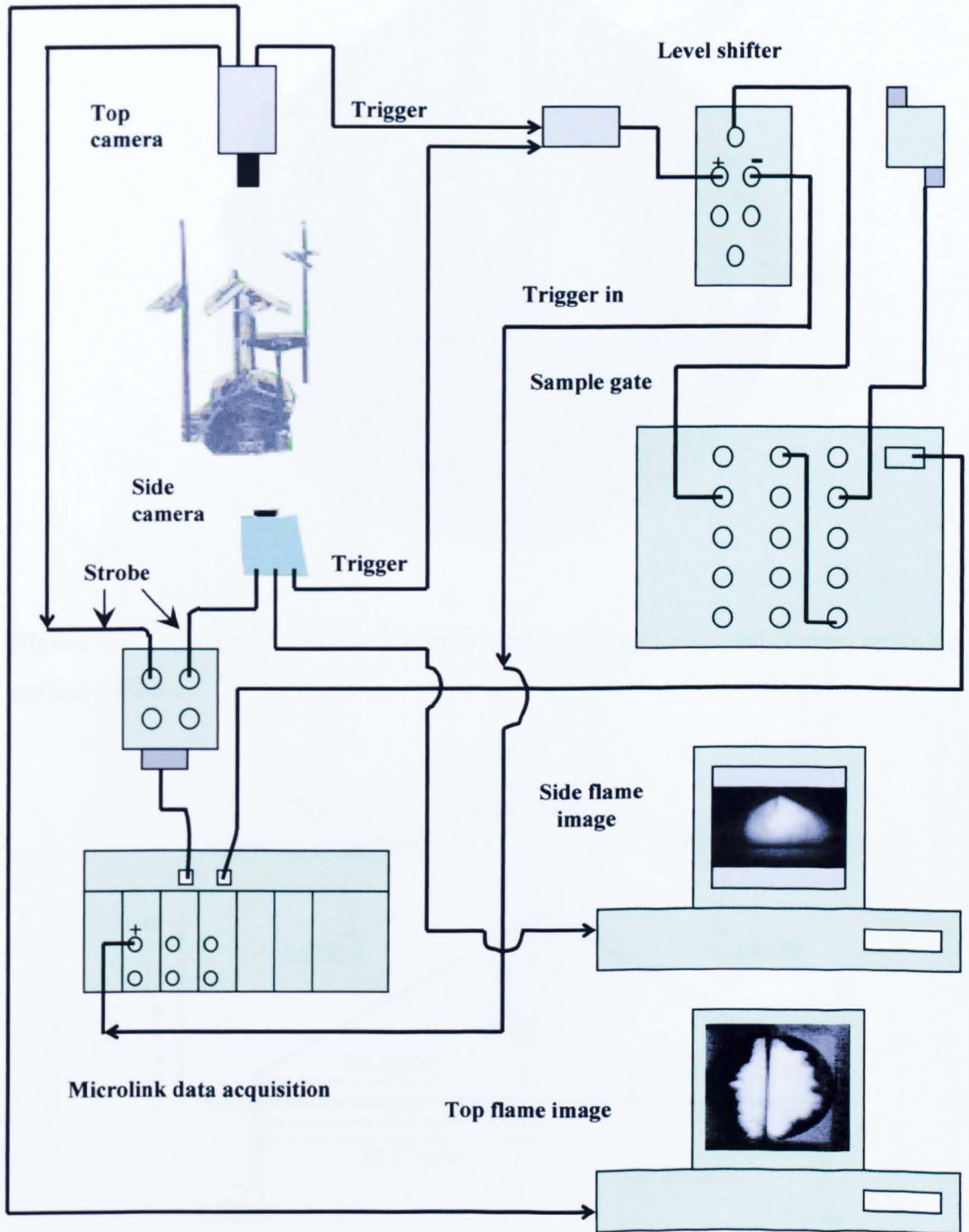


Figure 4.4 Schematic for simultaneous top and side natural light set-up (LUPOE2-P).

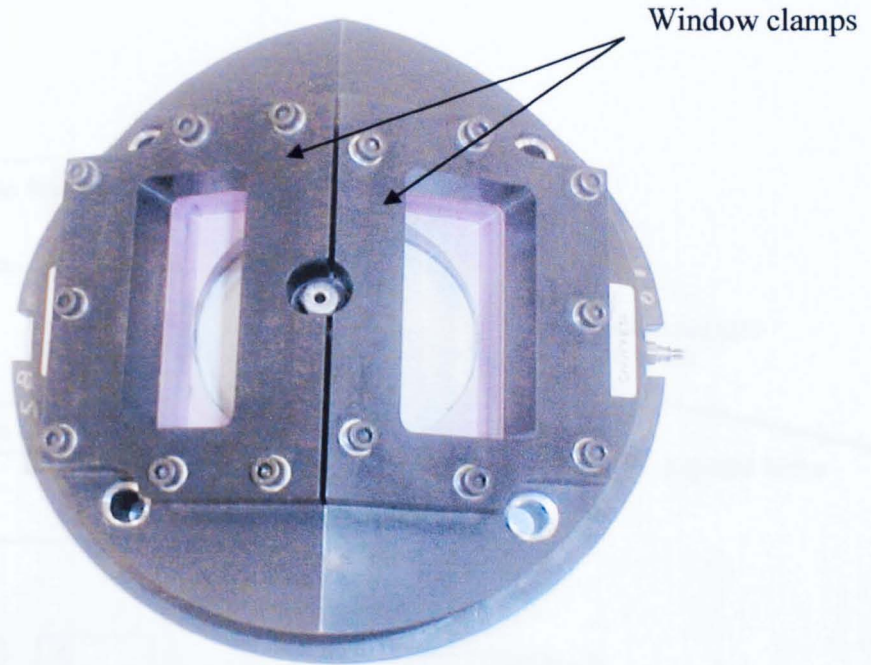


Figure 4.5 Top-view of LUPOE2-P pent-head, showing two metal clamps retaining the optical windows.

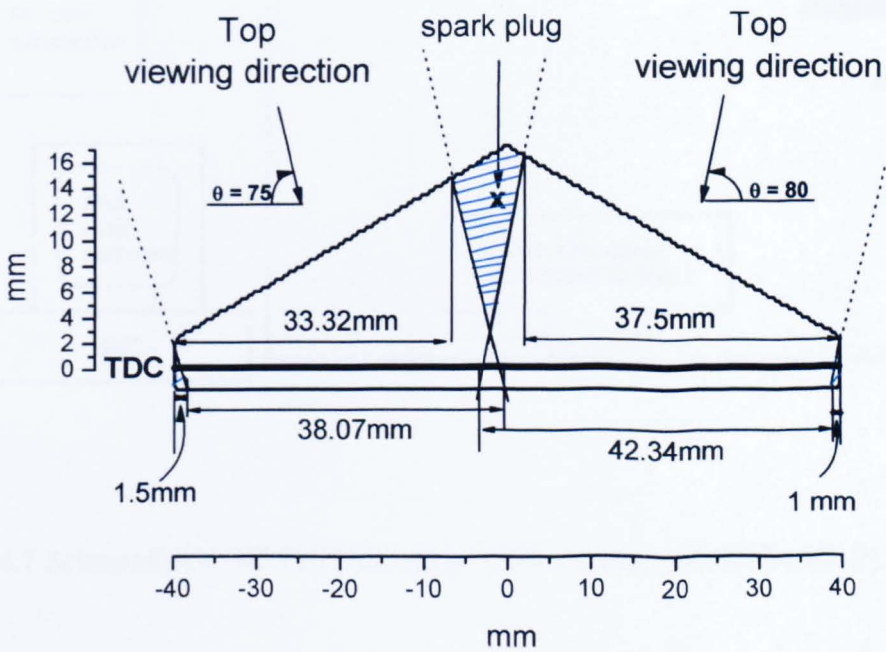


Figure 4.6 Side view of pent-head showing optically inaccessible (from top view) region.

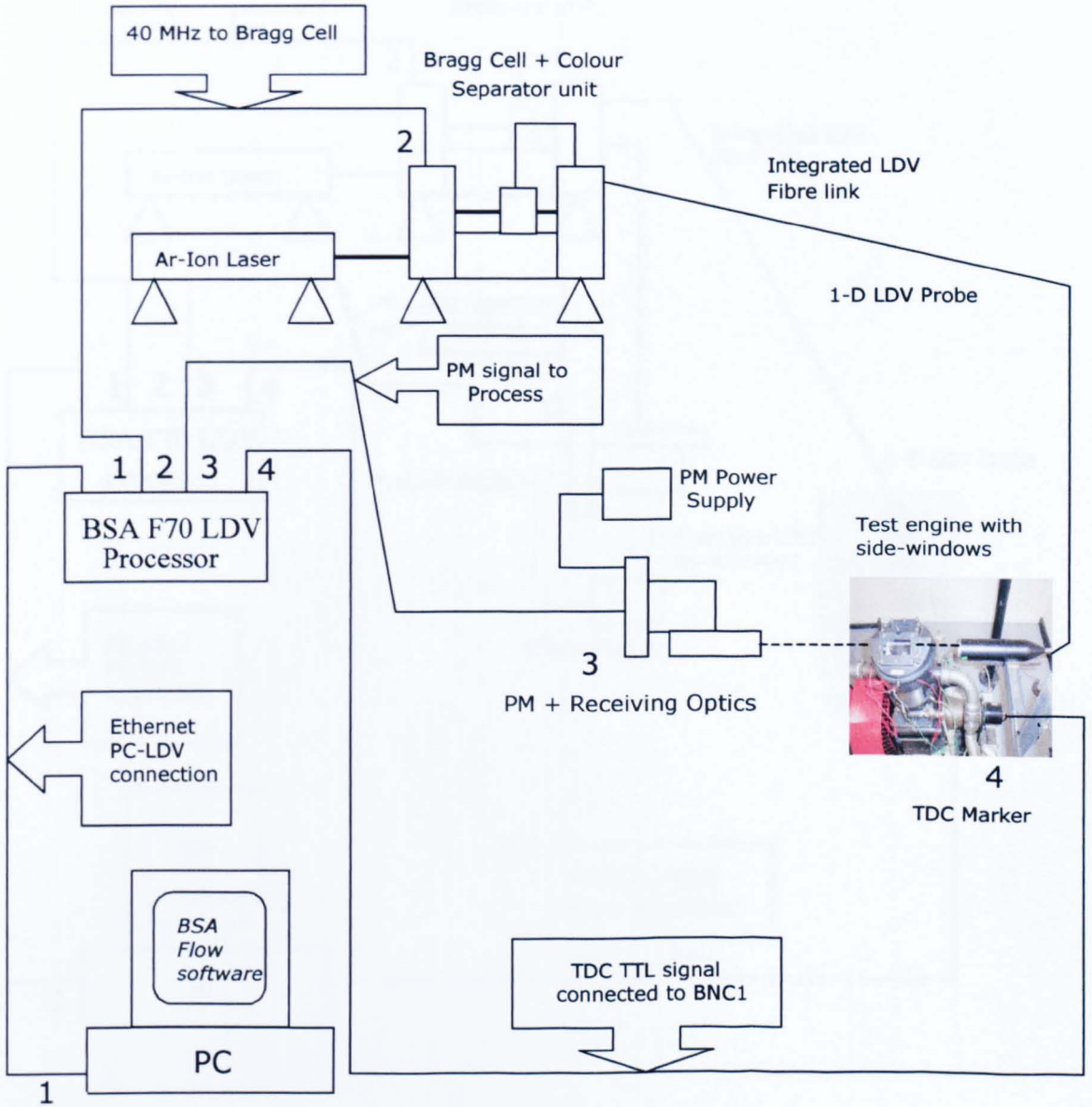


Figure 4.7 Schematic of 1-D forward scatter LDV experiment (LUPOE2-P).

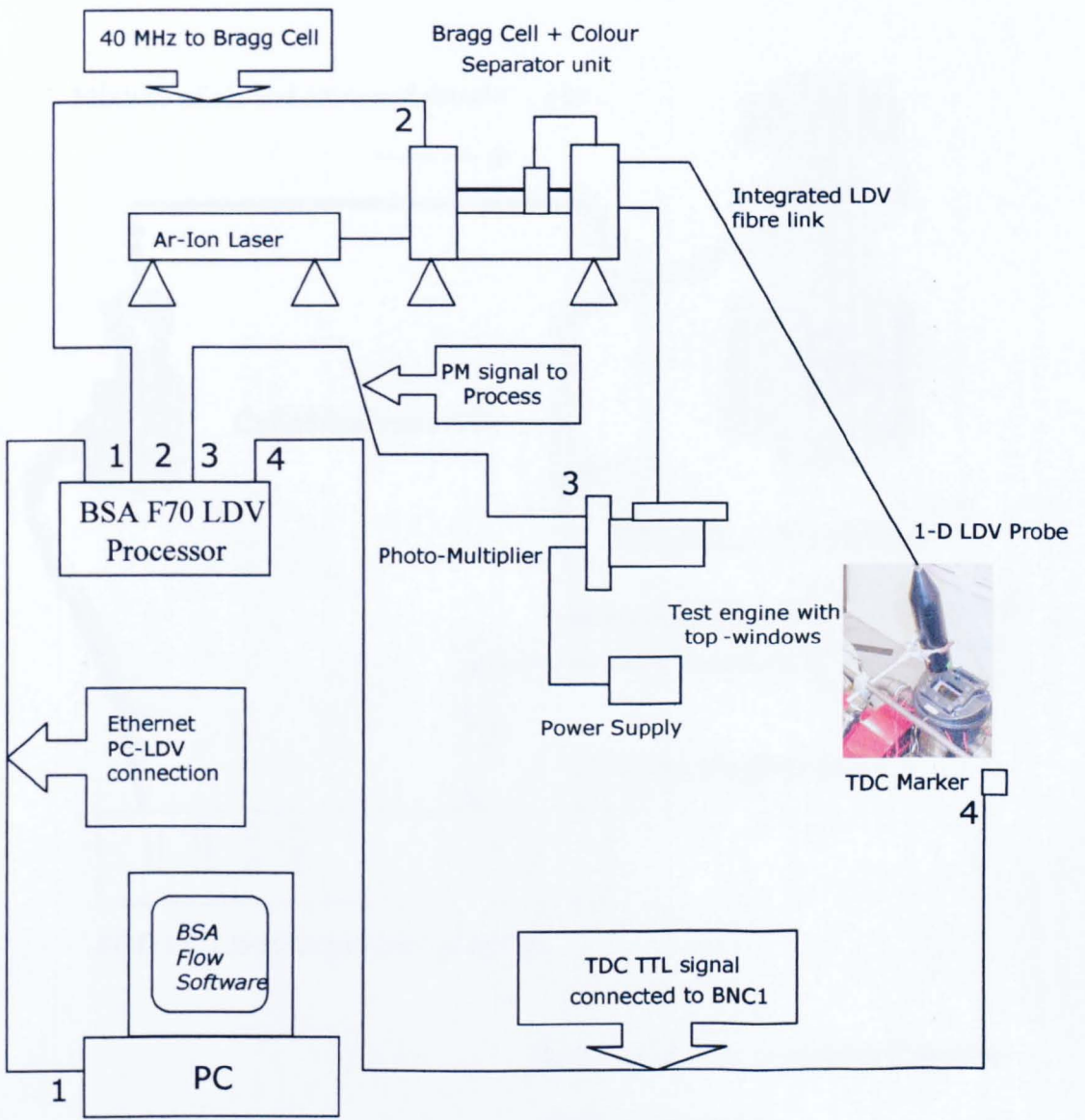
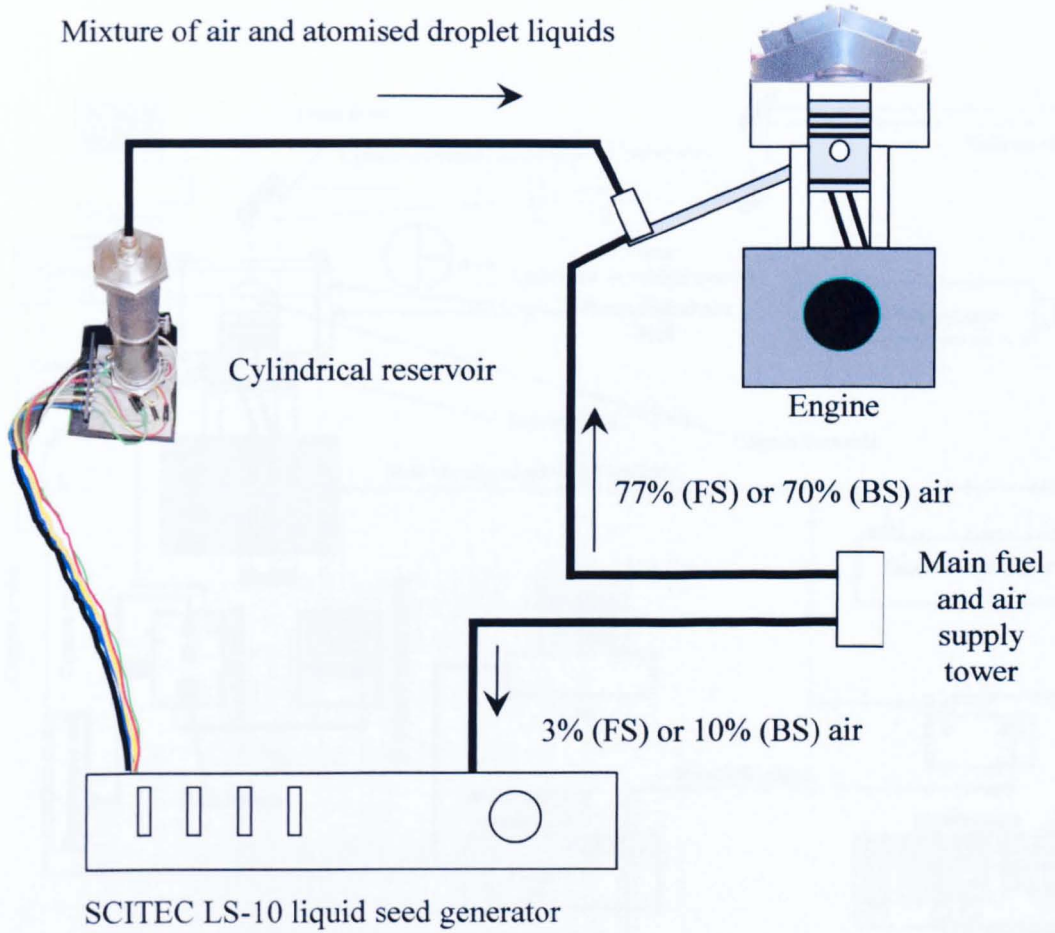


Figure 4.8 Schematic of 1-D back scatter LDV experiment (LUPOE2-P).



#: is out of 400L/min mass flow-rate

FS: forward scatter

BS: back scatter

Figure 4.9 Air-flow seeding for LDV (LUPOE2-P).

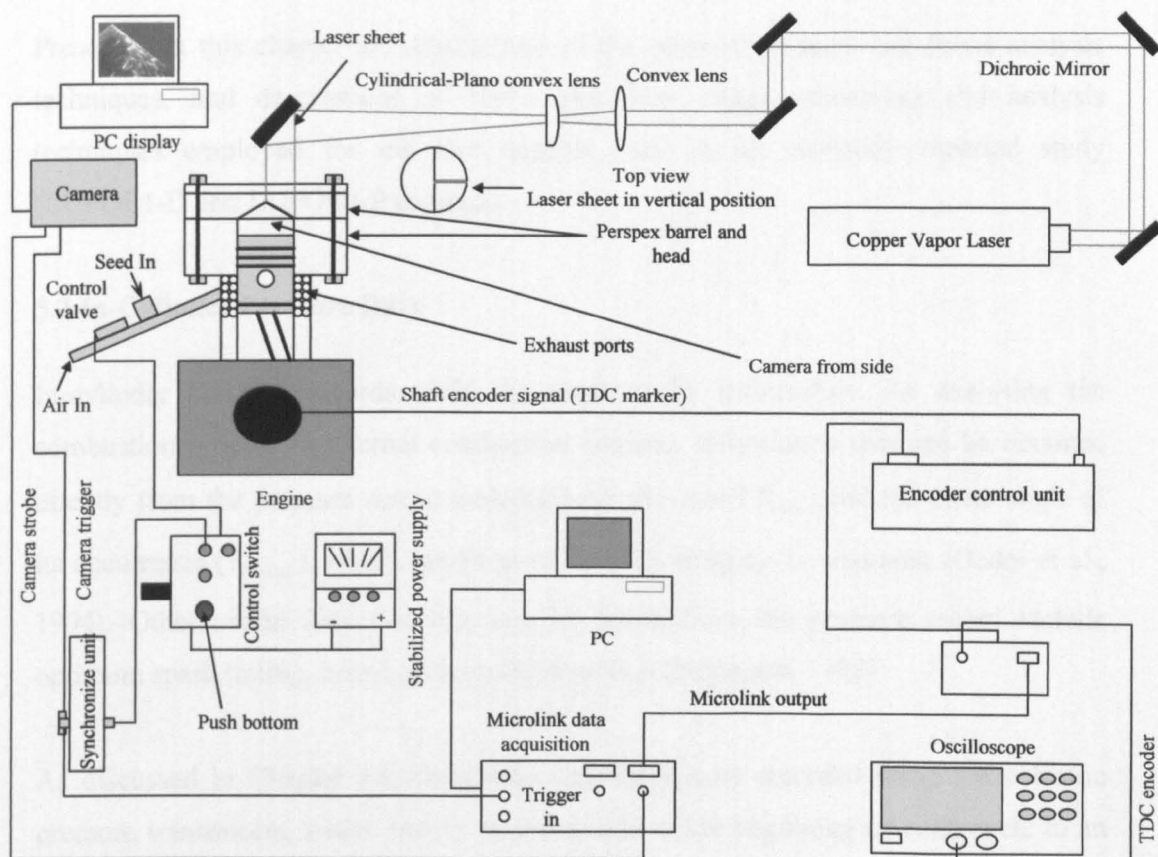


Figure 4.10 Laser sheet set-up for PTV using Perspex barrel and head (LUPOE2-P).

Chapter 5

Processing and Data Analysis

5.1 Introduction

Presented in this chapter are descriptions of the adopted pressure and flame analysis techniques, and descriptions of flame and flow image processing and analysis techniques employed for the two engines used in the currently reported study (LUPOE1-D and LUPOE2-P engines).

5.2 In-Cylinder Pressure Data

In-cylinder pressure records yield the most useful information for analysing the combustion process in internal combustion engines. Information that can be obtained directly from the pressure record includes peak pressure (P_{\max}) and the crank angle of its occurrence ($\theta_{P_{\max}}$), which can be used for evaluating cyclic variation (Ozdor et al., 1994). Other useful data that can also be found from the pressure record include optimum spark timing, knock and misfire detection (Heywood, 1988).

As discussed in Chapter 3.6, in-cylinder pressures were recorded using piezoelectric pressure transducers, which had to be referenced at the beginning of each cycle to an absolute pressure. Shown in Figures 5.1 (a) and (b), are examples of in-cylinder dynamic pressure records before and after referencing to an absolute pressure trace, respectively. The output of a piezoelectric pressure transducer is subject to 'short-term' thermal drift, which generates false readings on the pressure record. This thermal drift can be reduced by using water-cooled transducers or by covering the transducer tip with silicon grease, to be explained later in Section 6.2.

5.2.1 In-Cylinder Pressure Data Processing

As described in Section 3.9, after data acquisition was completed, the captured signals were ready to be stored, using the 'WAVECAP' software, supplied with the Microlink

system. The pressure and shaft encoder signals were extracted from the binary raw data files of one of the channels and were stored in the same sub-directory for that channel using the software 'SPLIT', supplied with the Microlink system. The use of this software was important (to split each signal in a sub-directory, e.g. dynamic pressure record, absolute record, TDC, clock, BDC and spark signals) in monitoring and observing all signals captured after each test, before proceeding to conduct more experiments. This proved necessary during the experimental work, where faulty signals were sometimes observed. These problems were generally related to damaged transducer washer, poor connections between transducer and amplifier, or faulty amplifier. Occasionally, spark interference was noted on the pressure graph, as shown in Figure 5.1 (a). Moving the spark lead away from the transducer cable generally eliminated such effects.

After the above binary data were saved and checked, a program (bin2asc), written by colleague (Wu, 2006), was used to convert the binary data to a readable format (an ASCII format). Later, a FORTRAN program (JLOPetterCam), written by Dr. Abdi Aghdam was used, to reference the dynamic pressure trace to an absolute pressure trace at exhaust port closure timing, 108.5° a/bTDC in the case of the LUPOE1-D engine and 80° a/bTDC in the case of the LUPOE2-P engine. After using the program, it was possible to select any firing cycle or any motoring before firing for the tested conditions.

5.3 Film Data

The combustion duration in a spark ignition engine is relatively short. Combustion starts when the spark ignites the mixture before the piston reaches TDC and finishes after the peak pressure point in the expansion stroke, e.g. for a combustion crank angle duration of 36° (e.g. starting at 20° bTDC and finishing at 16° aTDC) and an engine speed of 1500 rpm, combustion duration is:

$$Time = 36^\circ \times \frac{1 \text{ min}}{1500 \text{ rev}} \times \frac{1 \text{ rev}}{360^\circ} \times \frac{60 \text{ sec}}{1 \text{ min}} = 0.004 \text{ sec} = 4 \text{ ms}$$

It can be seen that the combustion duration is short and decreases with engine speed. High-speed electronic cameras were used to capture these fast combustion events. Shadowgraph and natural light methods (sometimes simultaneous) were used in the current study, as discussed in Chapter 4. The shadowgraph method was used in LUPOE1-D engine for early flame kernel development studies; sometimes with simultaneous natural light imaging (see Sections 4.2.2 and 4.2.3). Simultaneous 3D top and side natural light imaging was adopted with the LUPOE2-P engine (see Section 4.3).

5.3.1 Film Data Processing

After the high-speed camera/cameras captured images of turbulent flame development, they were downloaded directly to the computer and saved as ciné files. Phantom software was used, where the ciné files for each filmed cycle captured were split into ‘tif’ files and converted to ‘greyscale’ mode, in order to be used later in Adobe Photoshop Version 6 software. Every pixel of a greyscale image had a brightness value ranging from 0 (black) to 255 (white). The aim of using this software was to convert these images to black and white binary form via five processing steps, as shown in Figure 5.2. First, the raw image, converted to ‘greyscale’ mode, was selected, as shown in Figure 5.2 (a). The shadow of the spark wire can be observed in the image. In Figure 5.2 (b), the brightness level of the image was adjusted using the ‘level’ command under the drop down menu of ‘image-adjust’ commands in the software. This command allowed adjustment of the brightness and contrast of the image; it applied the same adjustment to every pixel in the image. Then, the spark plug wire was manually ‘filled’ using the ‘paintbrush’ tool in the software, as shown in Figure 5.2 (c). Next, a binarised black and white (B/W) image was created, as shown in Figure 5.2 (d), using the ‘threshold’ command under the drop down menu of ‘image-adjust’ commands. The adjustment of the threshold level was controlled, so that the white area covered the enflamed area. Hence, all pixels lighter than the threshold were converted to white; all pixels darker were converted to black. Finally, the ‘dust and scratches’ command under the drop down menu of ‘filter-noise’ commands was used, to remove any dissimilar pixel and smooth the flame edge of the thresholded image, as shown in Figure 5.2 (e). This procedure (converting the raw images to B/W images) was applied to the images derived from both engines (LUPOE1-D and LUPOE2-P) used in this study.

In the case of LUPOE1-D, the black and white (B/W) binarised images were converted to an EPS format, using Photoshop Version 6 software. The EPS format changed the images to a readable format (an ASCII format), using a FORTRAN program (Edgesab4), written by Dr. Woolley. This enabled the flame radius, centroid and flame edge co-ordinates to be determined. Other useful flame parameters were also analysed, using 'Excel' software (shape factor and flame kernel centroid convection).

To quantify the distortion of the flame from that of a circular shape, Buran (1998) and Gillespie (1998) defined a 'Shape Factor' (SF). The same parameter was applied for the study of cyclic variation in the early flame kernel development in LUPOE1-D, where the 'Shape Factor' was defined in terms of flame perimeter (P_f) relative to that (P_e) of circular flame of identical area, as follows:

$$\text{Shape Factor} = \frac{P_f}{P_e} \quad (5.1)$$

In the case of LUPOE2-P, the black and white (B/W) binarised images were converted to an EPS format, using Corel Photo-paint Version 9. Later, two FORTRAN programs (Top Film and Side Film) written by Dr. Abdi Aghdam were used to find the flame edge co-ordinates for both top and side films. In addition, flame radius for top and side films and flame centroid movement for side films were found and analysed using another two programs (lupoe2top and lupoe2side), written by Dr. Woolley. It was difficult to find the flame centroid movement for the top films, due to the existence of two metal clamps retaining the top optical windows, which precluded imaging the very earliest stages of flame development, hence it was difficult to determine the spark electrode position (Section 4.3, Figure 4.5).

5.4 Laser Doppler Velocimetry (LDV)-LUPOE2-P Engine

The LDV tests in this study were conducted on the LUPOE2-P engine with an air mass flow-rate of 6.89 g/sec. The LDV set-up for both forward and back scatter configurations has been described in Section 4.4.1. The LDV data collection and analysis is outlined below.

BSA flow processing software

The LDV data were collected and analysed using Dantec BSA flow V2.00.29 flow processing software, more details of the software used in the currently reported study are available elsewhere (Jakubik, 2002).

A Dantec F70 burst spectrum analyser (BSA) signal processor was used to analyse the LDA signals. It calculated the velocity by a Fast Fourier Transformation (FFT) technique.

Validation rate and data rate

Within the software, the following were selected and needed to be set correctly for successful measurements.

Centre frequency: this defined the centre frequency of the doppler signal to be measured. In the current case, it was defined as the expected mean velocity of flow in the measurement position; this was converted to frequency by the software.

Bandwidth: this defined the doppler frequency window, centred on the above frequency. Values presented in Appendix A, Table A4 indicated that velocities falling into the range from -9 m/s to $+9$ m/s were to be measured.

Proper choice of the above two parameters (centre frequency and bandwidth) resulted in a good Gaussian probability distribution function of the measured velocities.

Record length mode and Record length: these two parameters defined the number of samples for the applied record length, i.e. number of samples passing the measurement volume at the same time to be considered as a successful record or burst. Too high values tend to remove noise, but at the same time decrease data rate. “Therefore, a good balance needs to be found between these two” (Jakubik, 2002).

Signal gain: this was the gain of the PM signal amplifier. According to the Dantec user’s guide the recommended starting level should be around 24 dB. In the current

study, values of 26 dB and 24 dB were selected for forward scatter and back scatter configurations, respectively (Appendix A, Table A5).

Burst detector SNR level: sets the SNR (signal-to-noise ratio) threshold level of the burst detector. Default value was set at 0 dB, the same as Jakubik (2002).

Level validation ratio: this was the ratio between two highest peaks in the burst spectrum. The value recommended by Jakubik (2002), was adopted.

5.5 Particle Tracking Velocimetry (PTV) -LUPOE2-P Engine

The PTV particle tracking was performed using a manual tracking method for each individual particle.

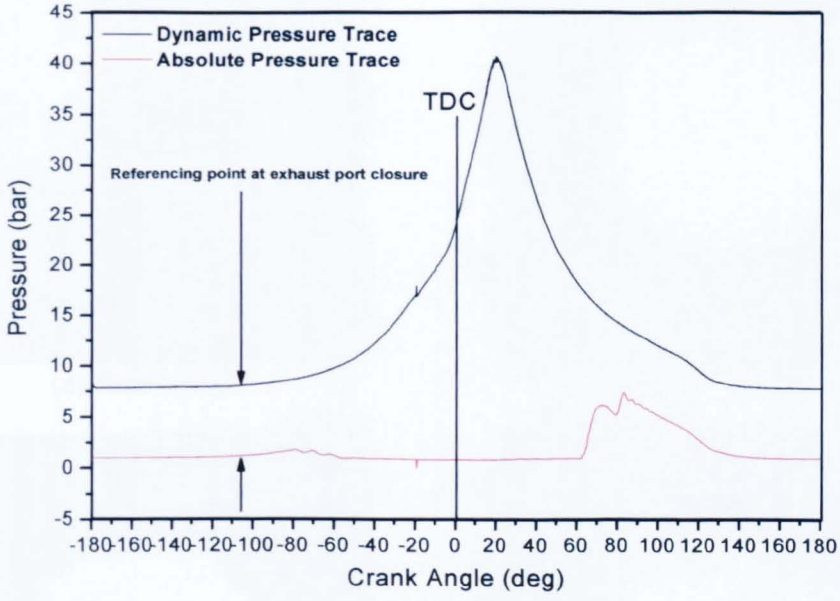
5.5.1 PTV Analysis

The laser was pulsed at 10 KHz and the camera ran at 2 KHz, therefore, during each camera exposure period the laser pulsed 5 times. This resulted in each particle producing 5 ‘spots’ on each frame, as shown in Figure 5.3. The PTV raw images were analysed using a manual treatment for every individual particle track, joining the five successive positions of the particle, as shown in Figure 5.3. Before choosing and analysing the particle tracks, the tracks created by individual particles in these successive camera exposures were examined; e.g. Figures 5.4 (a), (b) and (c). This was done to ensure selection of particles with clear 5 dots, and, to verify the direction of the analysed particle by considering its motion between frames. This procedure also ensured that the particle under analysis did not suffer interference by another particle, especially in regions of high seeding density, where overlapping particle tracks were observed, as shown in Figure 5.5. After this verification procedure, every particle track was then transformed into a local velocity vector using three steps. First, the measurement tool in ‘Photoshop’ software Version 6 was used to find the coordinates of each particle in each position, as shown in Figure 5.6. This tool was used manually to mark the particle displacement, where the start point of the particle was noted and tracked until the end of the exposure time for this particle. Then, the navigator command under the drop down ‘window’ menu showed the x, y, height (H) and width

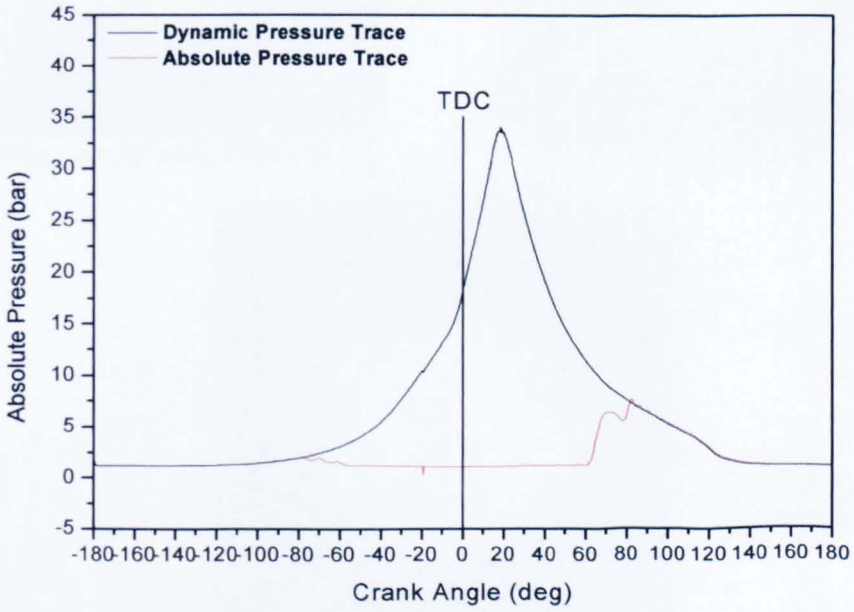
(W) coordinates necessary for vector (R) map calculations. Second, the magnitudes and directions for each individual particle were calculated from those coordinates using 'Excel' software. Finally, the data calculated from 'Excel', which represented the vector map, were plotted using 'Origin' graphic Version 7 software. This procedure yielded a vector field which revealed the large-scale structures in the flow studied, as shown in Figure 5.7.

In general, measurements were made at various crank angles for a number of cycles recorded at two engine speeds (750 rpm and 1500 rpm). This enabled investigation of the flow patterns for the two engine speeds as a function of crank angle for a number of different cycles. The results are presented later, in Section 7.3.1.1.

Following this description of processing and data analysis, the next chapter is concerned with LUPOE2-P preliminary engine mapping prior to presentation of the results and conclusions of the work.

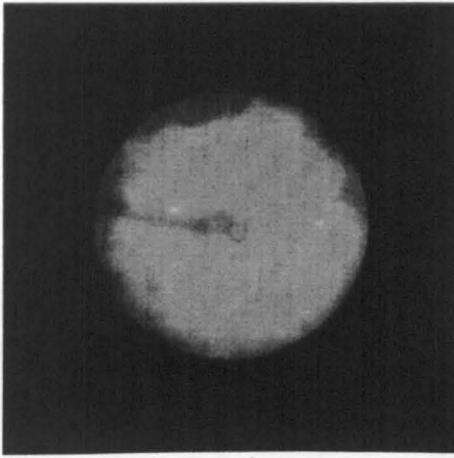


(a)

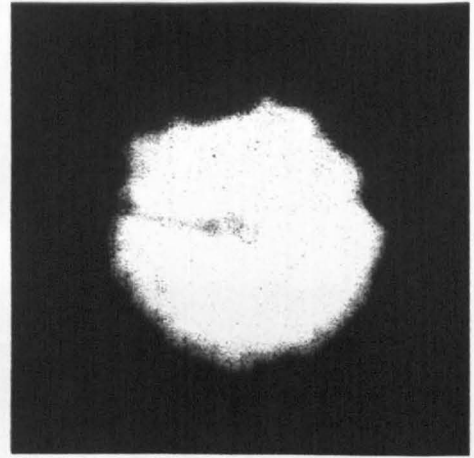


(b)

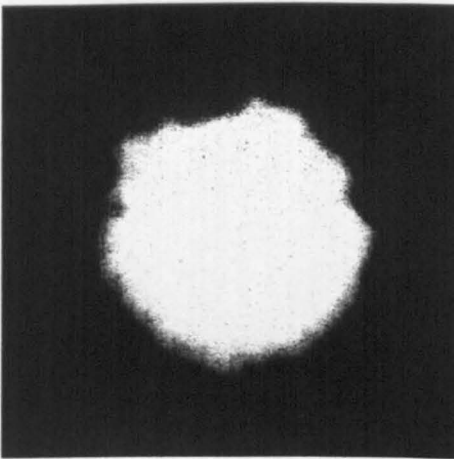
Figure 5.1 Dynamic pressure traces (a) before referencing to an absolute pressure trace, (b) after referencing.



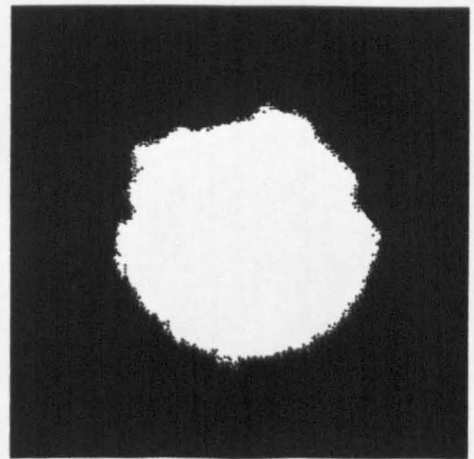
(a) Raw image



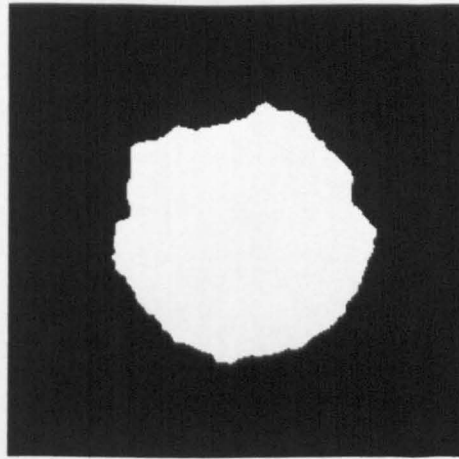
(b) Setting brightness level



(c) Filling spark wire and cleaning



(d) Threshold



(e) Removing noise from flame front

Figure 5.2 Sequences of flame image processing to produce binarised black and white image from raw image.

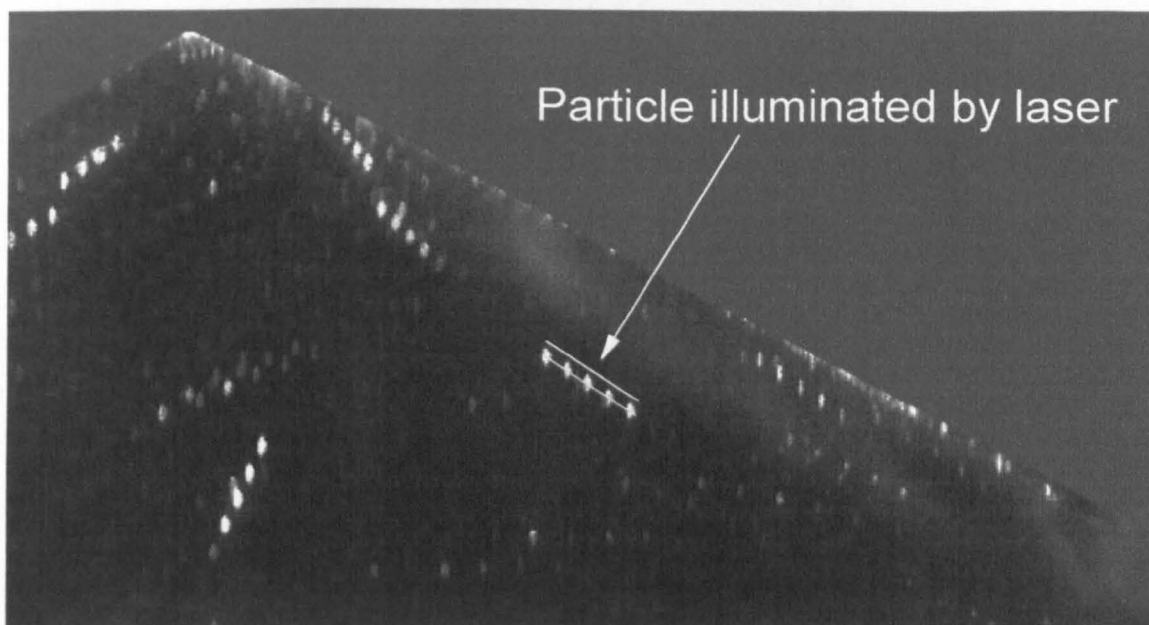
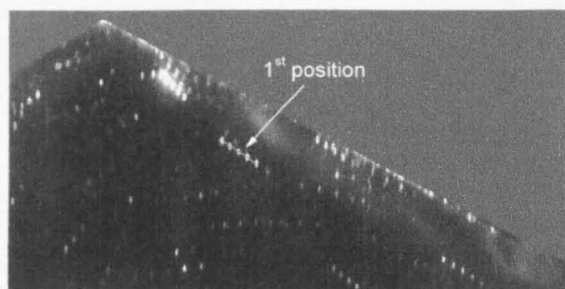
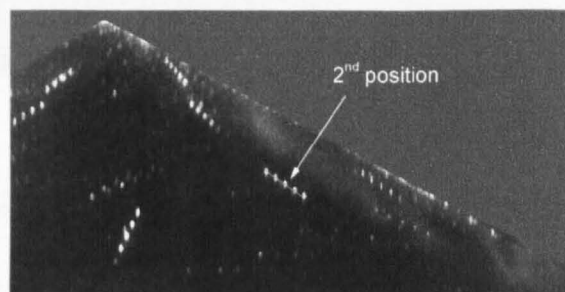


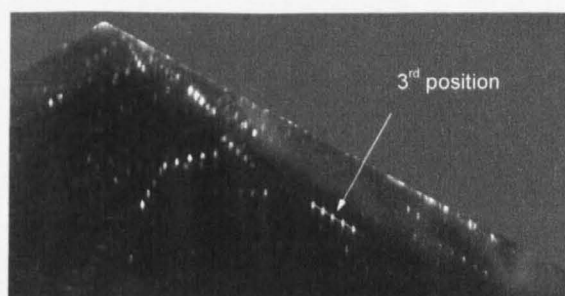
Figure 5.3 Raw image of seeded PTV flow, showing successive positions of each particle for five laser flames separated by 0.1 ms during a total camera frame exposure of 0.4 ms.



(a)



(b)



(c)

Figure 5.4 Sequence of individual particle movement through the cycle (4.5° CA between images) (a) image of particle before 4.5° CA of analysed image, (b) image of particle under analysis, (c) image of particle after 4.5° CA of analysed image.

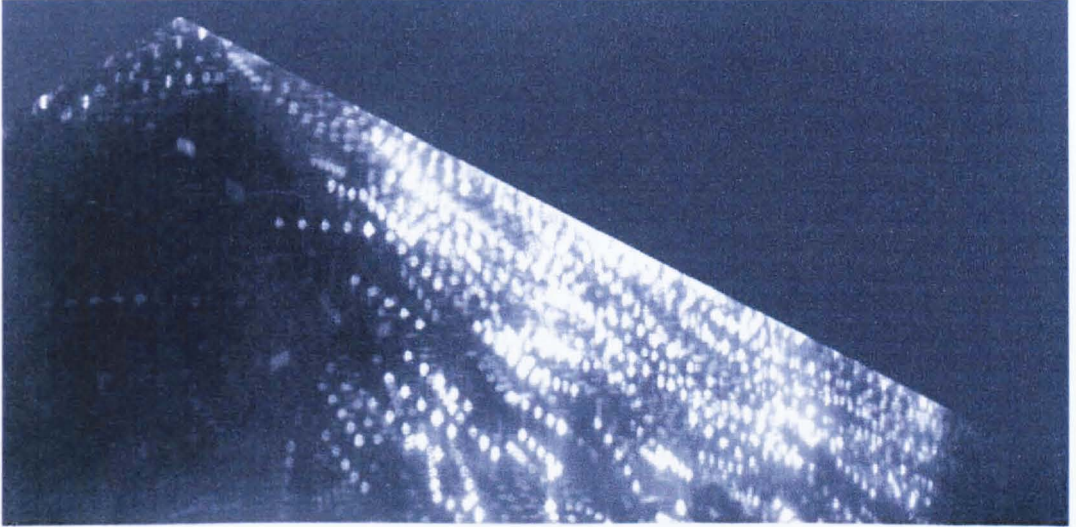


Figure 5.5 Overlapping particle tracks in regions of high seeding density.

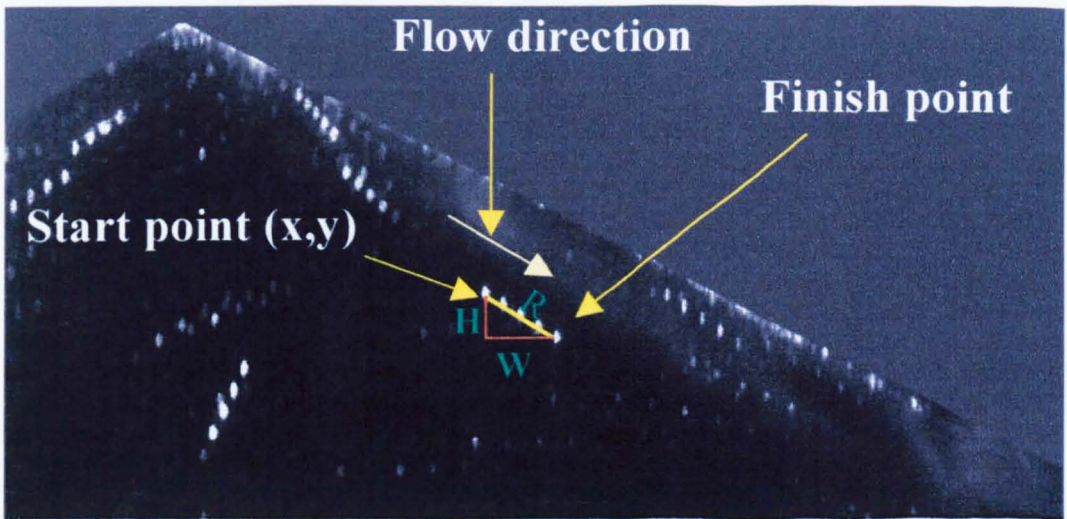


Figure 5.6 Manual tracking of individual particle, showing start point (x and y coordinates), finish point, height (H), width (W), resultant R (vector) and flow direction.

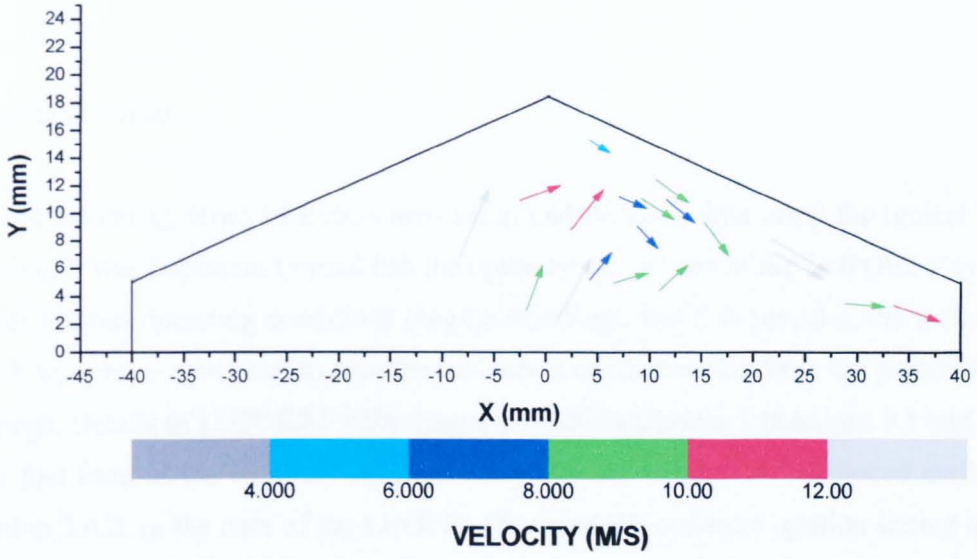


Figure 5.7 Example of vector map for one of the cycles tested at 1500 rpm (67.5° CA. bTDC).

Chapter 6

LUPOE2-P Preliminary Engine Mapping

6.1 Introduction

Before collecting series of simultaneous film and pressure data using the optical head version, it was important to establish the optimum conditions of the LUPOE2-P engine under various operating conditions (engine mapping). For this purpose, the metal (no window) version was used, to save the less robust optical version from the possibility of damage. Details of LUPOE2-P have been presented in Chapter 3 (Sections 3.1 and 3.3). The fuel used in the currently reported study was iso-octane, as mentioned earlier in Section 3.4.2. In the case of the LUOPE1-D engine the optimum ignition timing at the various operating conditions had previously been determined by Lee (1995) and Abdi Aghdam (2003), and no such mapping was therefore necessary in the current study.

Before finding the optimum conditions for the LUPOE2-P engine, the following tests were carried out:

1. A study of the effect of pressure transducer type (water-cooled and non-water-cooled) on peak cylinder pressure value and crank angle of its occurrence. Top cooled and side non-cooled transducers were used in the currently reported study, as shown in Figure 6.1.
2. A study of the effect of spark ground electrode orientation on peak pressure. Three orientations were selected, as shown in Figure 6.2.

Then the following investigations were conducted, with 50 cycles recorded for each test condition. With the air mass flow set at 8.62 g/sec, and using the water-cooled transducer with inlet and top barrel temperatures set to 70° C (except at 1900 rpm, for which inlet/head temperatures were set to 50° C, to be explained in Section 6.8), the following effects were explored:

1. Skip-firing ratio (5, 6, 7, and 8) at 1500 rpm on IMEP and COV_{IMEP} .
2. Engine speed (750, 1000, 1500 and 1900 rpm) on optimum ignition timing.
3. Engine speed (750, 1000, 1500 and 1900 rpm) on IMEP and COV_{IMEP} .
4. Equivalence ratio (0.7, 0.8, 1.0, 1.05 and 1.1) at 1500 rpm on IMEP and COV_{IMEP} .
5. Inlet/head temperature (50° , 60° and $70^{\circ}C$) at 1500 rpm on IMEP and COV_{IMEP} .
6. Air mass flow (8.62 and 10.34 g/sec) at 1500 rpm on IMEP and COV_{IMEP} .

Brunt et al. (1996) suggested that up to 300 engine cycles are required to achieve acceptable repeatability and accuracy in indicated mean effective pressure (IMEP) measurement. However, for the current study, a lower number (50 cycles) was adopted due to the limited number of cycles recordable in a single run with the available software to conduct the experiments.

6.2 Dynamic Pressure Transducers

The in-cylinder dynamic pressure transducers were exposed intermittently to flames and combustion gases. "This short-time heating in the range of milliseconds provides a measuring error due to thermal stress in the sensor (short-term drift)" (Kuratle et al., 1992). The output of a pressure transducer subjected to this 'short-term' thermal drift will generate false readings on the pressure record due to the deformation of the quartz crystal and, as a result, a transducer response even when pressure remains constant. Water-cooling of transducers can reduce short-term drift; it can be reduced also by covering the transducer tip with silicon grease (Brunt et al., 1996; Kuratle et al., 1992; Rosseel et al., 1999). Short-term drift can be detected by using two or more pressure transducers in the same cylinder.

Due to the limited space available in the top part of the optical pent-roof head version used in the current study, it was not possible to use a water-cooled pressure transducer; instead, a side flush-mounted, non-cooled Kistler Type 601A pressure transducer was adopted, as mentioned previously in Chapter 3 (Sections 3.3.2 and 3.6). Therefore, to study the effect of short-term drift associated with the non-cooled pressure transducer and to compare its output with that of a water-cooled pressure transducer, the metal pent-roof head (in which it was possible to use two types of Kistler pressure

transducers) was adopted. A Kistler Type 601A pressure transducer mounted in a standard water-cooled adapter was installed in the top of the metal pent-shaped cylinder head and a non-water-cooled Kistler Type 601A pressure transducer was fitted in the side, as described in Section 3.6.

The study showed that short-term drift had no effect on the peak pressure value (or the crank angle at which it occurred) for typical slow, middle and fast cycles at the reference condition, as shown in Figures 6.3, 6.4 and 6.5, respectively. There was no evidence of short-term drift in the peak region of the pressure-crank angle diagram; however, short-term drift began to affect recorded in-cylinder pressure at later crank angles. For the slow cycle, the drift started at about 30° aTDC, as shown in Figure 6.3. For the middle cycle, it started at about 26° aTDC, as shown in Figure 6.4. For the fast cycle, it started at about 21° aTDC, as shown in Figure 6.5. That is, earlier for increasingly fast combustion. It can be seen from the graphs that the pressure trace generated by the water-cooled pressure transducer corresponded well with the cylinder barrel absolute pressure trace at later stages of expansion, suggesting that it had been unaffected by short-term drift and gave a correct reading. However, the pressure trace for the non-water-cooled transducer did not match, suggesting that it had been affected by short-term drift.

For cycles of higher peak pressure, the drift started earlier. This was presumably due to higher temperature associated with the higher pressure of the fast burn engine.

As a result of the short-term drift experienced with the non-cooled transducer, the IMEP values were lower than for the water-cooled, as shown in Table 6.1. The IMEP values for the non-cooled transducer were low by about 8-12% compared with the water-cooled transducer.

Cycles	Water-cooled Transducer	Non-cooled Transducer
	IMEP	IMEP
Slow	9.6	8.8
Middle	9.7	8.7
Fast	9.7	8.5

Table 6.1 IMEP for water-cooled and non-cooled transducer.

As noted earlier, it was necessary to use a non-cooled transducer in the optical pent-roof head studies. However, these studies were primarily concerned with the combustion process rather than power output. Since the events of interest generally occurred shortly after the occurrence of peak pressure, the short-term drift problems were not considered serious.

On occasions when drift-free data were required, the transducer tip was coated with silicon grease. However, this was not done routinely, because of the time involved in dismantling the engine head regularly to renew the coatings.

6.3 Spark Plug Ground Electrode Orientation

Spark plug ground electrode orientation has been shown to affect engine performance (Burgett et al., 1972; Pischinger and Heywood, 1990).

In the current study, three orientations (A, B and C, as shown in Figure 6.2) were adopted in preliminary work. The results showed that the first orientation (A) resulted in the highest peak pressure. Moreover, it had higher pressure in the early stages (bTDC). The other two orientations (B and C) had nearly similar peak pressure values and positions, as shown in Figure 6.6. Orientation (A) was adopted in all subsequent tests for LUPOE2-P. In the current study, there was not time to investigate further the effects of the three orientations on the early stages of combustion; it might merit effort in some future work.

6.4 Effect of Skip Firing

At constant ignition advance, values of IMEP increased, and COV reduced, as skip fire ratio (SFR) was increased from 5 to 8. This was associated with improved scavenging of residuals (and possibly lower mixture temperatures), leading to higher charge concentration in the cylinder. However, at skip firing ratios of 7 and 8, the values were nearly the same, as shown in Figure 6.7. Hence, a skip fire ratio of 7 was selected for all engine speeds, except for 1900 rpm (where a skip fire ratio of 8 was adopted). At higher engine speed, less time was available for residual purging, and so the higher skip fire ratio was adopted for improved engine scavenging.

6.5 Effect of Engine Speed

The engine was tested at four speeds, 750 rpm, 1000 rpm, 1500 rpm and 1900 rpm. At each engine speed, ignition timing was varied in order to determine the optimum timing (on the basis of indicated mean effective pressure, IMEP), as shown in Figure 6.8. At any given condition, IMEP values were relatively insensitive to changes in ignition timing. At 750 rpm, no tests were conducted for ignition earlier than θ_{ig} of 2° bTDC, since the measured peak pressures for the mean cycles at that timing were found to occur at about $16\text{-}18^\circ$ aTDC (where maximum brake torque (MBT), and hence optimum spark timing, are expected (Heywood, 1988; Witze et al., 1983)). Ignition timing had greater effect on peak pressure value (P_{\max}) and its position ($\theta_{P_{\max}}$), as shown in Figure 6.9. As ignition timing advanced, higher peak pressure values were noted. The optimum timings and corresponding values of average IMEP for each engine speed are summarised in Table 6.2. The air mass flow was set at 8.62 g/sec with inlet and top barrel temperatures set to 70°C , except at 1900 rpm (for which inlet/head temperatures were set to 50°C), as mentioned in Section 6.1.

Engine Speed (rpm)	Equivalence Ratio (ϕ)	Optimum Ignition Timing (bTDC)	IMEP	Skip Firing Ratio
750	1.0	2	8.2	7
1000	1.0	4	9.1	7
1500	1.0	7	9.6	7
1900	1.0	10	10.5	8

Table 6.2 Optimum conditions at different engine speeds for LUPOE2-P.

The maximum IMEP increased with engine speed, as shown in Figure 6.10. This might be associated with increase in rms turbulent velocity, and hence turbulent burning velocity increase, although the time available for combustion would of course reduce as well. The trend might also be related to blow-by, which would reduce as engine speed increased. In addition, at low engine speed the incoming mixture would have time to pick up relatively more heat during entry to the cylinder at low engine speeds; this would result in lower charge density, less mass of charge at port closure (i.e. lower volumetric efficiency) and hence lower pressure development and IMEP. There would also be more time for heat transfer from the burned gases to the cylinder walls and so less work done on the piston (a consequence of the First Law of Thermodynamics). At the various engine speeds, cyclic variation was much the same, except at the lowest engine speed (750 rpm).

Comparing the results from LUPOE2-P with those of LUPOE1-D, the later optimum ignition timings for LUPOE2-P suggest rather faster combustion (Figure 6.11).

6.6 Effect of Equivalence Ratio

At 1500 rpm, the engine was operated at various equivalence ratios and the corresponding IMEP values at optimal ignition advance in each case were plotted. As expected, IMEP increased and COV reduced, and optimum ignition advance was later

as equivalence ratio increased over the range 0.7 to 1.1. However, these parameters all proved fairly constant for $\phi=1$ to 1.1, as shown in Figure 6.12.

6.7 Effect of Inlet/Head Temperature

As the (identical) set inlet mixture and cylinder head temperatures were reduced, the values of IMEP increased, as shown in Figure 6.13. At lower temperature, the density of air increased, leading to higher volumetric efficiency. However, at the lowest temperature (50°C), cyclic variation increased.

6.8 Effect of Air Mass Flow

In the tests reported in previous sections, an air mass-flow of 8.62 g/sec was used. For the work reported in this section, two air mass flow-rates (8.62 g/sec and 10.34 g/sec) were adopted in a study of the effects of air mass-flow. Higher mass flow-rates resulted in excessive fuel consumption and lower flow-rates resulted in 'run-on' problems. In the earlier LDV tests conducted with the same engine, an air mass flow as low as 6.89 g/sec was used; however, under firing conditions with the metal version of the pent-roof head set to 70°C, run-on problems occurred. At 8.62 g/sec, no run-on was encountered at engine speeds of 750 rpm, 1000 rpm and 1500 rpm. However, at the higher engine speed of 1900 rpm, run-on persisted, even at this air mass flow-rate; therefore (at 1900 rpm), the temperature was lowered gradually to 50°C, when no run-on was noted. The values of IMEP for the two air mass flow-rates adopted (8.62 and 10.34 g/sec) were identical, possibly because of the nearly complete scavenging in both cases at the high SFR adopted. Since less fuel was consumed with an air mass flow of 8.62 g/sec, that flow-rate was adopted in all subsequent experiments. In PTV flow studies, using the same perspex barrel and head as that used in the current study but with a GDI bowl piston (Alrefae, 2005), varying the air mass flow-rate had no significant effect on experimentally derived velocity vectors. This suggests that in this engine, flow and turbulence are governed more by engine speed and geometry than inlet flow velocity.

On the basis of the experimental work reported above, a ‘reference’ operating condition (Table 6.3) was selected for the later, more extensive, ‘optically-based’ experiments, and for associated model validation studies undertaken by colleagues.

Compression ratio	9.2
Equivalence ratio	1.0
Engine speed	1500 rpm
Ignition timing	7° bTDC
Intake air flow rate	8.62 g/sec
Type of fuel	Iso-octane

Table 6.3 Reference operating condition.

In the preliminary tests described above, using the ‘non-optical’ metal cylinder head, the inlet and top barrel temperatures were set at 70°C. However, a run-on problem occurred when series of tests were conducted with the optical ‘pent’ head version of LUPOE2-P. With that head, it proved necessary to reduce the temperature to 55°C, to avoid the possibility of run-on. The latter temperature was therefore adopted for the ‘reference condition’ in all subsequent optical head experiments.

Following this description of the preliminary engine mapping experimental work for the LUPOE2-P engine, the experimental results for the optical variants of both LUPOE1-D and LUPOE2-P engines are presented in Chapter 7.

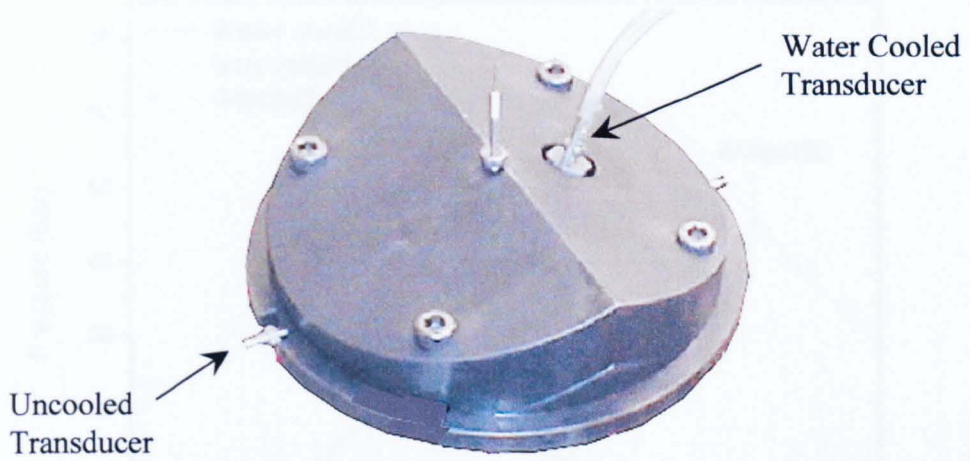


Figure 6.1 LUPOE2-P, metallic version pent-roof head.

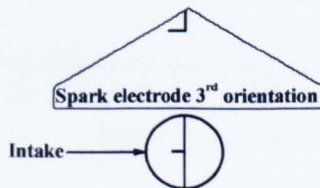
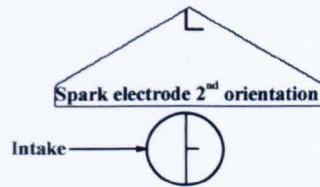
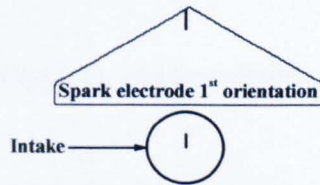


Figure 6.2 Selected orientations of spark plug ground electrode for LUPOE2-P.

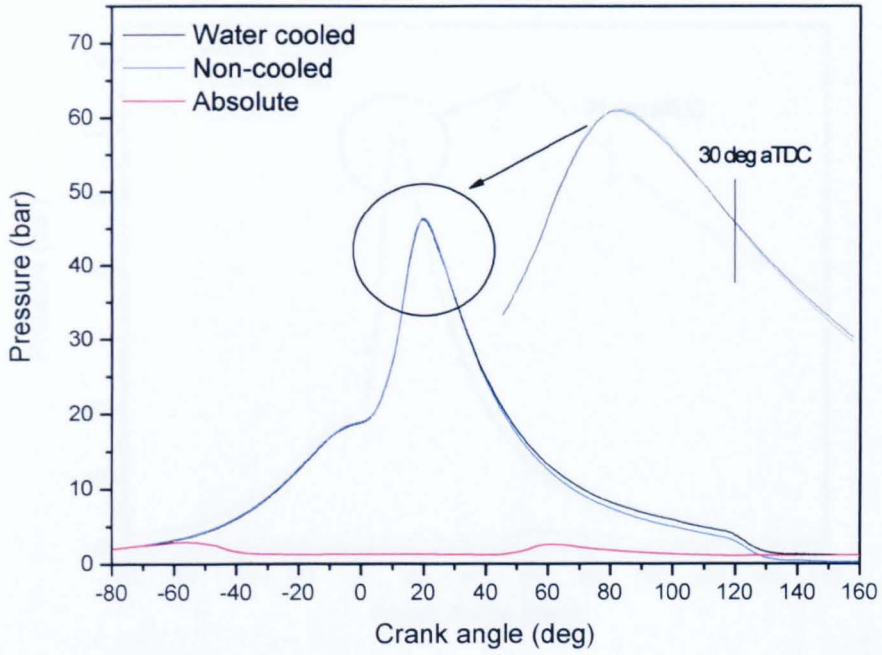


Figure 6.3 Effect of transducer type on peak pressure position and value for slow cycle.

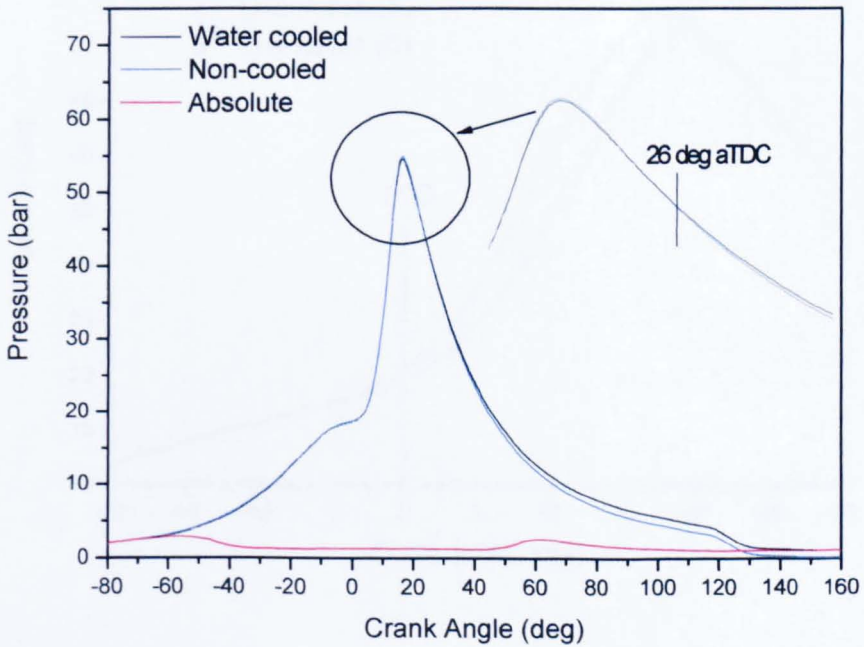


Figure 6.4 Effect of transducer type on peak pressure position and value for middle cycle.

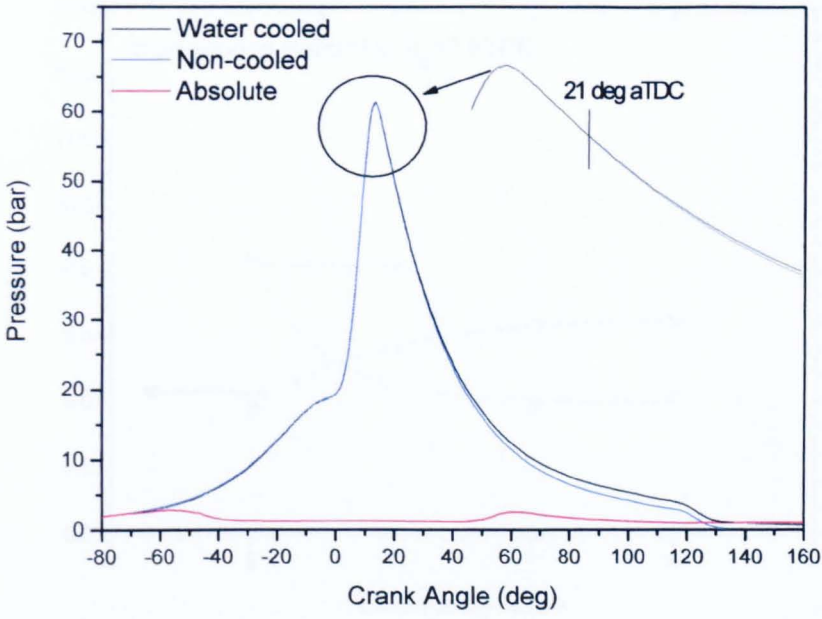


Figure 6.5 Effect of transducer type on peak pressure position and value for fast cycle.

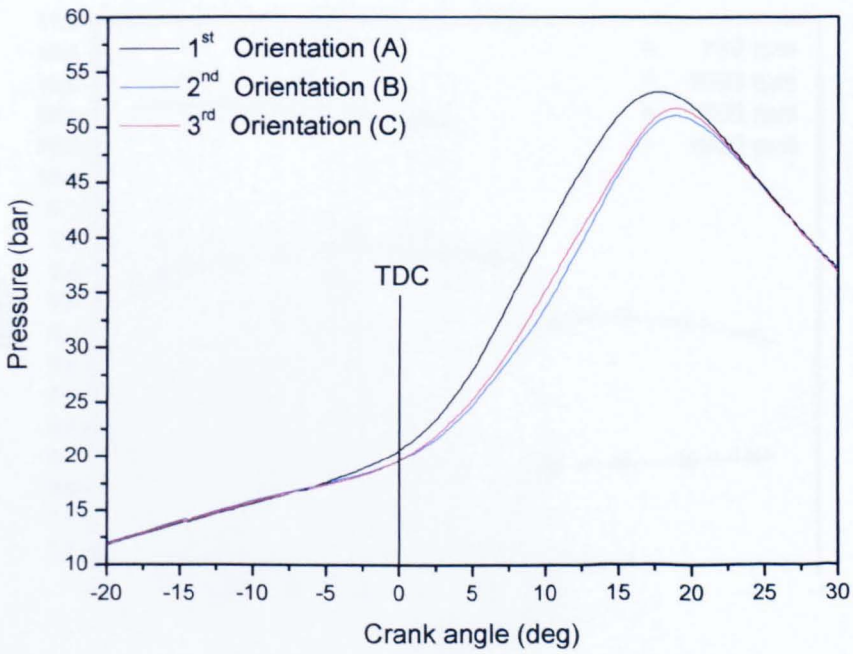


Figure 6.6 Effect of spark plug ground electrode orientations on peak pressure values.

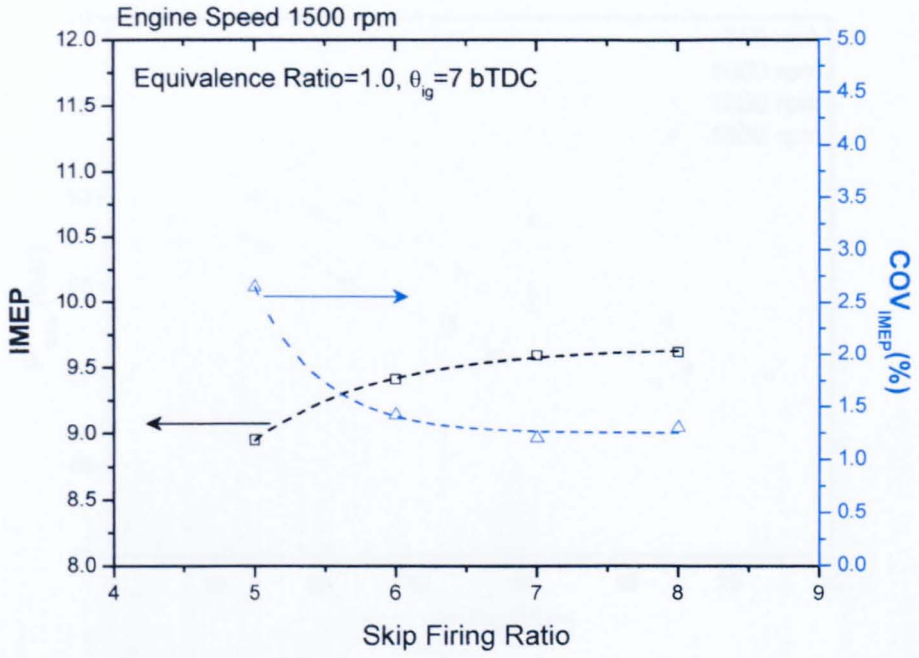


Figure 6.7 Effect of skip-firing ratios on IMEP and COV_{IMEP} at 1500 rpm.

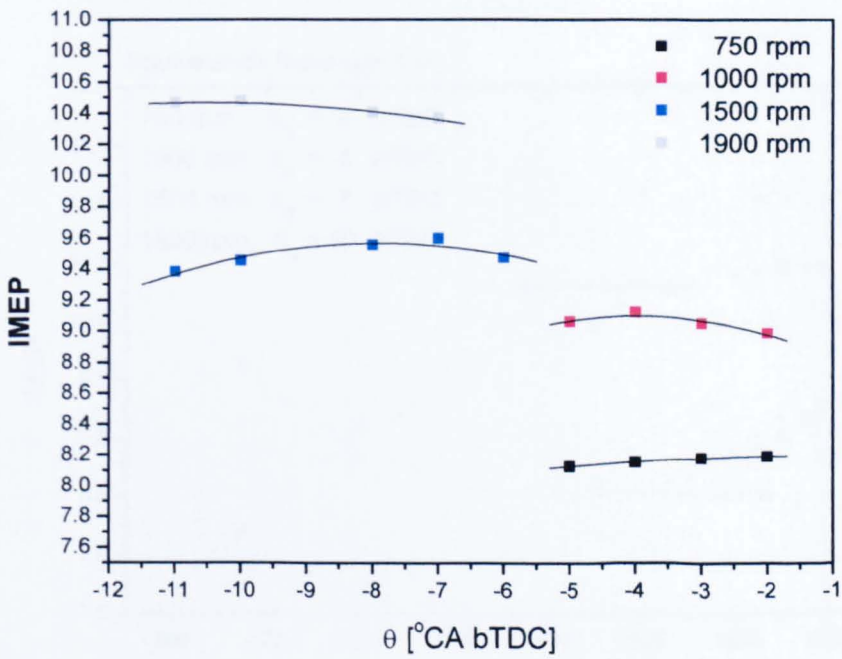


Figure 6.8 Optimum spark timing at different engine speeds.

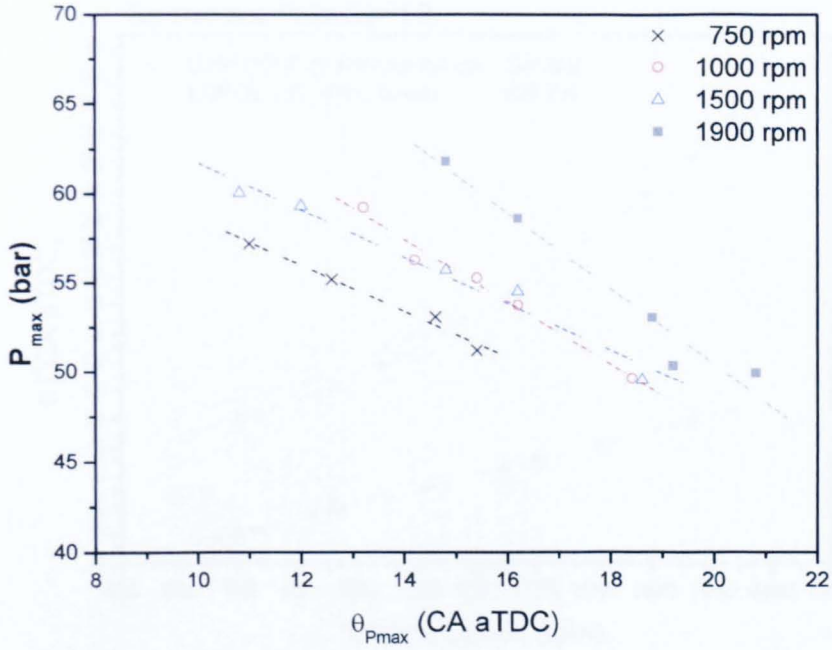


Figure 6.9 Influence of ignition timing on peak pressure (P_{max}) and its position ($\theta_{P_{max}}$).

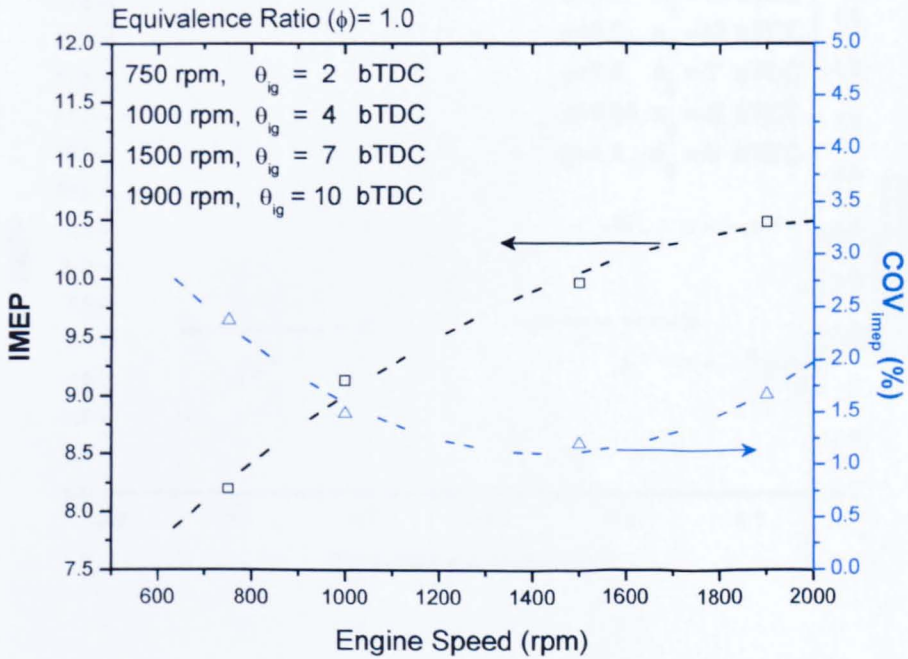


Figure 6.10 Effect of changing engine speeds on IMEP and COV_{IMEP} .

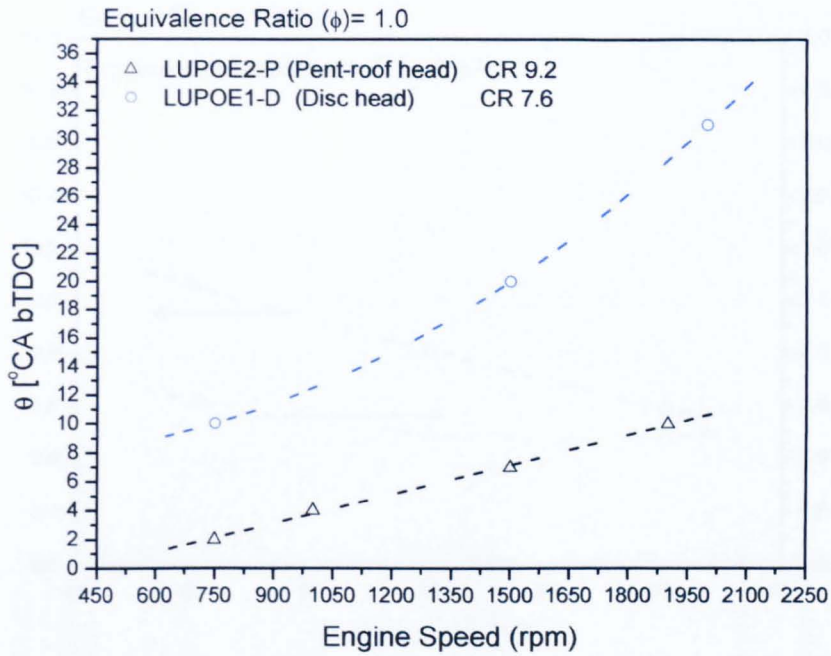


Figure 6.11 Comparison of optimum ignition timings for LUPOE1-D and LUPOE2-P.

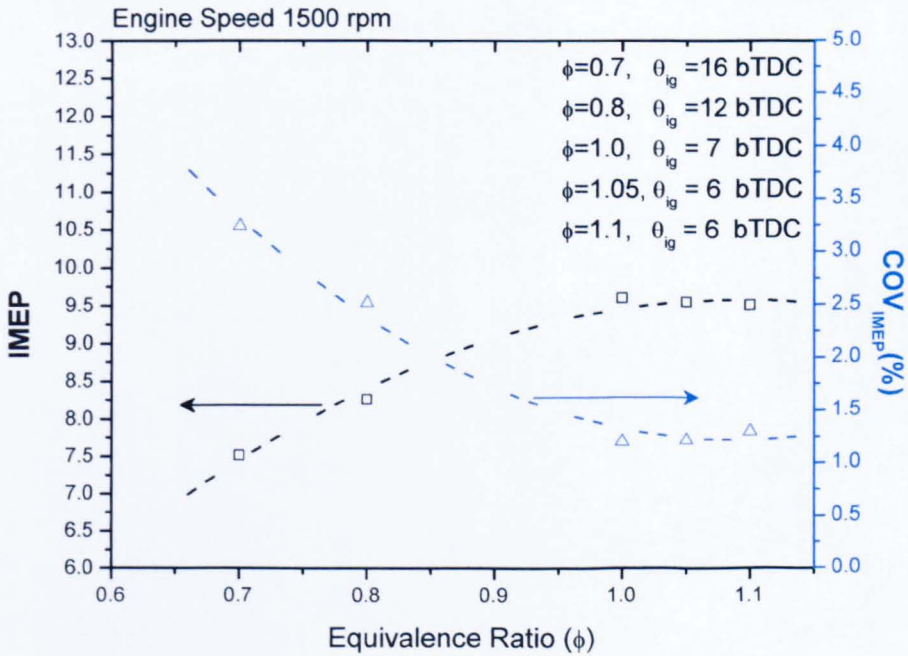


Figure 6.12 Effect of changing equivalence ratios on IMEP and COV_{IMEP} at 1500 rpm.

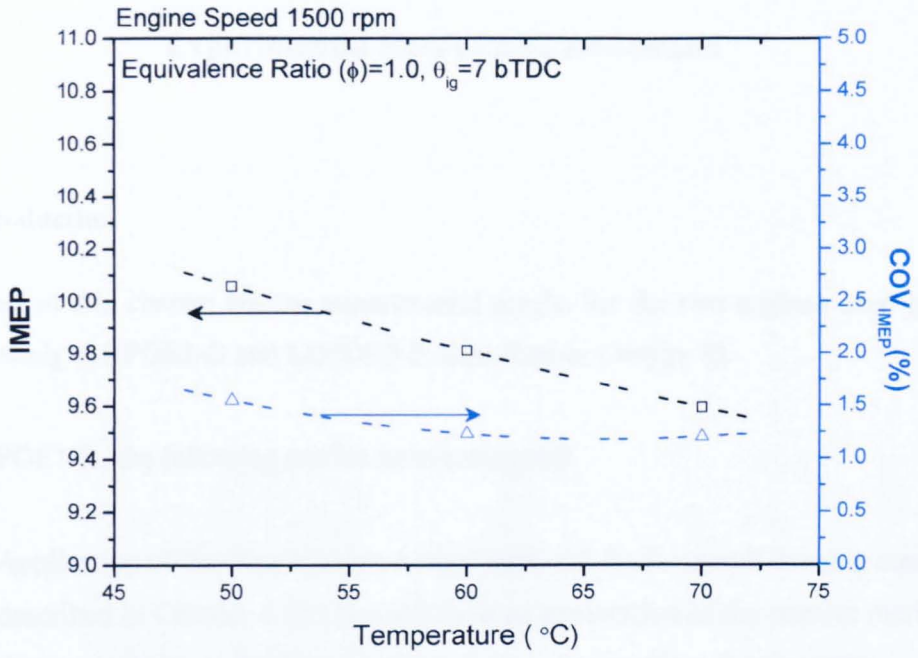


Figure 6.13 Effect of inlet/head temperatures on IMEP and COV_{IMEP} at 1500 rpm.

Chapter 7

Experimental Results and Discussion

7.1 Introduction

Presented in this chapter are the experimental results for the two engines used in the current study (LUPOE1-D and LUPOE2-P, described in Chapter 3).

For LUPOE1-D, the following studies were conducted:

1. Application of the simultaneous natural light and shadowgraph imaging methods described in Chapter 4 (Section 4.2.2) in an exploration of the relative merits of the two techniques for determination of mean flame radius development.
2. Investigation of early flame development using the shadowgraph technique discussed in Chapter 4 (Section 4.2.1) at a number of operating conditions (engine speed, equivalence ratio and ignition timing) with the inlet/head temperature set to 50° C.

For LUPOE2-P, the following studies were undertaken:

1. Characterisation of the flow and turbulence in the engine, using the LDV and PTV techniques discussed in Sections 4.4.1 and 4.4.2. In the LDV study, both forward and back scatter configurations were applied at a number of measurement points through the chamber space and two orthogonal velocity components which were generally measured, as discussed in Section 4.4.1. Data were analysed in terms of mean and RMS velocities. In the PTV study, in-cylinder flow patterns were visualised at two engine speeds (750 rpm and 1500 rpm).

2. The natural light ciné flame technique, for 3D simultaneous top and side imaging (described in Chapter 4, Section 4.3), was applied in conjunction with in-cylinder pressure recording. Derived data were analysed in terms of top and side view successive flame position contours and flame radii (for middle, fast and slow cycles based on peak pressure) and associated pressure development through the cycles. Side view flame centroid displacements were also analysed for these middle, fast and slow cycles.

7.2 Flame Study (LUPOE1-D)

A former colleague (Abdi Aghdam, 2003) conducted a study involving natural light imaging and simultaneous pressure data recording for a wide range of conditions for the LUPOE1-D engine. However, the natural light technique relies on flame luminosity for imaging; as a result, flame boundary definition is generally accepted to be less clear than with schlieren or shadowgraph photography. To assess the relative merits of the techniques for the current study and confirm the validity of Abdi Aghdam's earlier work, simultaneous natural light and shadowgraph imaging were undertaken, using the methods described in Section 4.2.3. Also, since flame definition in the low flame luminosity early stages of flame development was generally not good, shadowgraph imaging was applied in a study of cyclic variation in the early flame kernel growth over the central 40 mm of the chamber (Section 4.2.2). It has been suggested that early flame development is the controlling factor for the later combustion rate in engines (Hall, 1989; Witze et al., 1990); faster early flame kernel growth leading to higher unburned gas temperature and enhanced burning velocity later in the cycle.

7.2.1 Simultaneous Natural Light and Shadowgraph Study

Due to difficulties experienced with the Hitachi 16HM high-speed ciné camera used in the shadowgraph imaging (only one digital high speed camera was available at the time of undertaking these experiments, and this was used for natural light imaging), together with the limited time available for processing the shadowgraph images, this comparative study was undertaken at only one engine speed (750 rpm).

Simultaneous images were captured using both techniques, as shown in Figure 7.1. The mean flame radii determined from the two sets of images proved very similar, as shown in Figure 7.2, although the shadowgraph images yielded better flame definition in the very early stages of flame development.

7.2.2 Early Flame Development

Flame kernel formation depends on the mixture composition, thermodynamic state, fluid motion, ignition system and spark plug design (Herweg et al., 1988). Cyclic variation in flame development is associated with variations in these parameters. Shown in Figure 7.3 (a) is an example of symmetrical development of a stoichiometric flame, which remained centred on the spark plug, as illustrated. Also shown, in Figure 7.3 (b), (for another stoichiometric cycle) is an example of a flame convected and distorted in its development. An example of lean flame development is illustrated in Figure 7.3 (c); this kernel can be seen to develop more slowly, as well as being convected and distorted in its early stages.

In general, flames appeared to remain ‘anchored’ to the spark plug; with no examples of flames completely detached from the spark plug. This ‘flame holding’ by the spark plug has been noted by other researchers (Aleiferis et al., 2004).

Early flame development was investigated at a number of operating conditions, as shown in Table 7.1, with the inlet/head temperatures set to 50° C in each case.

Condition	Engine Speed (rpm)	Equivalence Ratio (ϕ)	Ignition Timing (bTDC)
1	1500	1.0	20
2	1500	1.1	18
3	1500	0.8	31
4	1500	1.0	31
5	1500	0.8	20
6	750	1.0	10
7	2000	1.0	31

Table 7.1 Conditions tested for early flame development.

7.2.2.1 Cyclic Analysis

Between 30 and 70 cycles were recorded at each condition, the number being restricted by the need to avoid long run times for the low lubricant mirrored piston conditions; mirror damage occurred relatively frequently. Cyclic variations in flame and pressure development were noted, the latter of the order experienced in production engines (Ozdor et al., 1994). This is illustrated in the cyclic variation in maximum cylinder pressure and the crank angle at which it obtained, Figure 7.4. The earlier peak pressure was achieved (i.e. the faster the combustion event), the higher was that peak pressure.

Marked on Figure 7.4 are the values of cyclic mean peak pressure and those at \pm two standard deviations from that mean. Three sets of data representative of ‘middle’, ‘fast’ and ‘slow’ cycles were chosen for further analysis. These were selected on the basis of having peak pressure close to the mean peak pressure and $\bar{p}_{\max} \pm 2\sigma_{p_{\max}}$, respectively.

(1) Flame Radius

Data obtained at the reference condition (Condition 1, Table 7.1) were analysed first. Mean flame radii for the middle, fast and slow cycles are shown in Figure 7.5. In general, cycles having earliest and highest peak pressure (i.e. faster cycles) did exhibit faster initial flame growth. Nevertheless, some overlap between growth rate of faster and slower cycles is apparent and some ‘fast’ cycles can be seen to have rather slow growth rate in their very early stages. Much the same pattern was observed for a rich mixture ($\phi=1.1$) at the same engine speed, with ignition adjusted to the optimum (MBT) at that condition, although one overall ‘fast’ cycle (based on a peak pressure) was amongst the slowest in terms of flame radius at 1.3 ms elapsed from ignition (Figure 7.6). For a lean mixture ($\phi=0.8$) at the same engine speed, with the ignition advance again re-set to MBT at that condition, the ‘overlaps’ and ‘cross-overs’ in flame radius development were more marked (Figure 7.7). The slower combustion associated with the lean mixture (accentuated by the lower gas temperatures associated with the reduced compression accompanying the advanced ignition), perhaps allowing more time for interaction between the (cyclically varying) turbulence local to the ignition site and the flame. It can be observed that at a given mean flame radius the spread in mean flame radius was similar for all the equivalence ratios (stoichiometric, rich and lean), with that

spread more apparent as time increases. Nevertheless, not all those flames faster at very early stages of flame development were also faster at later stages of combustion. Similar observations were noted at the other engine speeds and ignition timings adopted (Table 7.1).

(2) Flame Centroid

Kernel convection has been quantified using kernel centroid displacement with time, for the period from ignition to that where part of the flame circumference went beyond the 40 mm field of view. There was no correlation between direction of centroid migration and observed burn rate of fast, middle and slow cycles; nor between the cycles within each set for the tested conditions. However, it was noted that for conditions where flames were present in the turbulent flow field for longer times (e.g. for mixtures where the optimum ignition timing was advanced more), the centroid movements were greater; e.g. Figures 7.8 (a) and (c) for stoichiometric and lean ($\phi=0.8$) mixtures, respectively, at 1500 rpm. Similarly, for any given equivalence ratio, the fast cycles experienced less displacement, although there was little observable difference between the displacements of middle and slow cycles. There seemed to be an overall preferred migration direction towards the fourth quadrant; however, within this, the variation between the sets of cycles and within a set of cycles was apparently random. This was also the case at the other engine speeds and ignition timings adopted.

(3) Flame Shape Factor

Flame kernel distortion was quantified using a 'Shape Factor' parameter SF (a rough measure of flame 'circularity'). This 'Shape Factor' expresses the flame perimeter (P_f) relative to that (P_c) of a circular flame of identical area, i.e. it has a value increasingly greater than unity as flames become more distorted. Shown in Figure 7.9 are values of Shape Factor derived from successive flame front positions over the first 12° CA following ignition, for the fast, middle and slow cases discussed previously, for stoichiometric, rich and lean conditions. It can be seen that the SF remains close to unity for the first 1.5° CA after ignition, due to the fact that the flame kernel after ignition is smaller than most scales of turbulence and hence propagates at a rate close to the laminar burning velocity. This can be seen also in Figure 7.10, where the SF is plotted

versus mean flame radius rather than time; the value of SF remains close to unity at the flame radius of 1 mm for fast, middle and slow (stoichiometric, rich and lean) cases discussed above. However, as the flame surface increases, it can become wrinkled by an increasing spectrum of turbulent scales (Abdel-Gayed et al., 1984). Although the general trend is of increasing SF with crank angle (and time) and mean flame radius, there is no evidence that fast, middle and slow combustion is related to the degree of flame distortion, e.g. there are slow cycles with both high and low SF, likewise rich and lean cycles.

An alternative approach was also adopted in an examination of the effect of SF on the very early stages of flame kernel development. Shown in Figure 7.11 (a) are values of SF for the three fastest and slowest stoichiometric cycles based on the mean flame speed during the first 5° CA following ignition, determined from the flame images (as opposed to the much later peak cylinder pressure employed previously to characterise fast and slow cycles). Similar data for the rich ($\phi = 1.1$) and lean ($\phi = 0.8$) mixtures are presented in Figures 7.11 (b) and (c), respectively. In these diagrams, the empty triangles represent the high and the filled squares the low flame speed cycles, respectively. In general, it can again be seen that Shape Factors remain close to unity for the first 1.5° CA following ignition; from that point, flames became more distorted. For stoichiometric flames (Figure 7.11 (a)), the most distorted cycle was among the slowest burning cycles; however, 'overlaps' between the slow and fast cycles are again apparent and the least distorted cycle also proved slow. Contrary behaviour was noted for the rich and lean cases, the cycles with the most distorted flames were generally fast burning – with some overlap between fast and slow burn cycles again apparent towards the end of the burn period. From the above, there would seem to be no correlation between flame speed during the very early stages of flame kernel development and the degree of flame distortion.

7.3 Flow Investigation (LUPOE2-P)

As outlined in Section 7.1, both LDV and PTV techniques were used for flow and turbulence characterisation. The results are presented below in Sections 7.3.1 and 7.3.2.

7.3.1 PTV Flow Investigation

Although, the LDV study was conducted before the PTV flow investigation, the results of the PTV investigation are presented here first. The LDV data yielded ensemble-averaged values at a number of points and directions in the chamber accessible using the technique. However, the flow is better understood (and the LDV data easier to comprehend) by considering first the cyclically resolved whole field data generated with PTV.

7.3.1.1 PTV Results

The PTV method was adopted for motoring conditions, at two engine speeds (750 rpm and 1500 rpm), as described earlier in Section 4.4.2. Relatively few tests were conducted at each engine speed. This was due to the limited time available to conduct the experiments (as the same engine was used by a colleague, for more extensive flow studies within a GDI variant of the engine) and because the procedure was very time consuming. The latter was associated with the need to dismantle the head after each run, to clean the engine of seed particles. No tests were carried out at engine speeds above 1500 rpm, because the Perspex suffered excessive wear as engine speed increased and at high speeds engine vibration was experienced.

The experiments were conducted first at 1500 rpm, with the camera focused on the right side of the clearance volume (away from the inlet port) of the Perspex engine, as shown in Figure 7.12 (a). The reason for so doing was to concentrate the laser sheet to visualise the flow in the region where the tumble was expected (in the area near to the wall opposite the inlet) on the basis of the LDV study at this engine speed, as discussed later.

At 750 rpm, the camera was moved to a more central position, as shown in Figure 7.12 (b), to allow more complete observation of the flow in the clearance volume. For clarity, the results at 750 rpm are presented first. At the outset of the study,

it was thought that the pent roof geometry in conjunction with the inclined inlet duct would generate a strong ‘tumble’ swirling flow, as indicated in Figure 7.13 (possibly with weaker induced secondary vortices as shown), which would then ‘spin-up’ as compressed by piston motion before degenerating into more random (smaller scale, ‘turbulence’) motion at TDC. In the event, the PTV study revealed a rather more complex state of affairs.

750 rpm

In practice, at 750 rpm (at which the mean piston speed was 2.75 m/s), three quite separate basic patterns of flow were observed. These are illustrated by three examples in Figures 7.14, 7.15 and 7.16, respectively. The flow suggested by the data in Figure 7.14, representative of that recorded in about 15% of cycles, was generally in accord with expectation; with a principal anti-clockwise vortex in the observable region at 85.5 and 67.5° bTDC, at which piston speeds were 4.38 and 4.36 m/s, respectively. Towards TDC (22.5° CA to TDC), when piston speeds were 2.26 and 0 m/s, respectively, the particle tracks suggest this vortex moving to the right and degenerating into multiple smaller vortices, with a hint of the secondary contra-rotating vortices suggested in Figure 7.13 (a), although the seed density at the left was insufficient to allow good definition of this. The magnitude of the mean velocities was relatively low (6 m/s) compared with an estimated inlet jet velocity of the order 14.4 m/s. A further 7% of cycles demonstrated the behaviour set out in Figure 7.15, with no strong motion in the clearance volume at 85.5° CA. However, by 67.5° CA, an anti-clockwise vortex seemed to have developed to the left of the chamber, with a principal direction of motion primarily to the right (as shown). By 22.5° CA to TDC, this resulted in a fairly strong clockwise vortex centred at the middle of the chamber, with a hint of an induced anti-clockwise vortex to the left. However, the majority (78%) of cycles exhibited contrary behaviour, with an initial (85.5 and 67.5° CA) strong clockwise motion, as shown in Figure 7.16. Nevertheless, by 22.5° CA, this can be seen to have given way to a strong flow (with no apparent vortex motion in the field of view) in the reverse direction (i.e. to the left), a situation maintained to TDC. The reasons for this are not obvious; although this flow to the left must be compensated by flow to the right on planes other than the central plane illuminated by the laser sheet, i.e. as suggested in Figure 7.13b (i)

and consistent with later LDV derived mean velocities (Figures 7.21 (a), 7.24 (a) and 7.25 (a)).

1500 rpm

At 1500 rpm (at which the mean piston speed was 5.5 m/s), for about 25% of cycles, the flow pattern behaviour was similar to that noted in the majority of cases at the lower engine speed of 750 rpm (Figure 7.17) (for the same air mass flow and piston speed higher, one might expect flow to be more easily deflected up the left hand side of the cylinder). However, for the majority (75%) of cases at 1500 rpm, the strong motion to the right observed at 85.5 and 67.5° CA (where piston speeds were 8.77 and 8.72 m/s, respectively) was maintained to 22.5° CA and TDC (where piston speeds were 4.52 and 0 m/s, respectively) within the limited field of view, with a clockwise vortex motion, as shown in Figure 7.18. This flow to the right must be compensated by flow to the left on planes other than the central plane illuminated by the laser sheet, as shown in Figure 7.13b(ii) and consistent with later LDV derived mean velocities (Figures 7.21 (c), 7.24 (c) and 7.25 (c)).

7.3.2 LDV Study

Presented in this section are the results of LDV mean and turbulent measurements for the LUPOE2-P optical engine. All data were obtained under motoring conditions, over a range of engine speeds (750 rpm, 1000 rpm, 1500 rpm and 1900 rpm). The flow within the cylinder was unsteady and three-dimensional in nature. Therefore, measurements at various locations within the LUPOE2-P engine were carried out using both forward and backscatter configurations (as described earlier in Section 4.4.1), to provide more quantitative data at a restricted number of points to supplement the more qualitative 2D information derived from PTV.

Shown in Figure 7.19 is the co-ordinate system adopted in presenting the results. This system has its datum at the centre (C) of the piston crown at TDC. The measurement positions are labelled A, B, C, D, E and are defined by the co-ordinates x , y , z in the diagrams that follow. The LDV fibre optic probe access was generally via the side window, as shown in Figure 7.20; some later measurements were made via one of the

top windows, as shown in relevant later diagrams. Velocity components measured relative to the probe in these positions are defined in the diagrams at the appropriate times (see Table 7.2).

Measurement Point	Co-ordinates (x, y, z)	Velocity Components Measured
A	(0, 6.5, 20)	u, v
B	(0, 6.5, -20)	u
C*	(0, 6.5, 0)	u
D	(10, 5, 0)	$s_D (u v)** , w_D (z)***$
E	(20, 3, 0)	$s_E (u v)** , w_E (z)***$

* Datum in centre, point (C) of the piston crown at TDC.
 * y-axis datum, piston at TDC (0 mm).
 ** s component was a combination of u and v components of velocity

$$[s = (u^2 + v^2)^{\frac{1}{2}}].$$

 *** w component was measured in z direction.
 Forward scatter (FS), points (A, B, C).
 Back scatter (BS), points (D, E).

Table 7.2 Co-ordinates system for measured points.

7.3.2.1 Forward Scatter Experiments Results

First results will be presented for (i) the horizontal component of velocity u in a vertical plane (at right angles to the 'ridge' of the pent roof) through the centre (point C) of the chamber, to allow ready comparison with the PTV data already presented for that plane; for the same two engine speeds (750 and 1500 rpm) adopted in the PTV study; and for the two additional speeds (1000 and 1900 rpm). Then, (ii) results will be presented for points A and B in two planes parallel and to either side of the central plane, including at Point A data for the vertical component of velocity v in addition to the horizontal component u .

(i) Effect of Engine Speed (u-component of velocity at chamber centre, Point C)

The velocity component u , in the x-direction (Figure 7.19, Table 7.2) was measured at the centre of the chamber at Point C (co-ordinate 0, 6.5,0), some 6.5 mm above the piston crown position at TDC. For ready comparison with the PTV flow investigation presented earlier, LDV data for 750 and 1500 rpm are presented first.

High positive ensemble mean horizontal velocities (\bar{u}) were noted at Point C prior to port closure (IPC/EPC) at 750 rpm, as shown in Figure 7.21 (a), reducing towards port closure. The magnitude of this velocity component then increased after port closure; it reached a maximum value at around 75° bTDC before decreasing and reversing direction. This change in direction was also observed in the PTV flow pattern exhibited in the majority (78%) of cycles at this engine speed (750 rpm), as discussed earlier in Section 7.3.1.1. Ensemble averaged (over 100% of cycles) values of the \bar{u} component of velocity are shown (with a box surrounding the vectors) for successive CA positions superimposed on the PTV data shown in Figure 7.16. The LDV mean velocities (averaged over 100% of cycles) are consistent with the PTV data for both Figures 7.16 and 7.15 (together comprising 85% of cycles), but opposite in direction to the minority of cycles (15%) shown in Figure 7.14.

At 1500 rpm, constant positive mean horizontal velocities were noted at Point C before port closure (Figure 7.21 (c)). Then, as at 750 rpm, the mean velocity increased after port closure, reaching a maximum value at around 50° bTDC before decreasing. However, at 1500 rpm (unlike at 750 rpm), no change in direction occurred. This lack of change in direction is consistent with the PTV observations for the majority of cycles (75%) at this engine speed (1500 rpm). As before, LDV-derived vectors at Point C at the various crank angles are shown ('boxed') superimposed on the PTV information in Figure 7.18.

For both engine speeds, it can be seen that mean velocity at Point C is approximately constant and of relatively low magnitude (albeit in different directions at the two speeds) during the combustion period (2 to 7° CA bTDC). It is interesting to note that, during the combustion period, generally $|\bar{u}| < 2$ m/s (2 mm/msec); this would result (on average) in relatively little bulk transportation of the flame kernel in this direction

during the combustion event. Corresponding values of the rms turbulent velocity (u') at Point C for the two engine speeds are shown in Figures 7.21 (b) and (b). At this point in the chamber, values of u' can be seen to be relatively constant during induction and compression, with an increase in value as the piston approaches TDC, followed by a decay in u' from about 30° bTDC right through the expansion stroke. The values of u' at TDC for the two engine speeds (one double the other) were about 3 and 3.7 m/s for 750 and 1500 rpm, respectively.

Corresponding LDV-derived variations of \bar{u} and u' at Point C with crank angle are shown for the additional engine speeds of 1000 and 1900 rpm in Figure 7.22. The trends in \bar{u} and u' at the intermediate engine speed of 1000 rpm are similar to, and consistent with the data already presented and discussed for 750 and 1500 rpm. However, at the highest engine speed (1900 rpm), different trends in \bar{u} with c.a. were observed at Point C during the induction and early compression period, with very high values of \bar{u} before and after port closure (Figure 7.22 (c)). The reasons for this difference are not obvious. However, from about 50° bTDC and through the expansion until port opening, the \bar{u} behaviour can be seen to be more consistent with that noted at the lower engine speeds (Figure 7.23 (a)). At 1900 rpm, anomalous behaviour in u' during the critical 60° to TDC period is also very apparent, with a sharp increase in u' from the sort of values noted at other engine speeds to a peak of about 8 m/s (twice that at other speeds) at about 20° bTDC (Figure 7.22 (d)). This was followed by a decay in u' through the expansion stroke; this was more consistent with the behaviour at lower speeds, although the magnitude of u' was significantly higher than at lower engine speeds (Figure 7.23 (b)). Again, the reason for the anomalous behaviour was not obvious (the LDV data rate was satisfactory, ~ 12000 Hz). It may have been associated with 'structures' in the flow patterns/movements of vortex centres noted in the PTV studies, induced at the higher piston speed, with implications for ensemble averaged LDV data. Unfortunately, there was insufficient time to investigate this further; this is important for further study, possibly using time-resolved PIV.

(ii) Velocity variation with position (\bar{u} and u' at points A and B, \bar{v} and v' at Point A, at 750 and 1500 rpm)

Points A and B were on vertical planes parallel to that presented for Point C, equidistant 20 mm on either side of the central plane (Figure 7.19 and Table 7.2).

Positions A and B, (\bar{u}_A and \bar{u}_B) (u'_A and u'_B)

At 750 rpm, the variation in the magnitude of the mean velocity component \bar{u} with crank angle proved remarkably similar to that at C (central plane) at the corresponding positions A and B in the parallel planes, as shown in Figures 7.24 (a) and 7.25 (a); although at Point B, the flow direction reversal from approximately 40° bTDC seen at A and C did not occur (Figure 7.25 (a)). Likewise at 1500 rpm, the behaviour in magnitude of \bar{u} was very similar at all three positions, although this suggested flow reversals at about 40° bTDC at A and B, with little mean velocity after 20° aTDC at Point A and a further reversal of flow direction just after TDC at Point B (Figures 7.24 (c) and 7.25 (c)). However, it should be remembered that the mean velocities derived from LDV are the result of ensemble averaging, masking the switch of flow patterns suggested in the earlier PTV study; the latter effect may have disproportionate results on the mean values at the three positions. It should again be noted that the magnitudes of \bar{u} at the three positions during the critical combustion period is again suggested to be low, such that only minor translations of flame kernels might be expected in these directions during combustion.

Set out in Figures 7.24 (b) and 7.25 (b), and Figures 7.24 (d) and 7.25 (d), are corresponding rms turbulent velocity data (u'_A, u'_B) for engine speeds of 750 and 1500 rpm; to compare with earlier data for position C shown in Figures 7.21 (b) and (d). The u' data at all three positions can be seen to be very consistent in both trend and magnitude, particularly during the crank angle interval corresponding to the expected combustion period.

Position A (\bar{v}_A and v'_A)

Shown in Figure 7.26 are corresponding vertical velocity component (\bar{v}) and rms turbulent velocity (v') at Point A. At 750 rpm, the mean vertical velocity at this position remained low throughout the cycle; in the upward direction late in the compression stroke, reducing to approximately zero at TDC and reversing direction (towards the piston crown) after TDC, albeit at very low magnitude (Figure 7.26 (a)). A similar pattern pertained at 1500 rpm, with higher (but still low) velocity (Figure 7.26 (c)). The vertical rms velocity (v') reflected (with slightly lower magnitude) the behaviour noted previously for the horizontal component (u') at the same position (Point A) (Figure 7.24 (b) and (d)), at the two engine speeds. The slight difference in magnitude of the two components might be associated with ensemble averaging.

7.3.2.2 Back Scatter Experiments Results

The limited height available with the cylinder head side windows and the severe distortion created at the outer edges of these windows restricted the positions within the cylinder head for which it proved possible to apply the forward scatter technique. Hence, to obtain further insight into the flow in the pent head, the back scatter method was adopted to measure velocity at two other positions in the head. Application of the technique to more points was restricted by back-reflected light from the piston crown. As shown in Figure 7.27, the LDV fibre optic probe was held at right angles to one of the top windows. By rotation of the probe on its axis, two components of velocity were accessible: the w component aligned in the z direction and the other, s component, as shown in Figure 7.19 and Table 7.2. The s component was a combination of u and v components of velocity ($s = (u^2 + v^2)^{1/2}$). Mean and rms turbulent velocities were measured at two points, D and E, at co-ordinates (10, 5, 0) and (20, 3, 0), respectively (as shown).

Position D (\bar{s}_D, \bar{w}_D) and (s'_D, w'_D)

The mean velocity variation with crank angle, at both engine speeds (750 and 1500 rpm), followed the pattern described for the mean horizontal component of velocity (\bar{u}) at the same engine speeds as measured in the chamber centre (Position C,

Figure 7.21 (a)). At 750 rpm, flow reversal at about 30° bTDC occurred for component \bar{s}_D (Figure 7.28 (a)), whereas no reversal was observed at 1500 rpm for both positions C and D (Figures 7.21 (c) and 7.28 (c)). Similarly, rms velocities (s'_D) followed the patterns observed previously at 750 and 1500 rpm (Figures 7.28 (b) and (d)). The mean velocity component \bar{w}_D in the z direction remained low throughout the cycle (Figures 7.29 (a) and (c)) at both engine speeds – in particular, it was of the order 1 m/s during the combustion process interval. The pattern and magnitude of w'_D was again similar to that observed previously at other positions (Figures 7.29 (b) and (d)).

(ii) Position E (\bar{s}_E, \bar{w}_E) and (s'_E, w'_E)

Set out in Figures 7.30 and 7.31 are corresponding mean and rms velocity components \bar{s}_E , s'_E and \bar{w}_E , w'_E , respectively, for the two engine speeds (750 and 1500 rpm). The behaviour patterns were similar to those noted at Position D, although rms velocities were of slightly reduced magnitude.

7.4 Flame Study (LUPOE2-P Engine)

Simultaneous top and side natural light film imaging experiments (with concurrent in-cylinder pressure data recording) were conducted with the LUPOE2-P engine at the operating conditions detailed in Table 7.3. It proved impossible to conduct planned higher engine speed experiments at 1900 rpm, due to run-on problems.

Condition	Engine Speed (rpm)	Equivalence Ratio (ϕ)	Ignition Timing (bTDC)
1*	1500	1.0	7
2	1500	1.0	2
3	1500	1.0	12
4	1500	1.1	6
5	1500	0.8	12
6	750	1.0	2
7	1000	1.0	4
* Reference Condition Inlet/head temperatures set to 55°C, throughout. Ignition timing set optimal for all conditions except Conditions 2&3.			

Table 7.3 LUPOE2-P engine operating conditions.

At each operating condition, data were recorded for approximately 80 cycles and values of peak in-cylinder pressure (P_{\max}) were plotted versus the position of its occurrence ($\theta_{P_{\max}}$), e.g. Figure 7.32(a). As in the case of LUPOE1-D data analysis, Section 7.2.2.1, four representative ‘middle’, ‘fast’ and ‘slow’ cycles were selected for detailed examination on the basis of having peak pressure close to the mean peak pressure and $\bar{P}_{\max} \pm 2\sigma_{P_{\max}}$, respectively, Figure 7.32(a). The pressure – crank angle diagrams for these cycles, at the reference condition, are shown in Figure 7.32(b).

As described in Section 4.3, simultaneous overhead and side view natural light film flame images were collected using separate Phantom high-speed cameras. The overhead window clamping flanges, Figure 4.5 precluded overhead imaging of the very earliest

stages of flame development (the first 0.35 to 0.45 ms of flame development, for the majority of the cycles), Figure 4.6. The view of the flame via the side window, Figure 3.16(a) was subject to significant refraction effects at large flame radii.

7.4.1 Reference condition

(i) 'Middle' cycles at reference condition

Shown in Figure 7.33 are successive flame front positions (as recorded by overhead and side view cameras) for the four selected 'middle' cycles, at the reference condition ($\phi = 1$, 1500 rpm, 7° bTDC ignition). Viewed from above, the flames appear approximately circular in each case; although late in the combustion events the flames can be seen to approach the walls non-symmetrically, touching the wall at some points around its circumference and creating 'bubbles' of unburned gas (which later burn up) at other points. Two cycles, (a) and (d), show significant shifts of the enflamed zones to the right; in accord with the dominant (75% of cycles) flow pattern noted at this engine speed in the particle tracking experiments (Figure 7.18). In one case, Cycle (b), the flame remains fairly central and in the fourth, Cycle (c), the flame moves more to the left (in accord with the flow pattern behaviour noted in approximately 25% of cycles, Figure 7.17). In the corresponding side views, flames again appear relatively circular in their early development – although the centres of these 'circles' do not remain anchored on the spark position (as often assumed in models). The unburned 'bubbles' seen at later flame front positions in the overhead views are largely obscured in the side views – although in Cycle (c), and to a certain extent in Cycle (b), a similar 'bubble' is apparent just left of centre close to the piston crown; this is again consistent with the flow pattern noted at this position in Figure 7.17. In both views, enflamed regions appear completely to fill the chamber by the crank angle corresponding to peak cylinder pressure ($\sim 18^\circ$ aTDC) for these 'middle' cycles. Of the four selected cycles, Cycle (d) seems marginally faster in terms of flame propagation; this is reflected in pressure development for this cycle, vis à vis the other three, Figure 7.34 (a).

The successive positions of the flame fronts shown in Figure 7.33 were processed to determine the corresponding enflamed areas; the centroids of these areas and corresponding flame radii (that of a circular flame encompassing similar enflamed area

in each case) were then determined. The flame centroid migrations (determined from the side view), Figure 7.34(b), correspond with the earlier descriptions; i.e. Cycles (a) and (d) showing flame kernel movement to the right, Cycle (c) slightly to the left and Cycle (b) staying approximately central. In the horizontal direction, the average velocity of flame kernel migration for the four selected middle cycles was of the order 2mm/ms (2 m/s) – in the same direction and at almost the same magnitude noted in the ensemble averaged LDV measurements at the centre of the chamber (Point C), Figure 7.21(c). However, in each case, a strong downwards movement of the flame centroid from the spark position can be noted. Not surprisingly, late in the combustion events (by which time flames practically fill the entire chamber) the centroids co-incide with the chamber centroid.

Values of mean flame radius versus crank angle for the four selected ‘middle’ cycles are set out in Figure 7.34(c). In the early stages of combustion, radii could be determined only from the side views (because of window obscuration, Figure 4.5); in the later stages, those based on the overhead views are considered more reliable because of severe side window refraction effects at large radii. The radii determined from the two views can be seen to be reasonably consistent, with relatively little scatter for these four cycles of similar pressure development history. There is a suggestion that those cycles experiencing greater flame kernel migration to the right {(a) and (d)} exhibit faster flame radius development; however, the differences seem marginal. For cycle (b), the slow late burning suggested from the overhead view (Figure 7.34(c)) might be associated with the ‘bubble’ of unburned gas noted at the wall in Figure 7.33.

(ii) ‘Fast’ cycles

Shown in Figure 7.35 are similar diagrams illustrating successive flame front positions, overhead and side views, for the four selected ‘fast’ cycles (Figure 7.32). The faster burning is evident in the larger flames (c.f. ‘middle’ cycles, Figure 7.33) at the time corresponding close to TDC (the black contours in the diagrams) and the greater separation of the flame contours (more flame travel in the same time between flames). Also evident in the overhead views are, vis à vis the ‘middle’ cycles, generally more elliptical (i.e. less circular) flames, with faster burn in the direction of the ‘apex’ of the pent-roof chamber. Flames viewed from the side, also seem more ‘distorted’ from a

circular shape in the early stages of flame propagation, Figure 7.35. The flame growth patterns and kernel movements also seem more consistent between cycles, for these four selected faster burn cycles. This is evident in the diagrams (Figure 7.36(b)) showing the flame kernel centroid displacements (determined from the side view) and values of (equivalent circular area) flame radii, Figure 7.36(c). Unlike the ‘middle’ cycles, greater differences between radii determined from overhead and side views of the flame are apparent – consistent with the less spherical (and greater mean flame surface area per unit enflamed volume) noted c.f. the case for the middle cycles.

(iii) ‘Slow’ cycles

Similar successive flame front positions for the selected ‘slow’ cycles (Figure 7.32) are set out in Figure 7.37; with corresponding derived flame centroid displacements and flame radii given in Figures 7.38(b) and (c), respectively. These slower cases seem to exhibit relatively little movement to the left and right (as seen from the side view) and to tend to stay closer to the ‘roof’ of the chamber (particularly so in the slowest case, Cycle (c)), with corresponding loss of effective flame surface area (flames touching roof walls) early in the combustion events.

Comparison of representative ‘middle’, ‘fast’ and ‘slow’ cycles

Shown in Figure 7.39(a) are pressure versus crank angle diagrams for representative ‘middle’, ‘fast’ and ‘slow’ cycles at the reference condition; with corresponding derived (side view derived) flame centroid displacements and flame radii (for both overhead and side views) given in Figures 7.39(b) and (d), respectively. The representative middle cycle was selected as that having $\theta_{p_{\max}}$ closest to the mean, the fast and slow representative cycles were those nearest a line of mean slope ($dP_{\max}/d\theta_{\max}$) drawn through the representative mean point. At TDC, both middle and fast cycles exhibit a similar clockwise movement from spark position (about 5mm in the x-direction and 2.9mm in the y-direction from the spark position), as shown by the filled black square and the filled red circle, whereas, the slow cycle remained close to the spark at TDC, as shown by the filled blue triangle (as seen from the side view). This was also reflected in the pressure diagram where both middle and fast cycles showed some pressure

development at TDC, whereas, no development was noticed for the slow cycle (Figure 7.39(a)). In general, the corresponding flame radii at TDC (about 0.77 msec from ignition) derived from the side view exhibited the behaviour similar to that noted in both pressure and flame centroid graphs; i.e. middle and fast cycles had similar flame radii (about 10.3mm), c.f. ~ 6.6mm for the slow cycle, at TDC. The convection of both middle and fast cycles from the spark at TDC might have reduced the contact area (and hence reduced heat exchange) and so resulted in greater pressure and flame development than for the slow cycle (with its centroid close to the spark at TDC). Similar behaviour was noted for the other fast and slow cycles (Figure 7.39(c)). This accords with the findings of both Hacoheh et al. (1992) and Pajot et al. (2000); they reported that their largest flames were found relatively far from the electrodes, which they associated with reduced heat exchange with the electrodes. Conversely, Gatowski and Heywood (1984) found no such correlation between flame development and the direction and extent of flame kernel convection away from the spark plug.

7.4.2 Effect of Ignition Timing

The experiments reported in Section 7.4.1 (for the 'Reference' 1500 rpm case) were repeated for two different ignition timings (2 and 12° bTDC) at the same equivalence ratio ($\phi = 1.0$); Conditions 2 and 3, respectively, Table 7.3. No significant differences in flame growth behaviour between fast, middle and slow cycles (vis à vis that noted at the reference condition) were observed. For completeness, since the data are valuable for colleagues modelling the engine over a wide range of conditions, various diagrams corresponding to those at the reference condition are given in Appendices B1 and B2 (as well as fully reported in a technical report, Murad (2006)). However, only a summary diagram characterising some of the behaviour noted for the 'middle' cycles is presented here, Figure 7.40. It can be seen that ignition timing had a significant effect on peak pressure value and its position. As expected, advanced ignition led to earlier flame and pressure development and higher peak pressure; and vice-versa for retarded ignition. Mean flame radii derived from corresponding overhead and side views were again consistent for these 'middle' cycles. It was interesting to note that, slow initial flame development for the late ignition apart, flame speed (expressed as increase in flame radius/crank angle increment (Figure 7.40(b) and (c)) or flame radius/time increment

(Figure 7.41) was remarkably similar for all ignition timings. This was presumably associated with similar turbulence intensities in all three cases.

7.4.3 Effect of Equivalence Ratio

As for the disc-shaped engine, experiments were also conducted at two other equivalence ratios: rich, $\phi = 1.1$ and lean, $\phi = 0.8$ (Conditions 4 and 5, Table 7.3). At each operating condition, representative ‘middle’, ‘fast’ and ‘slow’ cycles were selected as before.

(i) Rich Mixture ($\phi = 1.1$)

The optimum ignition timing for the rich mixture was 6° bTDC, close to the optimal 7° bTDC for a stoichiometric mixture at the reference condition. The pattern of flame propagation (successive flame positions seen in top and side views) and flame kernel migration trends were very similar to those noted for $\phi = 1$ and are not shown here (they are available in Appendix B3 and technical report, Murad (2006)). Magnitudes of peak cylinder pressure and crank angle for its occurrence for middle, fast and slow cycles, Figures 7.42(a) and (b), were almost identical with the corresponding values for $\phi = 1$, Figure 7.32(a). Likewise, the flame radii derived from overhead and side views, Figure 7.43.

(ii) Lean Mixture ($\phi = 0.8$)

For the lean mixture, for maximum imep it was necessary that the ignition timing be advanced by 5° bTDC (to 12° bTDC) relative to that at ‘reference’ condition ($\phi = 1$), in order to compensate for the slower burning associated with a leaner mixture. As previously, representative middle, fast and slow cycles were selected (on the same basis as before) for further analysis, Figure 7.44. Set out in Figure 7.45 are successive flame front positions recorded by the overhead and side view cameras for the four ‘middle’ cycles. Vis à vis the richer mixtures, more flame front distortion (from circular) is evident in both overhead and side images; also, c.f. the middle cycles, there was less distortion in the fast cycles and more in the slow cycles, Figures 7.46 and 7.47,

respectively. This might be associated with the greater length of time available for a bigger proportion of the range of turbulent eddy sizes existing within the chamber to distort the flame. Note that the unburned gas temperature at ignition would be lower, with more advanced ignition timing, resulting (in conjunction with a lean mixture) in a lower laminar burning velocity, as well as reduced resistance to flame stretch rate effects.

Overhead and side view derived mean flame radius versus crank angle diagrams are set out in Figures 7.48(b) and (c). As noted for $\phi=1$, there was consistency between radii derived from the two separate views for middle and slow cycles and lack of consistency for the fast cycles. For the latter, overhead view estimated radii were greater, associated with elongated (elliptical) flows along the pent-roof. Unlike previous cases, the flame speeds indicated by the gradient of the radius/crank angle diagrams did not become similar for slow, fast and middle cycles but remained slower the slower the set of cycles considered. However, one of the middle cycles, Cycle (b) (see also Appendix B4 – Figures B4-1 and B4-2) showed higher pressure and faster flame radius (derived from both side and overhead views) development well before TDC (and continuing albeit occurring after TDC). Nevertheless, the peak pressure proved similar to those other middle cycles. Moreover, this particular cycle exhibited more rapid flame radius increase (derived from the side view) than the “fast” cycles (and of similar flame speed) derived from the overhead view, to those “fast” lean cycles. The reasons for the anomalous behaviour of this particular cycle are not understood.

As in all previous cases, for these lean cycles, flame centroids migrated down about 7 mm towards the piston crown over the combustion event. Most, and all fast, lean cycle flame kernels convected in a clockwise direction (Figure 7.48(a)).

(iii) Summary of Variation with Equivalence Ratio

As noted previously, results for stoichiometric and rich ($\phi=1.1$) operation were practically identical; lean ($\phi=0.8$) burning resulted in slower burning, lower pressure and greater cyclic variation, Table 7.4.

Equivalence ratio	P_{\max} (bar)	$\theta_{P_{\max}}$ ($^{\circ}$ CA) aTDC	$\sigma_{P_{\max}}$ (bar)	$COV_{P_{\max}}$ (%)	θ_{ig} ($^{\circ}$ CA) bTDC
$\phi = 0.8$	46.6	18.4	5.6	12.1	12
$\phi = 1.0$	55.6	17.3	3.1	5.6	7
$\phi = 1.1$	56.3	16.9	3.1	5.5	6

Table 7.4 Peak in-cylinder pressure data, including standard deviation ($\sigma_{P_{\max}}$) and coefficient of variation ($COV_{P_{\max}}$), for lean, stoichiometric and rich conditions.

Collected together in Figures 7.49 and 7.50 are pressure – crank angle and flame radius development diagrams for the middle cycles at all three equivalence ratios. For the lean cycles, it proved necessary to advance ignition to compensate the slow initial burn rate. However, having done this the mean flame radius at TDC was generally similar to that for the richer mixtures and the subsequent flame speed (gradient of the flame radius versus crank angle (time)) was much the same for all equivalence ratios (Figures 7.49(b) and (c) and 7.50). This suggests that the lower pressure developed for the lean mixture might be more associated with slower burn-up of mixture behind the flame and lower energy input of the weak mixture rather than slower flame propagation; i.e. above a certain critical laminar burning velocity (or chemical to eddy lifetime) entrainment rate and flame speed are largely a function of u' . The anomalous behaviour of one lean cycle has been discussed previously. Aleiferis et al. (2004) also encountered some lean mixture cycles burning at the same (higher) rate as stoichiometric ones (on the basis of having similar successive flame front positions). They suggested that these fast lean cycles might have experienced a richer than the average mixture strength in the vicinity of the spark plug at ignition. However, in the current work, such differences in mixture strength were eliminated by running the engine in skip firing mode (Chapter 3).

7.4.4 Effect of Engine Speed

The experiments reported in Section 7.4.1 (for the ‘reference’ 1500 rpm case) were repeated at 750 and 1000 rpm, at the same equivalence ratio ($\phi=1$); ignition timing was

adjusted to yield mean maximum indicated mean effective pressure at each speed (2° bTDC and 4° bTDC, respectively), as detailed in Section 6.5. It proved impossible to conduct planned tests at 1900 rpm, due to the run-on problems reported earlier (in Section 7.4).

Set out in Figure 7.51 is a P_{\max} versus $\theta_{P_{\max}}$ diagram for filmed cycles at the lower engine speed, 750 rpm. As before, representative ‘middle’, ‘fast’ and slow cycles were selected and have been highlighted in the diagrams.

Lower engine speed (750 rpm)

Shown in Figure 7.52 are the plotted successive flame positions for the four selected ‘middle’ cycles at 750 rpm. For cycles (a), (b) and (d), flame kernels are convected to the left (see also Figure 7.53(a)) at an average velocity in that direction of 2.2 m/s. This corresponds well with the flow pattern and ensemble averaged mean velocity observed in 78% of cycles at this engine speed, Figures 7.16 and 7.21(a). It can be seen that as these flames grow, they become significantly distorted from a circular shape at the right of the chamber (as viewed). In contrast, the flame in Cycle (c) can be seen to remain central and to grow quite symmetrically (circular), with the centroid first moving vertically down towards the piston before drifting left. This is consistent with the flow pattern seen in 15% of cycles at this engine speed, Figure 7.14. In all cases, the flame radii derived from the overhead views at any given crank angle appear greater than those evaluated from the side view for these middle cycles, Figures 7.53(b) and (c). This is possibly associated with the less circular nature of side viewed flames at this engine speed.

The same patterns of flame development pertained for the sets of fast and slow cycles and hence, for brevity, the corresponding diagrams are not shown here (they are available in Appendix B5 and technical report, Murad (2006)). Summary data for the fast and slow cycles are available in Figures 7.53(a), (b) and (c). Fast cycles appear associated with initial flame kernel migration to the right (as viewed in the diagrams), as in the flow pattern of Figure 7.15, and the slow cycles (apart from one showing strong

initial movement to the left) tended to be associated with no lateral motion (i.e. kernels centroids migrating slowly towards the piston).

The flame radii derived from side and overhead views seem more consistent for the fast and slow cycles than for the middle cycles. Initial flame kernel growth rate can be seen to be similar for fast, middle and slow cycles, later deviating with fast cycles continuously burning faster than middle and (in turn) slow cycles, Figures 7.53(b) and (c).

Intermediate Engine Speed (1000 rpm)

Shown in Figures 7.54(a) and (b) are the usual peak pressure versus crank angle of its occurrence and selected representative fast, middle and slow cycles. The overhead and side view successive flame contours are again omitted for brevity; as in the other test cases the same range of patterns occurred and individual flame growth patterns within a set of fast, middle and slow cycles seemed to have little effect on flame speed or pressure development (the full data are available in Appendix B6 and a technical report, Murad (2006)). Summary data for the fast, middle and slow cycles are presented in Figures 7.55(a), (b) and (c). The patterns of behaviour can be seen to be similar to those observed at 750 rpm; unfortunately, no PTV flow pattern data were available at 1000 rpm. However, in the horizontal direction, the average velocity of flame kernel migration for the four selected middle cycles was of the order 2.8mm/ms (2.8 m/s) – similar to the velocity noted for the same engine speed in the LDV measurements at the chamber centre (~2 m/s – a little lower due to the ensemble averaging nature associated with the LDV technique), Figure 7.22(a). At this engine speed, for the selected cycles, all fast cycles convected downwards, whilst all middle and slow cycles convected in an anti-clockwise direction (Figure 7.55(a)).

7.4.5 Comparison of Middle Cycles at Various Engine Speeds

Shown in Figure 7.56 are pressure versus crank angle as well as side and overhead view derived mean flame radius versus crank angle diagrams for the middle cycles at the three adopted engine speeds. Lower pressure values obtained at the lower engine speed

(750 rpm), even before ignition, this is probably related to increased blow-by for the ported engine as engine speed decreased.

As a function of time from ignition, flame speeds (gradient, dR/dt) can be seen to be lower at lower engine speeds, Figure 7.57. As a result greater ignition advance was required for optimum imep with higher engine speed. Nevertheless, the gradient of flame radius versus crank angle for developed flames proved very similar, Figures 7.56(b) and (c). That is to say, there is an increase in flame speed proportional to increase in engine speed (Figure 7.58) – this is consistent with flame speed increasing in proportion to turbulent burning velocity (with the latter increasing with u' and mean piston speed).

Closure

The key results of the experimental study are summarised and discussed in the following Conclusions chapter of this thesis.

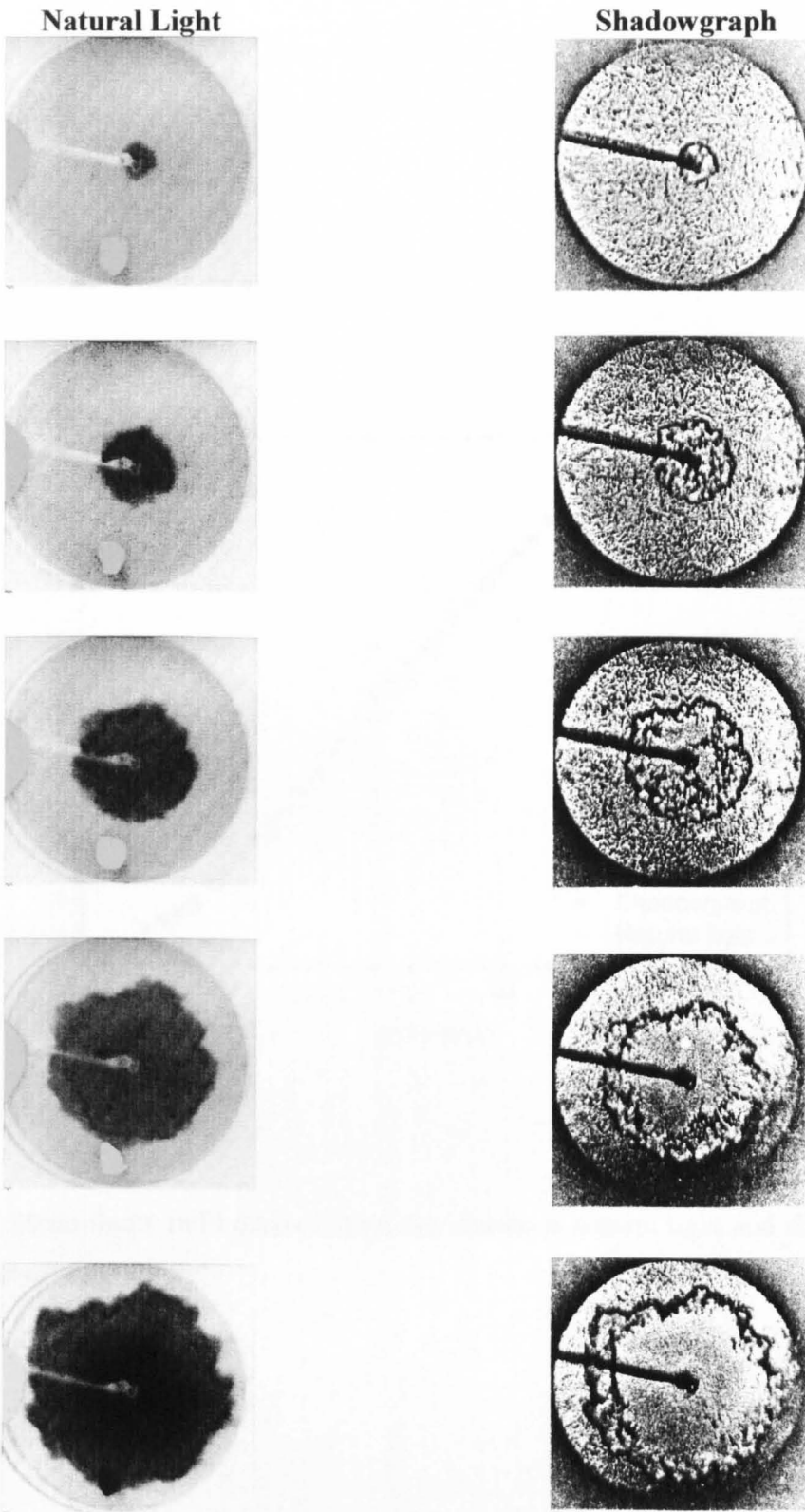


Figure 7.1 Natural light and shadowgraph images at same instant, 0.8 ms between images.

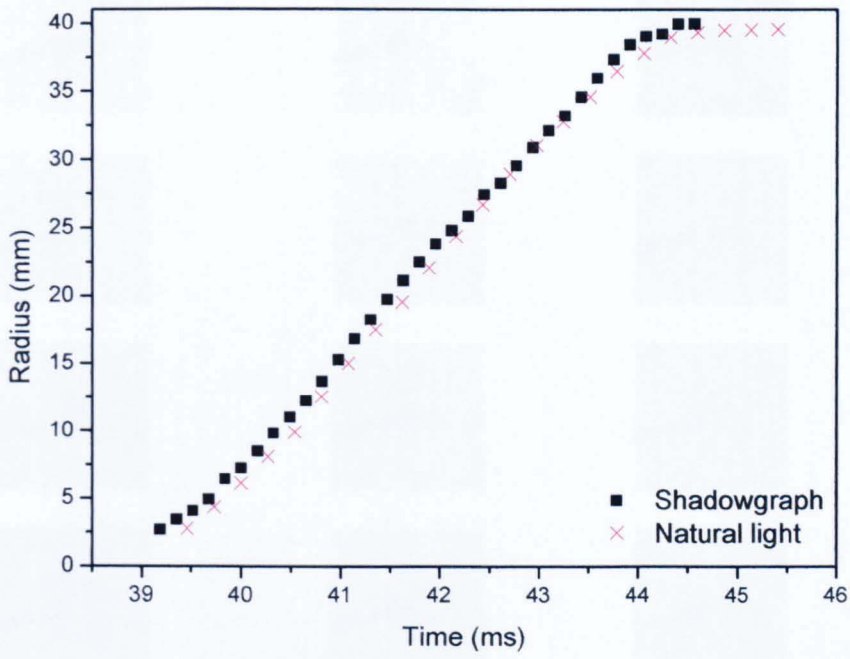


Figure 7.2 Mean flame radii derived from simultaneous natural light and shadowgraph imaging techniques.

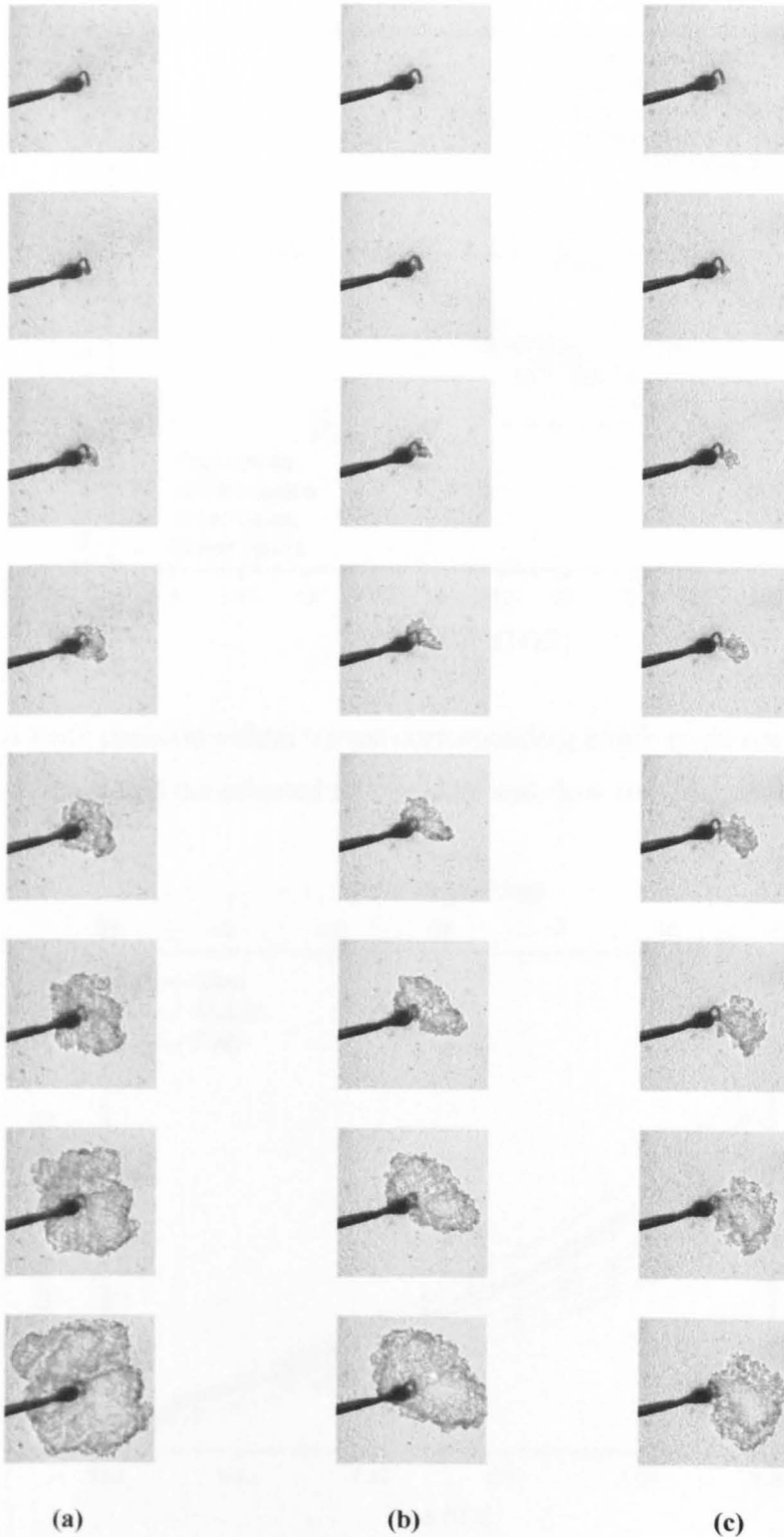


Figure 7.3 Shadowgraph images of flame development over central 40 mm of cylinder (bore of 80 mm), 2.4° CA between images. Flames (a) and (b) stoichiometric, 1500 rpm, ignition timing 20° bTDC; (c) $\phi = 0.8$, 1500 rpm, ignition timing 31° bTDC.

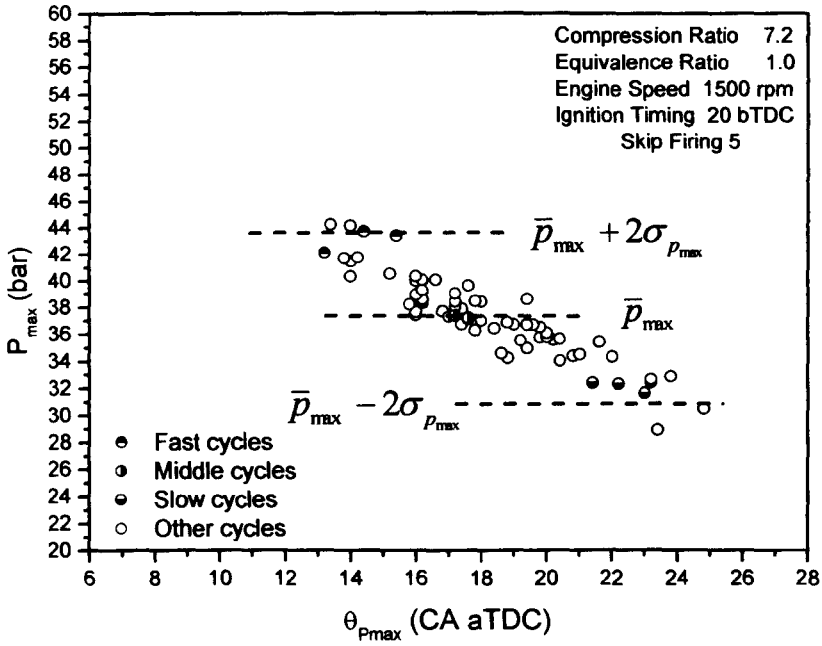


Figure 7.4 Peak pressure values versus corresponding crank angle occurrence with ensemble average and the selected fast, middle and slow filmed cycles.

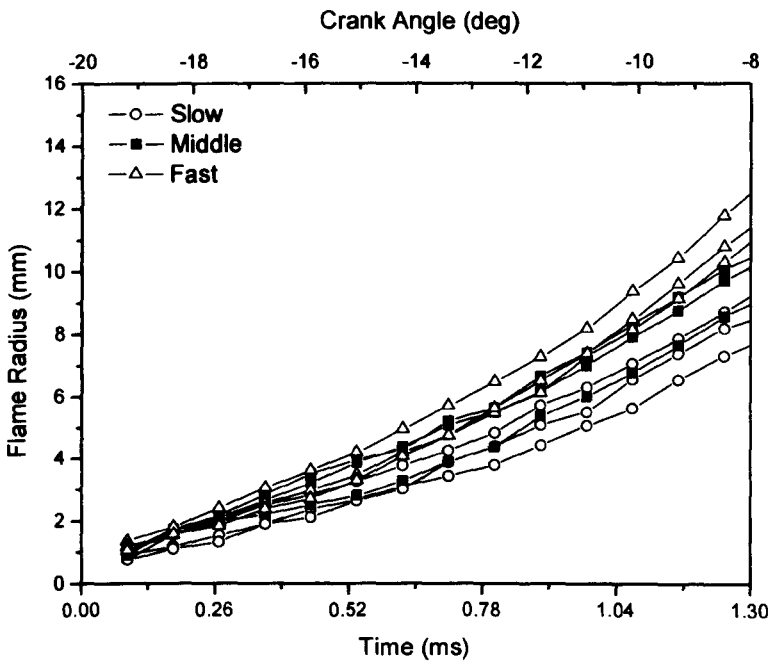


Figure 7.5 Selected fast, middle and slow mean flame radii for stoichiometric, 1500 rpm cycles, ignition timing 20° bTDC.

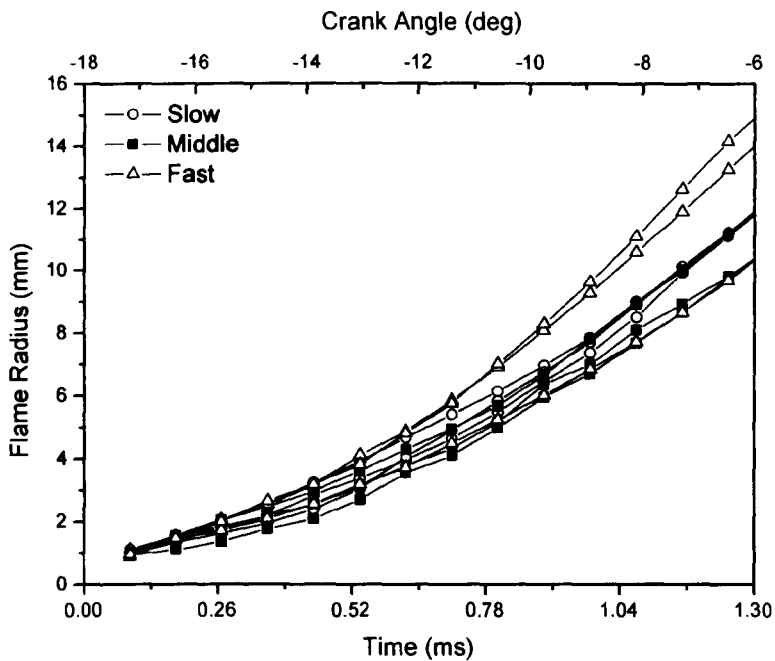


Figure 7.6 Selected fast, middle and slow mean flame radii for rich ($\phi = 1.1$), 1500 rpm cycles, ignition timing 18° bTDC.

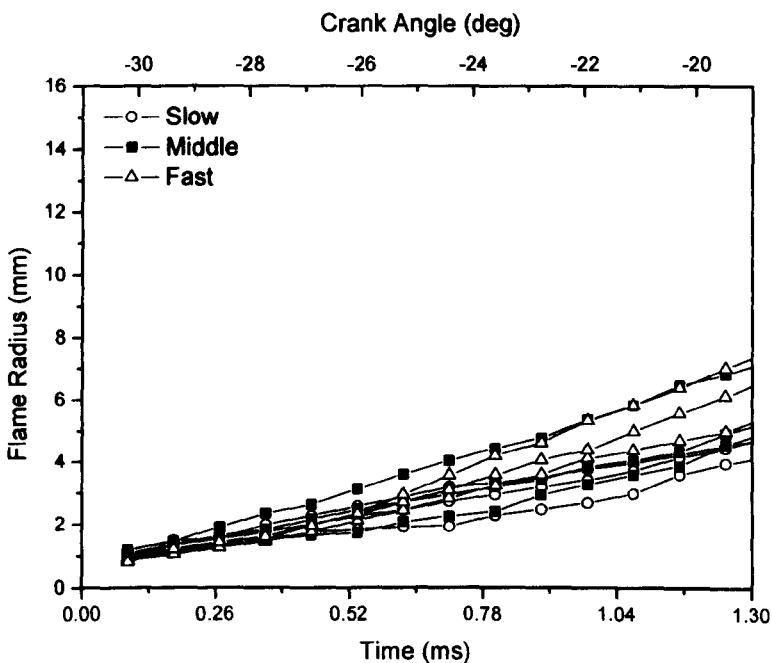
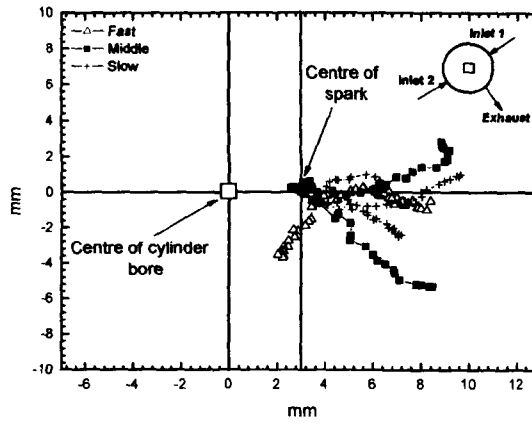
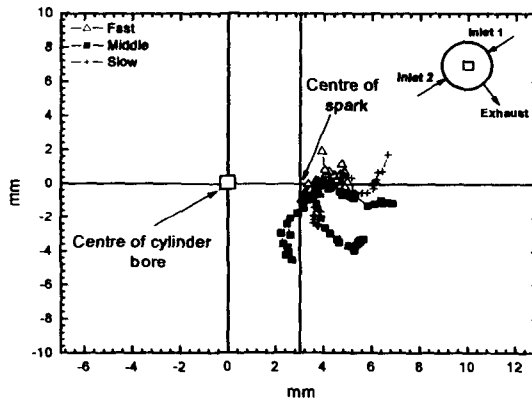


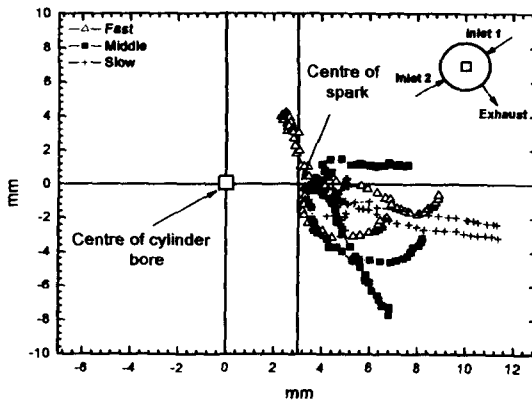
Figure 7.7 Selected fast, middle and slow mean flame radii for lean ($\phi = 0.8$), 1500 rpm cycles, ignition timing 31° bTDC.



(a)

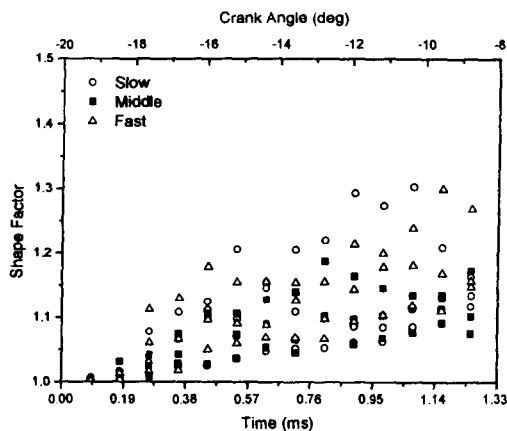


(b)

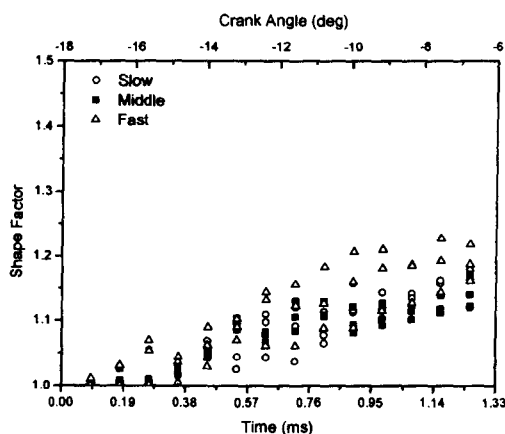


(c)

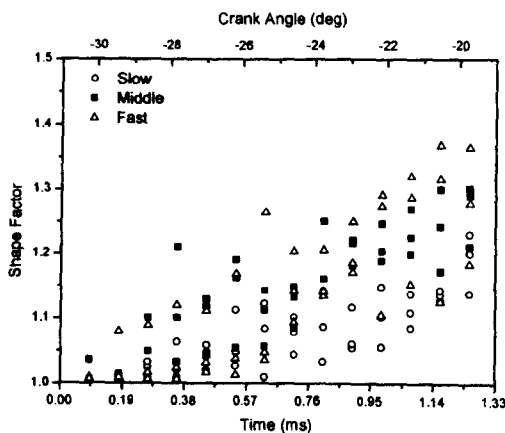
Figure 7.8 Centroid movement of middle, fast and slow cycles at 1500 rpm for (a) stoichiometric {ignition timing 20° bTDC} (b) rich ($\phi = 1.1$) {ignition timing 18° bTDC} and (c) lean ($\phi = 0.8$) {ignition timing 31° bTDC} mixtures.



(a)

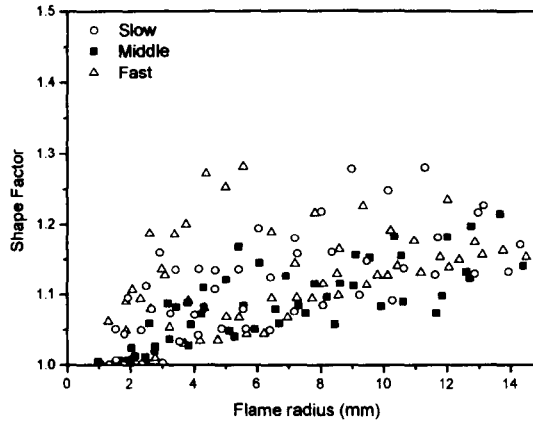


(b)

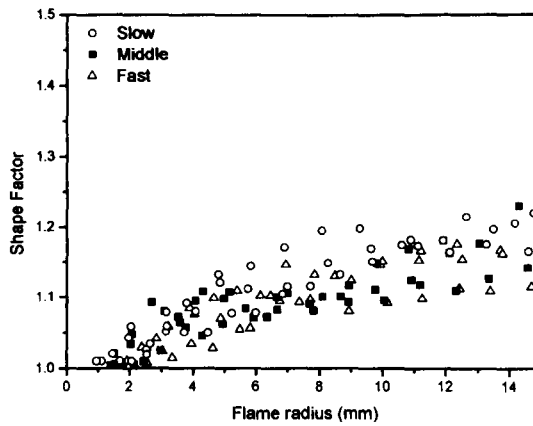


(c)

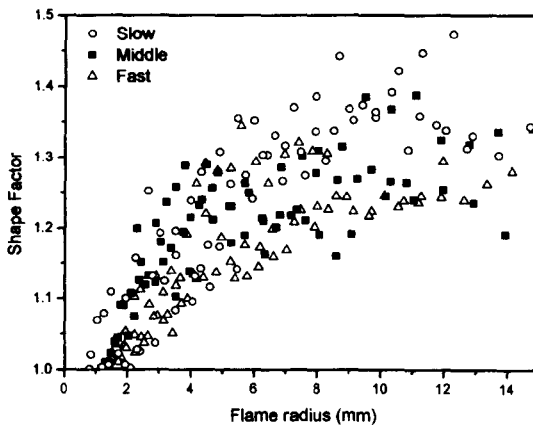
Figure 7.9 Shape Factor versus time and crank angle of middle, fast and slow cycles at 1500 rpm (over duration of 12° CA (1.33 ms) following ignition), for (a) stoichiometric {ignition timing 20° bTDC} (b) rich ($\phi = 1.1$) {ignition timing 18° bTDC} and (c) lean ($\phi = 0.8$) {ignition timing 31° bTDC} mixtures.



(a)

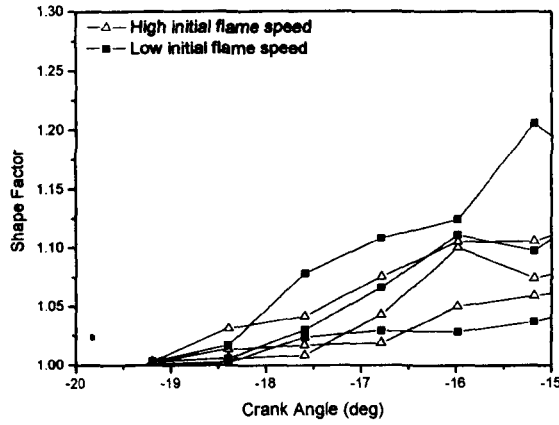


(b)

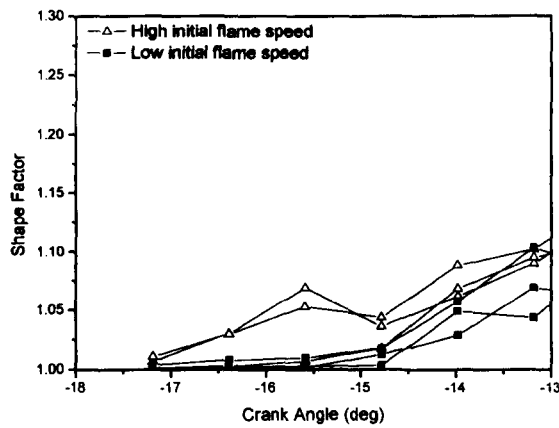


(c)

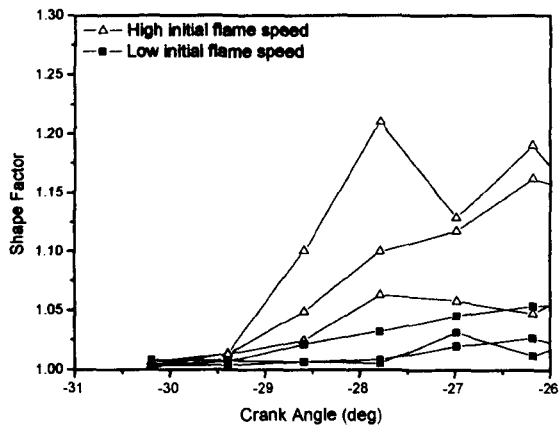
Figure 7.10 Shape Factor versus mean flame radius of middle, fast and slow cycles at 1500 rpm, for (a) stoichiometric {ignition timing 20° bTDC} (b) rich ($\phi = 1.1$) {ignition timing 18° bTDC} and (c) lean ($\phi = 0.8$) {ignition timing 31° bTDC} mixtures.



(a)

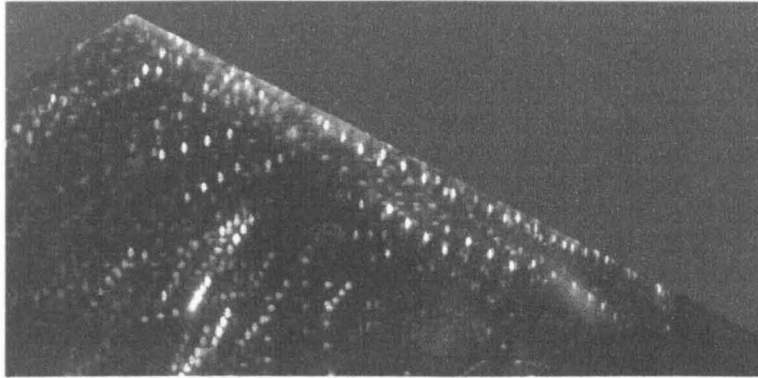


(b)

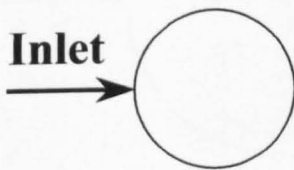
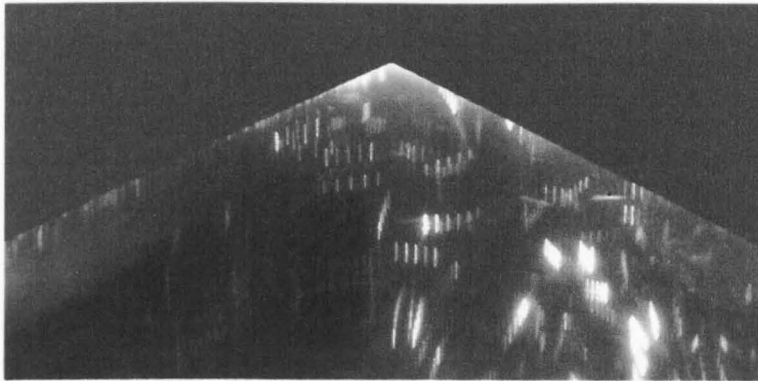


(c)

Figure 7.11 Shape Factor for three high and three low flame speed cycles during the first 5° CA, at 1500 rpm, (a) stoichiometric {ignition timing 20° bTDC} (b) rich ($\phi = 1.1$) {ignition timing 18° bTDC} and (c) lean ($\phi = 0.8$) {ignition timing 31° bTDC} mixtures.

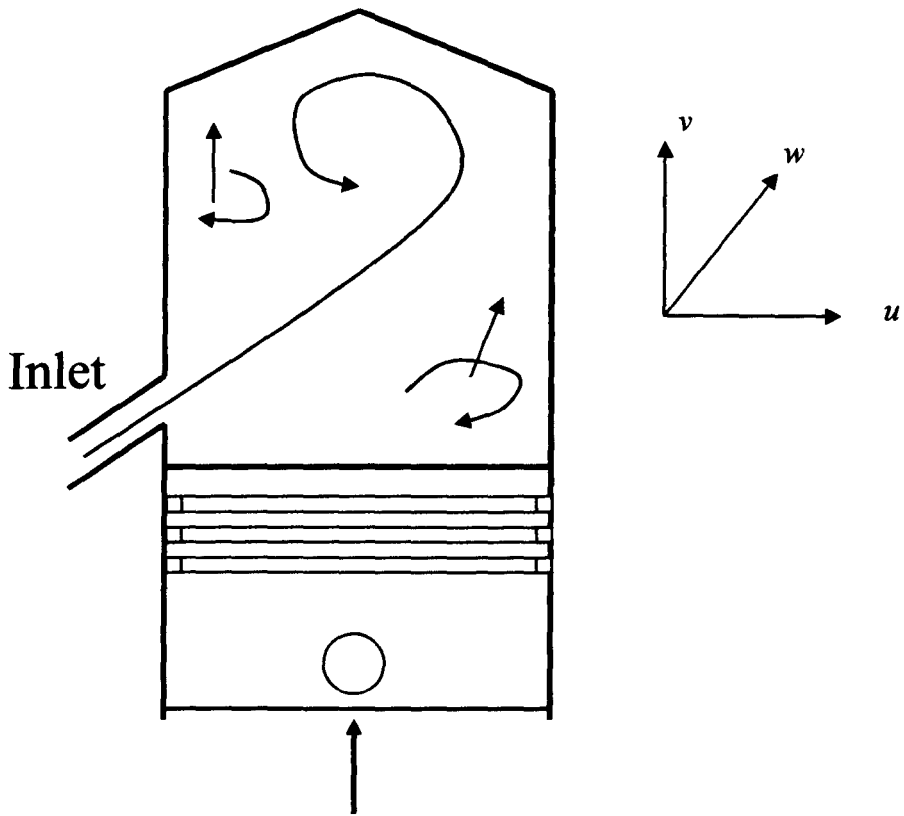


(a)

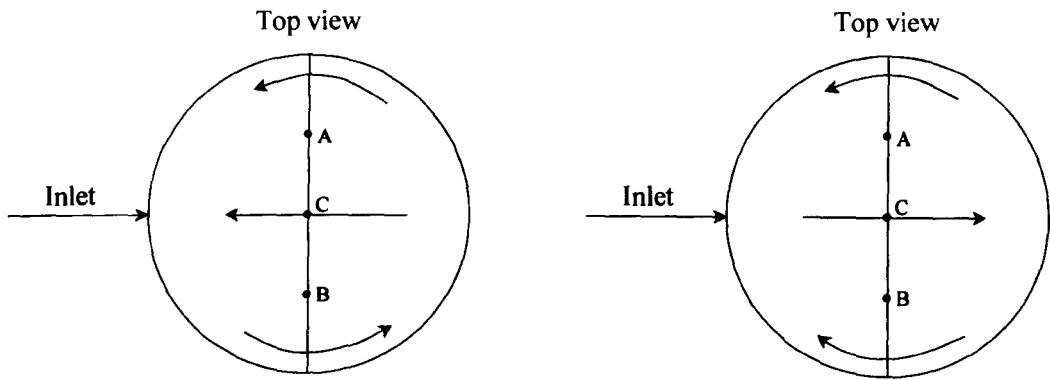


(b)

Figure 7.12 PTV flow investigation using side window of Perspex engine with inlet to left side of chamber, (a) focus on right side of clearance at 1500 rpm, (b) view of complete clearance volume at 750 rpm.



(a)



(i)

(ii)

(b)

Figure 7.13 (a) Anticipated tumble flow generated with pent-roof geometry in conjunction with inclined inlet duct, (b) observed flow in central plane illuminated by laser (and suggested by comparison LDV data) in (i) 78% of cycles at 750 rpm and (ii) 75% of cycles at 1500 rpm.

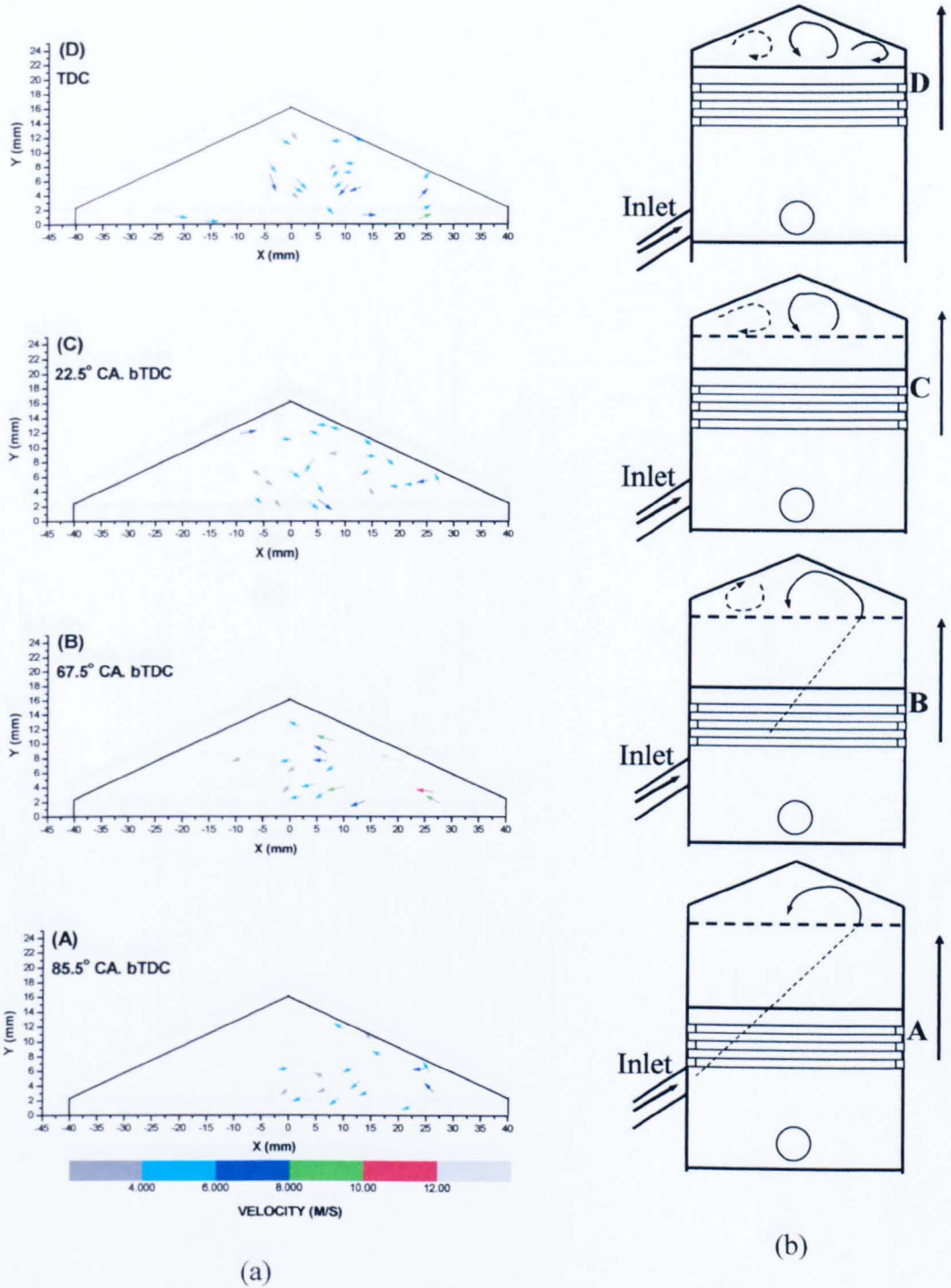
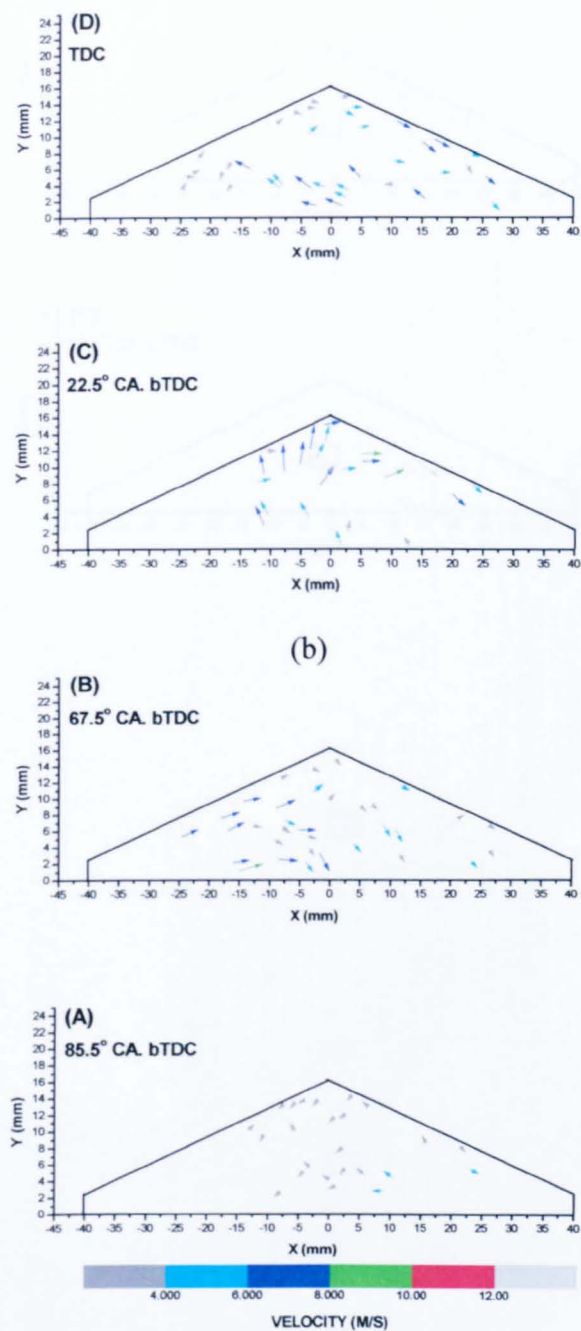
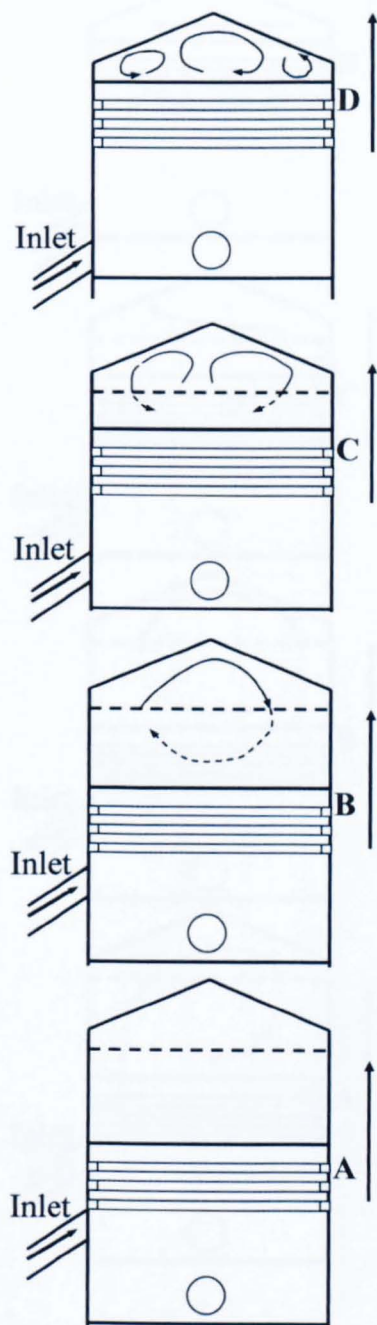


Figure 7.14 Flow pattern exhibited in 15% of cycles at 750 rpm, (a) sequence during compression at different piston positions (y-axis datum – piston crown position at TDC (0 mm)), (b) illustration of observed bulk flow within field of view with imagined (dashed) flow from inlet, as piston moves up.



(a)



(b)

Figure 7.15 Flow pattern exhibited in 7% of cycles at 750 rpm, (a) sequence during compression at different piston positions (y-axis datum – piston crown position at TDC (0 mm)), (b) illustration of observed bulk flow within field of view, as piston moves up.

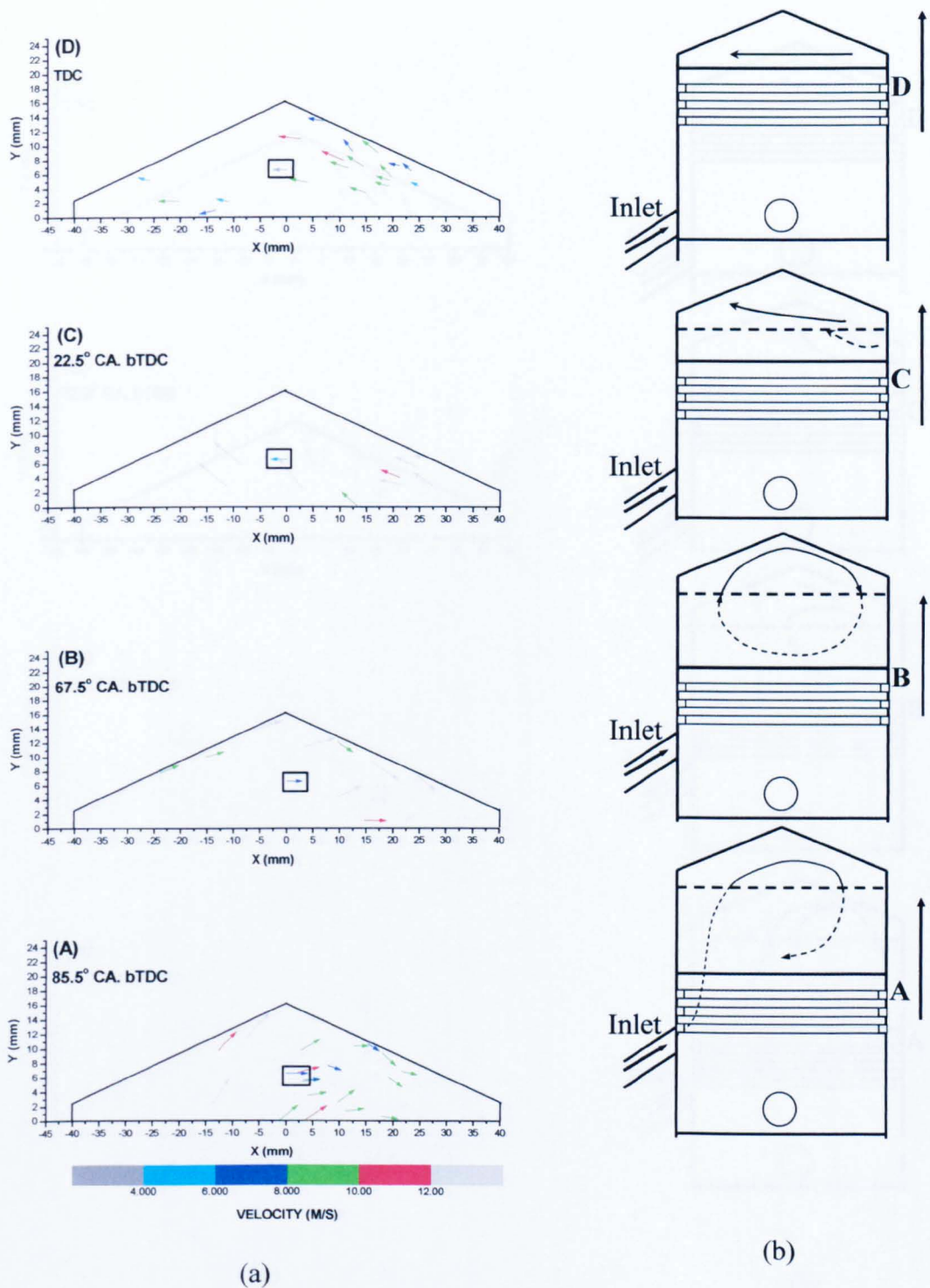
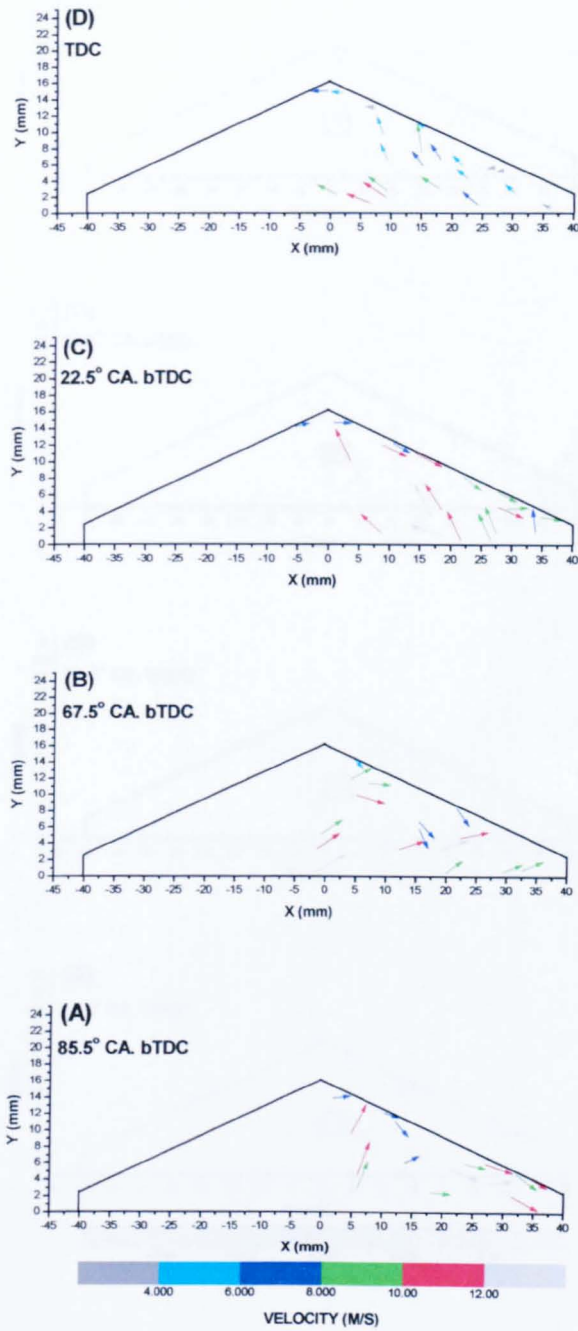
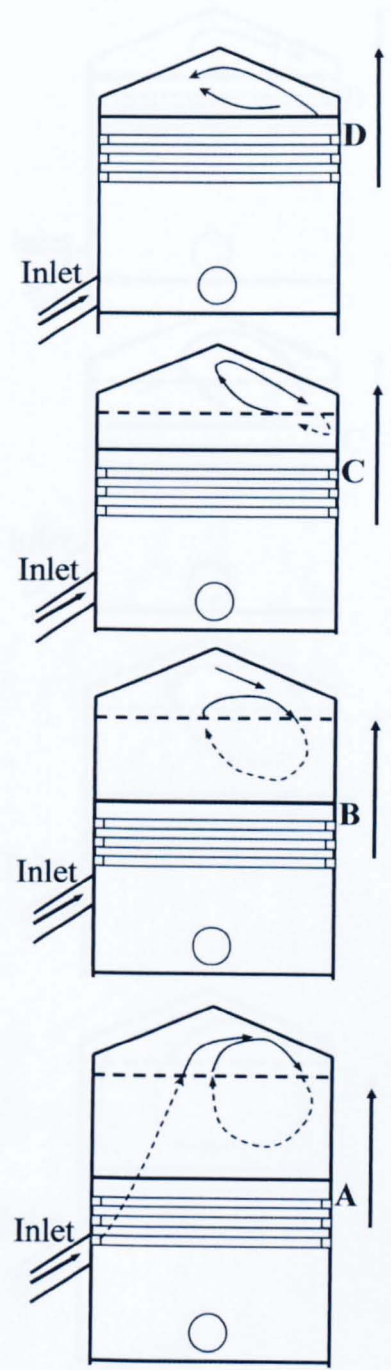


Figure 7.16 Flow pattern exhibited in 78% of cycles at 750 rpm, (a) sequence during compression at different piston positions with LDV ensemble averaged values of \bar{u}_c component of velocity (in centre) shown with a box surrounding vectors (y-axis datum – piston crown position at TDC (0 mm)), (b) illustration of observed bulk flow within field of view including imagined (dashed) flow from inlet, as piston moves up.



(a)



(b)

Figure 7.17 Flow pattern exhibited in 25% of cycles at 1500 rpm, (a) sequence during compression at different piston positions (y-axis datum – piston crown position at TDC (0 mm)), (b) illustration of observed bulk flow within field of view including imagined (dashed) flow from inlet, as piston moves up.

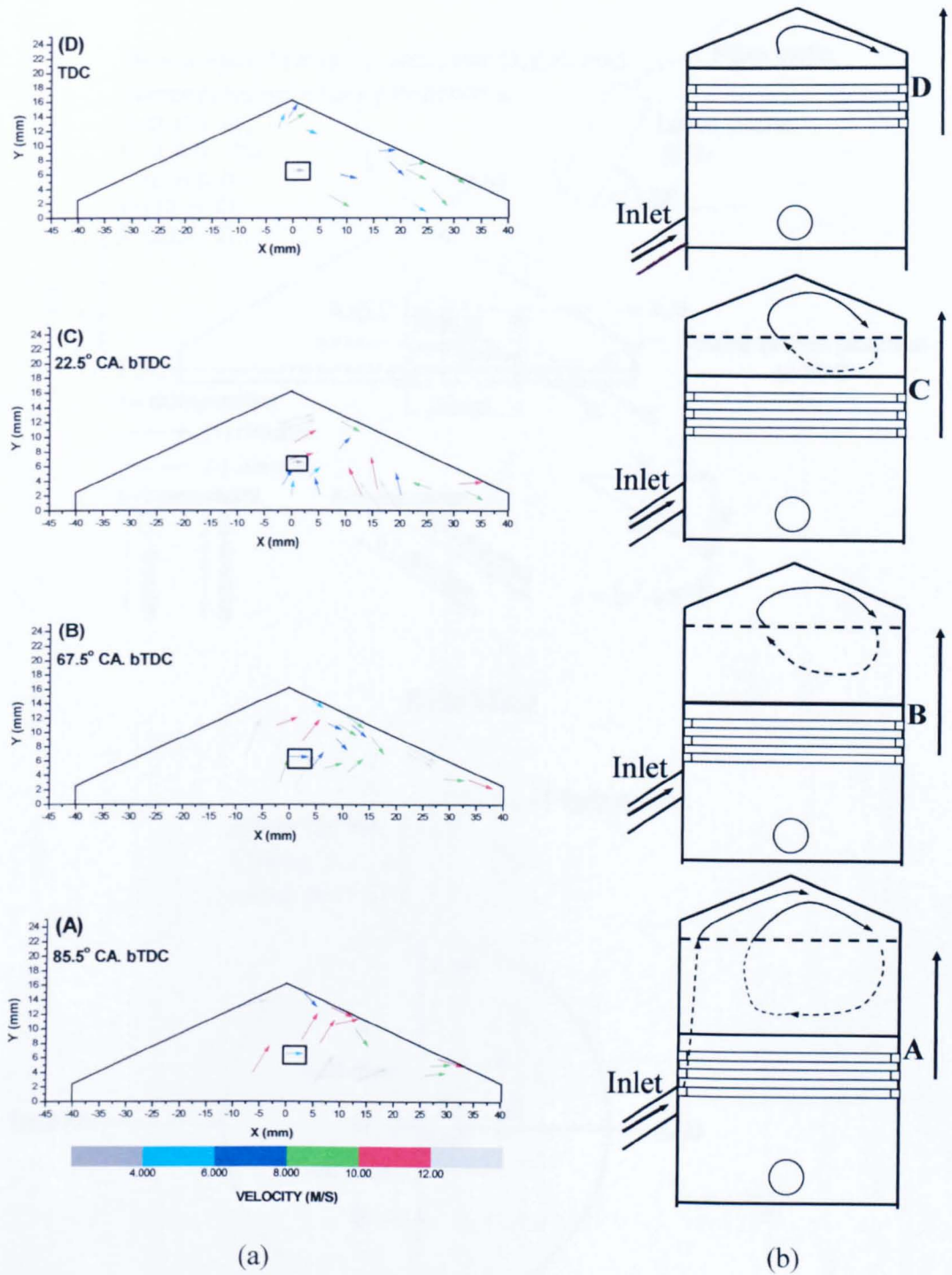
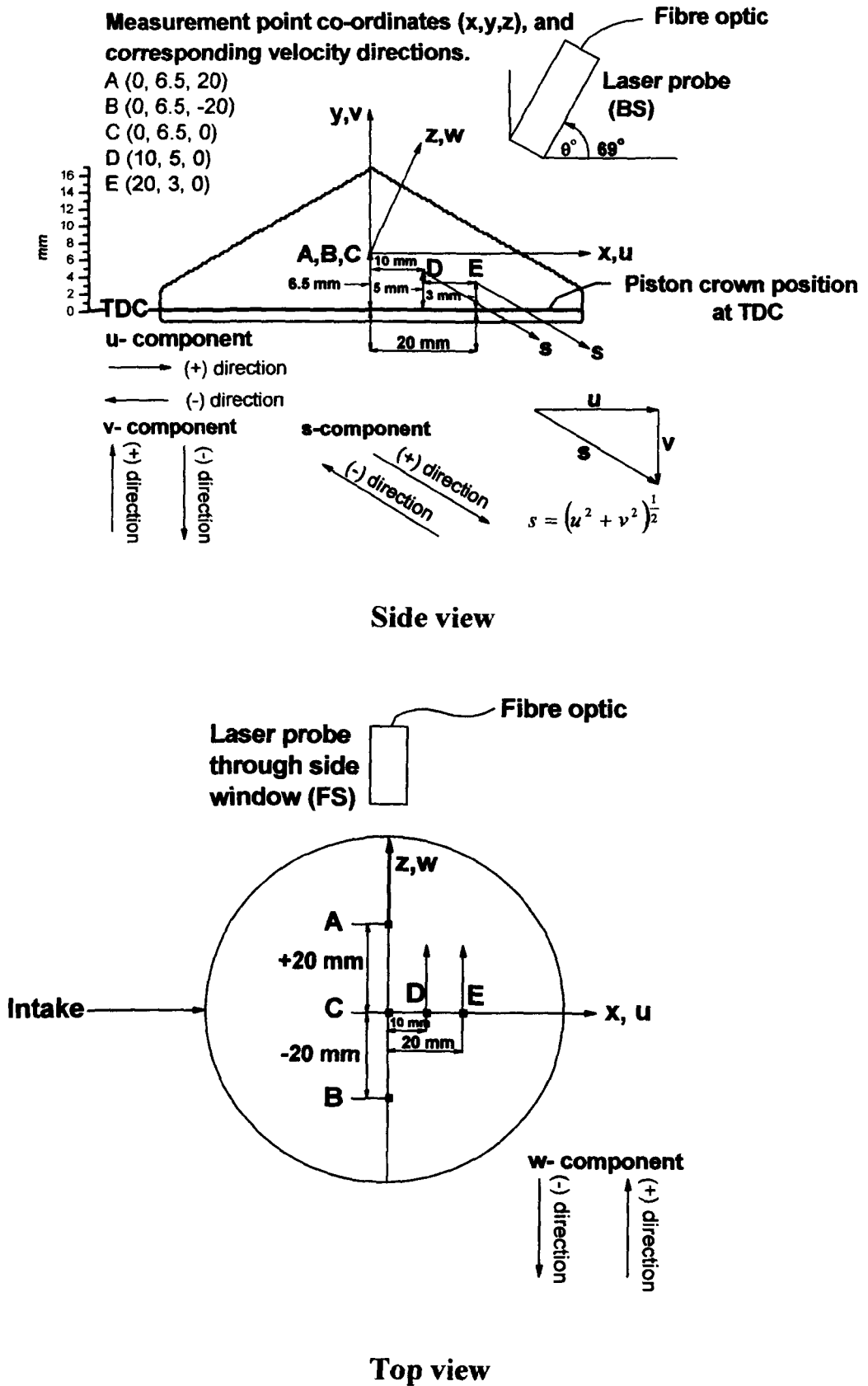


Figure 7.18 Flow pattern exhibited in majority of the cycles (75%) at 1500 rpm, (a) sequence during compression at different piston positions with LDV ensemble averaged values of the \bar{u}_c component of velocity (in centre) shown with box surrounding vectors (y-axis datum – piston crown position at TDC (0 mm)), (b) illustration of observed bulk flow within field of view including imagined (dashed) flow from inlet, as piston moves up.



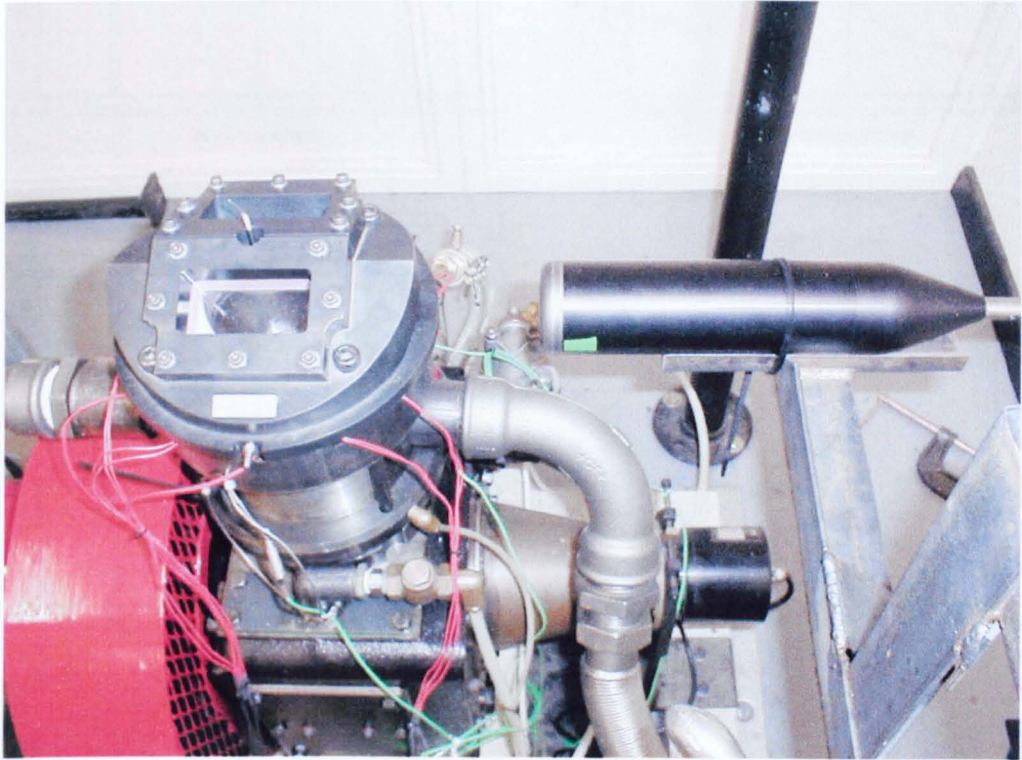


Figure 7.20 LDV fibre optic probe held via the side window (forward scatter configuration).

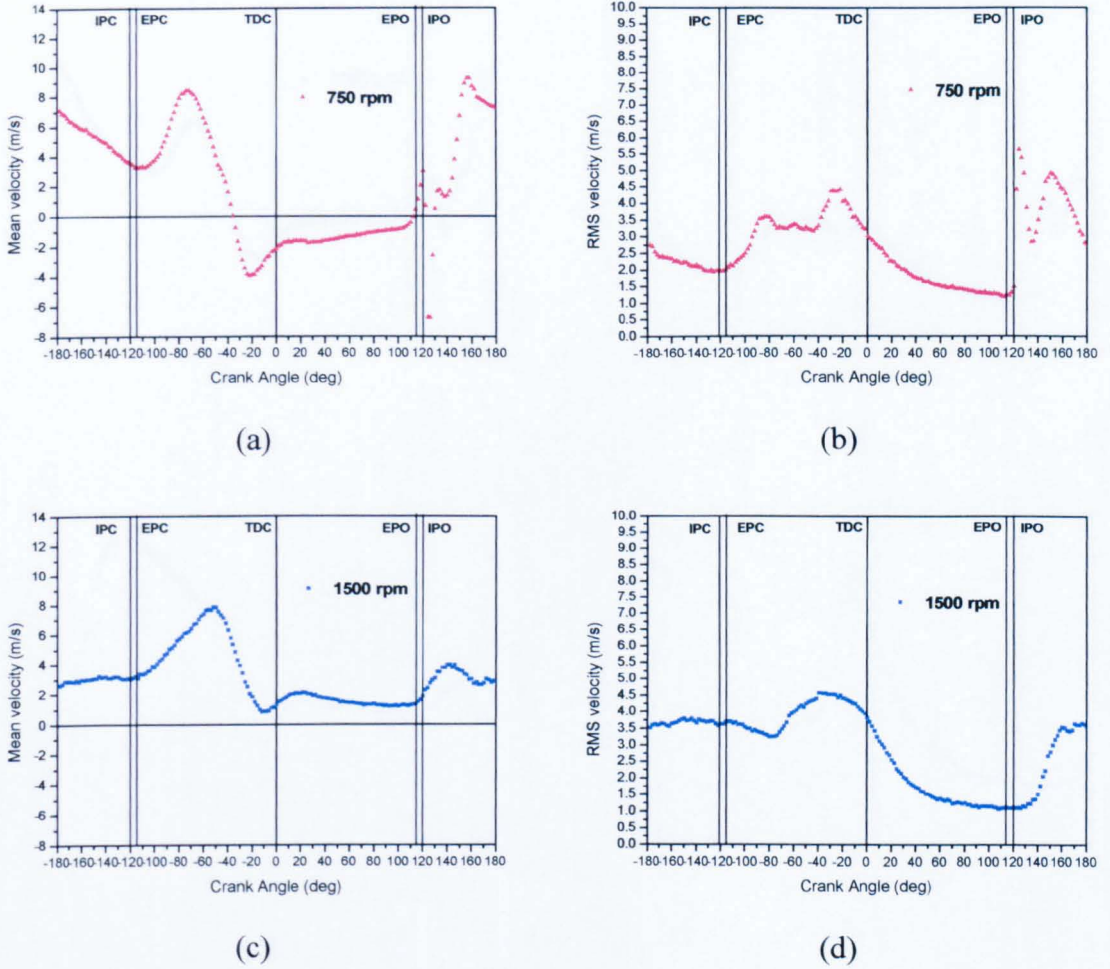


Figure 7.21 LDV-derived \bar{u}_C and u'_C variations with crank angle at Point C, (a) \bar{u}_C variation at 750 rpm, (b) u'_C variation at 750 rpm, (c) \bar{u}_C variation at 1500 rpm, (d) u'_C variation at 1500 rpm.

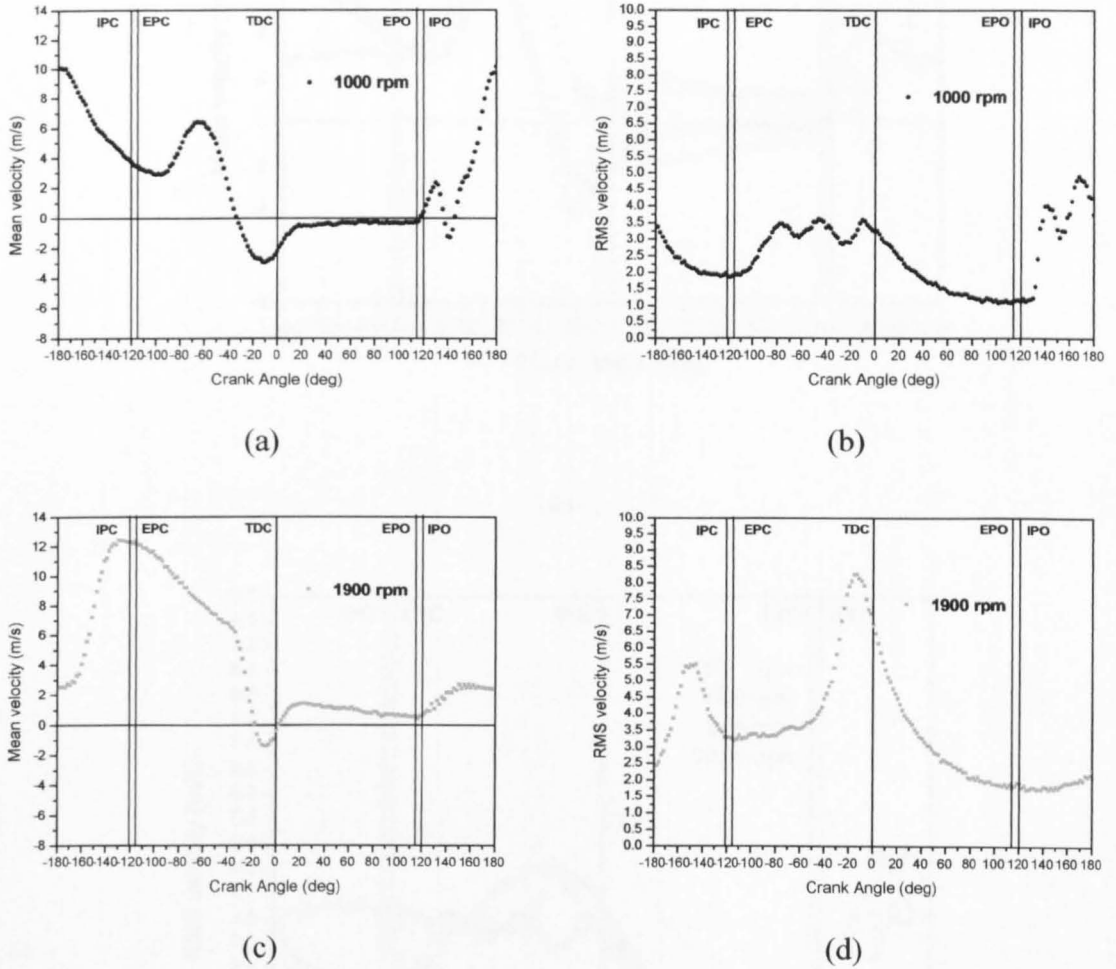
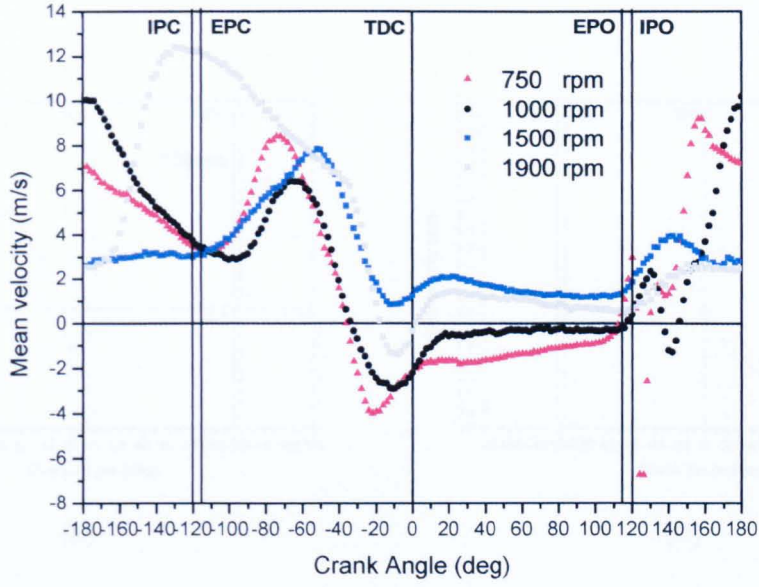
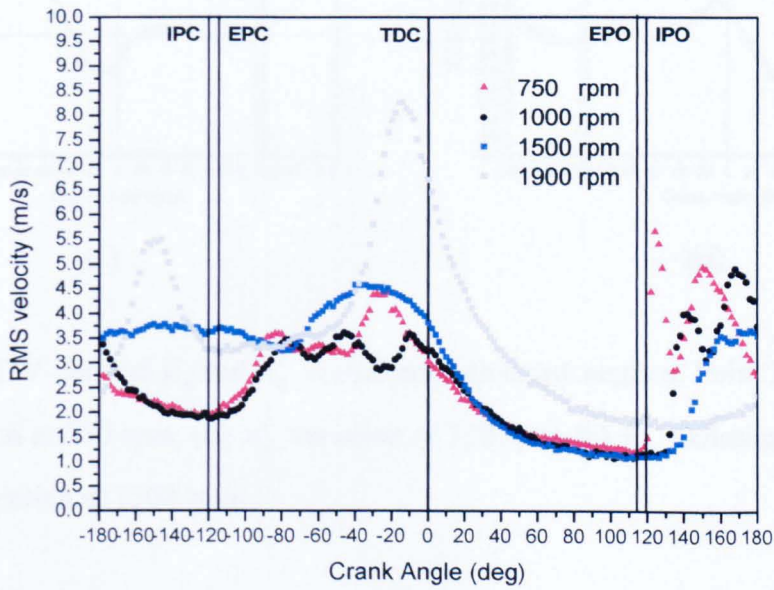


Figure 7.22 LDV-derived \bar{u}_C and u'_C variations with crank angle at Point C, (a) \bar{u}_C variation at 1000 rpm, (b) u'_C variation at 1000 rpm, (c) \bar{u}_C variation at 1900 rpm and (d) u'_C variation at 1900 rpm.



(a)



(b)

Figure 7.23 LDV-derived \bar{u}_c and u'_c variations with crank angle (at Point C) at all engine speeds tested (a) \bar{u}_c (b) u'_c .

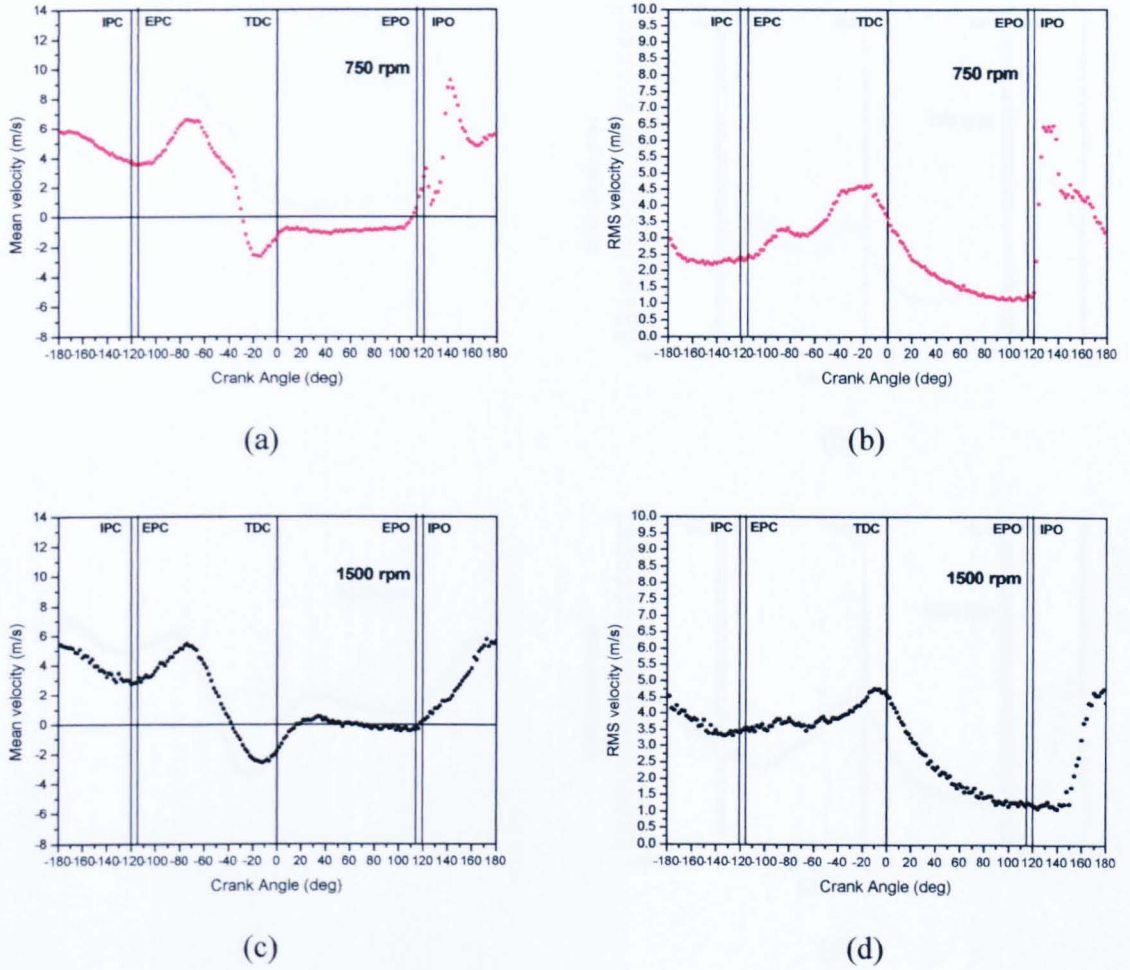
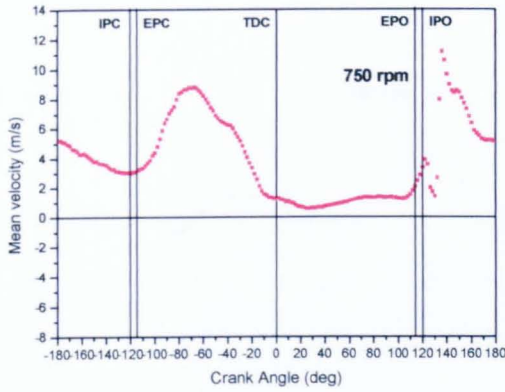
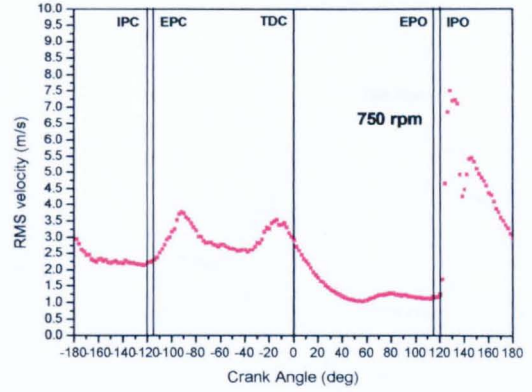


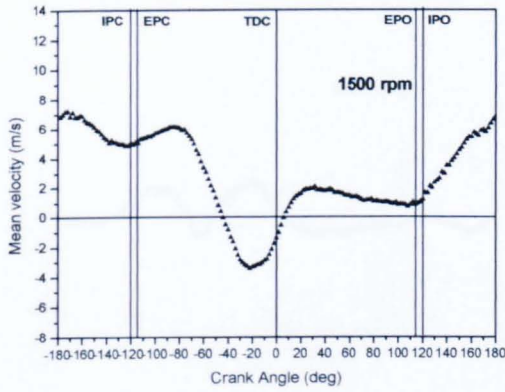
Figure 7.24 LDV-derived \bar{u}_A and u'_A variations with crank angle at Point A (0, 6.5, 20), (a) \bar{u}_A variation at 750 rpm, (b) u'_A variation at 750 rpm, (c) \bar{u}_A variation at 1500 rpm and (d) u'_A variation at 1500 rpm.



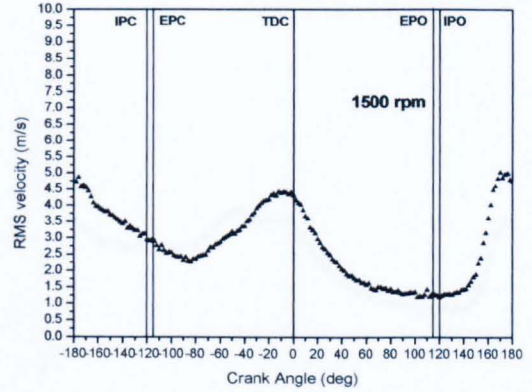
(a)



(b)

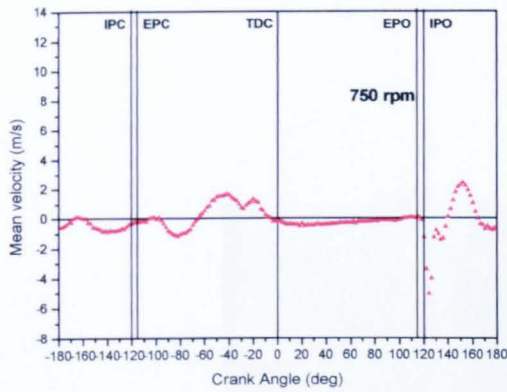


(c)

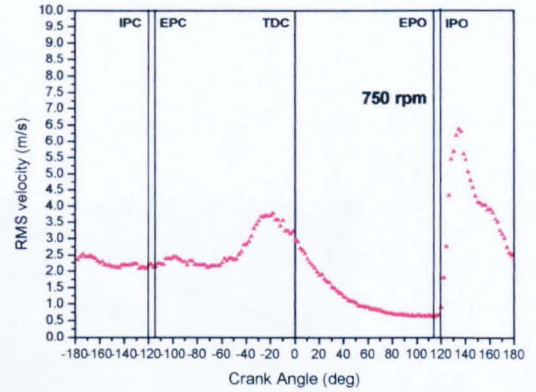


(d)

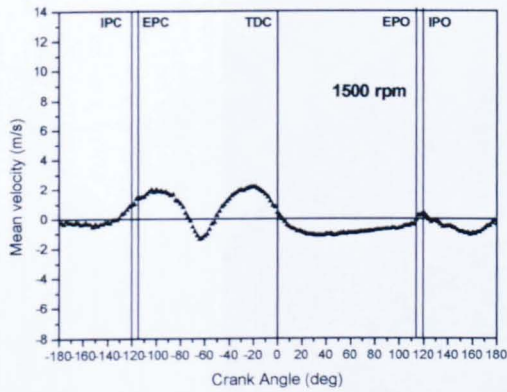
Figure 7.25 LDV-derived \bar{u}_B and u'_B variations with crank angle at Point B (0, 6.5,-20), (a) \bar{u}_B variation at 750 rpm, (b) u'_B variation at 750 rpm, (c) \bar{u}_B variation at 1500 rpm and (d) u'_B variation at 1500 rpm.



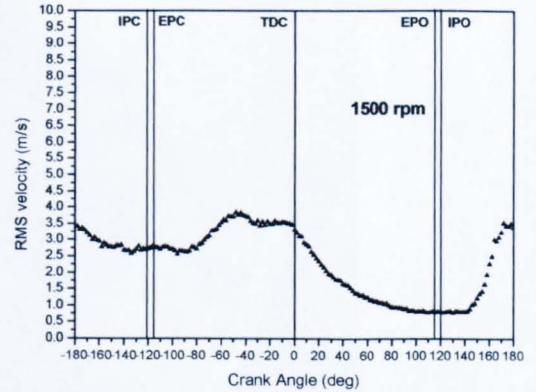
(a)



(b)



(c)

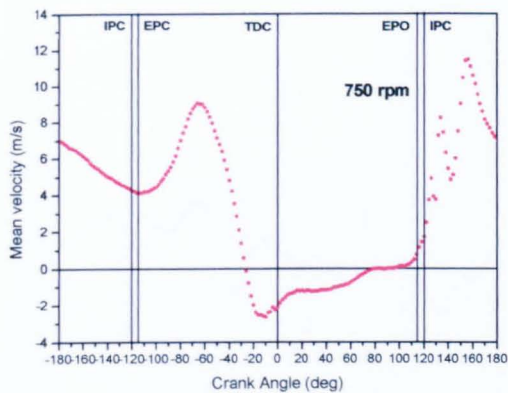


(d)

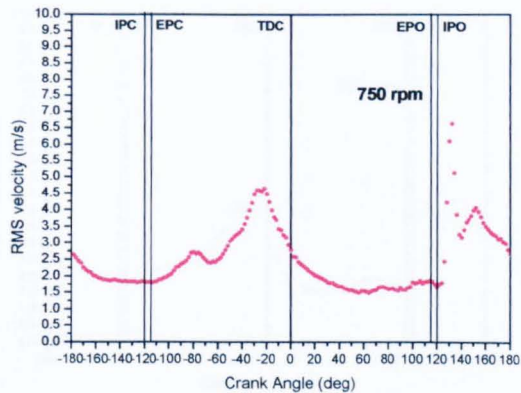
Figure 7.26 LDV-derived \bar{v}_A and v'_A (v_A component of velocity) variations with crank angle at Point A (0, 6.5, 20), (a) \bar{v}_A variation at 750 rpm, (b) v'_A variation at 750 rpm, (c) \bar{v}_A variation at 1500 rpm and (d) v'_A variation at 1500 rpm.



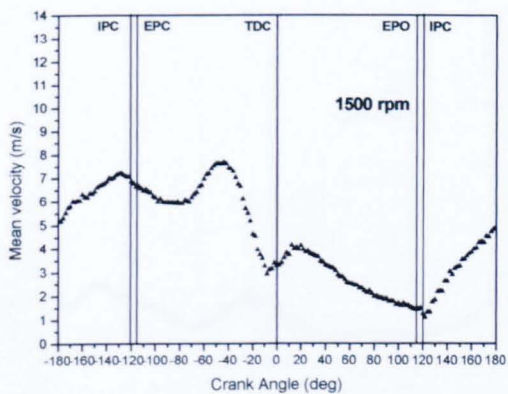
Figure 7.27 LDV fibre optic probe held at right angles to one of top windows (back scatter configuration).



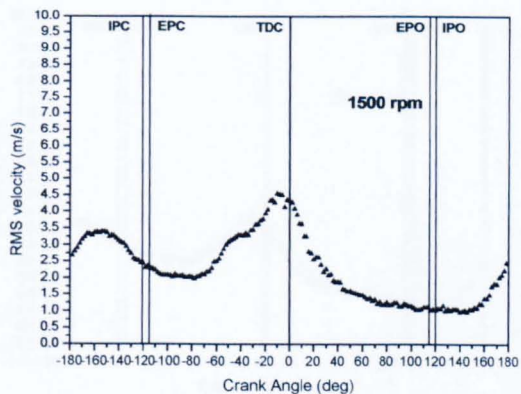
(a)



(b)

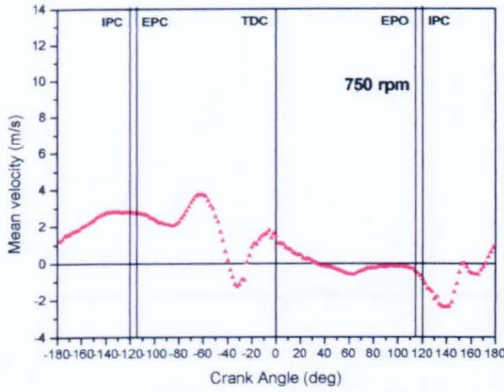


(c)

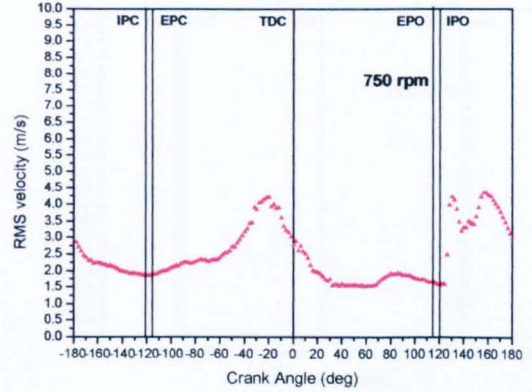


(d)

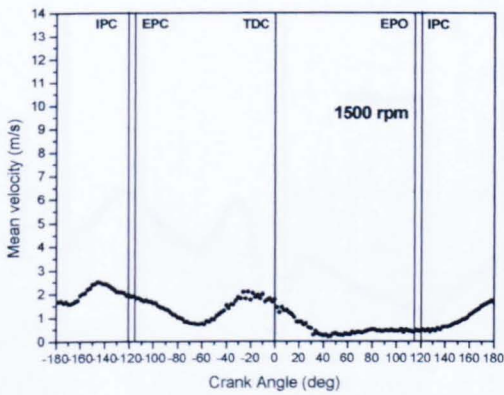
Figure 7.28 LDV-derived \bar{s}_D and s'_D (s_D component of velocity) variations with crank angle at Point D (10, 5, 0), (a) \bar{s}_D variation at 750 rpm, (b) s'_D variation at 750 rpm, (c) \bar{s}_D variation at 1500 rpm and (d) s'_D variation at 1500 rpm.



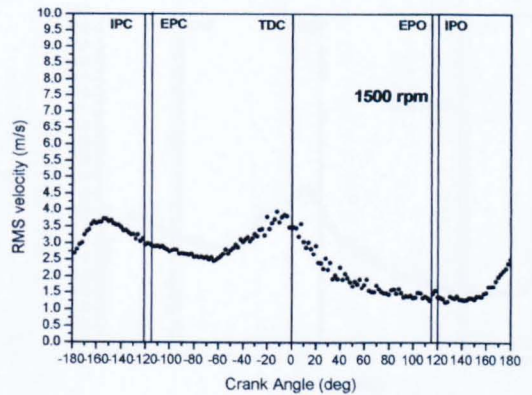
(a)



(b)



(c)



(d)

Figure 7.29 LDV-derived \bar{w}_D and w'_D (w_D component of velocity) variations with crank angle at Point D (10, 5, 0), (a) \bar{w}_D variation at 750 rpm, (b) w'_D variation at 750 rpm, (c) \bar{w}_D variation at 1500 rpm and (d) w'_D variation at 1500 rpm.

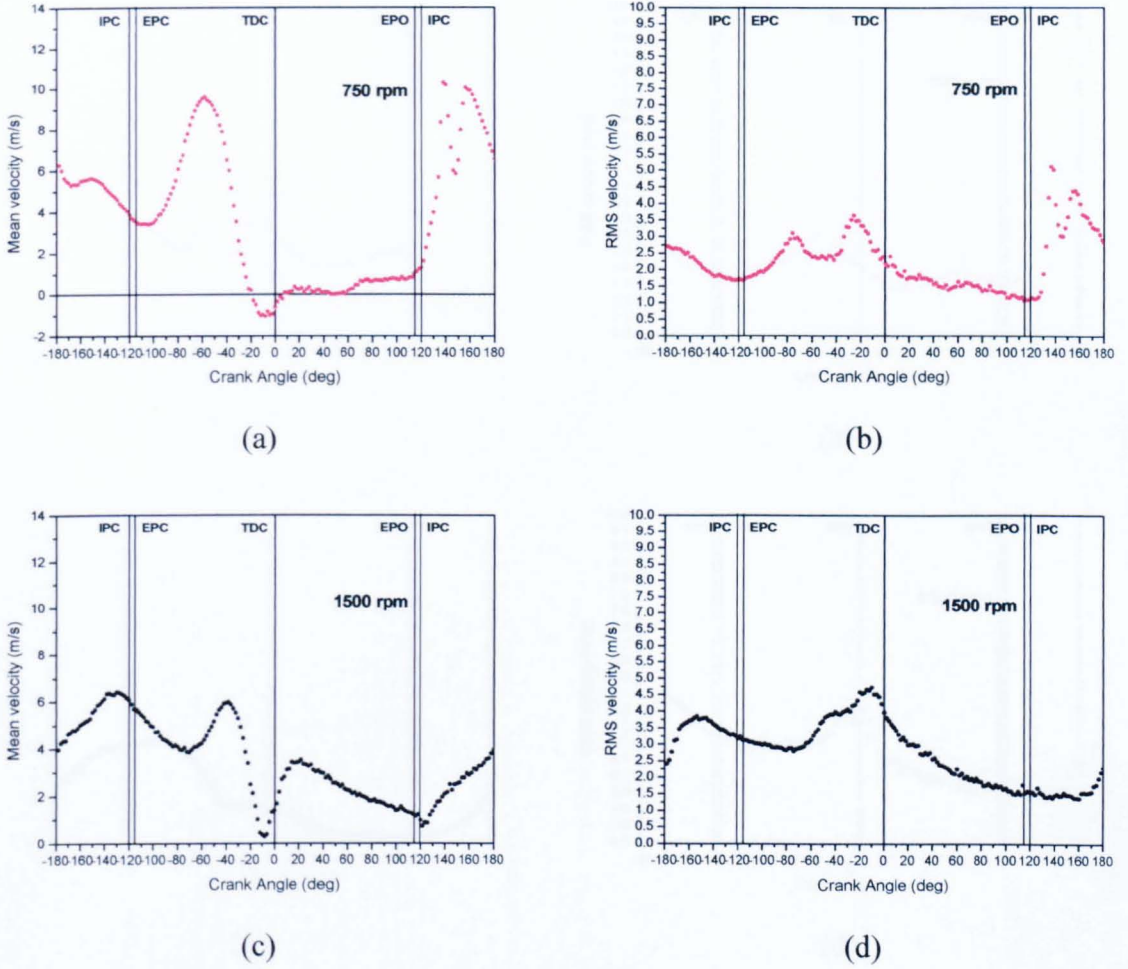


Figure 7.30 LDV-derived \bar{s}_E and s'_E (s_E component of velocity) variations with crank angle at Point E (20, 3, 0), (a) \bar{s}_E variation at 750 rpm, (b) s'_E variation at 750 rpm, (c) \bar{s}_E variation at 1500 rpm and (d) s'_E variation at 1500 rpm.

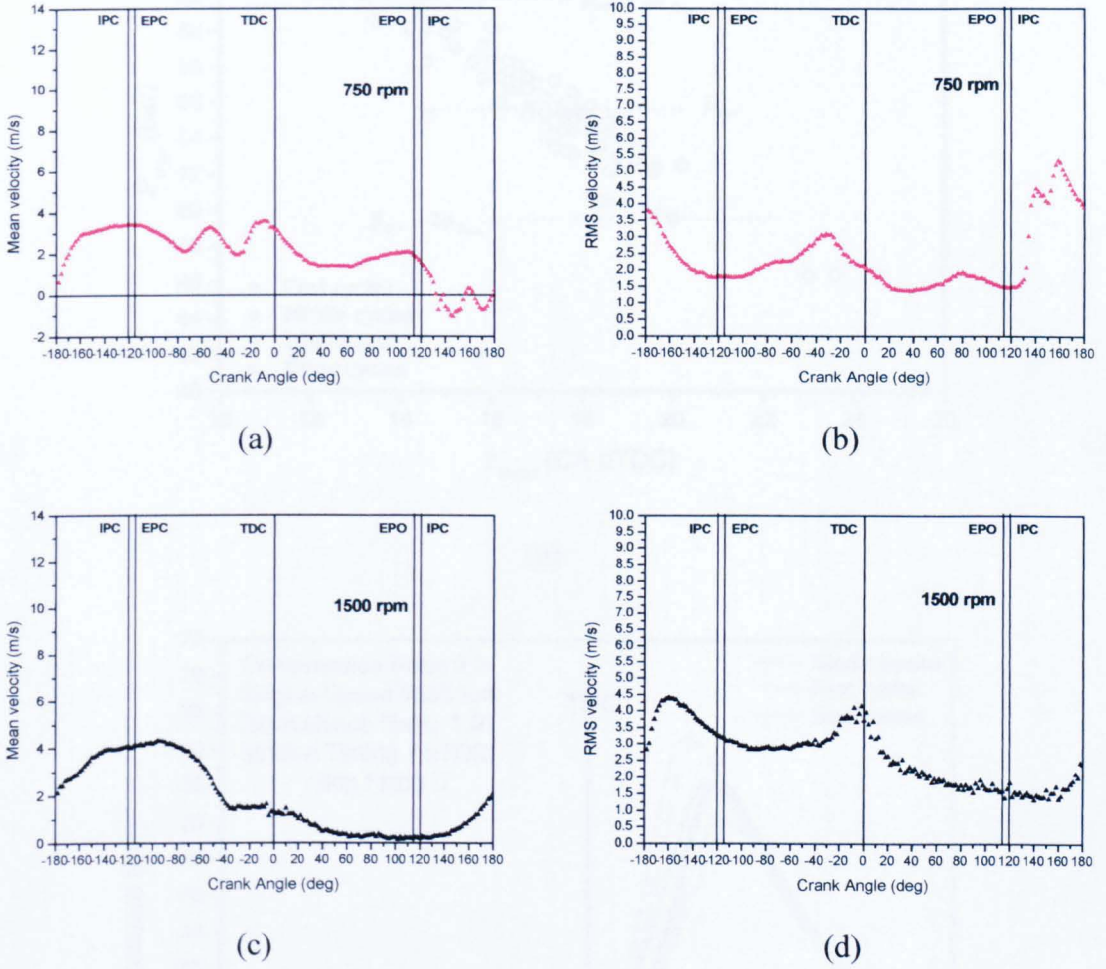
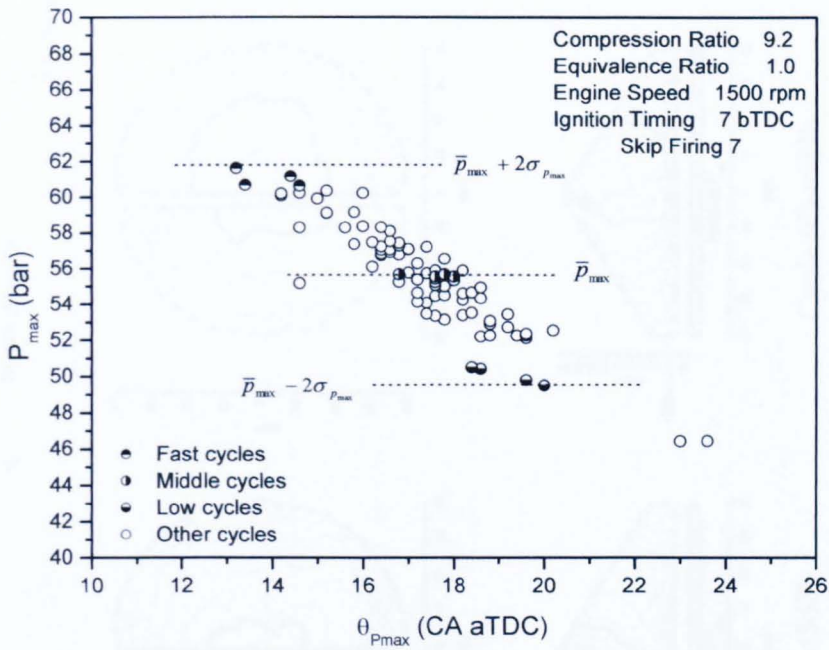
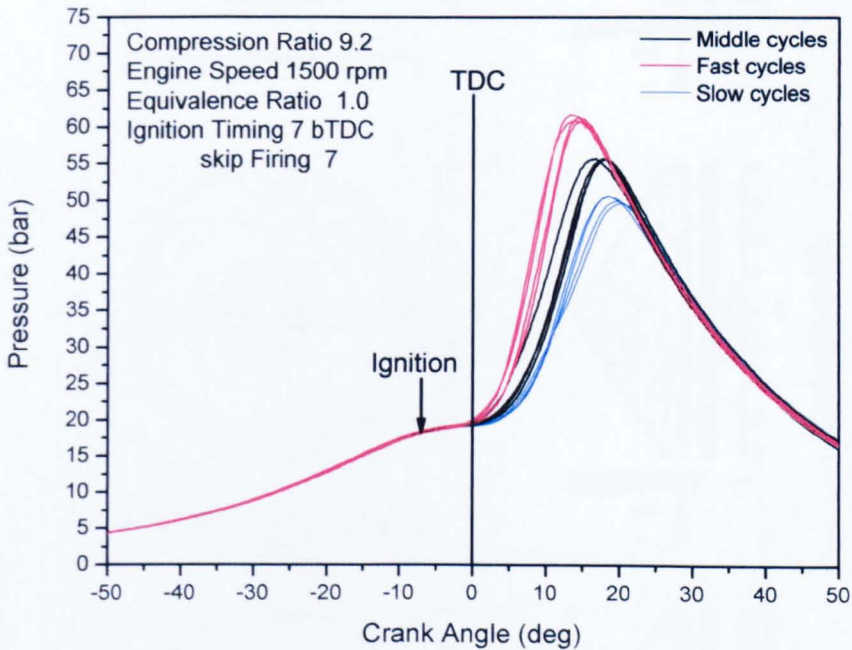


Figure 7.31 LDV-derived \bar{w}_E and w'_E (w_E component of velocity) variations with crank angle at Point E (20, 3, 0), (a) \bar{w}_E variation at 750 rpm, (b) w'_E variation at 750 rpm, (c) \bar{w}_E variation at 1500 rpm and (d) w'_E variation at 1500 rpm.



(a)



(b)

Figure 7.32 (a) Peak pressure versus corresponding crank angle for its occurrence and (b) pressure-crank angle diagrams for selected middle, fast and slow cycles for the 'reference' condition (stoichiometric, 1500 rpm, ignition timing 7° bTDC).

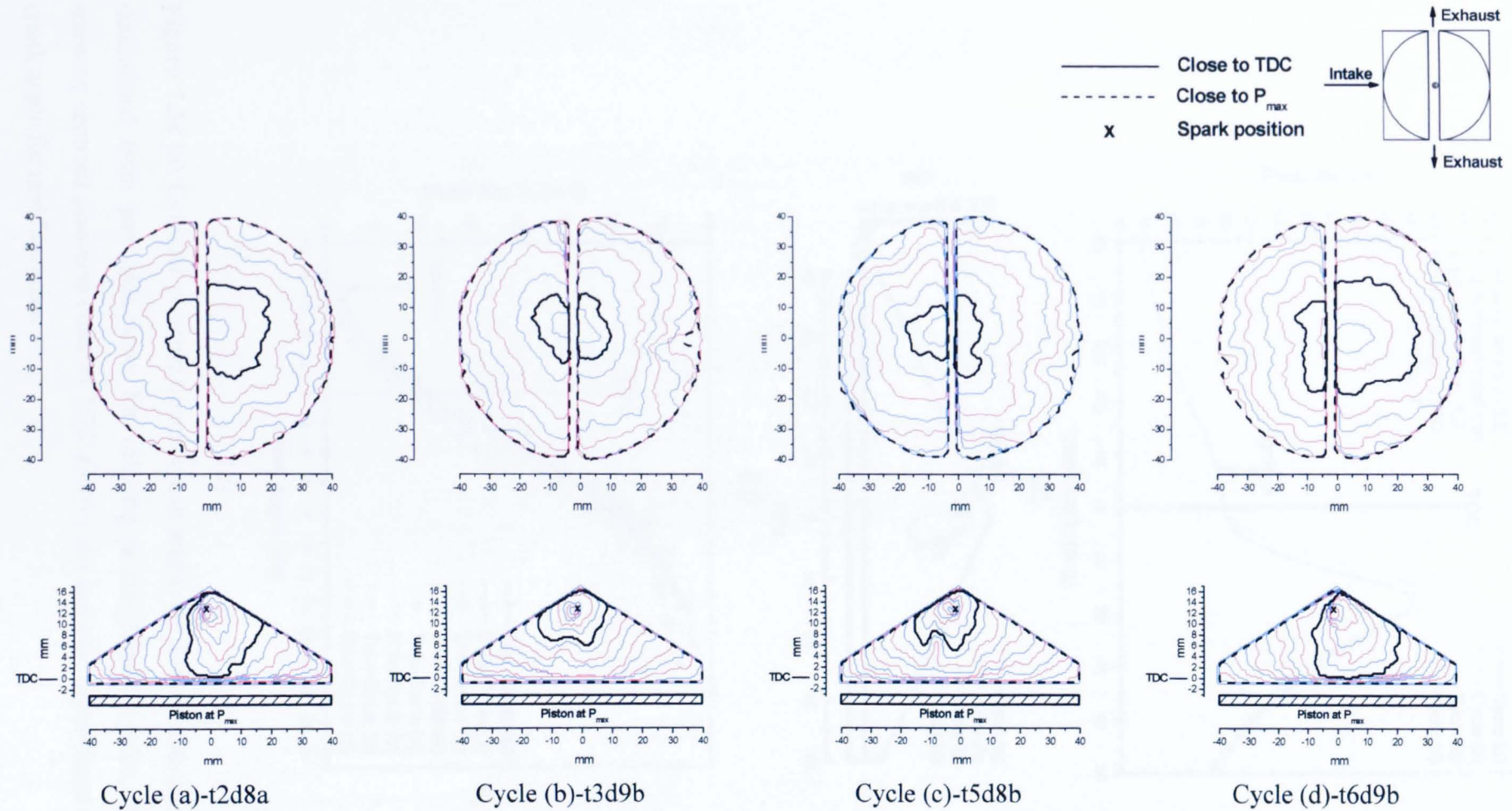


Figure 7.33 Successive flame front positions, overhead and side views, for the four selected ‘middle’ cycles at the reference condition (with top and side contours separated by ~ 2.5 and 1.26° CA, respectively).

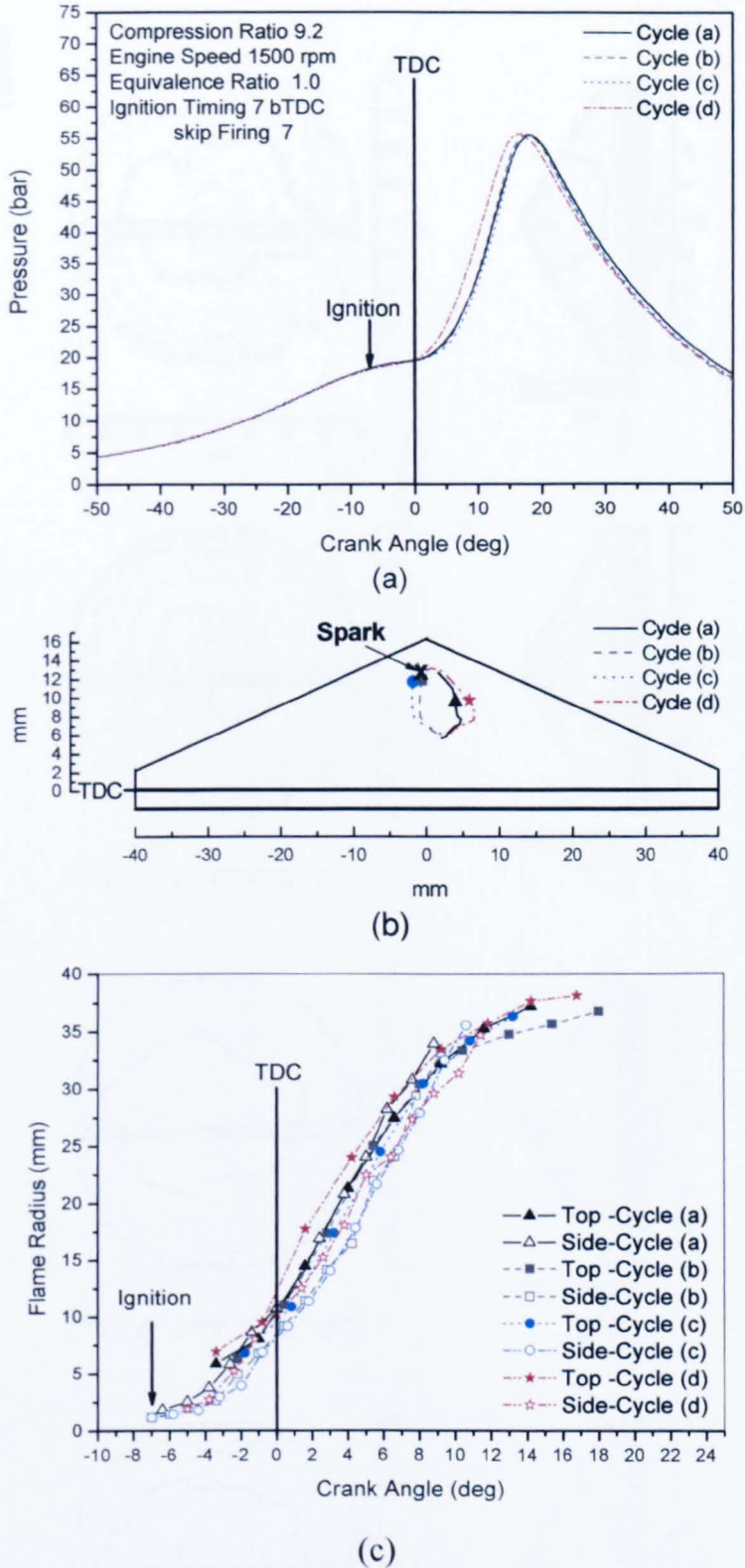
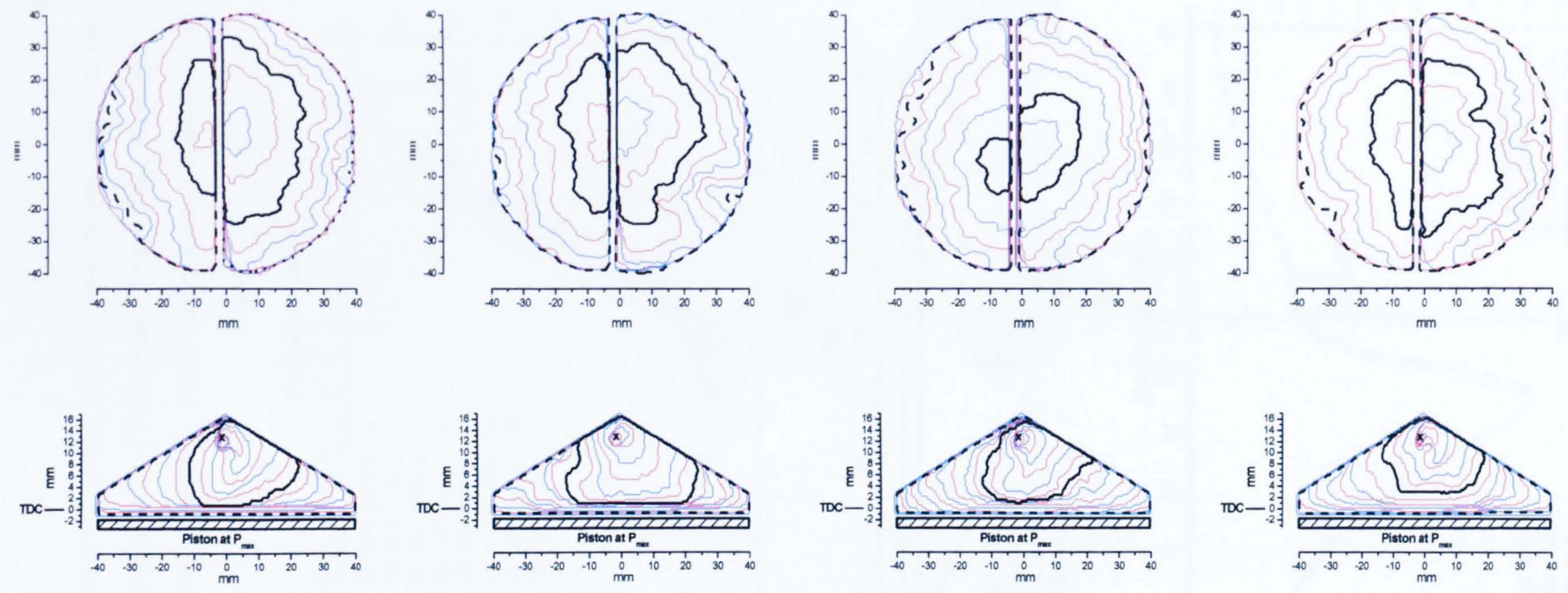
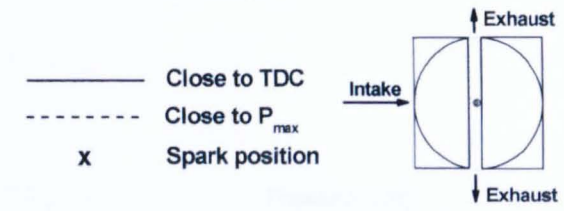


Figure 7.34 (a) Cylinder pressure versus crank angle, (b) flame centroid displacement determined from just side view for selected middle-filmed cycles, filled symbol showing centroid positions close to TDC and (c) top and side mean flame radius versus crank angle for middle cycles.



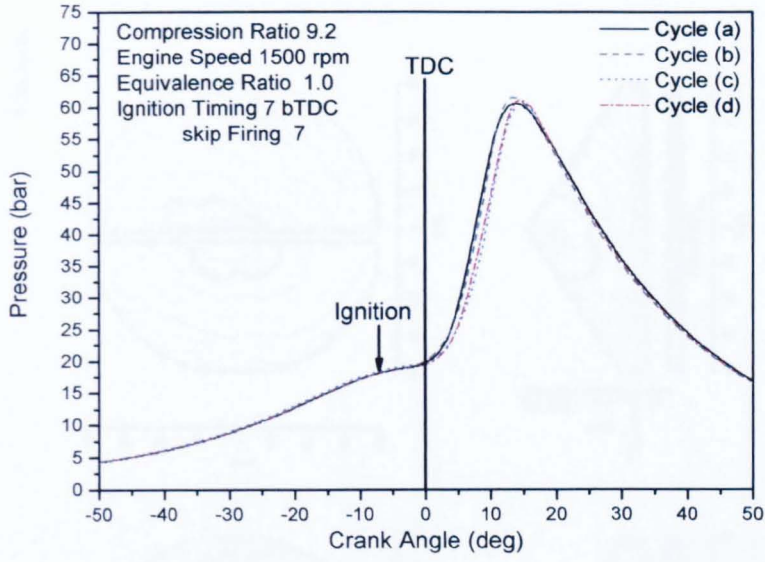
Cycle (a)-t10d8a

Cycle (b)-t10d8b

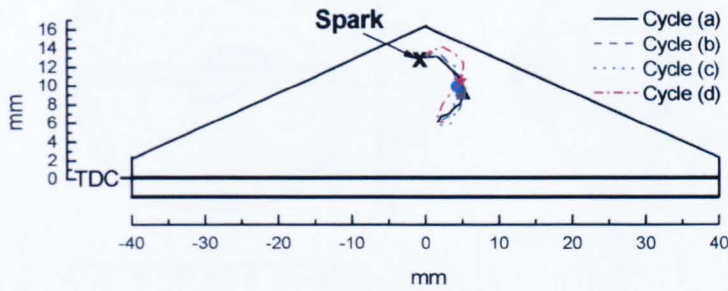
Cycle (c)-t11d8c

Cycle (d)-t13d8a

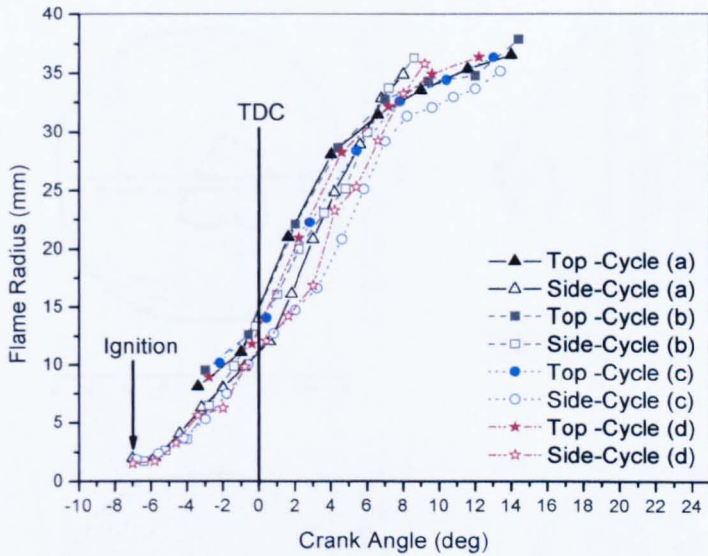
Figure 7.35 Successive flame front positions, overhead and side views, for the four selected ‘fast’ cycles at the reference condition (with top and side contours separated by ~ 2.5 and 1.26° CA, respectively).



(a)



(b)



(c)

Figure 7.36 (a) Cylinder pressure versus crank angle, (b) flame centroid displacement determined from just side view for selected fast-filmed cycles, filled symbol showing centroid positions close to TDC and (c) top and side mean flame radius versus crank angle for fast cycles.

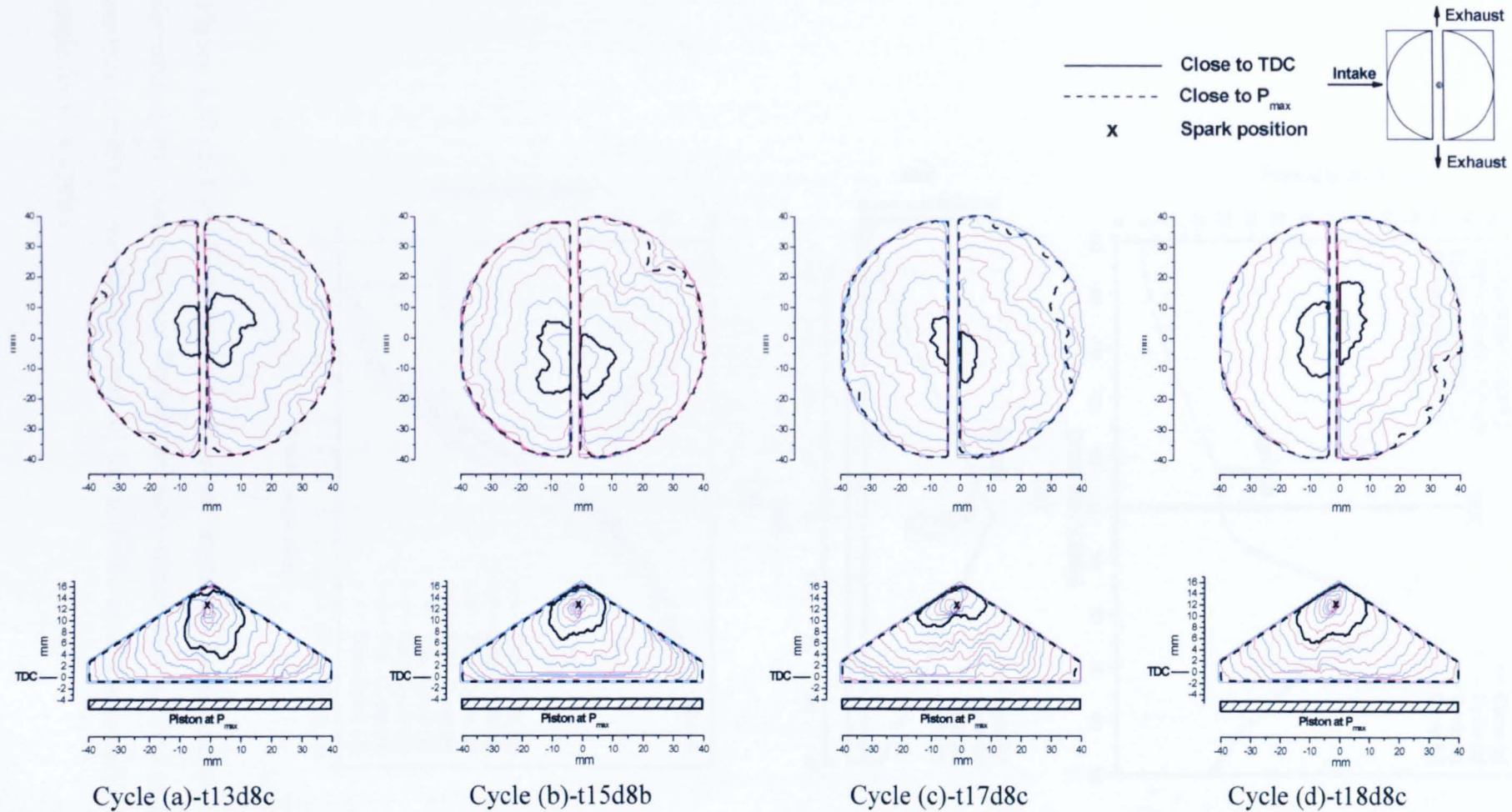
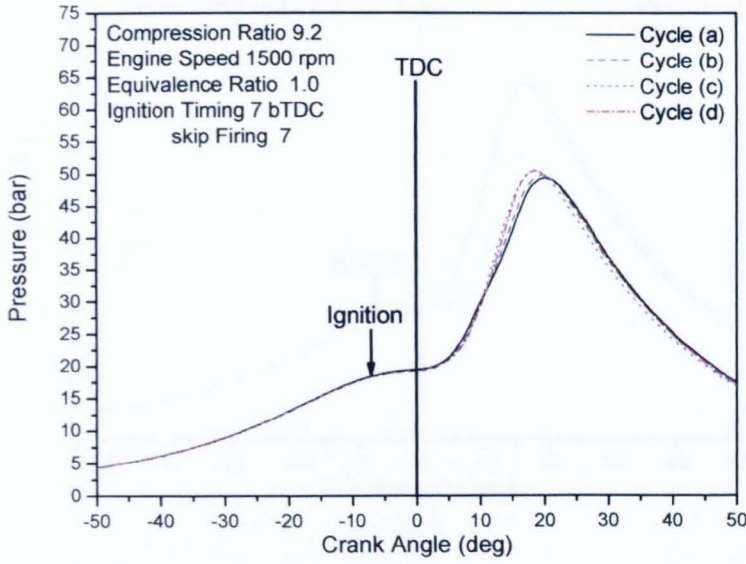
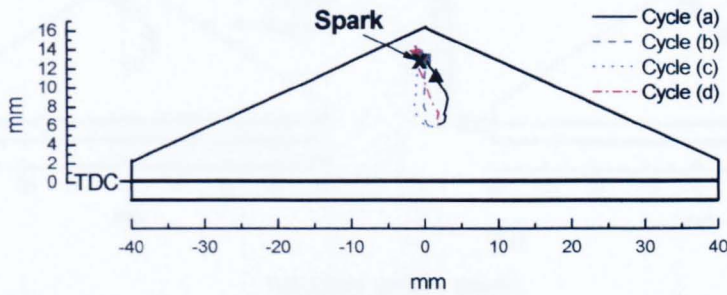


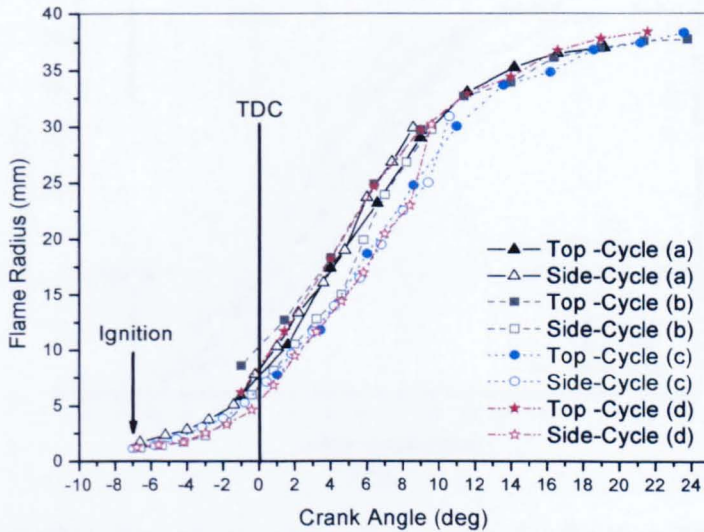
Figure 7.37 Successive flame front positions, overhead and side views, for the four selected ‘slow’ cycles at the reference condition (with top and side contours separated by ~ 2.5 and 1.26° CA, respectively).



(a)



(b)



(c)

Figure 7.38 (a) Cylinder pressure versus crank angle, (b) flame centroid displacement determined from just side view for selected slow-filmed cycles, filled symbol showing centroid positions close to TDC and (c) top and side mean flame radius versus crank angle for slow cycles.

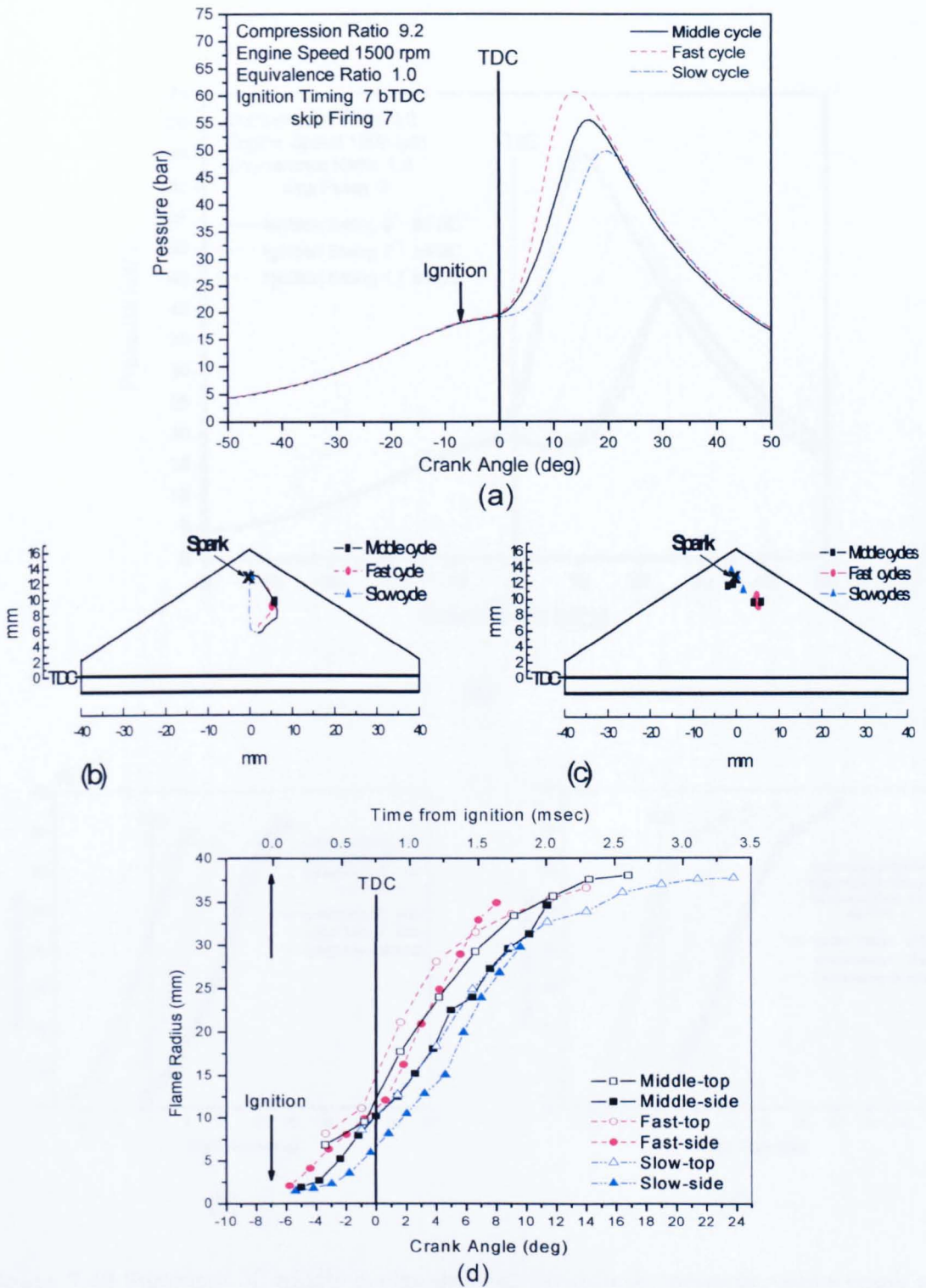
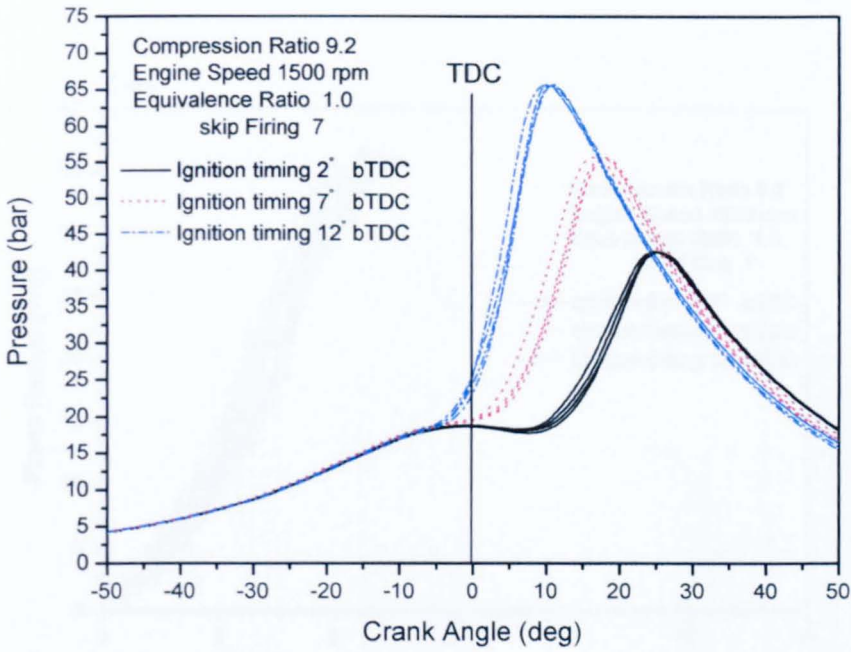
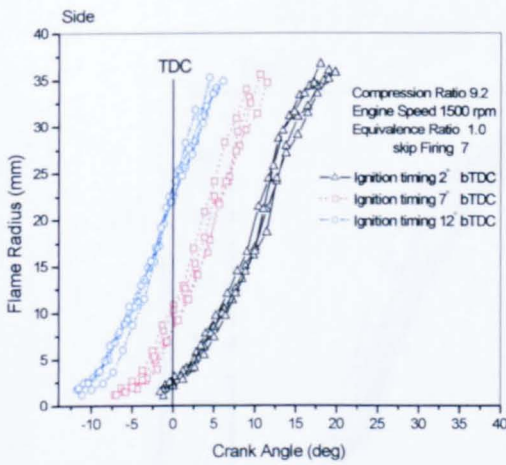


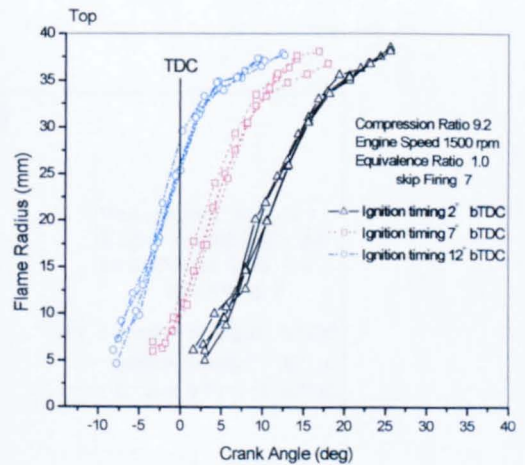
Figure 7.39 (a) Cylinder pressure versus crank angle, (b) flame centroid displacement determined from the side view for a typical ‘middle’, ‘fast’ and ‘slow’ cycles, (c) all representative middle, fast and slow cycles, at the reference condition, filled symbol showing centroid positions close to TDC and (d) top and side mean flame radius versus crank angle and time from ignition for a representative ‘middle’, ‘fast’ and ‘slow’ cycles at the reference condition.



(a)

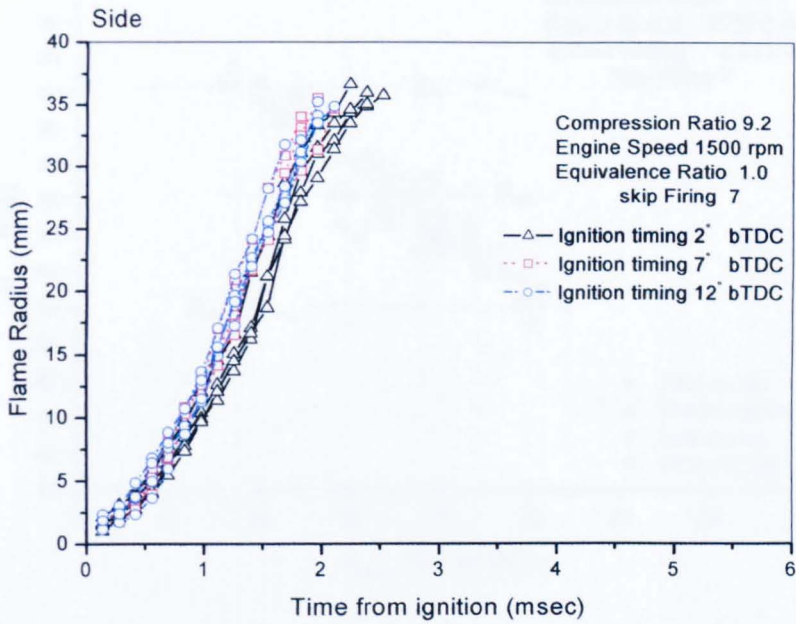


(b)

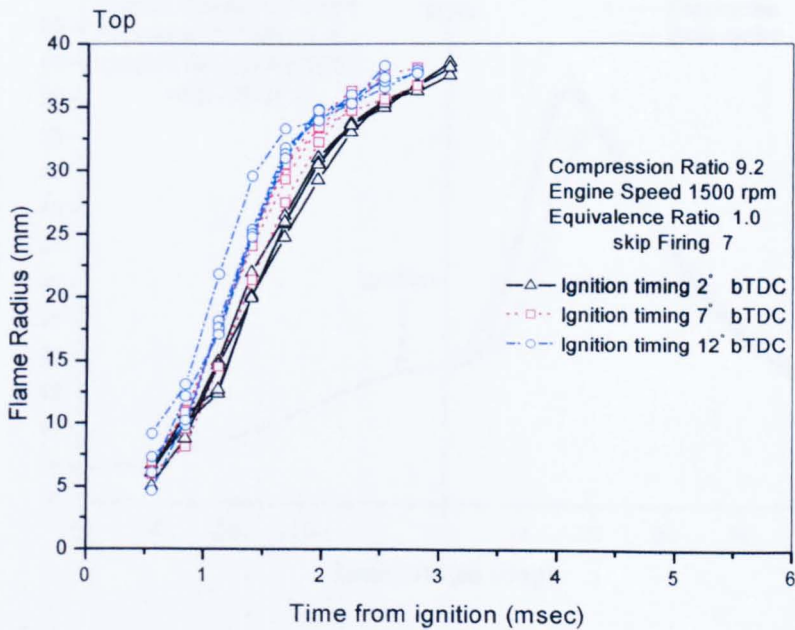


(c)

Figure 7.40 Summary of middle cycles showing (a) cylinder pressure versus crank angle and mean flame radius versus crank angle derived from (b) the side view and (c) the overhead view for two ignition timings additional to that at the reference condition.

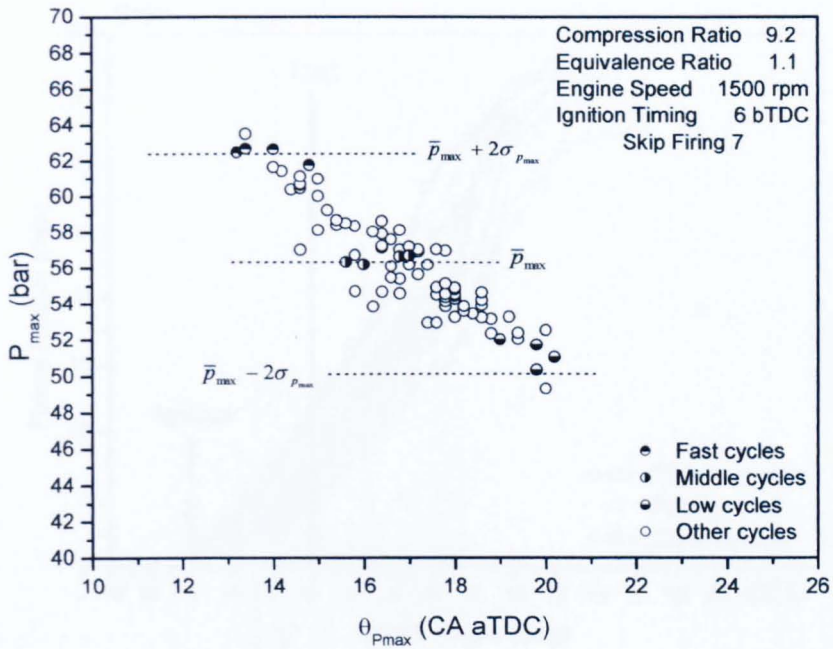


(a)

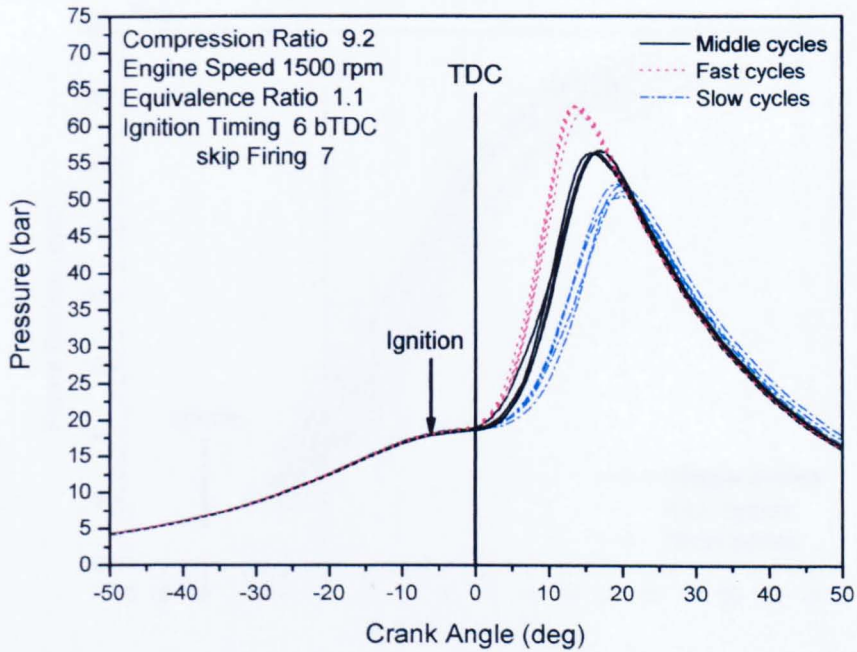


(b)

Figure 7.41 Mean flame radius versus time from ignition of middle cycles derived from (a) the side view and (b) the overhead view for two ignition timings additional to that at the reference condition.

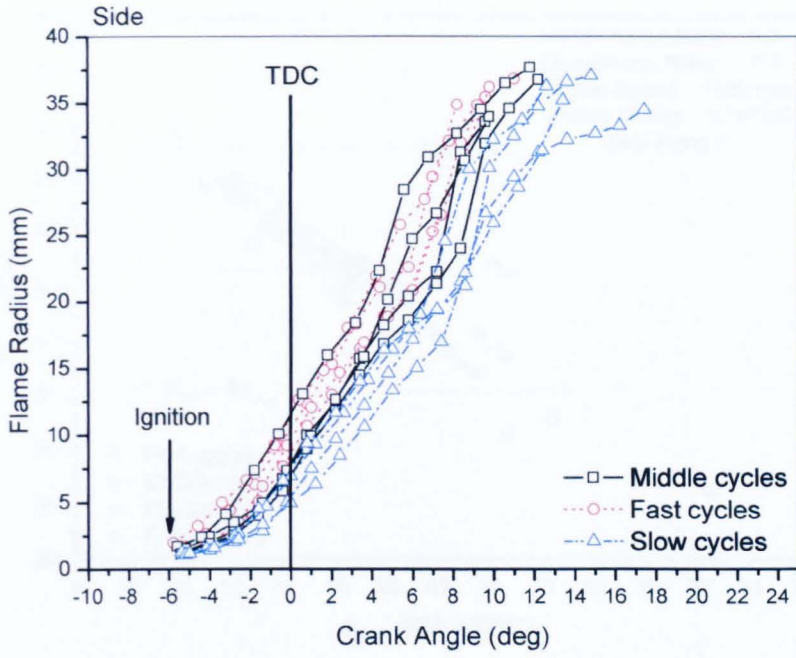


(a)

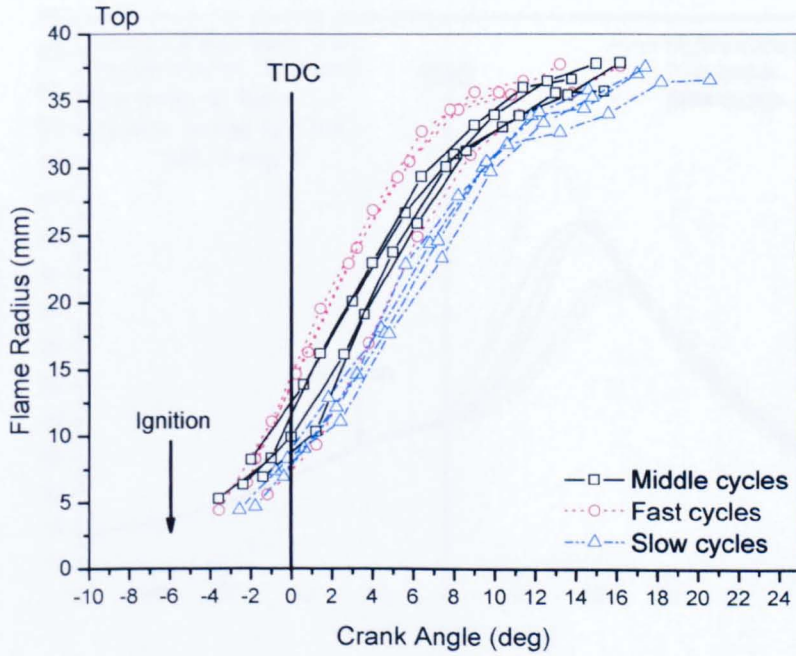


(b)

Figure 7.42 (a) Peak pressure versus corresponding crank angle for its occurrence and (b) pressure-crank angle diagrams for selected middle, fast and slow cycles for rich ($\phi = 1.1$), 1500 rpm, ignition timing 6° bTDC.

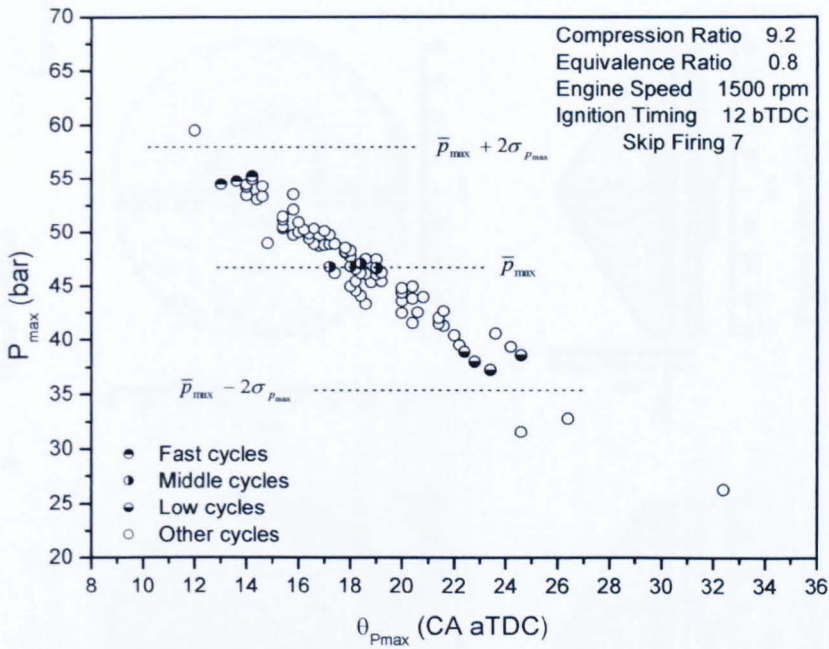


(a)

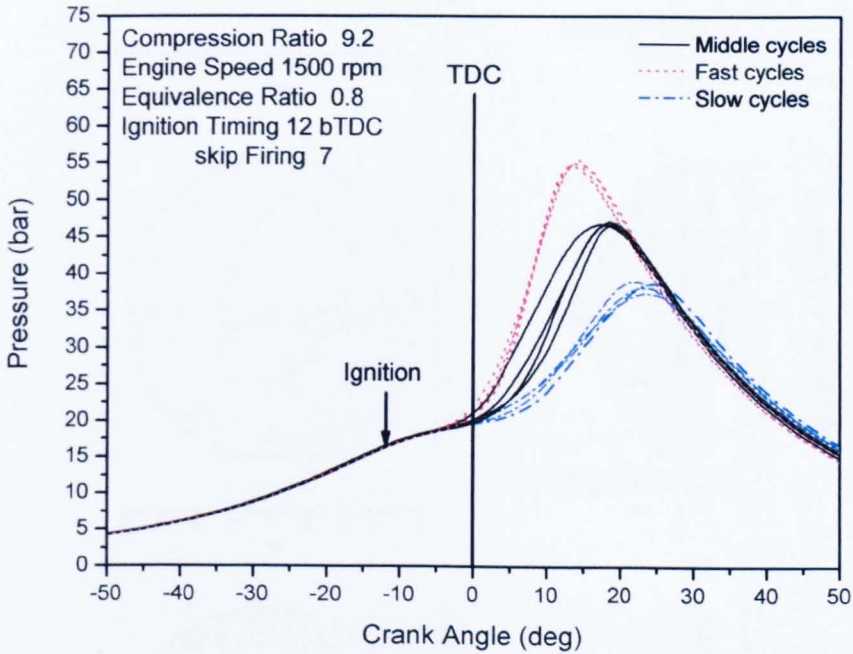


(b)

Figure 7.43 Mean flame radius versus crank angle derived from (a) the side view and (b) the overhead view for rich ($\phi = 1.1$), 1500 rpm, ignition timing 6° bTDC.



(a)



(b)

Figure 7.44 (a) Peak pressure versus corresponding crank angle for its occurrence and (b) pressure-crank angle diagrams for selected middle, fast and slow cycles for lean ($\phi = 0.8$), 1500 rpm, ignition timing 12° bTDC.

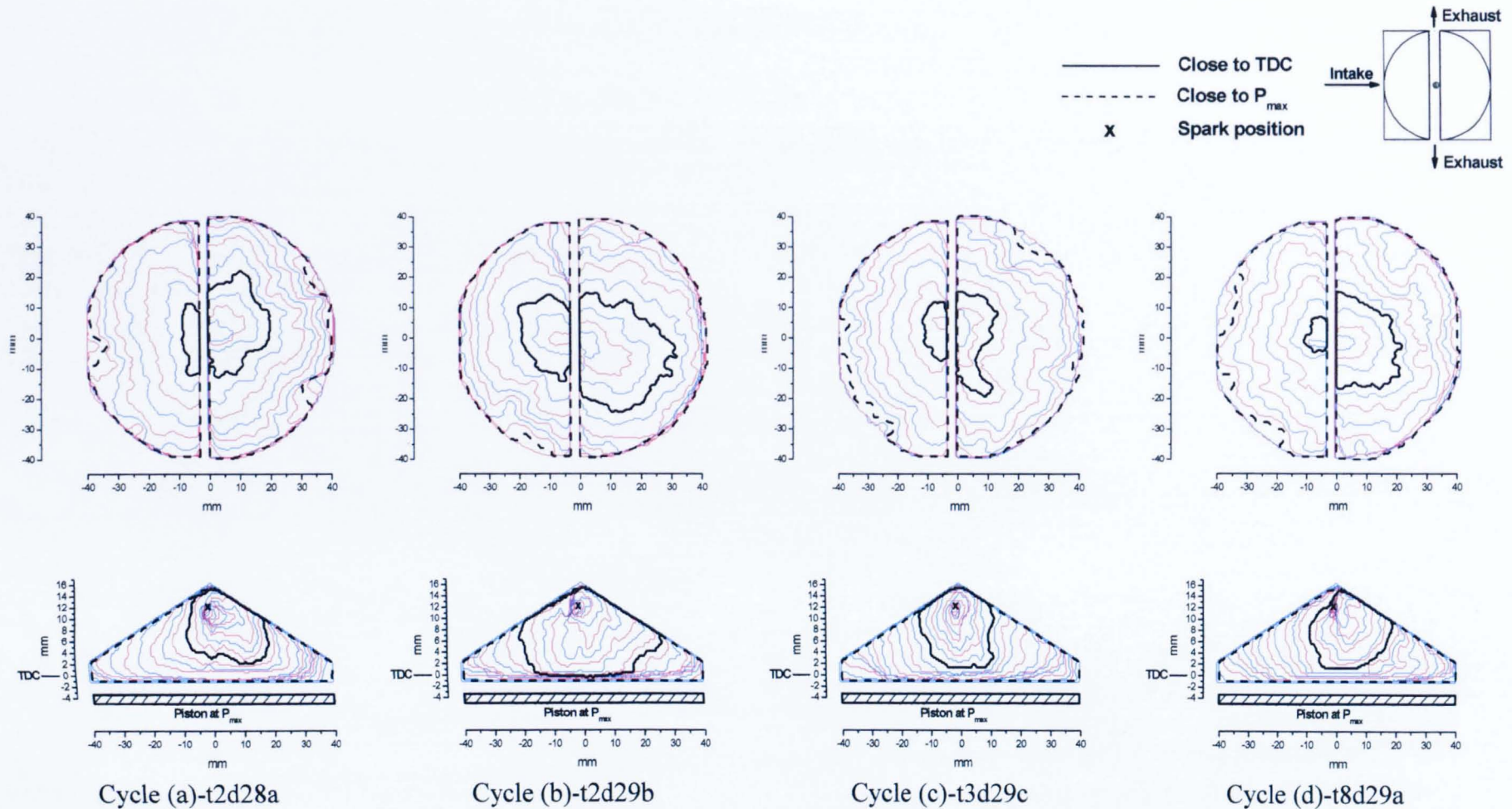


Figure 7.45 Successive flame front positions, overhead and side views, for the four selected ‘middle’ cycles for lean ($\phi = 0.8$), 1500 rpm, ignition timing 12° bTDC. (with top and side contours separated by ~ 2.5 and 1.26° CA, respectively).

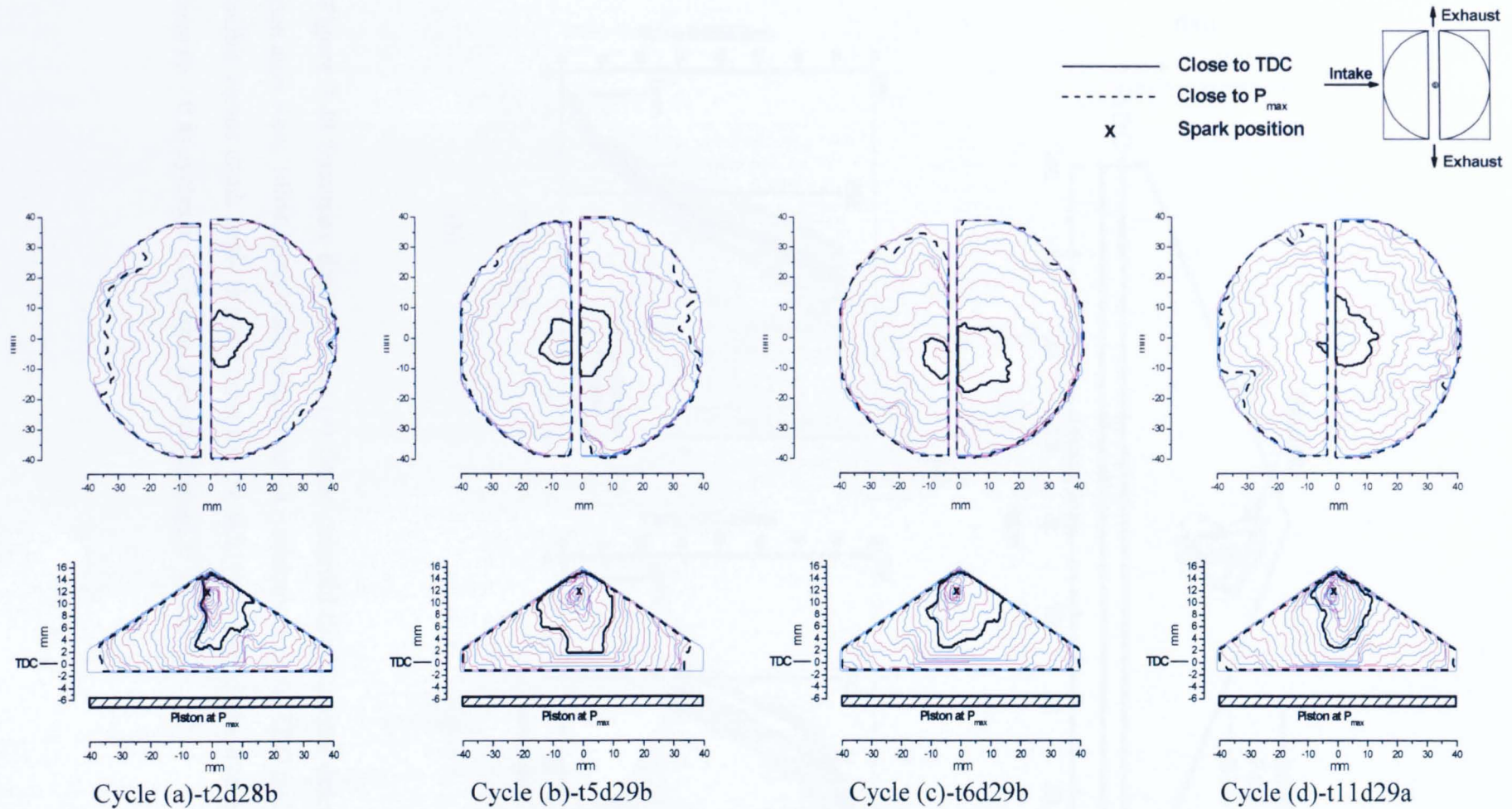
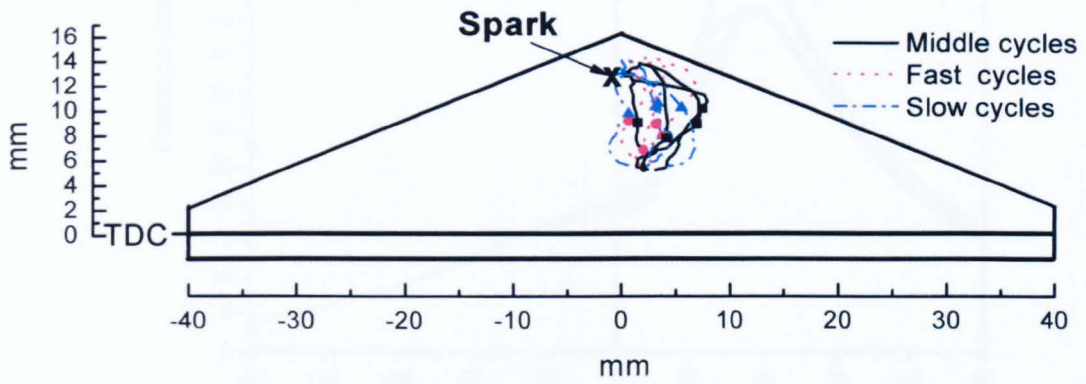
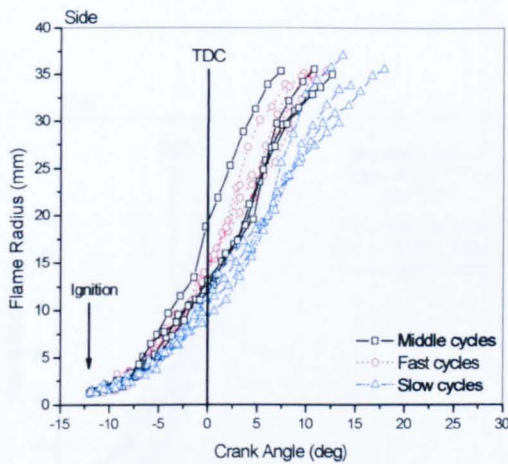


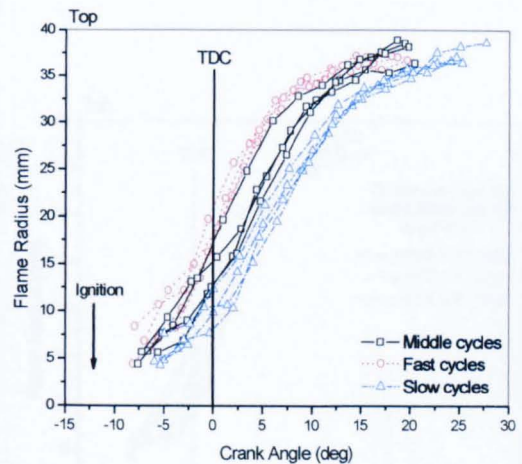
Figure 7.47 Successive flame front positions, overhead and side views, for the four selected 'slow' cycles for lean ($\phi = 0.8$), 1500 rpm, ignition timing 12° bTDC. (with top and side contours separated by ~ 2.5 and 1.26° CA, respectively).



(a)

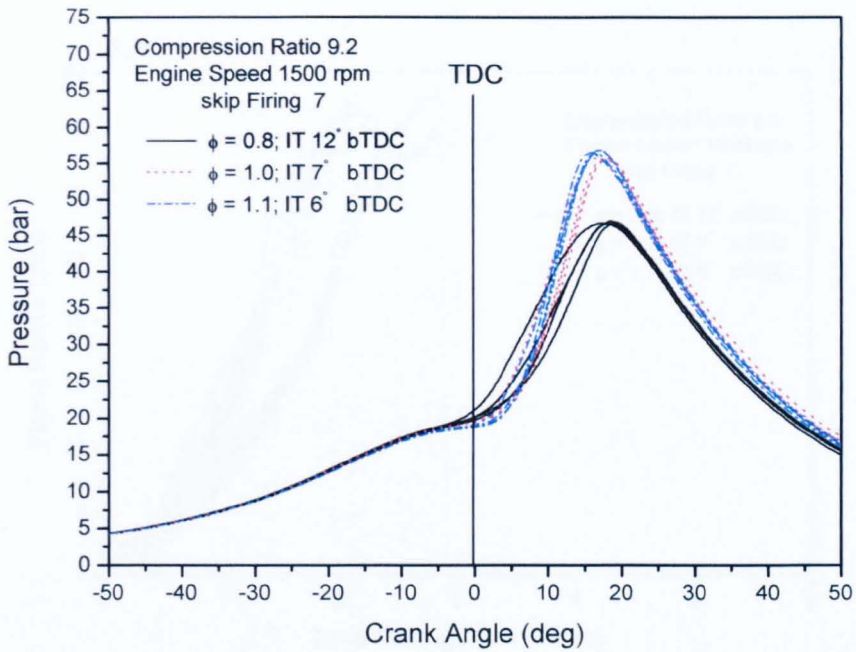


(b)

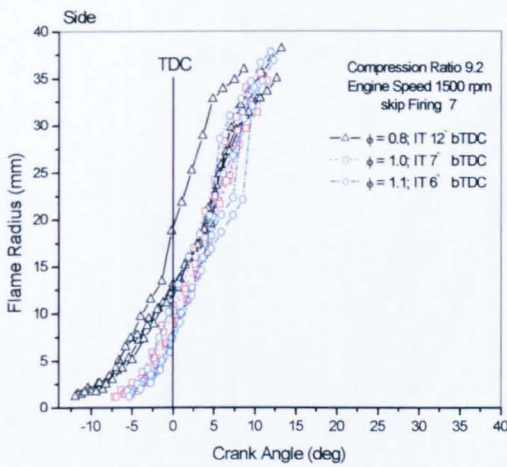


(c)

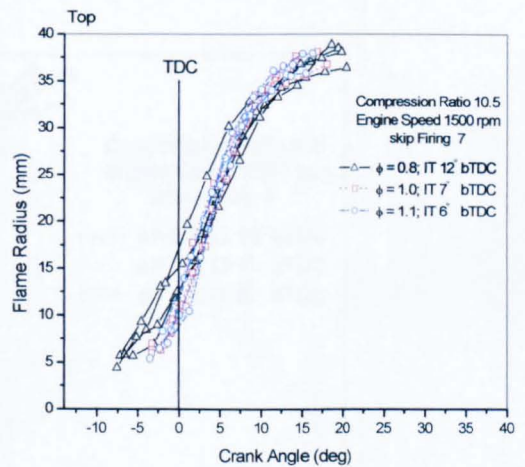
Figure 7.48 Summary data showing (a) flame centroid displacement determined from just side view, filled symbol showing centroid positions close to TDC and mean flame radius versus crank angle derived from (b) the side view and (c) the overhead view for lean ($\phi = 0.8$) cycles at 1500 rpm, ignition timing 12° bTDC.



(a)

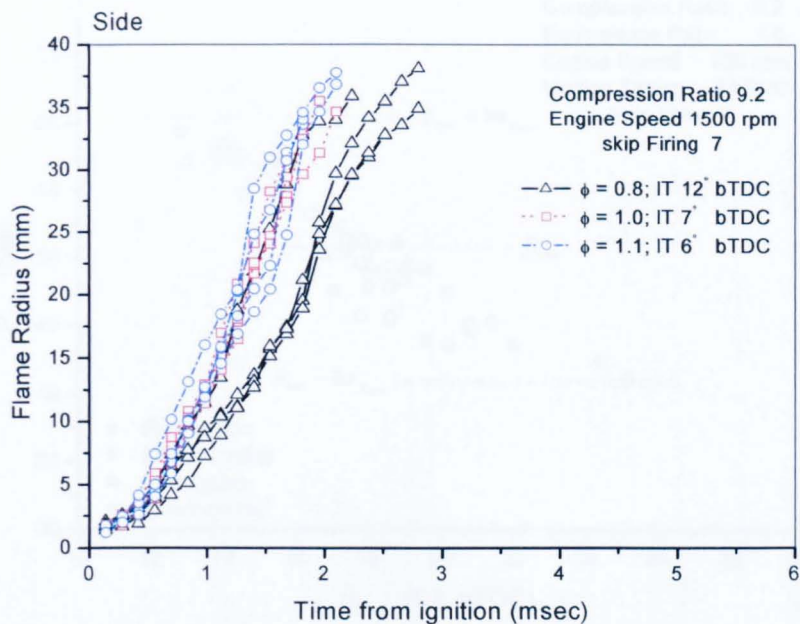


(b)

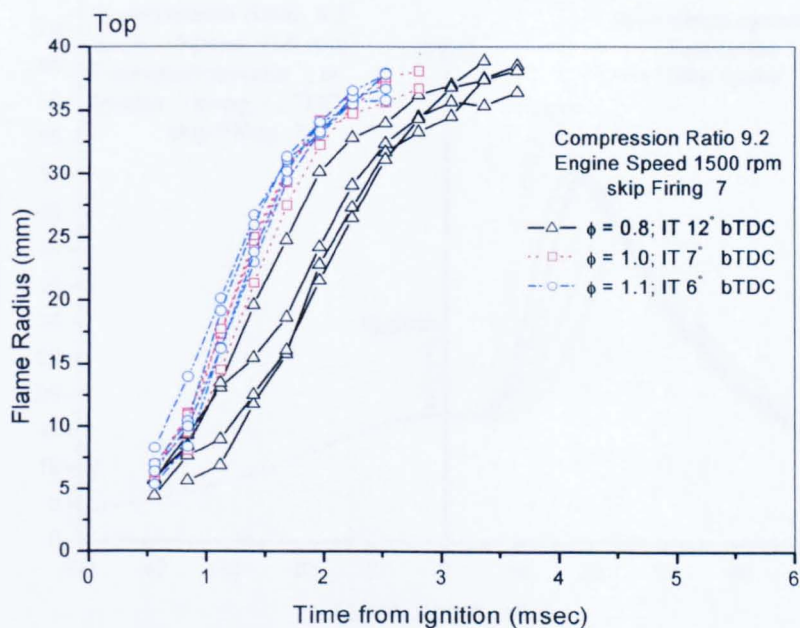


(c)

Figure 7.49 Summary data of middle cycles showing (a) cylinder pressure versus crank angle and mean flame radius versus crank angle derived from (b) the side view and (c) the overhead view for two equivalence ratios (rich ($\phi = 1.1$) and lean (0.8)) additional to that at the reference condition (stoichiometric).

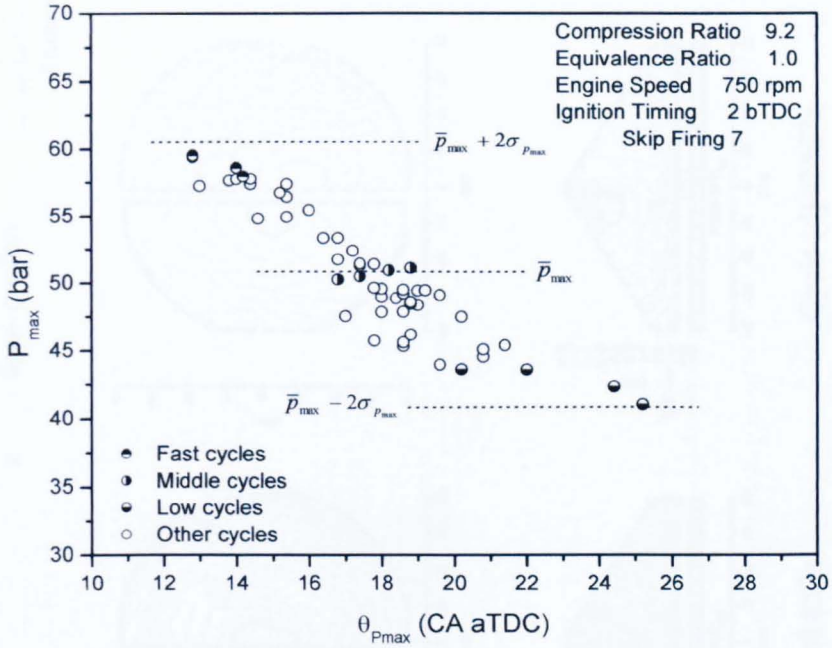


(a)

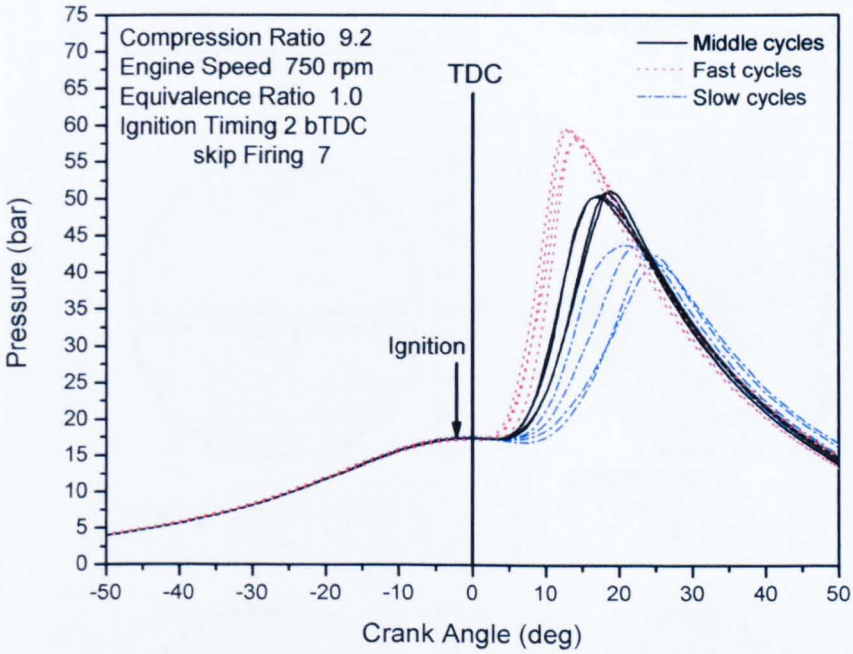


(b)

Figure 7.50 Mean flame radius versus time from ignition for middle cycles derived from (a) the side view and (b) the overhead view for two equivalence ratios (rich ($\phi = 1.1$) and lean (0.8)) additional to that at the reference condition (stoichiometric).



(a)



(b)

Figure 7.51 (a) Peak pressure versus corresponding crank angle for its occurrence and (b) pressure-crank angle diagrams for selected middle, fast and slow cycles for stoichiometric, 750 rpm, ignition timing 2° bTDC.

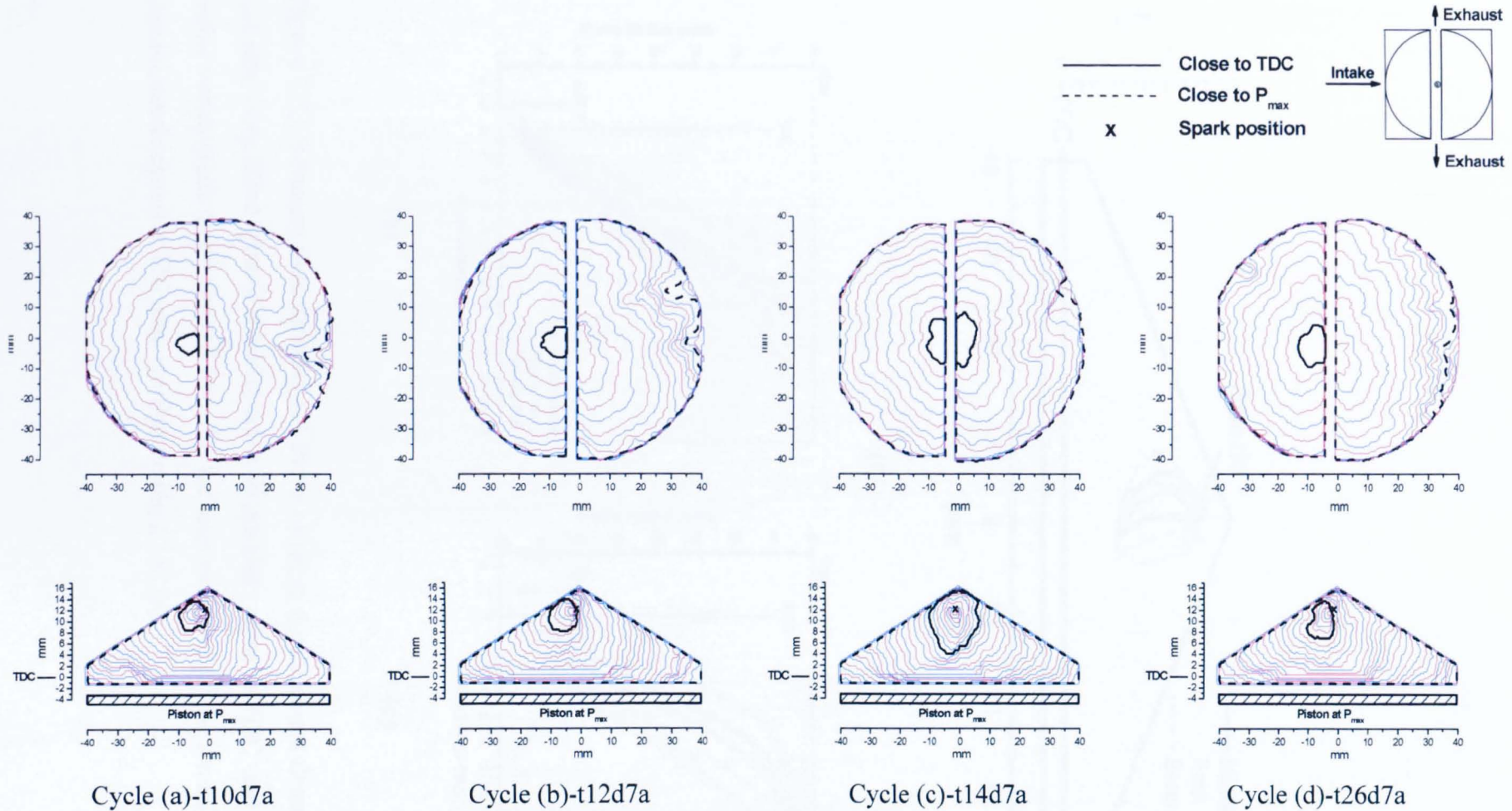
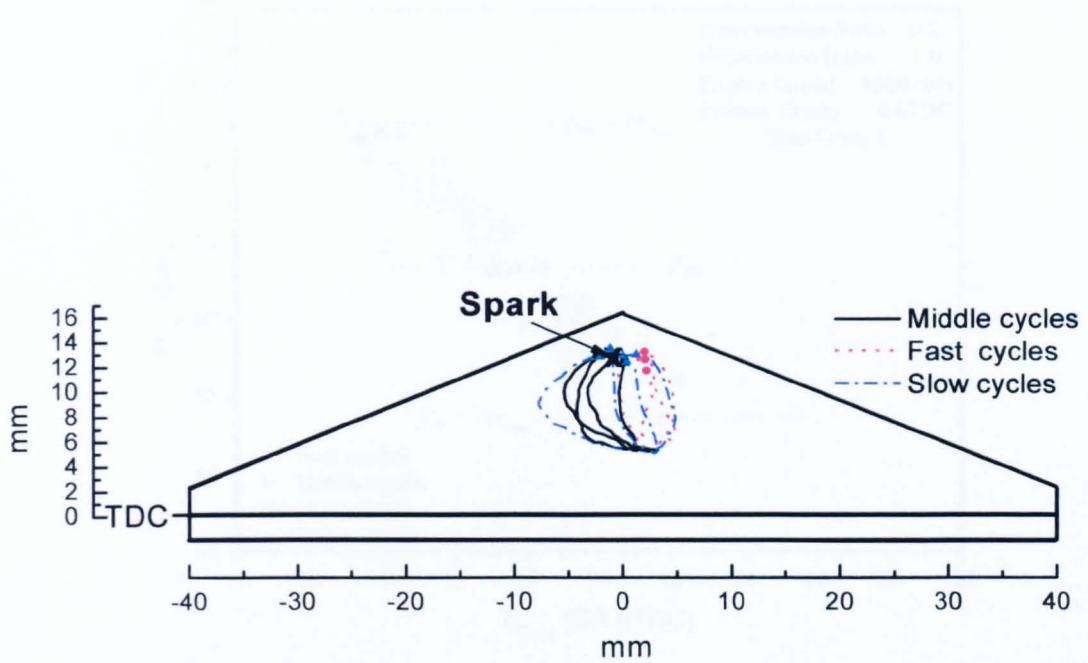
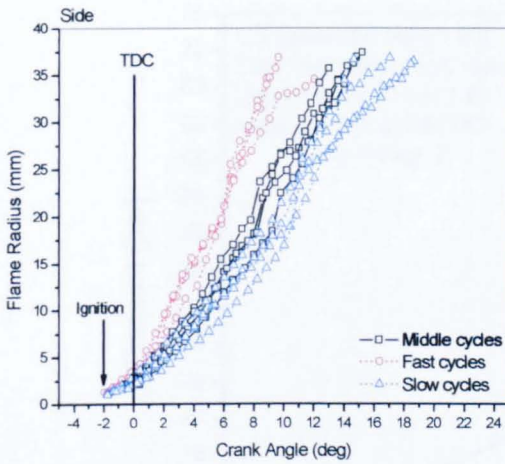


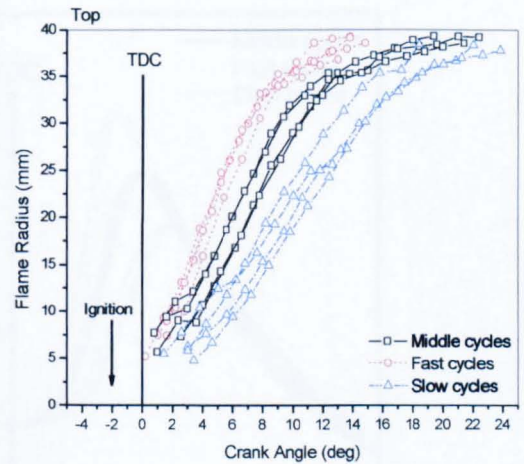
Figure 7.52 Successive flame front positions, overhead and side views, for the four selected ‘middle’ cycles for stoichiometric, 750 rpm, ignition timing 2° bTDC (with top and side contours separated by ~ 1.26 and 0.63° CA, respectively).



(a)

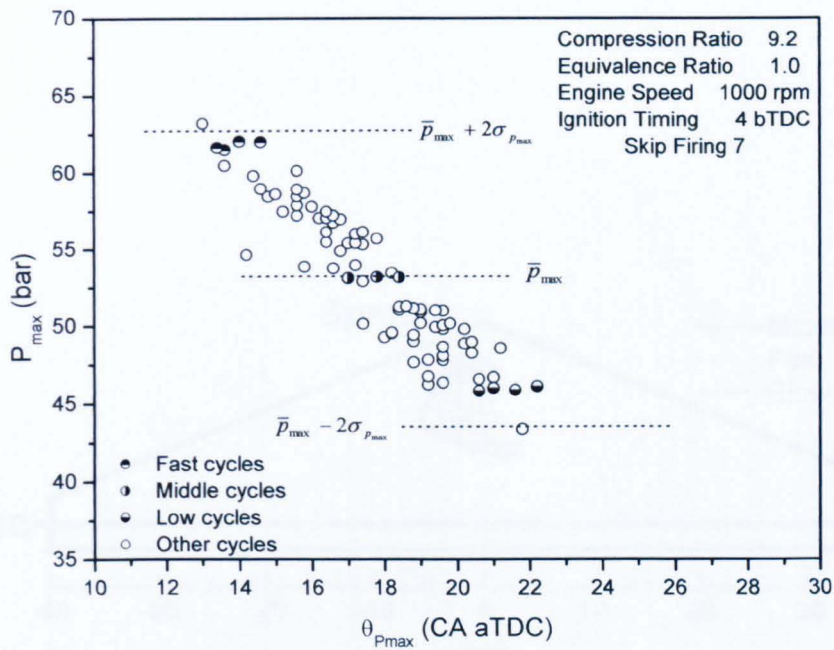


(b)

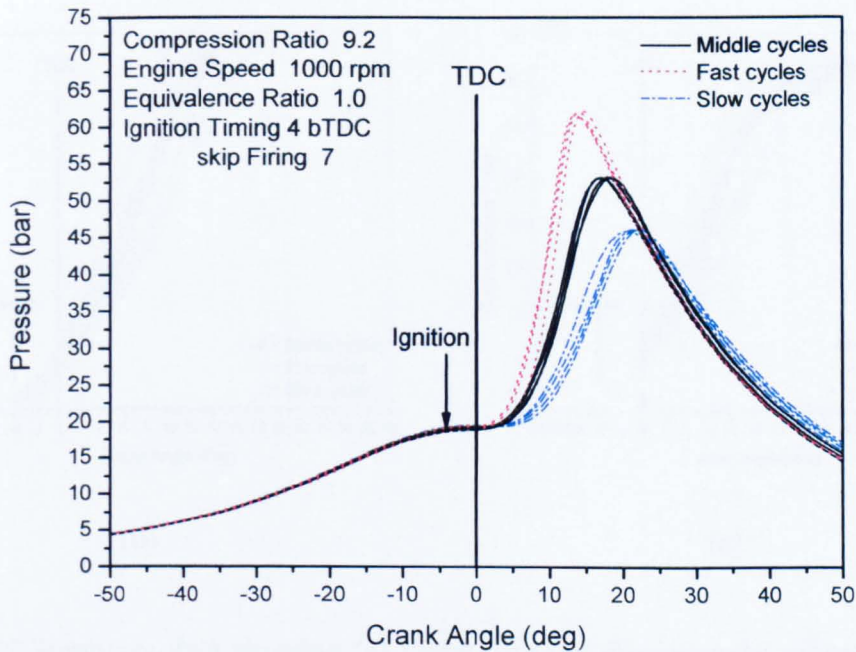


(c)

Figure 7.53 Summary data showing (a) flame centroid displacement determined from just side view, filled symbol showing centroid positions close to TDC and mean flame radius versus crank angle derived from (b) the side view and (c) the overhead view for stoichiometric cycles at 750 rpm, ignition timing 2° bTDC.

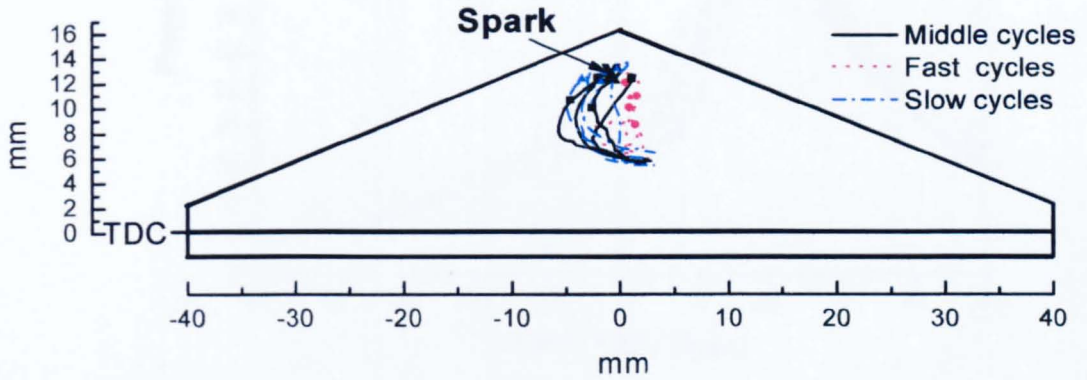


(a)

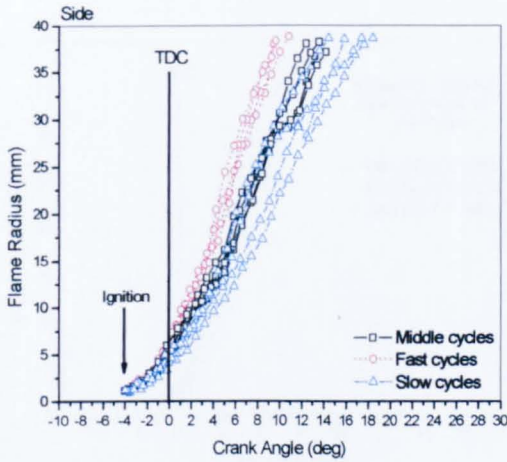


(b)

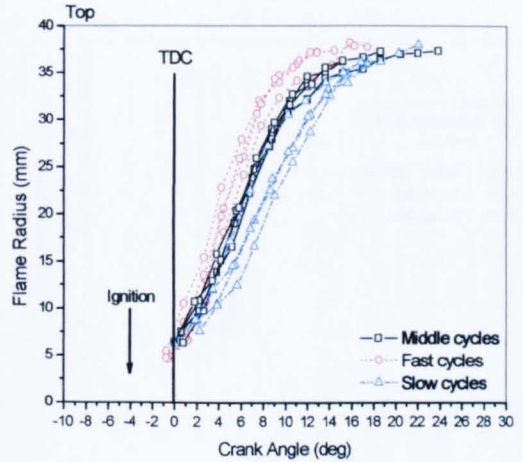
Figure 7.54 (a) Peak pressure versus corresponding crank angle for its occurrence and (b) pressure-crank angle diagrams for selected middle, fast and slow cycles for stoichiometric, 1000 rpm, ignition timing 4° bTDC.



(a)

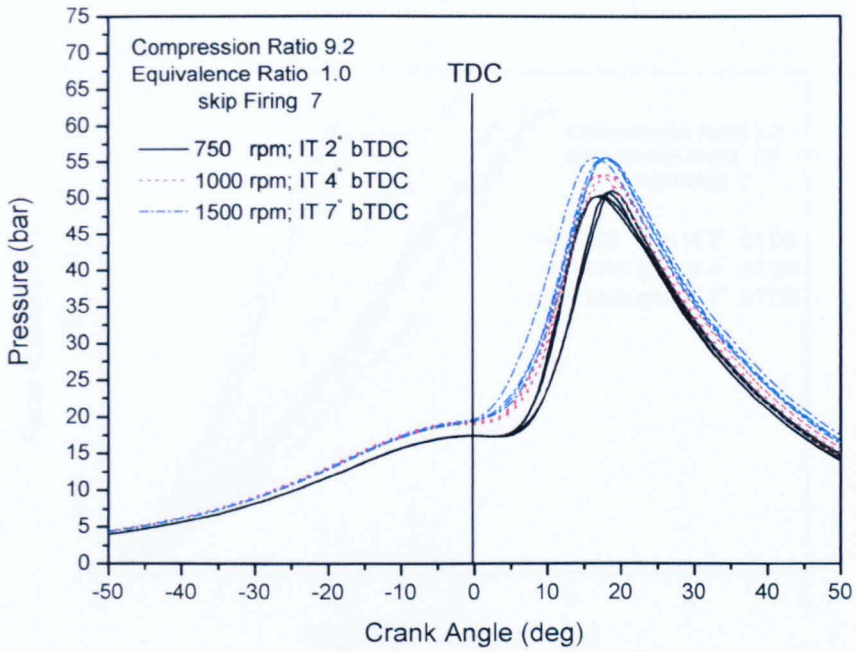


(b)

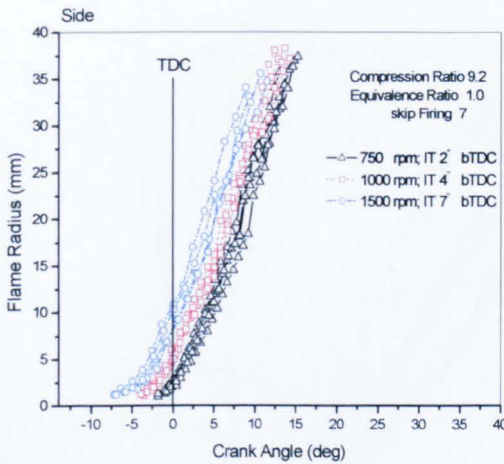


(c)

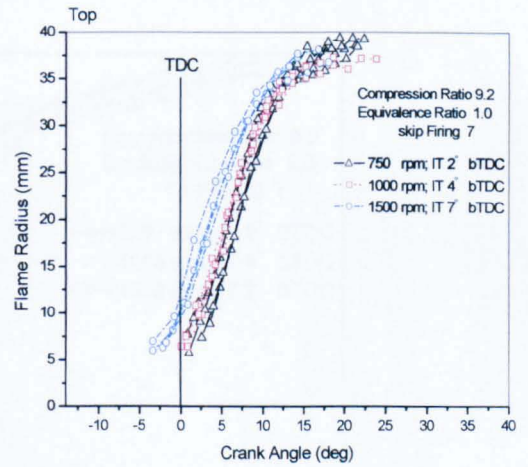
Figure 7.55 Summary data showing (a) flame centroid displacement determined from just side view, filled symbol showing centroid positions close to TDC and mean flame radius versus crank angle derived from (b) the side view and (c) the overhead view for stoichiometric cycles at 1000 rpm, ignition timing 4° bTDC.



(a)

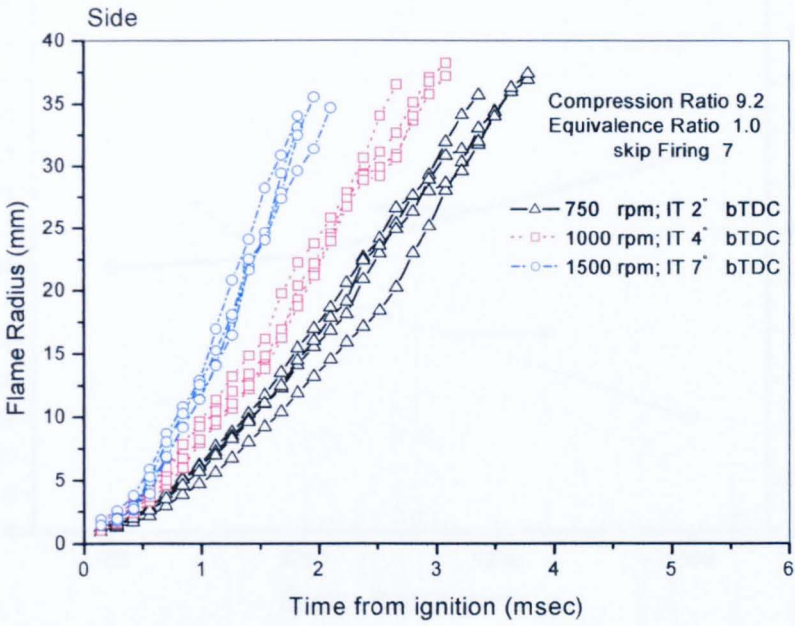


(b)

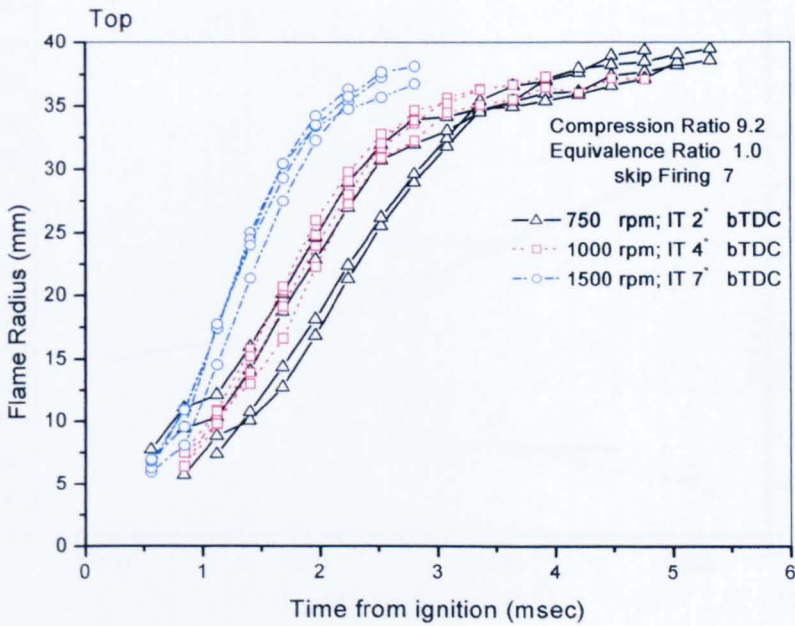


(c)

Figure 7.56 Summary of middle cycles showing (a) cylinder pressure versus crank angle and mean flame radius versus crank angle derived from (b) the side view and (c) the overhead view for two engine speeds (750 and 1000 rpm) additional to that at the reference condition (1500 rpm).

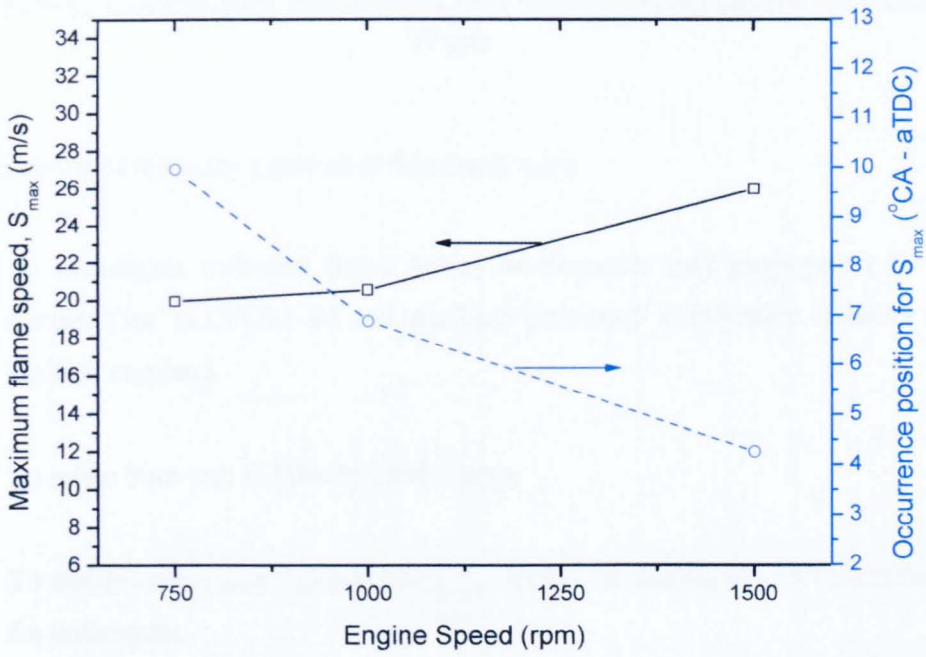


(a)

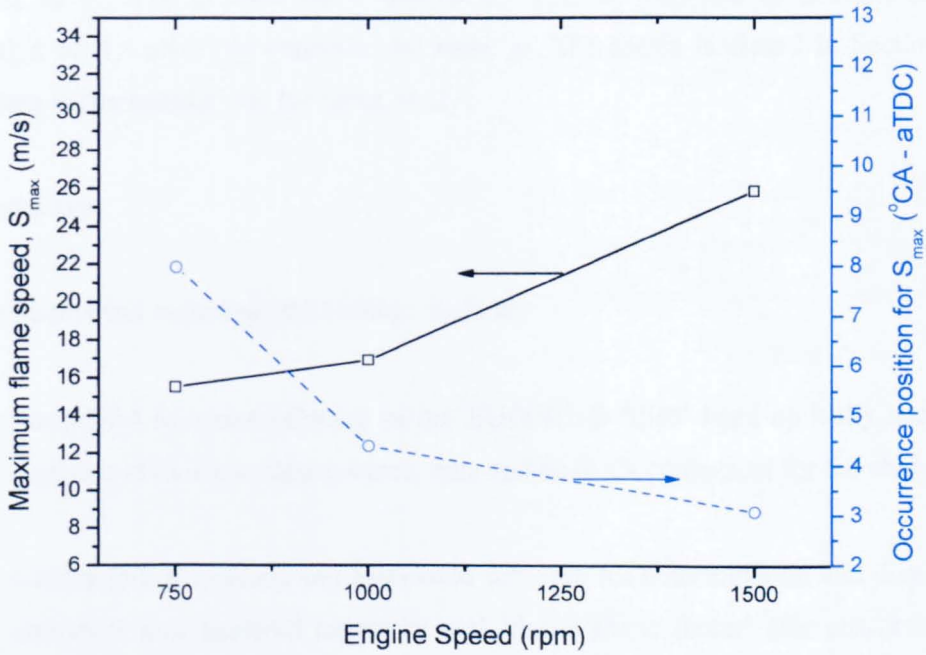


(b)

Figure 7.57 Mean flame radius versus time from ignition for middle cycles derived from (a) the side view and (b) the overhead view for two engine speeds (750 and 1000 rpm) additional to that at the reference condition (1500 rpm).



(a)



(b)

Figure 7.58 Maximum flame speed estimated from flame development derived from (a) side and (b) overhead views and its occurrence position versus engine speed for selected 'middle' cycles.

Chapter 8

Summary, Concluding Discussion and Recommendations for Future Work

The objectives of the study reported in this thesis were:

- i. To investigate turbulent flame kernel development and propagation (in both simple ‘disc’ (LUPOE1-D) and idealised ‘pent-roof’ combustion chamber spark ignition engines).
- ii. To relate burn rate to flow and turbulence.
- iii. To obtain comprehensive sets of engine model development and validation data for colleagues.

Set out in Section 8.1 is a summary listing the achievements and experimental results obtained in seeking to meet these objectives. This is followed in Section 8.2 by discussion of the principle experimental findings. The thesis is closed in Section 8.3 with some recommendations for future study.

8.1 Summary

Achievements and experimental findings include:

- Successful re-commissioning of the LUPOE1-D ‘disc’ head optically accessed engine and its associated systems, data and analysis equipment for the study.
- Generation of routines and associated software for determination and display of enflamed area centroid trajectory and ‘flame shape factor’ (for characterising flame perimeter distortion from the circular shape associated with idealised ‘spherical’ flames) development with flame growth.

- Development of optics for simultaneous natural (chemiluminescent) light and shadowgraph ciné imaging of flame development, particularly initial flame kernel growth. The shadowgraph technique involved a silver surfaced mirror bonded to the piston crown for back reflection of light and development of a special spark plug to give improved optical access to the plug gap and very early stages of flame initiation and growth.
- The shadowgraph technique yielded better flame definition in the early flame kernel development stages (when chemiluminescent output was low) and gave some insight into flame structure and turbulent flame thickness. Nevertheless, for most of the flame development period, mean flame radii determined from shadowgraph and natural light images proved very similar. This generated confidence in the library of flame progress data collected for LUPOE1-D using natural light photography by a previous worker (Abdi Aghdam, 2003) and in the use of this technique for later pent-roof engine investigations (where the optical access required for shadowgraph/schlieren methods was not available).
- Data on the early flame development period and whole combustion duration have been collected for a wide range of engine conditions (ignition timing $\theta_{ig} = 10^\circ$ bTDC to 31° bTDC), mixture strength ($\phi=0.8$ to $\phi=1.1$), engine speed (750 rpm to 2000 rpm) for residual free iso-octane air mixture at a nominal compression ratio of 7.2:1; these augment ciné laser sheet Mie-scatter flame imaging (Hicks, 1994; Lee, 1995), particle tracking velocimetry flow studies (Cairns, 2001), turbulence measurements (Atashkari, 1997; Jakubik, 2002) and autoignition/knock studies (König and Sheppard, 1990; König, 1993; Pan, 1994; Pan and Sheppard, 1994; Smallbone, 2004), information for the same engine for colleagues modelling the combustion process.
- At each engine condition, sets of data representative of ‘fast’, ‘middle’ and ‘slow’ cycles were systematically selected on the basis of having cycle peak pressure (p_{max}) close to the mean and $\bar{p}_{max} \pm 2\sigma_{p_{max}}$. Attempts to relate the speed of the overall combustion rate of these groups of cycles (as well as

individual cycles within these groups) to turbulence related parameters such as early flame kernel displacement and flame 'shape factor' proved inconclusive.

- A modified ported optical engine fitted with an idealised pent-roof cylinder head representative of the geometry of a modern 4-valve engine, but having almost completed overhead and side view optical access to the clearance volume combustion space, has been designed, built and commissioned. This engine (LUPOE2-P), based on the robust crankcase and connecting rod of a single cylinder Lister-Petter-PH1, was designed with a perforated barrel and annular exhaust gas removal system in an attempt to reduce the effects of exhaust flow on in-cylinder flow and turbulence noted in LUPOE1-D (Cairns, 2001; Cairns and Sheppard, 2000). A perspex barrel/head variant of the engine was also designed, built and commissioned to give complete optical access for LDV, PTV and (in future) PIV study of flow and turbulence under motoring conditions.
- In preliminary experiments, the performance of the LUPOE2-P engine was mapped, over a very wide range of conditions (equivalence ratios $\phi=0.7$ to $\phi=1.1$, skip-firing ratios 5 to 8, engine speeds 750 to 1900 rpm, inlet/head temperatures 50° to 70°C and air mass flow-rates 8.62 and 10.34 g/sec), using an all metal variant of the cylinder head, in order to establish its operating range and optimum ignition advance (for maximum indicated mean effective pressure) at each operating condition prior to the observations of flame development in the less robust optical head variant. An influence of spark plug gap orientation was noted, that yielding maximum peak cylinder pressure at the 'reference condition' ($\phi=1$, 1500 rpm, ignition timing $\theta_{ig} 7^\circ$ bTDC) was adopted in all subsequent experiments.
- Video laser sheet Mie scatter particle tracking velocimetry (PTV) techniques were developed and applied to study the flow in the motored perspex variant of LUPOE2-P. The flow proved complex and intermittent. At the 'reference' engine speed of 1500 rpm, about 75% of the cycles exhibited one general flow pattern; with most other cycles generally showing one other basic flow pattern. At 750 rpm, cycles similarly grouped into 3 basic flow patterns.

- The PTV study was augmented by application of laser Doppler velocimetry (LDV) to determine the ensemble average mean and rms turbulent velocities at selected points within the pent-roof chamber. The mean velocities were generally consistent with those of the dominant flow pattern determined in the PTV experiments. During the crank angle interval corresponding with the combustion period, mean flow velocities were generally small and the rms turbulent velocity proved relatively isotropic and homogeneous.
- A novel natural light ciné imaging system, employing two separate cameras, was set up to film (simultaneously) flame kernel development via both top windows and a side window. Processing methods were developed to produce plan view (parallel to the piston crown) and side elevation images of each flame surface and to determine associated mean flame radius (of a circle encompassing the same area) and flame kernel centroid position.
- A comprehensive library of in-cylinder pressure, mean flame radius and flame kernel trajectory data for a wide range of conditions (equivalence ratios $\phi=0.8$ to $\phi=1.1$, engine speeds 750 to 1900 rpm and inlet/head temperature 55°) has been established for colleagues attempting to model the engine.
- As for the LUPOE1-D case, at each engine condition, sets of representative ‘middle’, ‘fast’, and ‘slow’ cycles were selected on the consistent basis of having p_{\max} close to the mean and $\bar{p}_{\max} \pm 2\sigma_{p_{\max}}$.
- Analysis of successive flame positions for typical ‘middle’, ‘fast’ and ‘slow’ cycles at different conditions suggested no correlation between flame shape and burning rate. All flames were observed to be distorted from circular (spherical); with less distortion encountered at low engine speed (750 rpm) at ignition timing near TDC (2° bTDC) and more distortion seen at high engine speed (1500 rpm) with leaner mixture ($\phi =0.8$) and ignition timing advanced (12° bTDC) to compensate for the slow burning.

- At 1500 rpm (except for the lean mixture), the radii determined from the two views (top and side) for ‘middle’ cycles were reasonably consistent when flames viewed from overhead view were approximately circular. The opposite was true in the case of the ‘fast’ cycles. However, at low engine speed (750 rpm), the flame radii derived from side and overhead views seemed more consistent for the fast and slow cycles than for the middle cycles. These differences in behaviour might be related to the difference in flow patterns observed in the PTV flow investigation and the complex unresolved third dimension flow patterns.
- In general, the centroid migrations from the spark electrode were consistent with the flows observed in the PTV investigation. The average velocity of flame kernel migration was of the same order as the ensemble average measured near TDC using LDV (2mm/ms). There was a suggestion that those cycles experiencing greater flame kernel migration to the right (as viewed in Figure 7.36(b), for example) exhibited faster flame radius development; whereas no preferred direction was observed for middle and slow cycles.
- The maximum flame speeds noted for the LUPOE2-P engine proved higher and the cyclic variation lower, than those obtained for the LUPOE1-D engine (used also in the current study) by Abdi Aghdam (2003).

8.2 Concluding Discussion

8.2.1 In-cylinder Flow and Turbulence

Previous work (Cairns, 2001) had shown that even in the nominally quiescent disc shaped chamber (LUPOE1-D), where the ensemble average LDV experiments suggested near zero mean flow and approximately isotropic turbulence (Atashkari, 1997), there was a degree of intermittency with a number of flow patterns. This was even more marked in the pent-roof (LUPOE2-P) chamber, where the PTV data gathered in the motored ‘perspex’ engine showed a number of alternate distinct flow patterns – which varied with engine speed. Similar effects have been noted in recent PIV investigations showing cyclic variability of undirected (i.e. no axial swirl) flows in a

poppet – valve four stroke engine (Reuss, 2000) and an optically accessed single cylinder variant of a modern Jaguar pent-roof production engine, (Jarvis et al., 2005; Jarvis et al., 2006)

The intermittency was masked in the current LUPOE2-P LDV data, due to the ensemble averaging process implicit in the technique – where velocity data at a point in the combustion chamber during a crank angle interval (or ‘window’) has to be collected over many cycles in order to generate statistically relevant data (Heywood, 1988). The inherent cyclic variation hence leads to overestimates of the true rms turbulent velocity influencing a growing flame in an individual cycle – whilst possibly under – estimating the mean local velocity which might bodily transport the kernel in a particular cycle. To avoid such contamination of LDV data, some workers have therefore attempted cycle by cycle analysis, where the mean and rms velocities have been calculated for each engine cycle; achieved by employing a high data sampling rate (Liou and Santavicca, 1985; Corcione and Valentino, 1994). Other investigations have employed conditional sampling techniques (Libby et al., 1982; Swords et al., 1982; Witze and Martin, 1986; Plee et al., 1987), where similar engine cycles have been experimentally identified and then ensemble-averaged (Witze et al., 1984). This technique may be subject to a degree of arbitrariness, dependent upon on the selection of the conditioning parameters.

However, in the currently reported study, in common with most other engine flow studies available in the literature under motoring (Arcoumanis et al., 1994; Kang and Baek, 1998) and firing conditions (Hall, 1987; Miles et al., 1994) conditions, only ‘normal’ ensemble averaged data were generated. Nevertheless, clear similarity in trends and values of rms turbulent velocity noted for all directions at all measurement positions was encouraging. If true, this would prove a useful finding, allowing considerable simplification in combustion modelling. Shown in Figures 8.1 (a) and (b) are the rms velocity variations with c.a. for the directions recorded at the various measurement positions at the two principal engine speeds used (750 and 1500 rpm). It can be seen that the peak rms values at 1500 rpm were earlier (around TDC) than those at 750 rpm. However, the same trends were exhibited at both speeds (750 and 1500 rpm); with rms velocity increasing after port closure and through the compression stroke, then decreasing before TDC all the way through the expansion stroke.

Set out in Figure 8.2 (a), for both the current LUPOE2-P and earlier (Jakubik, 2002) LUPOE1-D experiments, are values of rms velocities at TDC plotted against mean piston speed, where the engine speed has been converted to mean piston speed (\bar{S}_p), using the relationship (Heywood, 1988):

$$\bar{S}_p = \frac{N}{60} \cdot \frac{2L}{1000} \quad (8.1)$$

where N is the engine speed in rpm and the stroke (L) for the LUPOE2-P engine was 110 mm. The data suggest that the in-cylinder turbulence in LUPOE2-P was somewhat higher than that in LUPOE1-D at all mean piston speeds tested. At 1500 rpm, u'/\bar{S}_p was in the range 0.6-0.9 for the pent-roof engine compared to 0.5-0.6 for the disc. Relative turbulence intensities have been reported to reach values as high as 1.0-1.2 times the mean piston speed (Arcoumanis et al., 1994; Gosman, 1986). It appears that the stronger the tumbling motion, the greater the turbulent kinetic energy release during its breakdown and the later this release in compression (Arcoumanis et al., 1990).

In the current study, a good fit to the pent roof rms turbulent velocity (all positions, all directions) (Figure 8.2 (b)), was obtained by the least squares method:

$$u' = 1.7 + 0.44\bar{S}_p \quad (8.2)$$

Compared in Figure 8.3 are the current and earlier Leeds data for rms turbulent velocity versus mean piston speed with some of those reported in the literature (for conditions listed in Table 8.1 (Hattrell, 2006)). Although the trends (disc versus pent-roof, experimental and CFD) are qualitatively the same – considerable variation is evident for the engines listed.

	Port/Valve	Measurement Location	Compression Ratio	Chamber Geometry	Chamber Flow	Note
LUPOE2-P LDV	Port	Chamber mean	9.2	Pent	Tumble	Ensemble averaged u' used, chamber mean calculated by taking average of all measuring points
LUPOE1-D LDV	Port	Centre of the chamber	7.6	Disc	Quiescent	Ensemble averaged u' used
LUPOE1-D CFD	Port	Chamber mean	7.6	Disc	Quiescent	Chamber mean from k-epsilon model used
VWOE CFD	Valve	Chamber mean		Pent	Tumble	u' determined from k-epsilon model as $\sqrt{2/3k}$
Corcione & Valentino	Valve	Inside bowl, close to edge	21	Flat head, piston with bowl	Squish	Both ensemble averaged u' and u' with attempt to filter out bulk velocity fluctuations presented. Ensemble averaged results used here
Hall & Bracco	Port	$r = 0.77 \times bore$	7.5	Disc	Swirl	Arbitrary cut-off frequency used to separate u' from bulk motion
Kang & Baek	Valve	Centre of bore	8.5	Pent	High tumble or normal	Cut-off frequency as suggested by Catania and Mittica used to separate u' from bulk motion variations
Hong & Tarng		Not specified	4	Disc		Measurements giving both ensemble averaged u' and cycle resolved u' with bulk velocity fluctuations filtered out

Table 8.1 Specification of engines used in the literature reported by various researchers, see also Figure 8.3 (Hattrell, 2006). (continued overleaf)

	Port/Valve	Measurement Location	Compression Ratio	Chamber Geometry	Chamber Flow	Note
Kim et al.	Valve	Mean along bore axis	9.2	Pent	Tumble	Paper not specific, text suggests that averaged u' used
Arcoumanis et al.	Valve	Mean along bore axis	10.5	Pent	Tumble	No cut-off frequency used. Data for non-sleeved valves used. Difficult to estimate accurately given the quality of the graphs in the paper
Johansson & Olsson	Valve	Spark gap location (centre)	12	Not stated (probably pent)		Arbitrary cut-off frequency used. Only results for flat piston used. Other pistons show very different levels of turbulence.
Liu et al.	Valve	Centre of combustion chamber	7.4	Wedge	Swirl	Only motoring data used
Nordgren et al.	Valve	8 mm below head	12	Not stated (probably disc)	Swirl	Motoring data from truck engine, u' is chamber average determined by PIV
Lee & Lee	Valve	PIV average from centre of bore	10.4	Pent	Depends on valve used	PIV motoring data with three different valves: normal, tumble and swirl

(continued)

8.2.2 Effect of Flow and Turbulence on Combustion

Differences in mixture strength (Petrovic, 1982; Swords et al., 1982; Tagalian and Heywood, 1986), residual gas concentration, temperature and spark plug earth electrode orientation (Burgett et al., 1972; Pischinger and Heywood, 1990; Aleiferis, 2000) have all been proposed as sources of cyclic variation in engine combustion rate. However, even though the experimental methods adopted in the currently reported study (LUPOE1-D engine) eliminated variation in all these parameters with approximately mean zero flow, cyclic variation of a similar order to that experienced in production engines (Wu, 2006) still occurred. It is considered that this can only be due to cyclic variation in turbulence at ignition and during subsequent flame propagation. Nevertheless, attempts to relate the speed of the overall combustion rate of individual cycles (designated fast, middle or slow) to turbulence-related parameters such as early flame kernel displacement and Shape Factor (thought to characterise the particular turbulent eddies affecting the ignition kernel in individual cycles early in its development) proved inconclusive. This may be related to flame development in the third unresolved dimension, to the unmeasured energy contained in small-scale structures local to the ignition/early flame development, or to the importance of scales of turbulence smaller than could be investigated using the available techniques.

In general, kernel convection for slow cycles seemed to exhibit relatively little movement to the left and right (as seen from the side view) and tended to stay closer to the 'roof' of the chamber of LUPOE2-P engine, with corresponding loss of effective flame surface area. Moreover, there is a suggestion that most cycles experiencing greater flame kernel migration to the right of the chamber (as seen from the side view, e.g. Figure 7.36(b)) exhibited faster flame radius development. This was also supported by the findings of other researchers (Herweg et al., 1990; Hacoheh et al. 1992; Pajot et al., 2000). They found that faster flames were observed far from the electrodes. However, other researches (Witze et al., 1981) showed opposite results. Moreover, Holmstrom and Denbratt (1996) showed that random movement of the flame kernel has a significant effect on the cyclic variation. These differences in observations might be related to the changes in the flow around the electrodes (Herweg et al., 1988; Pischinger and Heywood, 1990), or the effect of rms turbulent burning velocities at early flame propagation (Loye and Bracco, 1987). Both effects (functions of mean and rms

velocities) would have been masked to a certain extent in analysis of the current LUPOE2-P LDV data, due to the ensemble averaging process implicit in the LDV technique.

For the LUPOE2-P engine, as speed increased from 750 rpm to 1500 rpm, the flame became more wrinkled and distorted. Loye and Bracco (1987) showed that as engine speed increased, the shape, size and location of the initial kernel became less repeatable, and that the kernel flame front became more convoluted. Some kernels had a fairly continuous flame front, while others had a much more discontinuous appearance.

In preliminary study, using the metal variant of the LUPOE2-P engine, three spark orientations were chosen. The orientation yielding maximum peak cylinder pressure at the 'reference condition' ($\phi=1$, 1500 rpm, ignition timing θ_{ig} 7° bTDC) was adopted in all subsequent experiments. Other researchers (Burgett et al., 1972; Pischinger and Heywood, 1990; Aleiferis, 2000) have also shown spark plug ground electrode orientation to affect engine performance. This might be attributed to changes in the flow field in the vicinity of the spark plug electrodes, electrical spark energy loss to the electrodes and heat transfer between the flame kernel and the electrodes. The results of Aleiferis (2000) showed similar spark orientation effects to those noted in the current LUPOE2-P experiments.

The reduced cyclic variation in the LUPOE2-P engine vis à vis the LUPOE1-D engine might be related to the reduction in combustion duration associated with the increased turbulent burning velocity accompanying the higher rms turbulent velocity with increased tumble flow. These findings were in accord with other researchers (Hu et al., 1992; Li et al., 2004). However, yet other researchers showed opposite results. This might be related to the design of the inlets, pent-roof and piston geometries (Kuwahara et al., 1994), which affect the tumble strength and hence the cyclic variation. Arcoumanis et al. (1994) using a single cylinder four-valve, pent-roof chamber engine of compression ratio of 10.5) confirmed the correlation between stronger tumble during induction and higher convective velocity and turbulence levels near the spark gap at the time of ignition; this resulted in faster combustion rates and more stable combustion under lean mixture conditions.

8.2.3 Modelling Database

In order to reduce development lead times and expensive testing, motor manufacturers are increasingly relying on computer modelling of engines – to the extent of developing ‘virtual’ powertrains and even complete vehicles (Eluga, 1993; Richardson, 1997). There are many important aspects to such models, including intake/exhaust tuning (Chow and Wyszynski, 1999), fuel injection (port and direct) and evaporation (Anderson et al., 1996; Wallesten et al., 2002; Wyszynski et al., 2002), charge mixing (Bo et al., 1997; Dec, 1997), turbocharging (Han et al., 1997), autoignition and knock (Chun, et al., 1988; Cowart, et al., 1990; Zheng, et al., 2002) etc.

One of the most intractable problems in engine modelling remains that of the flame propagation and pressure development in the spark ignition engine. In many cases, for study of engines which exist (or are of proposed design similar to available engines), the problems can be met reasonably well using relatively simple 1-D thermodynamic cycle models employing ‘Wiebe’ (or similar) empirical expressions for determining the combustion rate in idealised ‘two-zone’ (burned and unburned) combustion space – with the functions empirical constants adjusted to match experimentally available in-cylinder pressure data for a range of conditions (Krieger and Borman, 1966; Guezennec and Hamama, 1999). However, as suggested, such models are only applicable for interpolating or mildly extrapolating knowledge from pre-existing experimental data – they can not properly accommodate radical changes in engine chamber geometry, ignition site (or multiple sites), running conditions (e.g. high EGR) or fuel type. Some success in coping with such requirements has been claimed for more complex ‘quasi-dimensional’ two or three zone thermodynamic cycle models employing turbulent burning velocity expressions coupled to assumptions on flame and combustor wall surface areas – usually making truncated ‘spherical’ flame surface approximations (Liu, 2004) and sometimes allowing flame kernel centre movement in response to in-cylinder flow (Keck et al., 1987) with flame to wall approach and heat transfer expressions of varying complexity (Annand, 1963; Woschni, 1967; Morel et al., 1985). However, such models often lack generality and often ‘fitted’ to rather sparse experimental data – they also rarely take into account the cyclic variation evident in many experimental studies, including the current work.

Others have advanced 3-D CFD codes to meet engine modelling requirements (Sazhina et al., 1999; Lee, et al., 2000; Nishiwaki, et al., 2000). The current 'state of the art' in such modelling usually employ RANS (Reynolds Averaged Navier Stokes) formulations, which by their nature are incapable of correctly representing cyclic variation and have often been shown to be deficient in flows of having strong recirculation features. Such CFD models can often prove useful in aiding flow visualisation, although tuning to match experimental data is sometimes necessary and portability to very different combustion chambers with fixed model constants is debateable. The combustion modelling in such CFD codes is generally less reliable than flow prediction and requires the greater part of the computational time. Large eddy scale (LES) CFD codes are being developed to address cyclic variation and flow modelling deficiencies and possible represent the best long term solution for simulation of complex engines. Nevertheless, although such models may be useful for research into specific features of engine flow and combustion, it is generally recognised that they are currently too computer intensive for routine engine development work.

If computer models (advanced quasi-dimensional or CFD) are to be improved, it is essential that reliable experimental data are available for their development and validation. Many experiments have been conducted on optical engines of various designs (Whitelaw and Xu, 1993; Jarvis et al., 2005) as well as more real production engines modified to give varying levels of restricted access for instrumentation (Hentschel et al., 2001; Kim et al., 2002; Wu, 2006).

The Leeds LUPOE1-D (disc) and LUPOE2-P (idealised pent-roof) flame propagation and in-cylinder pressure development database over wide ranging conditions (to which the current study has contributed a lot) represents possibly the most consistent and comprehensive information available for validation of the combustion phase of spark ignition burning under simple well defined conditions; this is considered an essential step if a model's predictive capacity for more complex but less well defined situations is to be accepted as more than fortuitous. The findings (for the current engines) that the rms turbulent velocity is relatively isotropic, that flames remain approximately 'spherical', that mean flow velocities are such that flame kernels are bodily transported relatively little during the available combustion period and the consistent definition of 'fast', 'middle' and 'slow' cycles for residual free homogenous fuel-air mixtures are

useful features for step by step model development (before application to more complex flows).

The validity of ported engine data for validation of modelling of poppet-valved production engines has sometimes been questioned. Clearly the engine breathing (e.g. volumetric efficiency) flow and turbulence generation processes will be different. However it is argued that once the ports/valves are closed, the combustion process will be governed by the same laws of physics and chemistry in both ported and valved engines and that models incapable of modelling combustion in the current engines (LUPOE1-D and LUPOE2-P) must also be deficient for poppet-valve engines. The problem becomes that of defining the parameters (e.g. u' , L) controlling the burn rate in thermodynamic cycle modelling and defining the 'boundary conditions' for CFD modelling. The latter involves modelling the flow into the ported engine, currently being undertaken using Ricardo's VECTIS CFD code at Volkswagen (GET-CO2 final report, 2005), or comprehensively defining the in-cylinder flow and turbulence at port closure via experiment.

8.3 Recommendations for Future Work

Disc Chamber

The database for the current LUPOE1-D engine build, with radially opposed intake ducts to create essentially quiescent (turbulent but no mean flow) conditions during the combustion period, is considered essentially complete. However, it would be useful to build a disc version of LUPOE2-P in order to see whether the 'colander' exhaust arrangement reduces the intermittent cyclic variation in flow pattern noted by Cairns (2001) and so cyclic variation in flame development. Such a version might also enable extension of the database to higher nominal compression ratio. Similarly, it would be useful to explore higher engine speed (i.e. above 2000 rpm) – although this would require a different dynamometer and checks on the maximum speed safely attainable with the engine crankcases/crankshafts/connecting rods/pistons currently available.

It might also be worth bringing the prior database for the axial versions of LUPOE1-D, with tangentially oriented intakes (Lee, 1995; Atashkari, 1997; Gillespie, 1998; Cairns, 2001), to the level attained for the quiescent case. Similarly, examination of alternative spark plug locations might provide useful additional model validation data (by changing the relationship between flame radius and flame/wall wetted surface areas), as well as allow systematic investigation of the effects of the spark gap orientation noted in the current pent-roof preliminary experiments and in the work of others (Burgett et al., 1972; Pischinger and Heywood, 1990; Aleiferis, 2000).

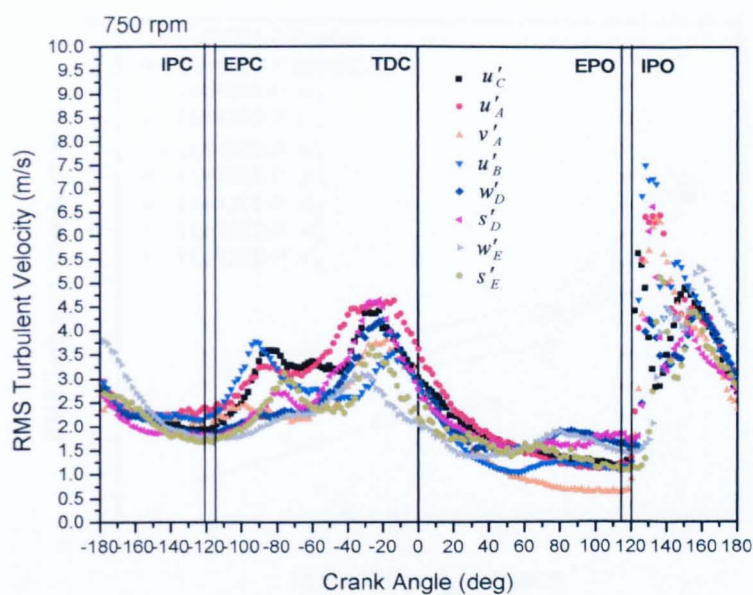
Pent-Roof Chamber

Although the geometry of the LUPOE2-P idealised pent-roof chamber was simple, the flow within the chamber proved complex. The 2-D PTV experiments gave a good insight into the general features of the flow for the central plane; however, the basically uni-directional flow suggested at some conditions requires reverse direction flow in other planes (in order to satisfy continuity) which could not always be confirmed by the LDV measurements. This might have been associated with the ensemble average nature of the LDV measurements or possibly, by strong circumferential flows close to the cylinder walls, where measurement was impossible. Further investigation (PIV, LDV possibly involving conditional sampling and/or PTV), is necessary to define properly the flow in the LUPOE2-P engine.

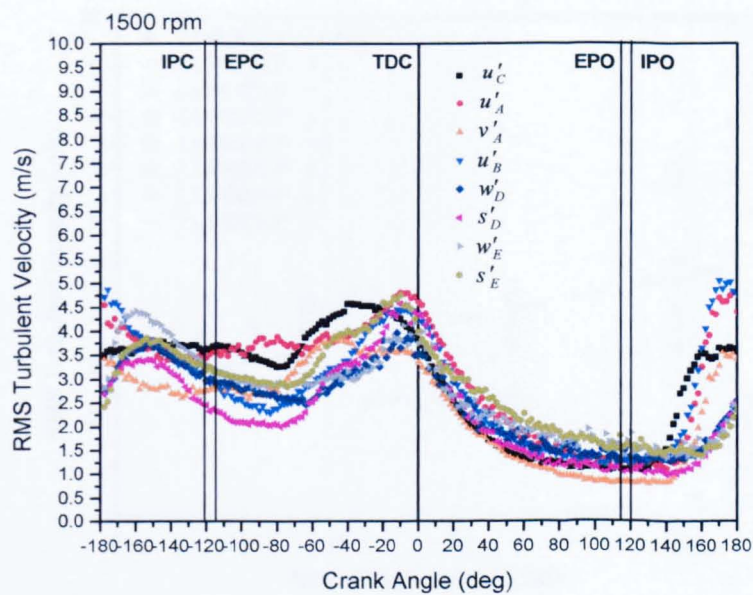
As well as better defining the conditions in the current build of LUPOE2-P, in order to obtain maximum benefit of the data collected to date, it would be useful to explore the effects on intake/exhaust geometry and flow rates in an attempt to establish the more regular flow patterns initially expected for this idealised pent-roof design.

In the current study, investigation of the in-cylinder flow and turbulence was concentrated on those pertaining during the combustion period. To assist CFD validation, it would be beneficial to define fully the in-cylinder conditions at port closure. This would provide appropriate boundary conditions for CFD modelling; this might possibly avoid the need to encompass modelling of intake and (closing) port flows, associated with the need to extend the CFD domain to include these to establish a reliable model boundary condition (GET-CO2 final report).

In order to provide a well defined 'baseline' condition for modelling development/validation, the current study adopted residual free running on pure iso-octane reference fuel. The database should be extended to encompass controlled levels of simulated residual gas (adopting the system developed by Smallbone (2004), involving skip-fired operation with metered quantities of residual gases into the intake charge) and primary reference fuels (iso-octane/n-heptane mixtures) as well as commercially available gasolines and surrogates (well defined mixtures of pure hydrocarbons representative of the major alkane/aromatics etc. constituently of real gasolines). Similarly, it would be sensible to conduct experiments in the Leeds bombs (Bradley et al., 1998) to establish laminar burning velocity data to be used in models applied to the suggested new engine data.

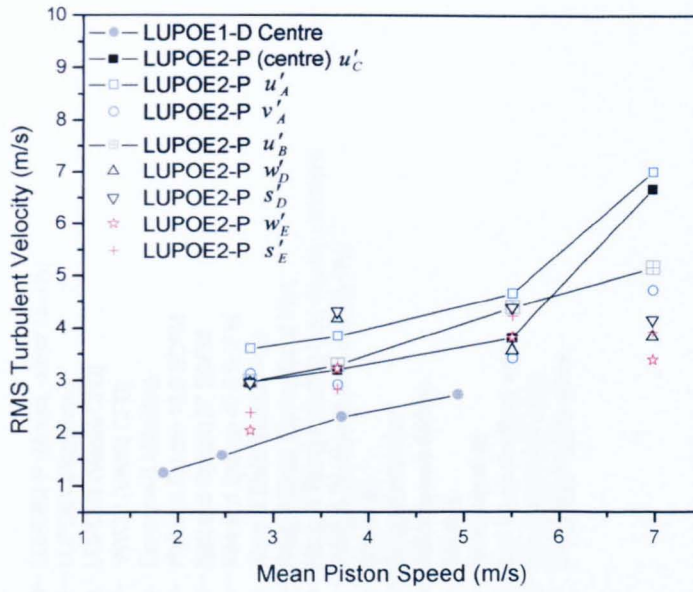


(a)

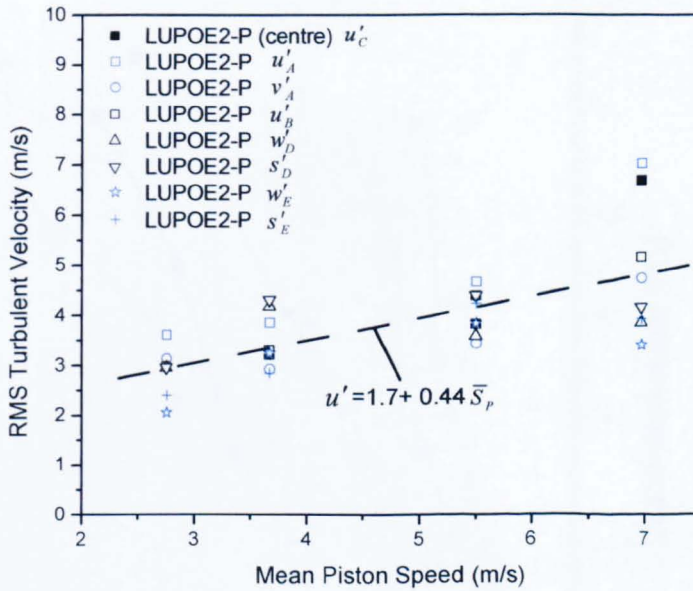


(b)

Figure 8.1 LDV-derived RMS turbulent velocities versus crank angle for all positions and directions at (a) 750 rpm, (b) 1500 rpm.



(a)



(b)

Figure 8.2 LDV-derived RMS turbulent velocities at TDC versus mean piston speeds for, (a) LUPOE1-D (in the centre) and LUPOE2-P (at different positions through the chamber), (b) line fitted through the measured points at TDC for LUPOE2-P with equation of the line.

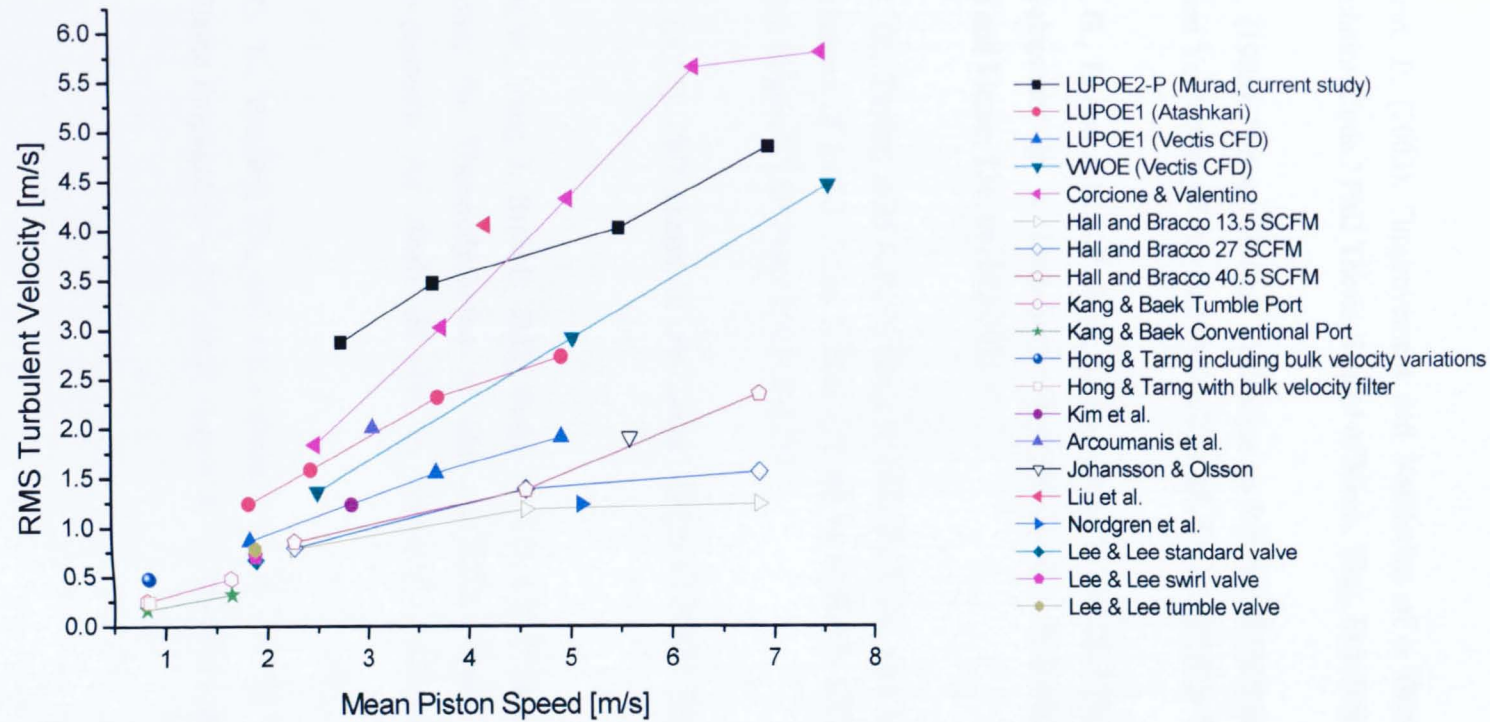


Figure 8.3 Variation of rms turbulent velocity at TDC with mean piston speed reported by various researchers, see also Table 8.1 (Hattrell, 2006).

References

- Abdel-Gayed, R. G., Bradley, D., and Lawes, M. (1987). "Turbulent Burning Velocities: A General Correlation in Terms of Straining Rates." *Proc. R. Soc. Lond.*, A414, pp. 389-413.
- Abdi Aghdam, E. (2003). "Improvement and Validation of a Thermodynamic S.I. Engine Simulation Code." PhD Thesis, School of Mech. Eng., University of Leeds.
- Adrian, R.J. (1986). "Image Shifting Technique to Resolve Directional Ambiguity in Double-Pulsed Velocimetry." *Applied Optics* Vol. 25, No.21, pp3855-3858.
- Aleiferis, P. G., Taylor, A.M.K.P., Ishii, K., and Urata, Y. (2004). "The Nature of Early Flame Development in a Lean-Burn Stratified-Charge Spark-Ignition Engine." *Combustion and Flame*, 136, pp. 283-302.
- Aleiferis, P. G., Taylor, A.M.K.P., Whitelaw, J.H., Ishii, K., and Urata, Y. (2000). "Cyclic Variations of Initial Flame Kernel Growth in a Honda VTEC-E Lean-Burn Spark-Ignition Engine." SAE Paper 2000-01-1207.
- Alrefae, W. (2005). PhD Thesis, in preparation, Dept. of Mech. Eng., University of Leeds.
- Anderson, R.W., Yang, J., Brehob, D.D., Vallance, J.K. and Whiteaker, R.M. (1996). "Understanding the Thermodynamics of Direct Injection Spark Ignition (DISI) Combustion Systems: An Analytical and Experimental Investigation." SAE Paper 962018.
- Andrews, G. E., Bradley, D., and Lwakabamba, S. B. (1975). "Turbulence and Turbulent Flame Propagation - A Critical Appraisal." *Combustion and Flame*, 24, pp. 285-304.

Annand, W. J. D. (1963). "Heat Transfer in the Cylinder of Reciprocating Internal Combustion Engines." Proc. Instn. Mech. Engrs Vol.177, 36, pp. 973-990.

Arcoumanis, C., Bae, C.S., and Hu, Z. (1994). "Flow and Combustion in a Four-Valve, Spark-Ignition Optical Engine." SAE Paper 940475.

Arcoumanis, C., Enotiadis, A.C., and Whitelaw, J.H. (1991). "Frequency Analysis of Tumble and Swirl in Motored Engines." I. Mech. E.

Arcoumanis, C., Hu, Z., Vafidis, C., and Whitelaw, J.H. (1990). "Tumbling Motion: A Mechanism for Turbulence Enhancement in Spark-Ignition Engines." SAE Paper 900060.

Atashkari, K. (1997). "Experimental Study of Flow and Turbulence in a V-Flame Burner and a S.I. Engine." PhD Thesis, Dept. of Mech. Eng., University of Leeds.

Baby, X., Dupont, A., Ahmed, A., Desiandes, W., Charnay, G., and Michard, M. (2002). "A New Methodology to Analyze Cycle-to-Cycle Aerodynamic Variations." SAE Paper 2002-01-2837.

Bade Shrestha, S. O., and Karim, G. A. (2001). "Considering the Effects of Cyclic Variations when Modeling the Performance of a Spark Ignition Engine." SAE Paper 2001-01-3600.

Bo, T., Clerides, A.D., Theodossopoulos, P. (1997). "Prediction of The Flow and Spray Processes in An Automobile DI Diesel engine." SAE Paper 970882.

Bopp, S., Vafidis, C., and Whitelaw, J.H. (1986). "The Effect of Engine Speed on the TDC Flow-Field in a Motored Reciprocating Engine." SAE Paper 860023.

Bradley, D., Haq, M.Z., Hicks, R.A., Kitagawa, T., Laws, M., Sheppard, C.G.W., and Woolley, R. (2003). "Turbulent Burning Velocity, Burned Gas Distribution, and Associated Flame Surface Definition." Combustion and Flame, 113, pp. 415-430.

- Bradley, D., Hynes, J., Laws, M., and Sheppard, C.G.W. (1988). "Limitations to Turbulent Enhanced Burning Rates in Lean Burn Engines." Mech. Eng. Paper C46/88.
- Bradley, D., Lau, A.K.C., and Laws, M. (1992). "Flame Stretch Rate as a Determinant of Turbulent Burning Velocity." Phil. Trans.R.Soc., London, A338, pp. 359-387.
- Brunt, M. F. J., and Emtage, A.L. (1996). "Evaluation of IMEP Routines and Analysis Errors." SAE Paper 96069.
- Brunt, M. F. J., and Pond, C.R. (1997). "Evaluation of Techniques for Absolute Cylinder Pressure Correction." SAE Paper 970036.
- Buran, D. (1998). "Turbulent Flame Propagation in a Methane-Fuelled Spark-Ignition Engine." PhD Thesis, School of Mech. Eng., University of Leeds.
- Burgett, R. R., Leptich, J. M., and Sangwan, V. S. (1972). "Measuring the Effects of Spark Plug and Ignition System Design on Engine Performance." SAE Paper 720007.
- Cairns, A. and Sheppard, C.G.W. (2000). "Cyclically Resolved Flame and Flow Imaging in a Spark Ignition Engine." SAE Paper 2000-01-2832.
- Cairns, A. (2001). "Turbulent Flame Development in a Spark Ignition Engine." PhD Thesis, School of Mech. Eng., University of Leeds.
- Calendini, P. O., Duverger, T., Lecerf, A., and Trinite, M. (2000). "In-Cylinder Velocity Measurements with Stereoscopic Particle Image Velocimetry in a SI engine." SAE Paper 2000-01-1798.
- Chapman, J., Garrett, M.W., and Warburton, A. (1991). "A New Standard for Barrel Swirl Movement." IMechE Paper C427/18/156.
- Chow, A. and Wyszynski, M.L. (1999). "Thermodynamic modelling of complete engine systems – a review. " Proc. Instn Mech Engrs, Vol. 213, Part D.

- Chun, K. M., Heywood, J. B. and Keck, J. C. (1988). "Prediction of Knock Occurance in a Spark-Ignition Engine." 22nd Symposium (International) on Combustion/ The Combustion Institute pp455-463.
- C. Wu. (2006). "Flow Field and Combustion Studies Relating to Downsized Spark Ignition Engines." PhD Thesis (in progress), School of Mech. Eng., University of Leeds.
- Corcione, F.E. and Valentino, G. (1994). "Analysis of In-Cylinder Turbulent Air Motion Dependence on Engine Speed." SAE Paper No. 940284.
- Cowart, J.S., Keck, J.C, Heywood, J.B., Westbrook, C.K. and Pitz, W.J. (1990). "Engine Knock Predictions using a Fully-Detailed and Reduced Chemical Kinetic Mechanism." 23rd Symposium (International) on Combustion/The Combustion Institute pp1055-1062.
- Dec, John E. (1997). "A conceptual Model of DI Diesel Combustion Based on laser-Sheet Imaging." SAE Paper 970873.
- Douglas, R., Kee, R.J., and Carberry, B.P. (1997). "Analysis of In-cylinder Pressure Data in Two-Stroke Engines." SAE Paper 972792.
- Drain, L. E. (1980). "The Laser Doppler Technique." John Wiley & Sons.
- Durst, F., Melling, A., and Whitelaw, J.H. (1976). "Principles and Practice of Laser-Doppler Anemometry." Academic Press INC. (London) LTD.
- Eluga, Eric C. (1993). "Modeling of The Complete Vehicle Powertrain Using Enterprise." SAE Paper 931179.
- Eric, R., Michel, T., Frederic, D., Alain, F., and Afif, A. (1997). "Particle Image Velocimetry Measurements in a High Tumble Engine for In-Cylinder Flow Structure Analysis." SAE 972831.

Fansler, T.D. and French, D. (1988). "Cycle-Resolved Laser Velocimetry Measurements in a Reentrant-Bowl-in-Piston Engine." SAE Paper 880377.

Fraser, R. A., Felton, P.G., Bracco, F.V, and Santavicca, D.A. (1986). "Preliminary Turbulent Length Scale Measurements in a Motored Internal Combustion Engine." SAE Paper 860021.

Fujimoto, M., Iwai, K., Kataoka, M., and Tabata, M. (2002). "Effect of Combustion Chamber Shape on Tumble Flow, Squish-Generated Flow and Burn Rate." JSAE Review 23, pp. 291-296.

Gatowski, J. A., Heywood, J.A., and Deleplace, C. (1984). "Flame Photographs in a Spark-Ignition Engine." Combustion and Flame, 56:71.

GET-CO2, "Gasoline Engine Turbo-charging: Advanced Gasoline Powertrain for reduced consumption and CO2 emissions," CEC Contract G3RT-CT-2000-0034, Project CRD1-2000-25618, Final report, February, 2005.

GET-Drive, "Drivability development of downsized, highly turbocharged gasoline engines," CEC Contract G3RD-CT-2002-00789, Project GRD2-2001-51803, Final report, February, 2005.

GET-Engine "Gasoline Engine Turbo-charging: Advanced Engine Cycle Development," CEC Contact G3RD-CT-2000-00373, Project GRD1-2000-25730, Final Report, February, 2003.

Ghandhi, J. B., and Martin, J.K. (1992). "Velocity Field Characteristics in Motored Two-Stroke Ported Engines." SAE Paper 920419.

Gillespie, L. (1998). "Imaging and Analysis of Turbulent Flame Development in Spark Ignition Engines." PhD Thesis, School of Mech. Eng., University of Leeds.

- Gillespie, L., Lawes, M., Sheppard, C.G.W., and Woolley, R. (2000). "Aspects of Laminar and Turbulent Burning Velocity Relevant to SI Engines." SAE Paper 2000-01-0192.
- Glover, A. R. (1986). "Towards Bias-Free Estimates of Turbulence in Engines." 3rd Int. symp. On Applications of Laser Anemometry to Fluid Mechanics, Lisbon.
- Glover, A. R., Hundleby, G.E., and Hadded, O. (1988). "An Investigation into Turbulence in Engines using Scanning LDA." SAE Paper 880378.
- Gosman, A. D. (1986). "Flow Processes in Cylinders, in The Thermodynamics and Gas Dynamics of Internal Combustion Engines." Volume II, (Eds. J. H. Horlock and D. E. Winterbone), Clarendon Press, Oxford.
- Gosman, A. D., Tsui, Y.Y., and Vafidis, C. (1985). "Flow in a Model Engine with a Shrouded Valve. A Combined Experimental and Computational Study." SAE Paper 850498.
- Guezennec, Y.G. and Hamama, W. (1999). "Two Heat Release Analysis of Combustion Data and Calibration of Heat Transfer Correlation in an I.C. Engine." SAE Paper 1999-01-0218.
- Hacohen, J., Belmont, M.R., Thurley, R.W.F., Thomas, J.C., Morris, E.L., and Buckingham, D.J. (1992). "Experimental and Theoretical Analysis of Flame Development and Misfire Phenomena in a Spark-Ignition Engine." SAE Paper 920415.
- Halderman, J. D., Mitchell, C.D., Marchant, J., and Davey, R. (2005). "Automotive Technology Principles, Diagnosis, and Service." Prentice Hall, Inc., Upper Saddle River, New Jersey.
- Hall, M. J. (1989). "The Influence of Fluid Motion on Flame Kernel Development and Cyclic Variation in Spark Ignition Engine." SAE Paper 890991.

- Hall, M. J., and Bracco, F.V. (1987). "A Study of Velocities and Turbulence Intensities Measured in Firing and Motored Engines." SAE Paper 870453.
- Hamamoto, Y., Tomita, E., Tanaka, Y., Katayama, T., and Tamura, Y. (1987). "The Effect of swirl on Spark-Ignition Engine Combustion." JSME, Vol.30, No.270.
- Han, S. B., Lee, N. H., Lee, S. (1997). "Analysis of Thermal Loading in a Turbocharged gasoline Engine." SAE Paper 970205.
- Hattrell, T. (2006). PhD Thesis, in preparation, Dept. of Mech. Eng., University of Leeds.
- Hentschel, W., Block, B., Hovestadt, T., Meyer, H., Ohmstede, G., Richter, V., Stiebels, B. and Winkler, A. (2001). "Optical Diagnostics and CFD-Simulations to Support the Combustion Process Development of the Volkswagen FSI Direct-Injection Gasoline Engine." SAE-Paper 2001-01-3648.
- Herron, D. (2001). "Flow Visualisation Experiments in a Single Cylinder Spark Ignition Engine." MECH 4810 Professional Project (Level 4).
- Herweg, R., and Ziegler, G. F. W. (1990). "Flame Kernel Formation in a Spark-Ignition Engine." Proceedings International Symposium COMODIA 90, pp. 173-178.
- Herweg, R., Begleris, Ph., Zettlitz, A., and Ziegler, G.F. W. (1988). "Flow Field Effects on Flame Kernel Formation in a Spark-Ignition Engine." SAE Paper 881639.
- Heywood, J. B. (1988). "Internal Combustion Engine Fundamentals.", McGraw-Hill.
- Hicks, R. A. (1994). "Turbulent Flame Structure and Autoignition in Spark Ignition Engines." PhD Thesis, Dept. of Mech. Eng., University of Leeds.
- Higuma, A., Suzuki, T., Yoshida, M., and Oguri, Y. (1999). "Improvement of Error in Piezoelectric Pressure Transducer." SAE Paper 1999-01-0207.

- Hill, P. G., and Zhang, D. (1994). "The Effects of Swirl and Tumble on Combustion in Spark Ignition Engines." *Prog. Energy and Comb. Science*, 20, pp. 373-429.
- Holmstrom, K., and Denbratt, I. (1996). "Cyclic Variation in an SI Engine Due to the Random Motion of the Flame Kernel." SAE Paper 961152.
- Hu, Z., Whitelaw, J.H., and Vafidis, C. (1992). "Flame Propagation Studies in a Four-Valve Pentroof-Chamber Spark Ignition Engine." SAE Paper 922321.
- Hynes, J. (1986). "Turbulent Effects on Combustion in Spark Ignition Engines." PhD Thesis, Dept. of Mech. Eng., University of Leeds.
- Jakubik, T. (2002). "Engine LDV Technique, Progress Report." Dept. of Mech. Eng., University of Leeds.
- Jarvis, S., Justham, T., Clarke, A., Garner, C.P., Hargrave, G.K. and Halliwell, N.A. (2005) "Time Resolved Digital PIV Measurements of Flow Field Cyclic Variation in an Optical IC Engine." Proceedings of the Second International Conference on Optical and Laser Diagnostics (ICOLAD 2005), City University, London, UK, September 2005, pp 19-26.
- Jarvis, S., Justham, T., Clarke, A., Garner, C.P., Hargrave, G.K. and Richardson, D. (2006) "Motored SI IC Engine In-Cylinder Flow Field Measurement Using Time Resolved Digital PIV for Characterisation of Cyclic Variation." SAE Paper No 2006-01-1044.
- Jeonghoon, S., and Myoungho S. (2000). "A Modeling and Experimental Study of Initial Flame Kernel Development and Propagation in SI Engines." SAE Paper 2000-01-0960.
- Kang, K. Y., and Baek, J.H. (1996). "Tumble Flow and Turbulence Characteristics in a Small Four-Valve Engine." SAE Paper 960265.

- Kang, K. Y., and Baek, J.H. (1998). "Turbulence Characteristics of Tumble Flow in a Four-Valve Engine." *Experimental Thermal and Fluid Science*, Vol. 18, pp. 231-243.
- Keck, J.C., Heywood, J.B. and Noske, G. (1987). "Early Flame Development and Burning Rates in Spark Ignition Engines and Their Cyclic Variability." SAE paper 870164.
- Kent, J. C., and Trigul, N. (1994). "Characterization of Intake Generated Fluid Flow Field in IC Engines Using 3-D Particle Tracking Velocimetry (3-D PTV)." SAE Paper 940279.
- Kim, B., Kaneko, M., Mitani, M., Ikeda, Y. and Nakajima, T. (2002). "In-cylinder Turbulence Measurements with a Spark Plug-in Fibre LDV." 11th Internal Symposium, Application of Laser Techniques to Fluid Mechanics, Lisbon, Portugal.
- König, G. (1993). "Autoignition and Knock Aerodynamics in Engine Combustion." PhD Thesis, School of Mech. Eng., University of Leeds.
- König, G. and Sheppard, C.G.W. (1990). "End Gas Autoignition and Knock in SI Engines." SAE-Paper 902135.
- Krieger, R.B. and Borman, G.L. (1966). "The Computation of Apparent Heat Release for Internal Combustion Engine." ASME 66-W/DGP-4.
- Kuratle, R. H., and Marki, B. (1992). "Influencing Parameters and Error Sources During Indication on Internal Combustion Engines." SAE Paper 920233.
- Kuwahara, K., Watanabe, T., Takemura, J., Omori, S., Kume, T., and Ando, H. (1994). "Optimization of In-Cylinder Flow and Mixing for a Center-Spark Four-Valve Engine Employing the Concept of Barrel-Stratification." SAE Paper 940986.
- Lading L. (1994). "Principles of laser anemometry". Optical diagnostics for flow processes. New York: Plenum Press, p 85-125.

- Lee, A. P. (1995). "The Effects of Bulk Air Motions and Turbulence on Combustion in Spark Ignition Engines." PhD Thesis, Dept. of Mech. Eng., University of Leeds.
- Lee, K. H., and Foster, D.E. (1995). "Cycle-by-Cycle Variations in Combustion and Mixture Concentration in the Vicinity of Spark Plug Gap." SAE Paper 950814.
- Lee, Y., Pae, S., Min, K. and Kim, E. S. (2000). "Prediction of knock onset and the autoignition site in spark-ignition engines." Proc. Instn. Mech. Engrs Vol 214 vol D.
- Lewis, B., and Von Elbe, G. (1987). "Combustion, Flames and Explosions of Gases." (Third Edition) Academic Press Inc.
- Li, Y., Zhao, H., Leach, B., Ma, T., and Ladommatos, N. (2004). "Characterization of an In-Cylinder Flow Structure in a High-Tumble Spark Ignition Engine." Int. J. Engine Res. Vol. 5 . No. 5.
- Libby, P.A., Chigier, N. and LaRue, J.C. "Conditional Sampling in Turbulent Combustion." Prog. Energy Combust. Sci., Vol. 8, pp 203-231, (1982).
- Liou, T. M., and Santavicca, D.A. (1983). "Cycle Resolved Turbulence Measurements in a Ported Engine with and without Swirl." SAE Paper 830419.
- Liou, T.M. and Santavicca, D.A. "Cycle Resolved LDV Measurements in a Motored IC Engine." ASME Journal of Fluid Engineering, Vol. 107, pp232-240, (1985).
- Lipatnikov, A. N., and Chomiak, J. (2002). "Turbulent Flame Speed and Thickness: Phenomenology, Evaluation, and Application in Multi-Dimensional Simulations." Progress in Energy and Combustion Science, 28, 1-74.
- Liu, K. (2004). "User manual for LUSIE and LUSIEDA 1D Thermodynamic code." Department of Mechanical Engineering, University of Leeds.
- Loye, A. O. Z., and Bracco, F.V. (1987). "Two-Dimensional Visualization of Ignition Kernels in an IC Engine." Combustion and Flame, 69, pp. 59-69.

- Lumley, J. L. (1999). "Engines An Introduction." Cambridge University Press.
- Maly, R. (1984). "Spark Ignition: Its Physics and Effect on the Internal Combustion Engine." (Eds. Hilliard and Springer) Plenum Press, pp. 91-148.
- Merdjani, S. and Sheppard, C.G.W. (1993). "Gasoline Engine Cycle Simulation Using the Leeds Turbulent Burning Velocity Correlations." SAE paper 932640.
- Miles, P. C., Green, R.M., and Witze, P.O. (1994). "Comparison of In-cylinder Scavenging Flows in a Two-Stroke Cycle Engine Under Motored and Fired Conditions." Proceedings of Seventh International Symposium on Applications of Laser Techniques to Fluid Mechanics. July 11-14, 1994.
- Morel, T. and Keribar, R. (1985). "A Model for Predicting Spatially and Time Resolved Convective Heat Transfer in Bowl-in-Piston Combustion Chambers." SAE paper 850204.
- Motavalli, J. (2000). "Forward Drive, The Race to Build "Clean" Cars for the Future." Sierra Club Books in conjunction with Crown Publishers, New York.
- Neußer, H. J., Spiegel, L., and Ganser, J. (1995). "Particle Tracking Velocimetry- A Powerful Tool to Shape the In-Cylinder Flow of Modern Multi-Valve Engine Concepts." SAE Paper 950102.
- Newman, A. W. (1993). "Laser Doppler Anemometer Measurements in a Four-Valve Pent Roof Combustion Chamber." IMechE, C465/035/93.
- Nishiwaki, K., Yoshihara, Y. and Saijyo, K. (2000). "Numerical Analysis of the location of knock initiation in S.I. engines." SAE Paper 2000-01-1897.
- Oxfordlasers (2005) www.oxfordlasers.com/imaging/pdfs/prodseedinggenerator.pdf
- Ozdor, N., Dulger, M., and Sher, E. (1994). "Cyclic Variability in Spark Ignition Engines. A Literature Survey." SAE Paper 940987.

- Pajot, O., and Mounaïm-Rousselle, C. (2000). "Instantaneous Flow Field Effects on the Flame Kernel in S.I. Engine by Simultaneous Optical Diagnostics." SAE Paper 2000-01-1796.
- Pan, J. (1994). "End-Gas Autoignition Modes and Spark-Ignition Engine Knock Severity." PhD Thesis, Department of Mechanical Engineering, University of Leeds.
- Pan, J. and Sheppard, C.G.W. (1994). "A Theoretical and Experimental Study of the Modes of End Gas Autoignition Leading to Knock in S.I. Engines." SAE-Paper 942060.
- Petrovic, S. (1982). "Cycle by Cycle Variations of Flame Propagation in a Spark Ignition Engine." SAE Paper 820091.
- Plee, S. L., Remboski, D. J., and Martin, J. K. (1987). "Application of Conditional Sampling to the Study of Cyclic Variability in a Spark-ignition Engine." SAE Paper 871173.
- Pischinger, S., and Heywood, J. B. (1990). "How Heat Losses to the Spark Plug Electrodes Affect Flame Kernel Development in an SI-Engine." SAE Paper 900021.
- Richardson, S.H., Riding, D.H. (1997). "Predictive Design Support in The Achievement of Refined Power for The Jaguar XK8 ." SAE Paper 972041.
- Reuss, D. L. (2000). "Cyclic Variability of Large-Scale Turbulent Structures in Directed and Undirected IC Engine Flows." SAE Paper 2000-01-0246.
- Rosseel, E., and Sierens, R. (1999). "Evaluating Piezo-electric Transducer Response to Thermal Shock from In-Cylinder Pressure Data." SAE Paper 1999-01-0935.
- Rui-Lin, L., Chun-Run, Z., Liang-Qin, W., Xiang-Bi, A., Yi-Kun, Y., Shu-Min, L., Ming-Zhi, F., and Chong-Lin, S. (1996). "A Study on the Mechanism of In-Cylinder Tumble Generation by Directed Intake Ports." SAE Paper 962089.

Saxena, V., and Rask, R.B. (1987). "Influence of Inlet Flow on the Flow Field of an Engine." SAE Paper 870369.

Sazhina, E.M., Sazhin, S.S., Heikal, M.R. and Marooney, C.J. (1999). "The Shell autoignition model: applications to gasoline and diesel fuels." *Fuel* 78: 389-401.

Semenov, E. S. (1963). "Studies of Turbulent Gas Flow in Piston Engines." NASA Tech. Trans., F-97.

Seong-Soo, K., and Sung-Soo, K. (1995). "Effects of Swirl and Spark Plug Shape on Combustion Characteristic in a High Speed Single-Shot Visualized SI Engine." SAE Paper 951003.

Smallbone, A. (2004). "Fuel and Residual Effects on Knock Onset in S.I. Engines." PhD Thesis, School of Mech. Eng., University of Leeds.

Stevenson, W. H. (1976). "Principles of Laser Velocimetry." Invited paper received August 6.

Stone, C. R., Brown, A.G., and Beckwith, (1996). "Cycle-by-Cycle Variations in Spark Ignition Engine Combustion- Part II: Modelling of Flame Kernel Displacements as a Cause of Cycle-by Cycle Variations." SAE Paper 960613.

Stone, R. (1999). "Introduction to Internal Combustion Engines.", Macmillan.

Swords, M. D., Kalghatgi, G.T., and Watts, A.J. (1982). "An Experimental Study of Ignition and Flame Development in a Spark Ignition Engine." SAE Paper 821220.

Tabaczynski, (1976). "Turbulence and Turbulent Combustion in Spark Ignition Engines." *Prog. Energy and Comb. Science*, 2, pp. 143-165.

Tagalian, J., and Heywood, J. (1986). "Flame Initiation in a Spark-Ignition Engine." *Combustion and Flame*, 64, pp. 243-246.

- Taylor, A.M.K.P. (1992) "Instrumentation for Flows with Combustion.", Academic Press.
- Tennekes, H., and Lumley, J. (1972). "A First Course in Turbulence." MIT Press.
- Towers, D. P., and Buckberry, C.H. (1996). "Application of Two-Color PIV to In-Cylinder Flow Velocity Measurement." SAE Paper 964085.
- Urusihara, T., Murayama, T., Takagi, Y., and Lee, K. (1995). "Turbulence and Cycle-by-Cycle Variation of Mean Velocity Generated by Swirl and Tumble Flow and Their Effects on Combustion." SAE Paper 950813.
- Urusihara, T., Nakada, T., Kakuhou, A., and Takagi, Y. (1996). "Effects of Swirl/Tumble Motion on In-Cylinder Mixture formation in a Lean-Burn Engine." SAE Paper 961994.
- Wallesten, J., Lapatnikov, A. and Chomiak, J. (2002). "Simulations of Fuel/Air Mixing, Combustion, and Pollution Formation in a Direct Injection Gasoline Engine." SAE Paper 2002-01-0835.
- Weaving, J. H. (1990). "Internal Combustion Engineering Science and Technology." Elsevier Science.
- Whitelaw J.H. and Xu. H.M. (1993). "An Experimental Study of Gas Velocity, Flame Propagation and Pressure in a Spark Ignition Engine." SAE paper 932702.
- Whitelaw J.H. and Xu. H.M. (1995). "Cyclic variations in a lean-burn spark ignition engine without and with swirl." SAE paper 950683.
- Witze, P. O., and Vilchis, F.R. (1981). "Stroboscopic Laser Shadograph Study of the Effect of Swirl on Homogeneous Combustion in a Spark -Ignition Engine." SAE Paper 810226.

Witze, P. O., Hall, M.J., and Bennett, M.J. (1990). "Cycle-Resolved Measurements of Flame Kernel Growth and Motion Correlated with Combustion Duration." SAE Paper 900023.

Witze, P. O., and Martin, J.K. (1986). "Cyclic Variation Bias in Spark Ignition Engine Turbulence Measurements." In *Laser Anemometry in Fluid Mechanics*, Ed. By Adrian R. J., et al.

Witze, P. O., Martin, J.K., and Borgnakke, C. (1983). "Measurements and Predictions of the Precombustion Fluid Motion and Combustion Rates in a Spark Ignition Engine." SAE Paper 831697.

Witze, P.O., Martin, J.K. and Borgnakke, C. (1984). "Fluid Motion During Flame Propagation in a Spark ignition Engine." SAE Paper No. 840377.

Woolley, R. (2005). Private communication. School of Mech. Eng., University of Leeds.

Woschni, G. (1967). "A Universally Applicable Equation for the Instantaneous Heat Transfer Coefficient in the Internal Combustion Engine." SAE Paper 670931.

Wyszynski, L.P., Stone, C.R. and Kalghatgi, G.T. (2002). "The Volumetric Efficiency of Direct and Port Injection Gasoline Engines with Different Fuels." SAE Paper 2002-01-0839.

Xu, H.M. (1995). "Turbulent Flow and Combustion in a Lean-burn spark ignition engine." PhD Thesis, Imperial College, University of London.

Yeh, Y., and Cummins, H.Z. (1964). "Localised Flow Measurements with An He-Ne Laser Spectrometer." *Applied Physics Letters*, 4, 176.

Zheng, J., Yang, W., Millar, D.L., and Cernansky, N.P. (2002). "A Skeletal Chemical Kinetic Model for the HCCI Combustion Process." SAE Paper 2002-01-0422.

Zhao, H., and Ladommatos, N. (2001). "Engine Combustion Instrumentation and Diagnostics.", Society of Automotive Engineers, Inc.

Zimont, V. L. (1979). "Theory of Turbulent Combustion of a Homogeneous Fuel Mixture at High Reynolds Number." *Combustion, Explosion, and Shock Waves*, 15, pp. 305-311.

Appendices

Appendix A		220
Appendix B	Additional LUPOE2-P experimental results not included in Chapter7.	226
Appendix B1	Retarded ignition timing	226
Appendix B2	Advanced ignition timing	234
Appendix B3	Rich mixture	242
Appendix B4	Lean mixture	248
Appendix B5	Low engine speed (750 rpm)	251
Appendix B6	Intermediate engine speed (1000 rpm)	256

APPENDIX A : LDV General specifications and setting adopted

Set-up	No. of valves* open	Seeded air flow rate [%]	Main air flow rate [%]
Back scatter set up (BS)	1 at 750&1000rpm	10	70
	1&1/2 at 1500 rpm		
	2 at 1900 rpm		
Forward scatter set up (FS)	1 at all speeds	3	77
<p>* Number of valves opened in SCITEC LS-10 liquid seed generator, shown in Figure 4.9.</p> <p>The combined % of each BS or FS was 80% of the 400L/min of the air mass flow (equivalent to 6.89 g/sec).</p>			

Table A1 Air flow-rate set up for forward and back scatter configurations (LUPOE2-P)

<i>Advanced</i>	
High voltage activation	Manual
Anode current warning level	90%
Data collection mode	Burst
<i>Frequency shift</i>	
40 MHz frequency shift	Enable
Variable frequency shift	Disable
<i>Synchronisation Input Signals</i>	
Sync. 1	BNC1
Sync. 2	None
Trigger edge sync. 1	Positive
Trigger edge sync. 2	Negative
Reset encoder	None
Encoder	None
Start measurement	None
Stop measurement	None
Burst detector enable	None
External burst detector trigger	None
Reference clock mode	Internal

Table A2: DANTIC LDV Processor properties settings (Thomas, 2002)

Max. Samples	200000
Max. Acquisition time	60.00s at 1500&1900 rpm 120.000s at 750&1000 rpm
Filter method	Overlapped
Scope zoom	400 %
Encoder data	Excluded
High voltage	Off

Table A3 Group 1 properties

Centre frequency	0.00 m/s
Bandwidth	18.00 m/s
Record length mode	Fixed
Record length	128
Maximum record length	128
High voltage level	1000 V
Signal gain	26 dB for Forward scatter 24 dB for Back scatter
Burst detector SNR level	0 dB
Scope display	Burst signal
Scope trigger channel	this
Level validation ratio	4

Table A4 LDV1 channel properties

Engine Speeds	750 rpm	1000 rpm	1500 rpm	1900 rpm
Record length mode	Fixed	Fixed	Fixed	Fixed
Record length	128	128	128	128
Signal gain	26* dB	26* dB	26* dB	26* dB
Burst detector SNR level	-3,0** dB	-3,0** dB	-3,0** dB	-3,0** dB
Level validation ratio	4	4	4	4

** value -3 dB for back scatter and 0 dB for forward scatter configuration

* value 24 dB for back scatter configuration and 26 dB for forward scatter configuration

Table A5 Some LDV1 channel properties used in this work (LUPOE2-P)

Wavelength	514.500 nm
Focal length	160.000 mm
Beam diameter	1.400 mm
Expander ratio	1.000
Beam spacing	38.000 mm

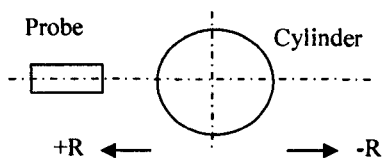
Table A6 Optical LDV System properties

In forward scatter, the beams were focused through a curved side window. Due to this effect, both the focal length and beam-crossing angle were corrected, as shown in Table A7.

In back scatter, transition of beams through thick quartz window refracted the position of the beam crossing and moved its position forward. This shift can be calculated using Snell's law for light beams entering an optically denser medium according to Atashkari:

$$z' = z + b \left(1 - \frac{\cos \alpha}{\sqrt{n^2 - \sin^2 \alpha}} \right)$$

where $z = 160$ mm is the original focal length of front lens, $b = 40$ mm is window thickness, $n = 1.4$ is refractive index of quartz and $\alpha = 6.7$ degrees is beam crossing half angle. Applying this refractive index correction, the correct focal length was 165.8 mm.



Radial position in cylinder [mm]	30	20	10	0	-10	-20	-30
Beam-cross angle [deg]	10.43	9.41	8.31	7.82	7.15	6.84	6.31
Corrected focal length (BSA software input) [mm]	208.2	230.8	261.5	278	304.1	318	344.7

Table A7: Measured beam-cross angles and the corresponding software input focal lengths (Thomas 2002)

LDV Channel Properties (Forward and back scatter configurations)

(1) Forward scatter-LUPOE2-P Engine

At various probe positions (A, B, C – centre) within the pent-roof chamber, refer to Table 7.2 and Figure 7.19.

Point A

LDV1 channel properties for Point A (u- component)

Engine Speeds	<i>750 rpm</i>	<i>1000 rpm</i>	<i>1500 rpm</i>	<i>1900 rpm</i>
Centre frequency	0.00 m/s	0.00 m/s	0.00 m/s	0.00 m/s
Bandwidth	35.27 m/s	47.03 m/s	47.03 m/s	70.55 m/s

LDV1 channel properties for Point A (v- component)

Engine Speeds	<i>750 rpm</i>	<i>1000 rpm</i>	<i>1500 rpm</i>	<i>1900 rpm</i>
Centre frequency	0.00 m/s	0.00 m/s	0.00 m/s	0.00 m/s
Bandwidth	24.54 m/s	24.54 m/s	24.54	49.08 m/s

Point C (centre)

LDV1 channel properties for Point C (u- component)

Engine Speeds	<i>750 rpm</i>	<i>1000 rpm</i>	<i>1500 rpm</i>	<i>1900 rpm</i>
Centre frequency	0.00 m/s	0.00 m/s	0.00 m/s	0.00 m/s
Bandwidth	42.44 m/s	56.59 m/s	56.59 m/s	56.59 m/s

Point B

LDV1 channel properties for Point B (u- component)

Engine Speeds	<i>750 rpm</i>	<i>1000 rpm</i>	<i>1500 rpm</i>	<i>1900 rpm</i>
Centre frequency	4.03 m/s	6.06 m/s	6.06 m/s	8.09 m/s
Bandwidth	32.35 m/s	48.52 m/s	48.52 m/s	64.7 m/s

(2) Back scatter-LUPOE2-P Engine

At two probe positions (D and E) within the pent-roof chamber, refer to Table 7.2 and Figure 7.19.

Point D**LDV1 channel properties for Point D (s_D)**

Engine Speeds	<i>750 rpm</i>	<i>1000 rpm</i>	<i>1500 rpm</i>	<i>1900 rpm</i>
Centre frequency	6.13 m/s	6.13 m/s	8.18 m/s	8.18 m/s
Bandwidth	49.08 m/s	49.08 m/s	65.45 m/s	65.45 m/s

LDV1 channel properties for Point D (w_D)

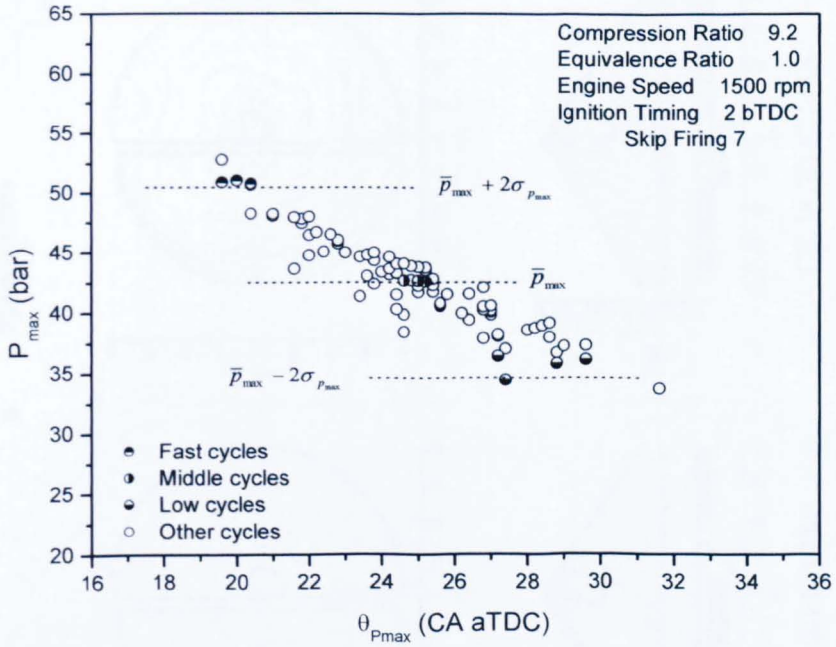
Engine Speeds	<i>750 rpm</i>	<i>1000 rpm</i>	<i>1500 rpm</i>	<i>1900 rpm</i>
Centre frequency	6.13 m/s	0.00 m/s	0.00 m/s	0.00 m/s
Bandwidth	49.08 m/s	49.08 m/s	65.45 m/s	65.45 m/s

Point E**LDV1 channel properties for Point E (s_E)**

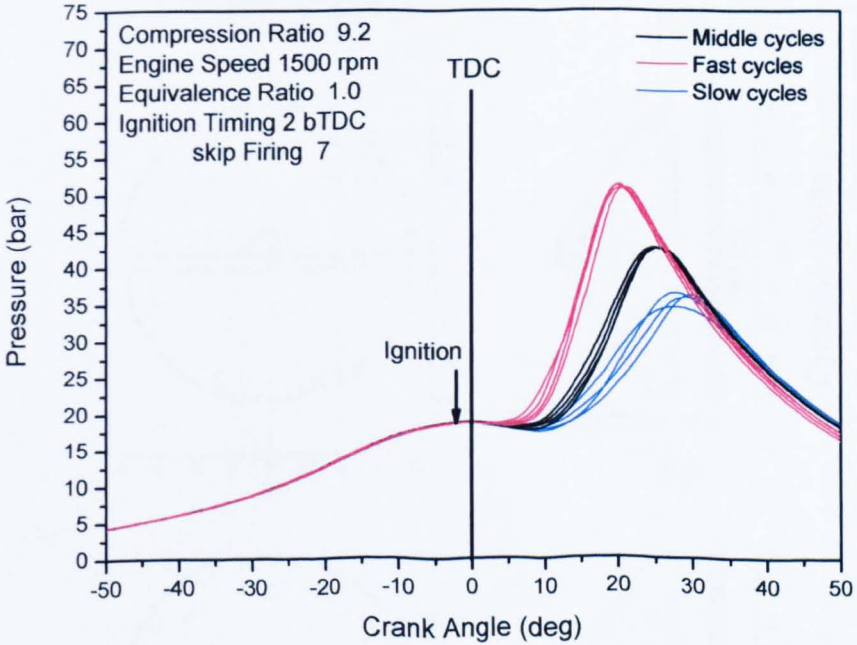
Engine Speeds	<i>750 rpm</i>	<i>1000 rpm</i>	<i>1500 rpm</i>	<i>1900 rpm</i>
Centre frequency	6.13 m/s	6.13 m/s	8.18 m/s	8.18 m/s
Bandwidth	49.08 m/s	49.08 m/s	65.45 m/s	65.45 m/s

LDV1 channel properties for Point E (w_E)

Engine Speeds	<i>750 rpm</i>	<i>1000 rpm</i>	<i>1500 rpm</i>	<i>1900 rpm</i>
Centre frequency	0.00 m/s	0.00 m/s	0.00 m/s	0.00 m/s
Bandwidth	49.08 m/s	49.08 m/s	65.45 m/s	65.45 m/s



(a)



(b)

Figure B1-1 (a) Peak pressure versus corresponding crank angle for its occurrence and (b) pressure-crank angle diagrams for selected middle, fast and slow cycles for stoichiometric, 1500 rpm, ignition timing 2° bTDC).

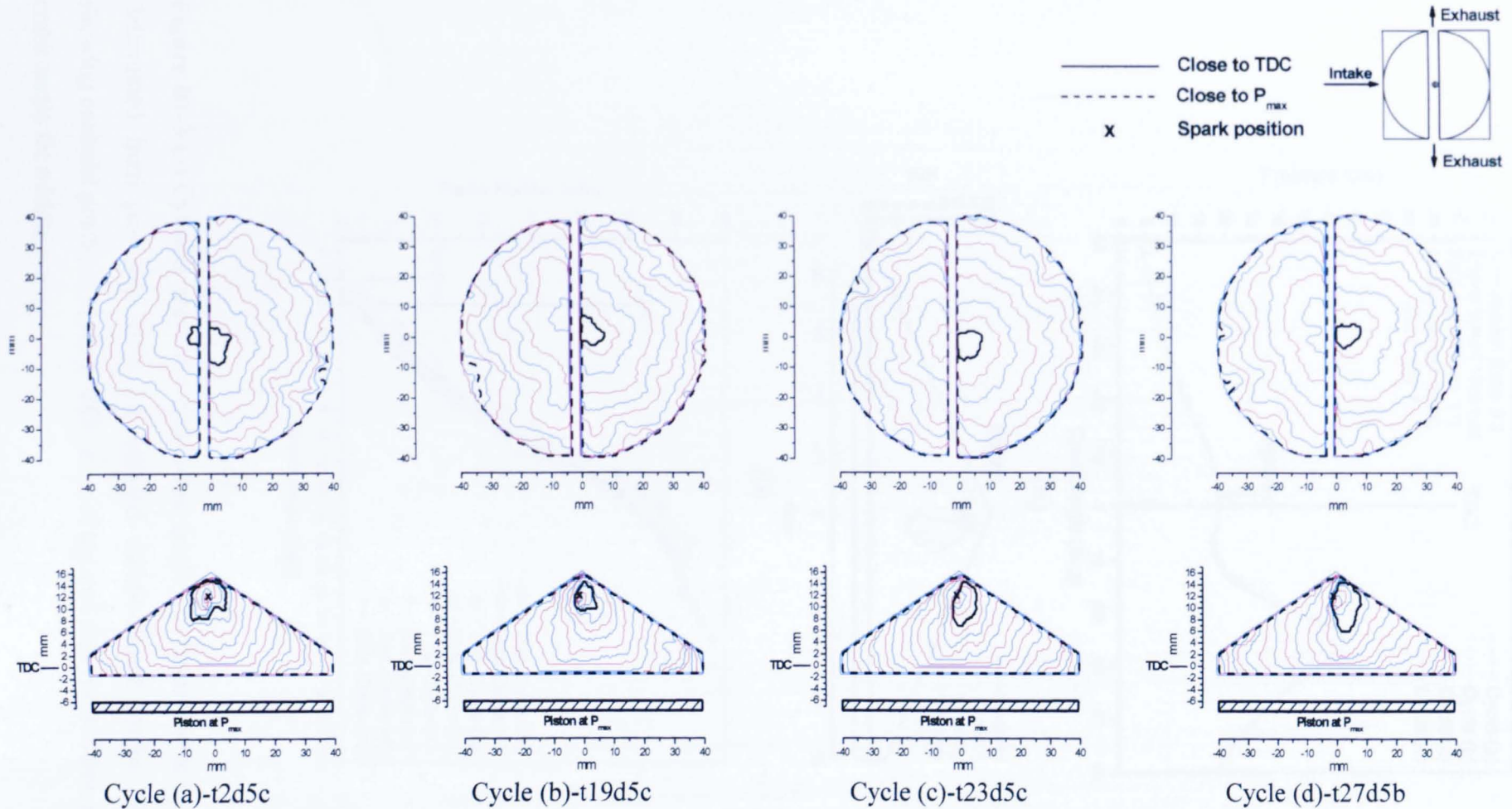
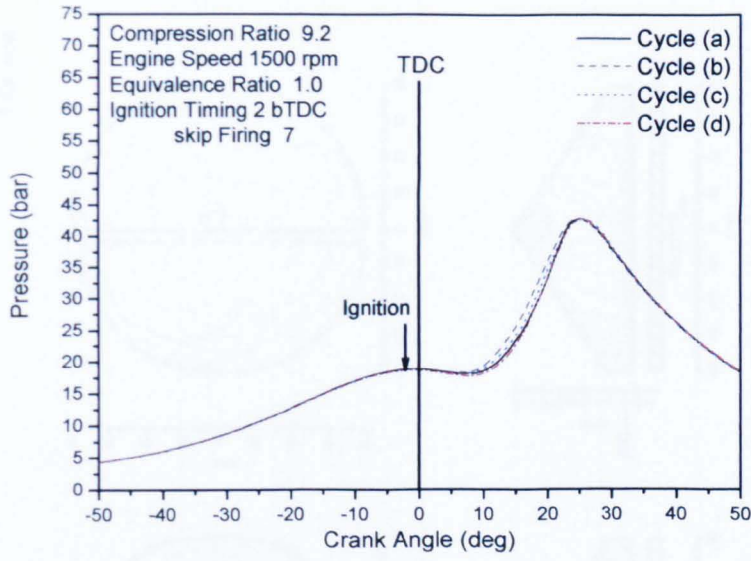
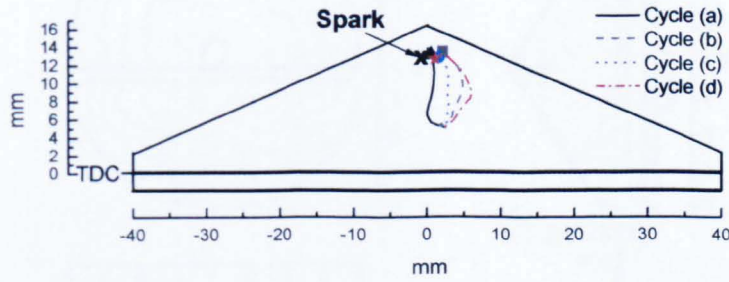


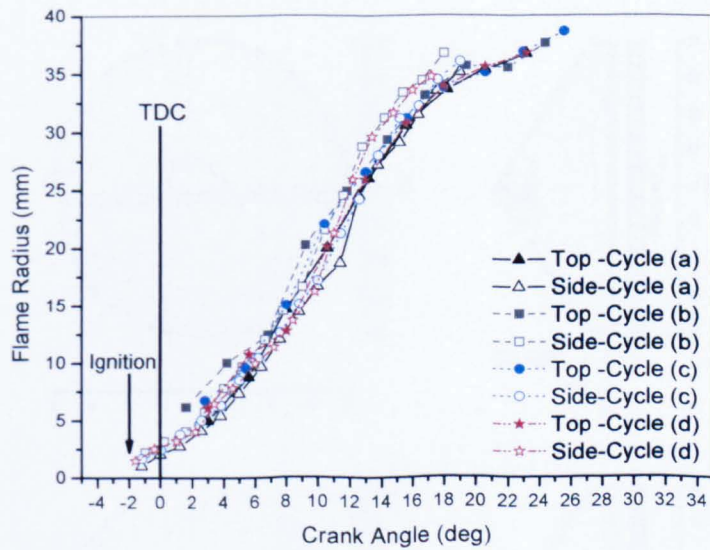
Figure B1-2 Successive flame front positions, overhead and side views, for the four selected 'middle' cycles for 1500 rpm, stoichiometric, ignition timing 2° bTDC (with top and side contours separated by ~ 2.5 and 1.26° CA, respectively).



(a)



(b)



(c)

Figure B1-3 (a) Cylinder pressure versus crank angle, (b) flame centroid displacement determined from just side view for selected middle-fired cycles, filled symbol showing centroid positions close to TDC and (c) top and side mean flame radius versus crank angle for middle cycles.

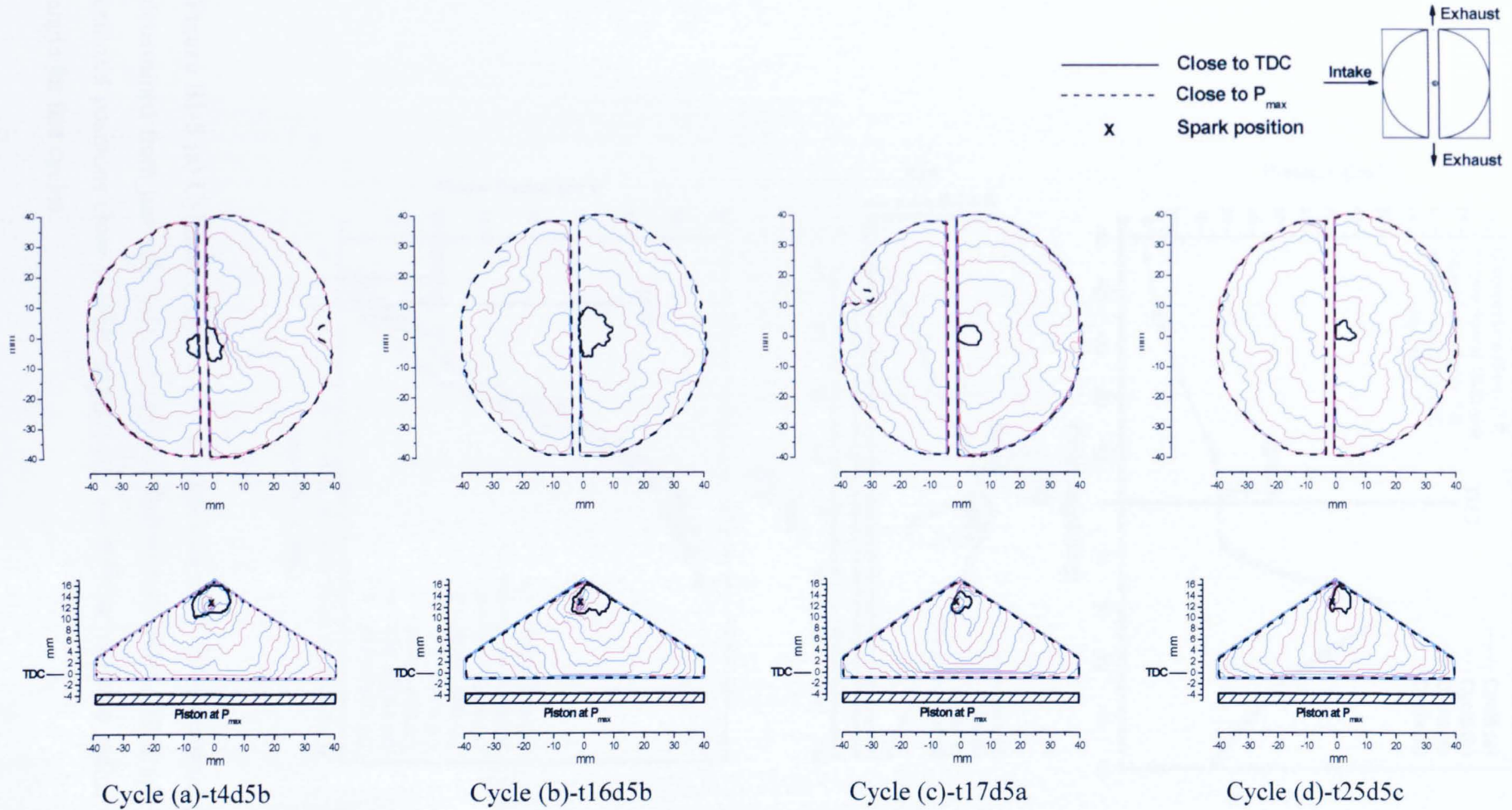
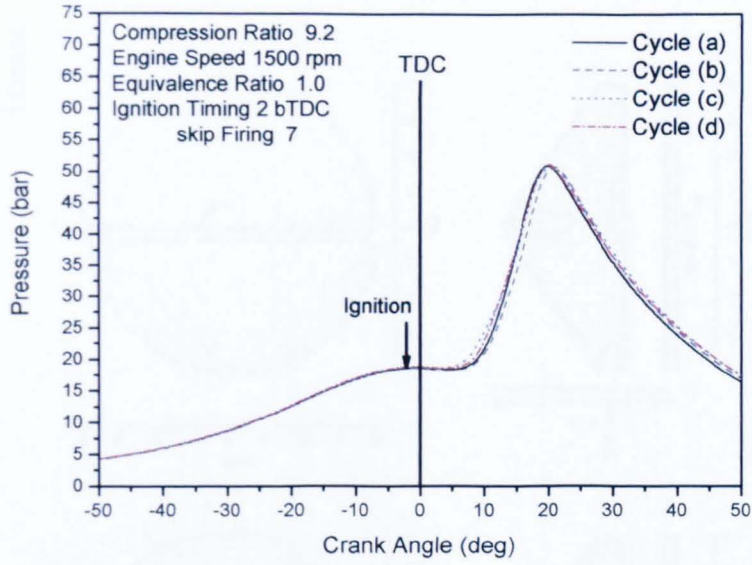
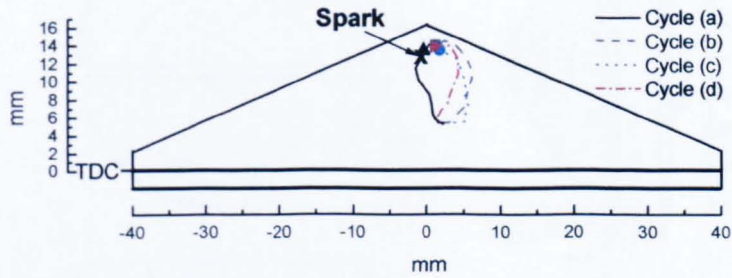


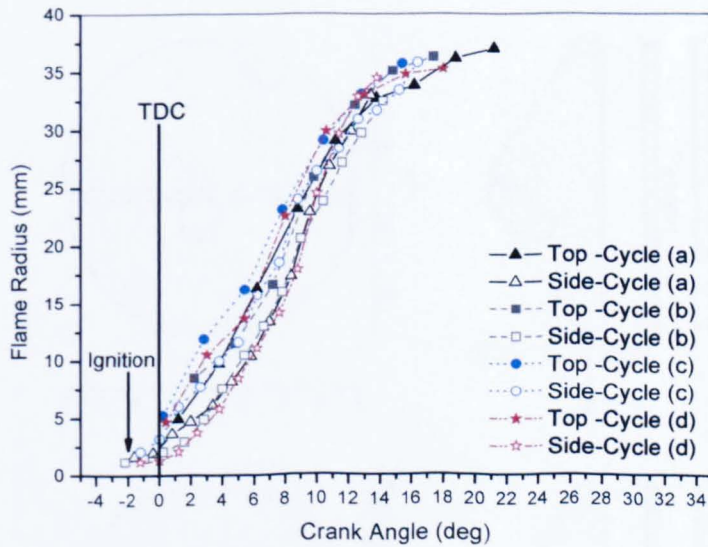
Figure B1-4 Successive flame front positions, overhead and side views, for the four selected ‘fast’ cycles for 1500 rpm, stoichiometric, ignition timing 2° bTDC (with top and side contours separated by ~ 2.5 and 1.26° CA, respectively).



(a)



(b)



(c)

Figure B1-5 (a) Cylinder pressure versus crank angle, (b) flame centroid displacement determined from just side view for selected fast-filmed cycles, filled symbol showing centroid positions close to TDC and (c) top and side mean flame radius versus crank angle for fast cycles.

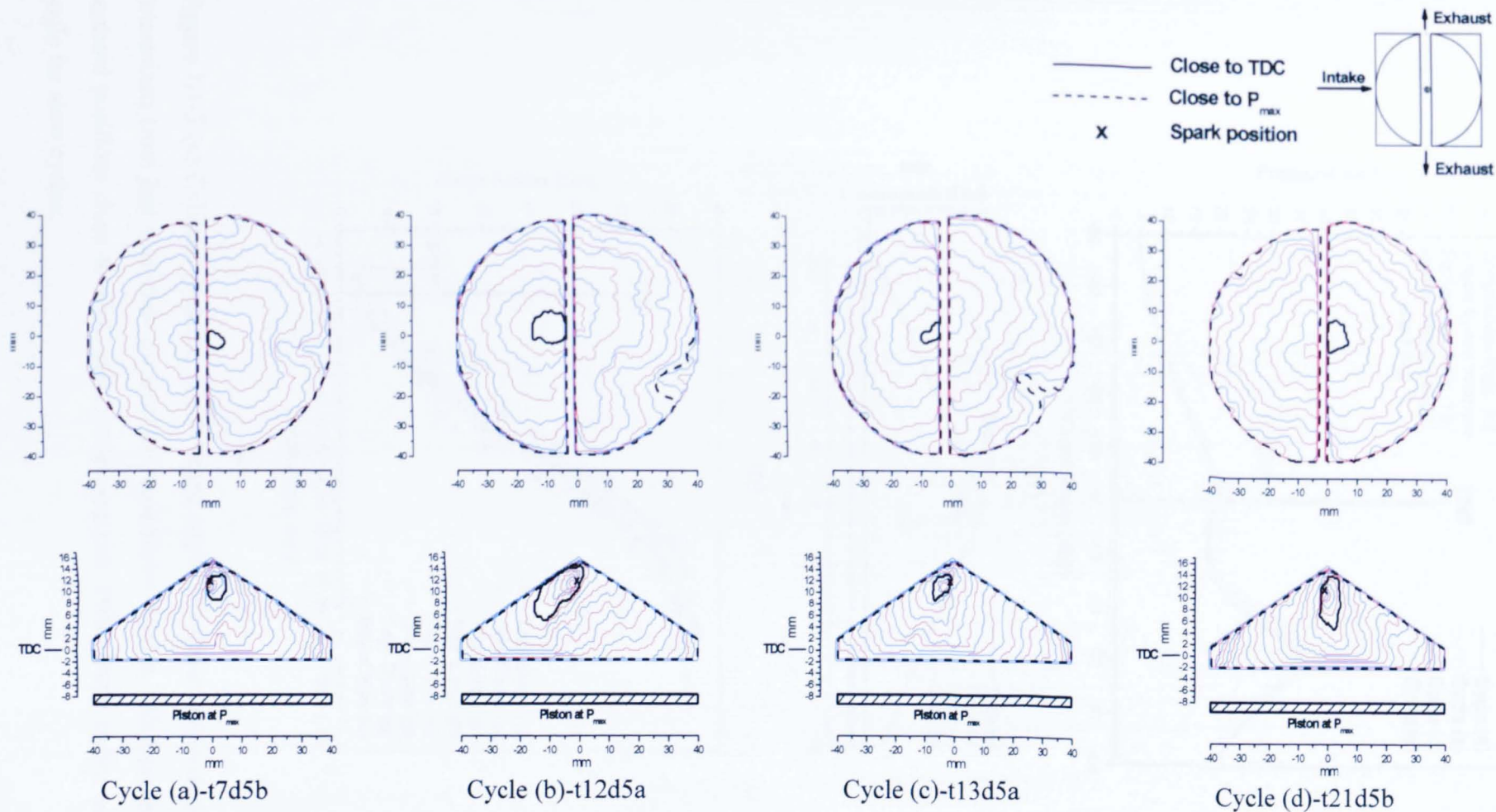
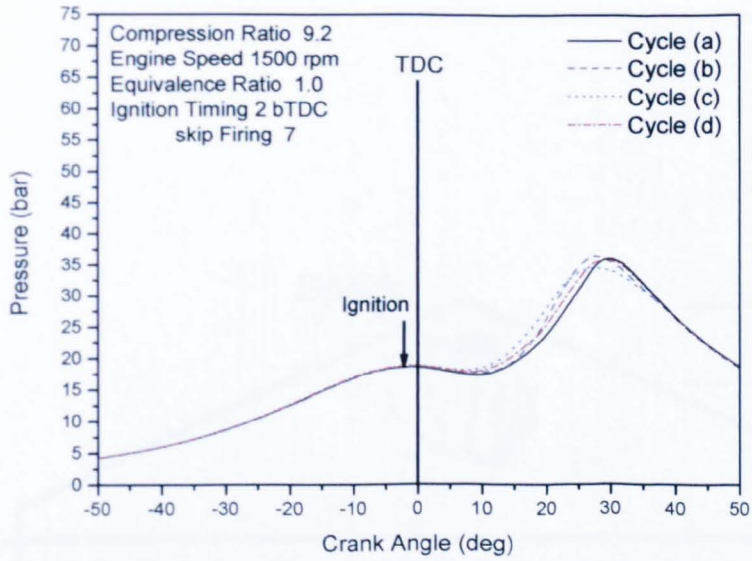
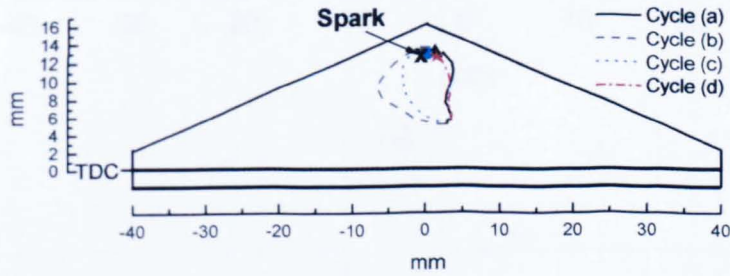


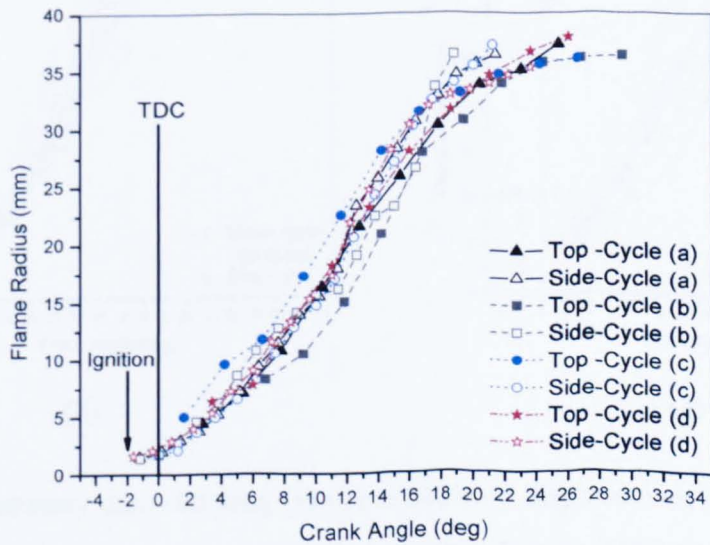
Figure B1-6 Successive flame front positions, overhead and side views, for the four selected 'slow' cycles for 1500 rpm, stoichiometric, ignition timing 2° bTDC (with top and side contours separated by ~ 2.5 and 1.26° CA, respectively).



(a)

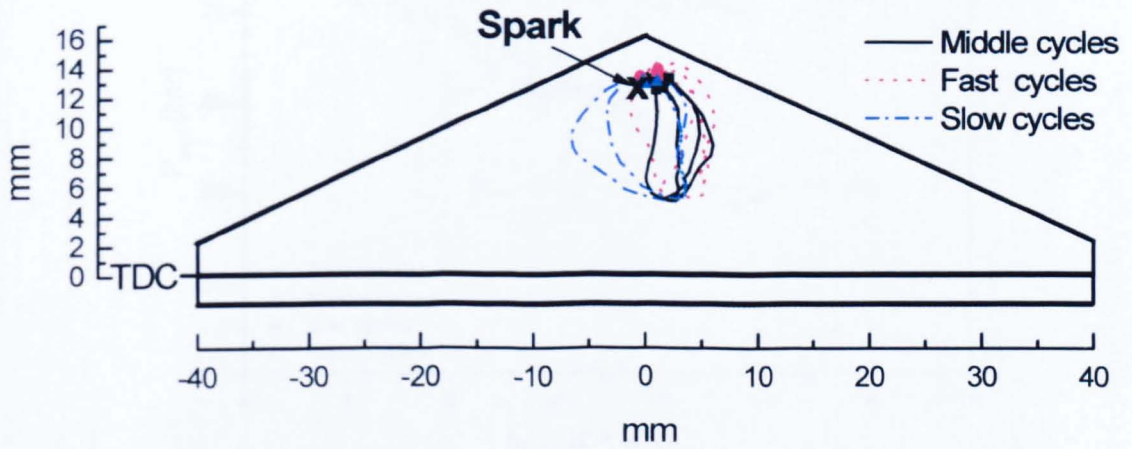


(b)

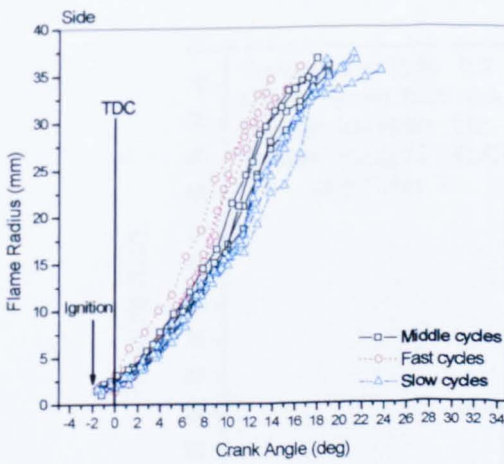


(c)

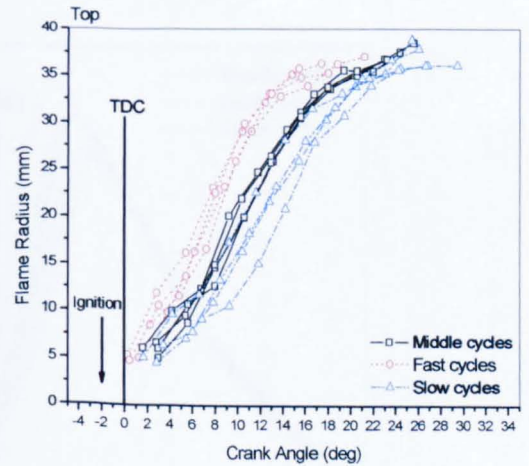
Figure B1-7 (a) Cylinder pressure versus crank angle, (b) flame centroid displacement determined from just side view for selected slow-filmed cycles, filled symbol showing centroid positions close to TDC and (c) top and side mean flame radius versus crank angle for slow cycles.



(a)

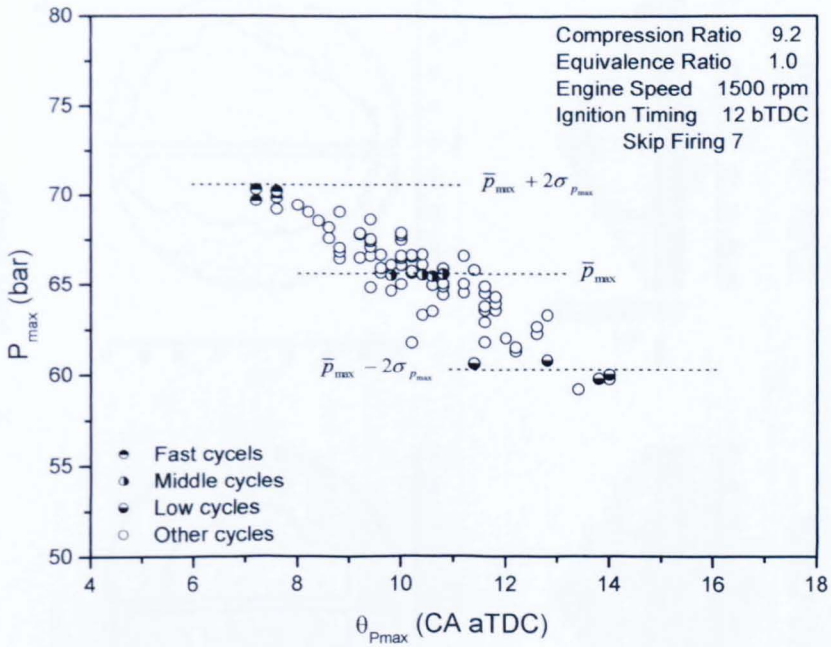


(b)

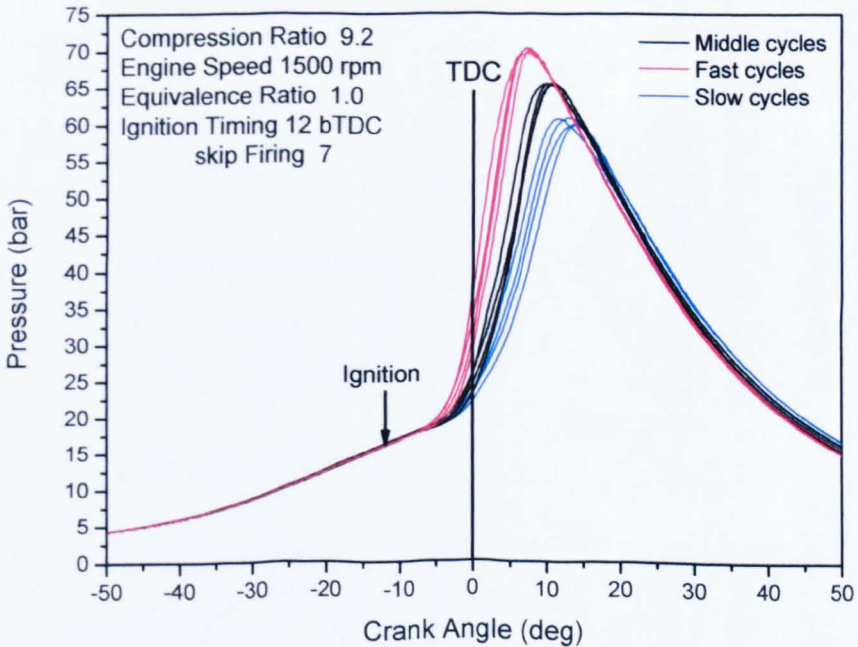


(c)

Figure B1-8 Summary data showing (a) flame centroid displacement determined from just side view, filled symbol showing centroid positions close to TDC and mean flame radius versus crank angle derived from (b) the side view and (c) the overhead view for 1500 rpm, stoichiometric, ignition timing 2° bTDC.



(a)



(b)

Figure B2-1 (a) Peak pressure versus corresponding crank angle for its occurrence and (b) pressure-crank angle diagrams for selected middle, fast and slow cycles for stoichiometric, 1500 rpm, ignition timing 12° bTDC).

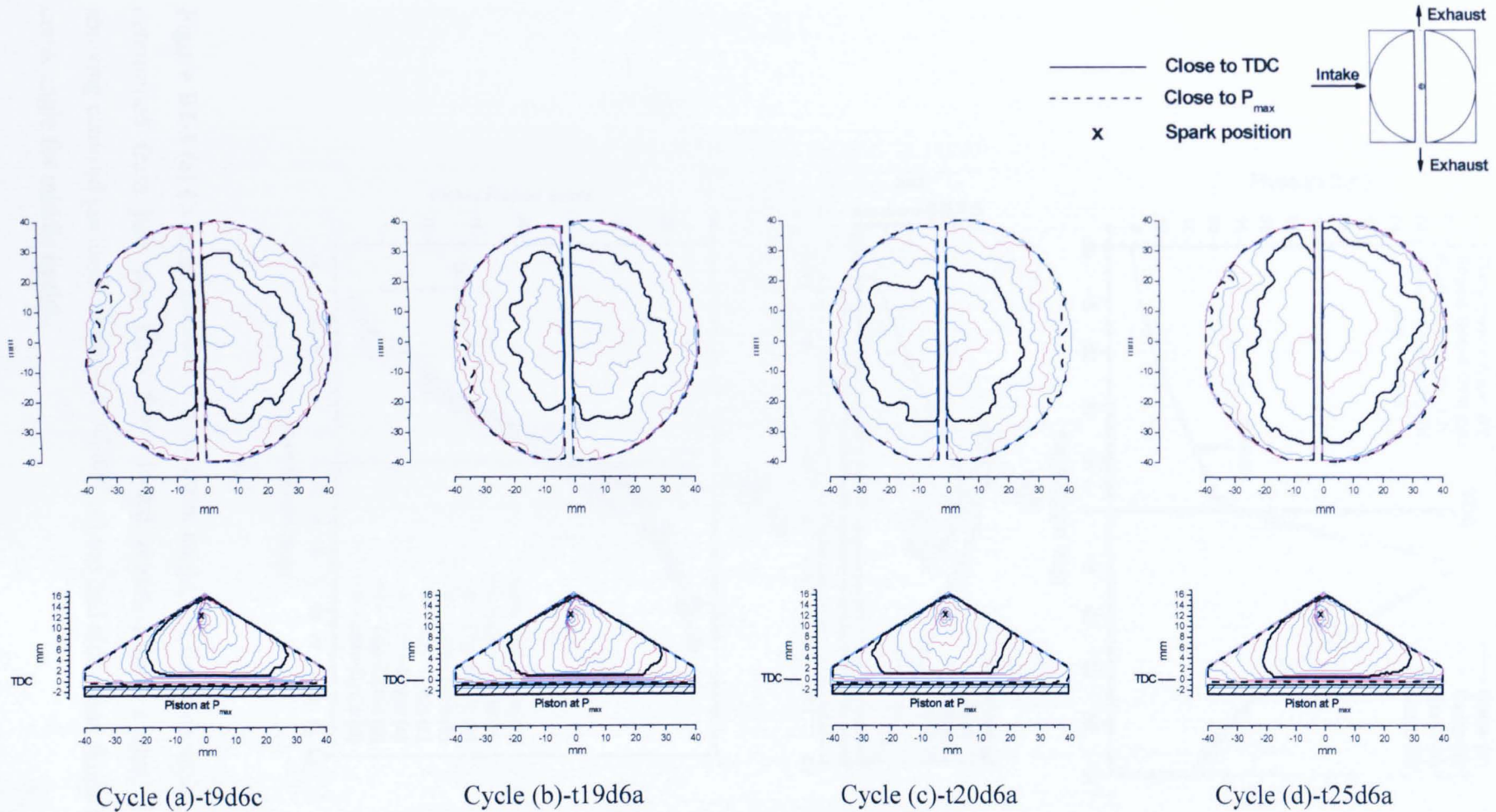


Figure B2-2 Successive flame front positions, overhead and side views, for the four selected 'middle' cycles for 1500 rpm, stoichiometric, ignition timing 12° bTDC (with top and side contours separated by ~ 2.5 and 1.26° CA, respectively).

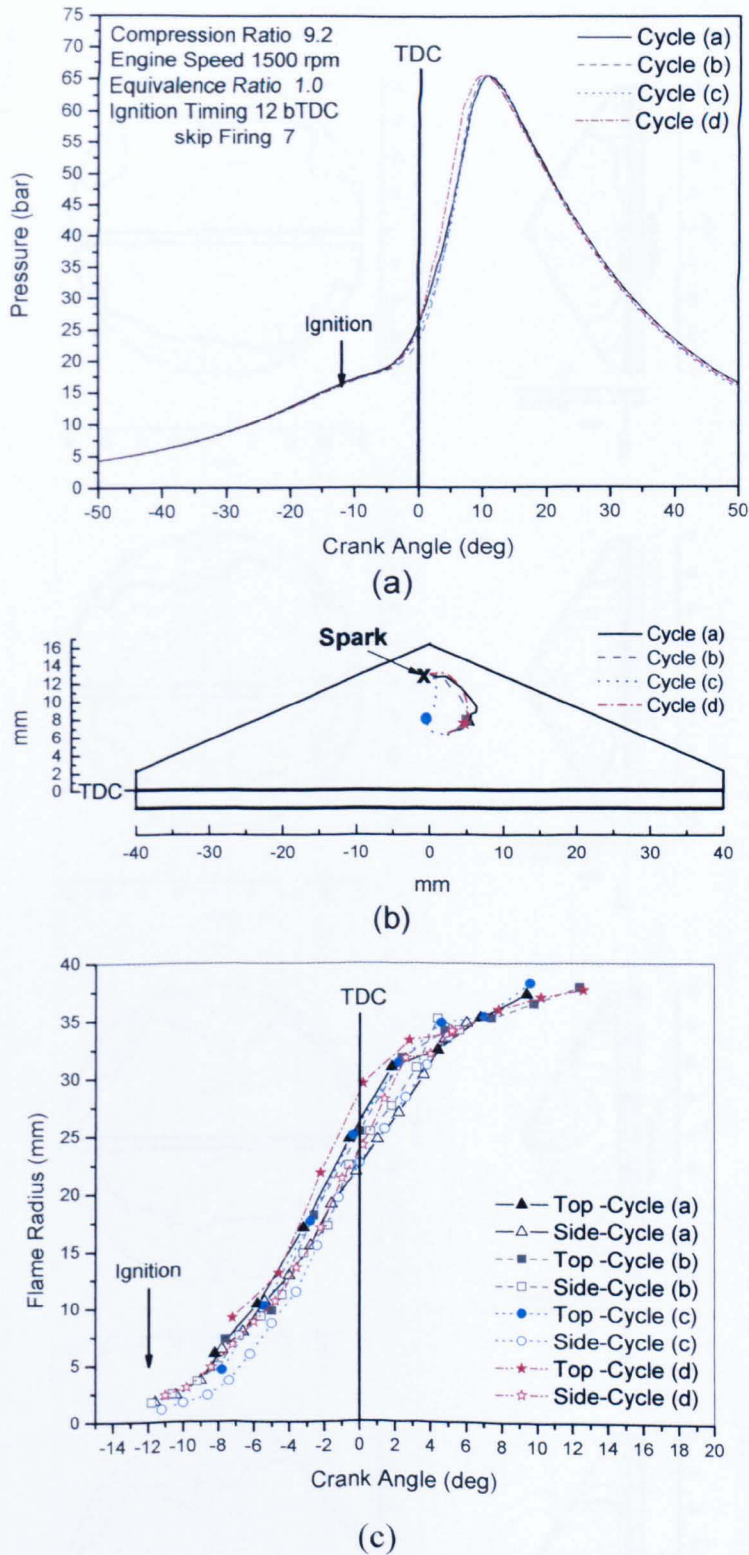


Figure B2-3 (a) Cylinder pressure versus crank angle, (b) flame centroid displacement determined from just side view for selected middle-fired cycles, filled symbol showing centroid positions close to TDC and (c) top and side mean flame radius versus crank angle for middle cycles.

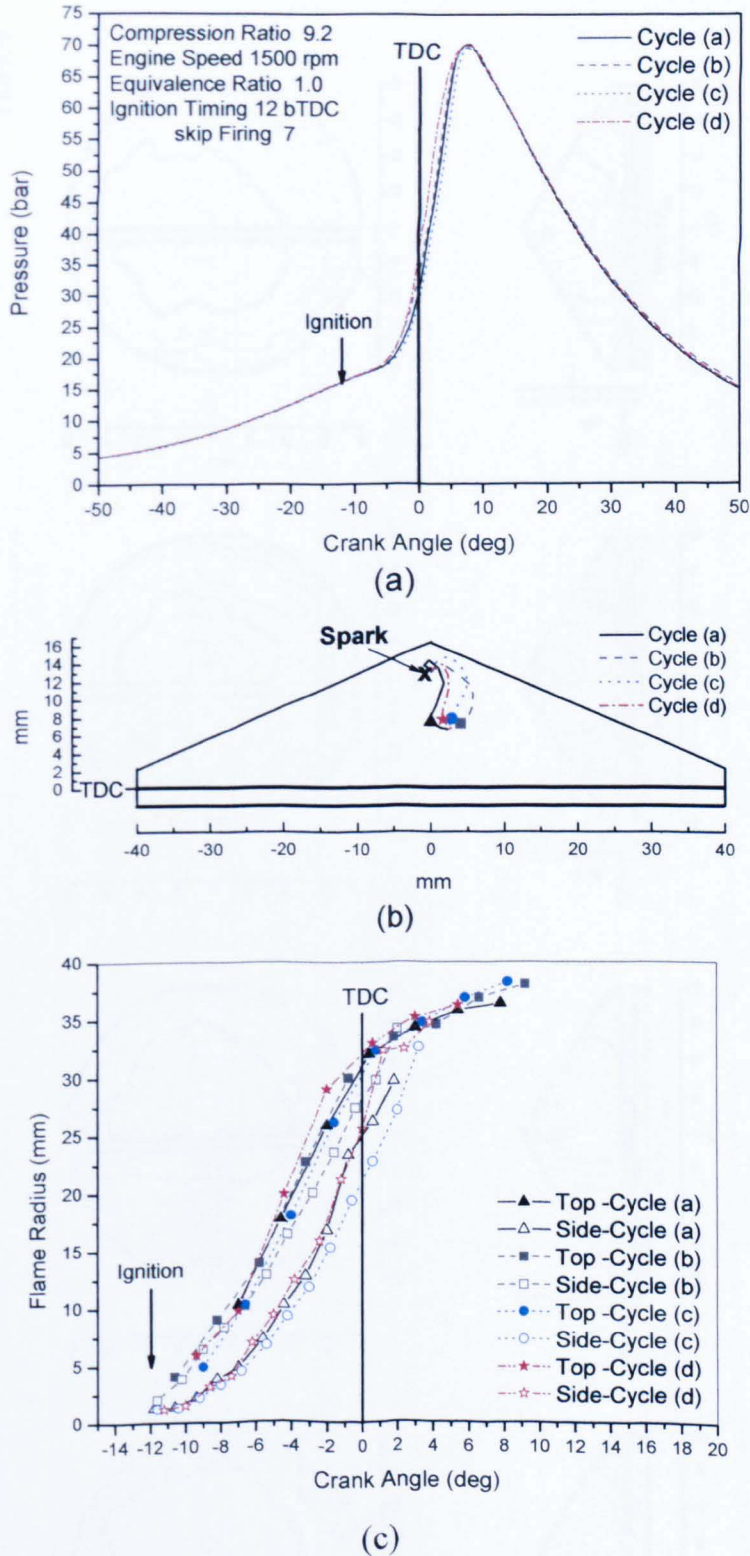


Figure B2-5 (a) Cylinder pressure versus crank angle, (b) flame centroid displacement determined from just side view for selected fast-filmed cycles, filled symbol showing centroid positions close to TDC and (c) top and side mean flame radius versus crank angle for fast cycles.

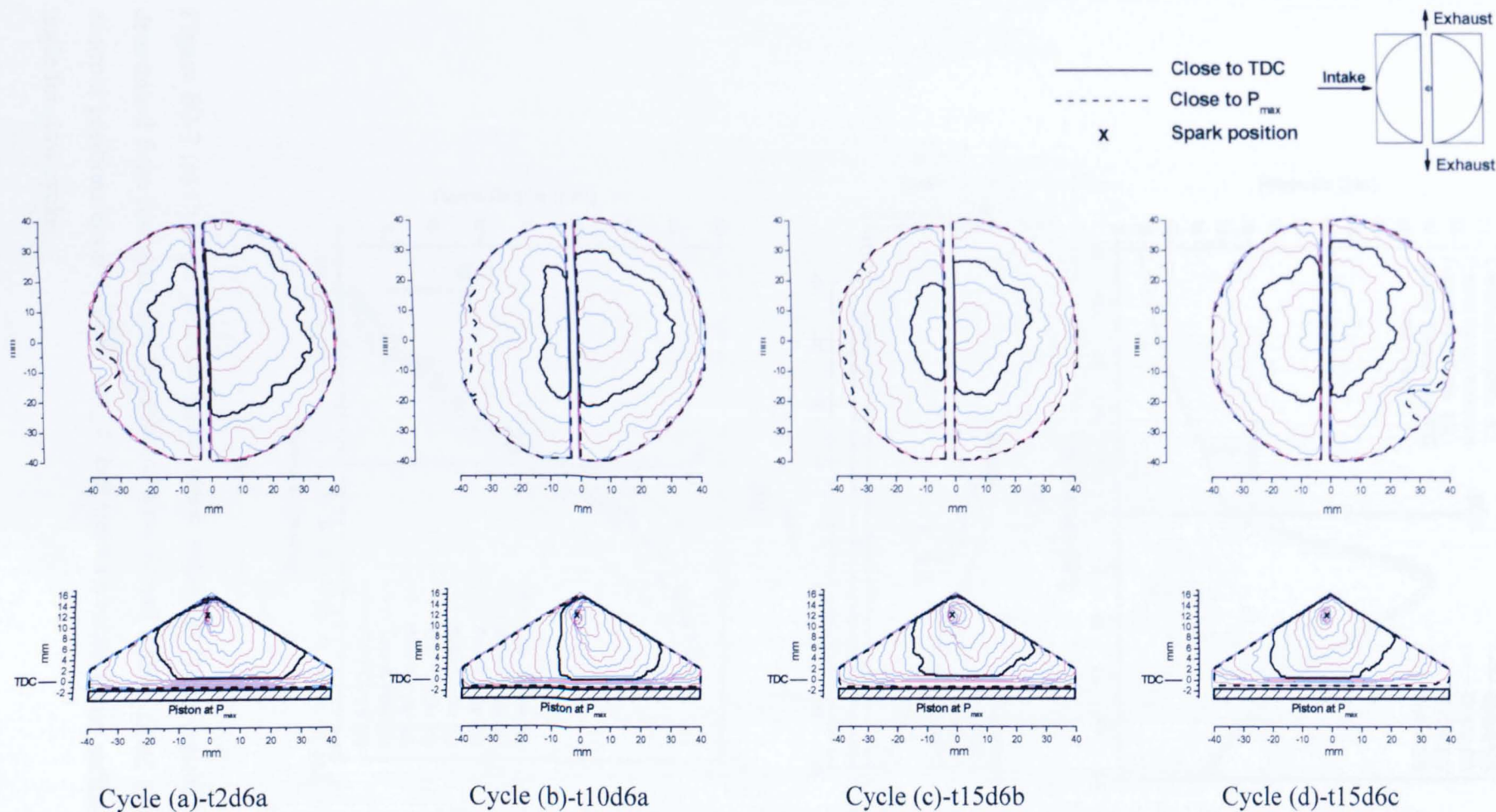
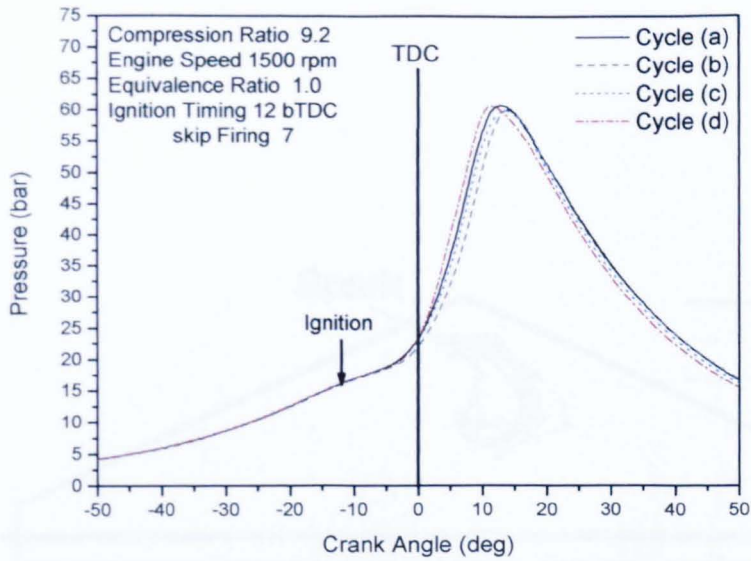
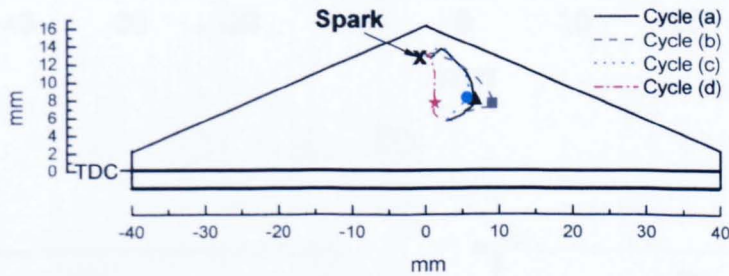


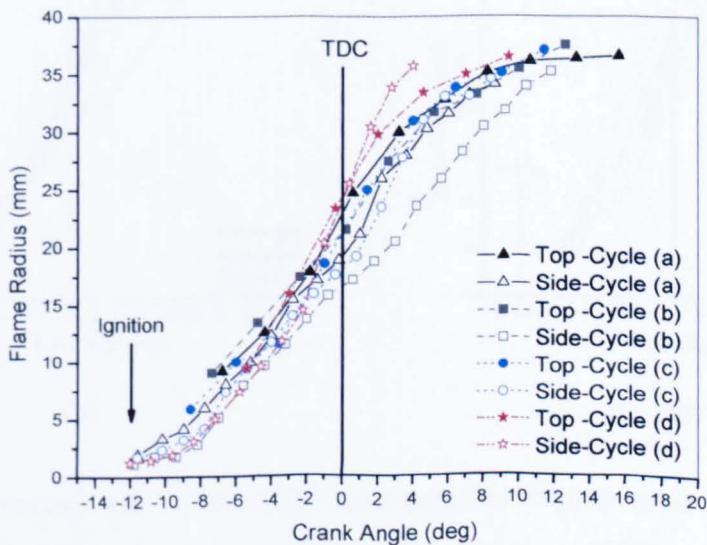
Figure B2-6 Successive flame front positions, overhead and side views, for the four selected ‘slow’ cycles for 1500 rpm, stoichiometric, ignition timing 12° bTDC (with top and side contours separated by ~ 2.5 and 1.26° CA, respectively).



(a)

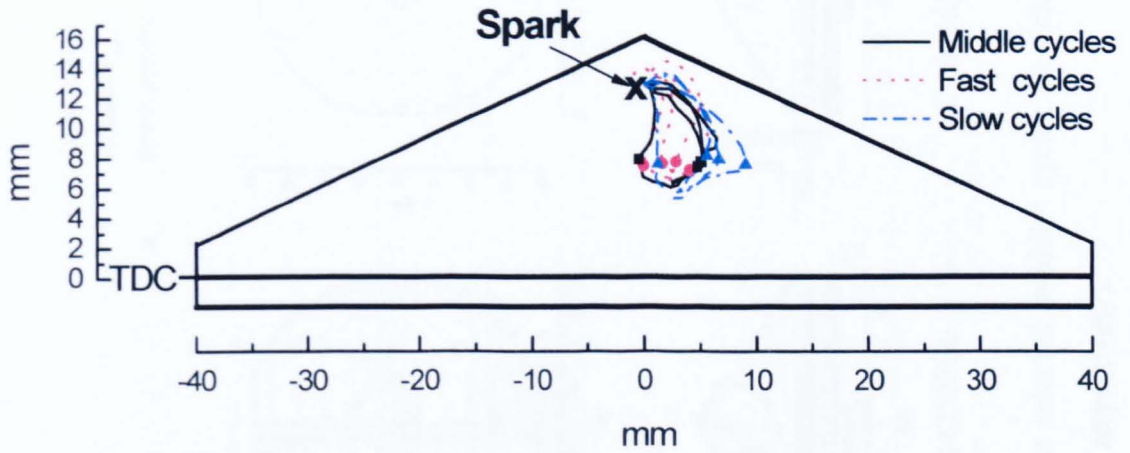


(b)

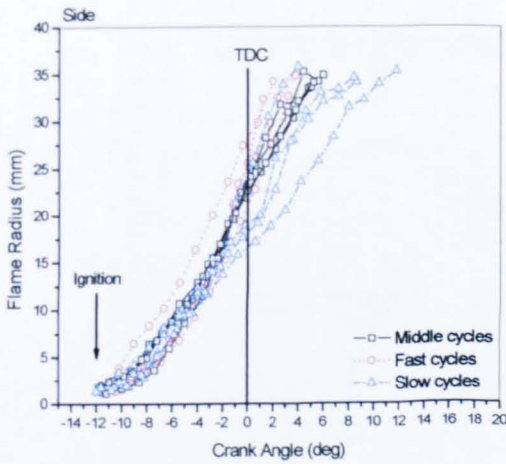


(c)

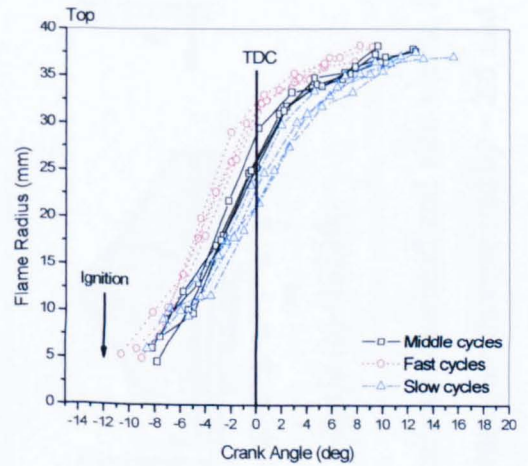
Figure B2-7 (a) Cylinder pressure versus crank angle, (b) flame centroid displacement determined from just side view for selected slow-filmed cycles, filled symbol showing centroid positions close to TDC and (c) top and side mean flame radius versus crank angle for slow cycles.



(a)



(b)



(c)

Figure B2-8 Summary data showing (a) flame centroid displacement determined from just side view, filled symbol showing centroid positions close to TDC and mean flame radius versus crank angle derived from (b) the side view and (c) the overhead view for 1500 rpm, stoichiometric, ignition timing 12° bTDC.

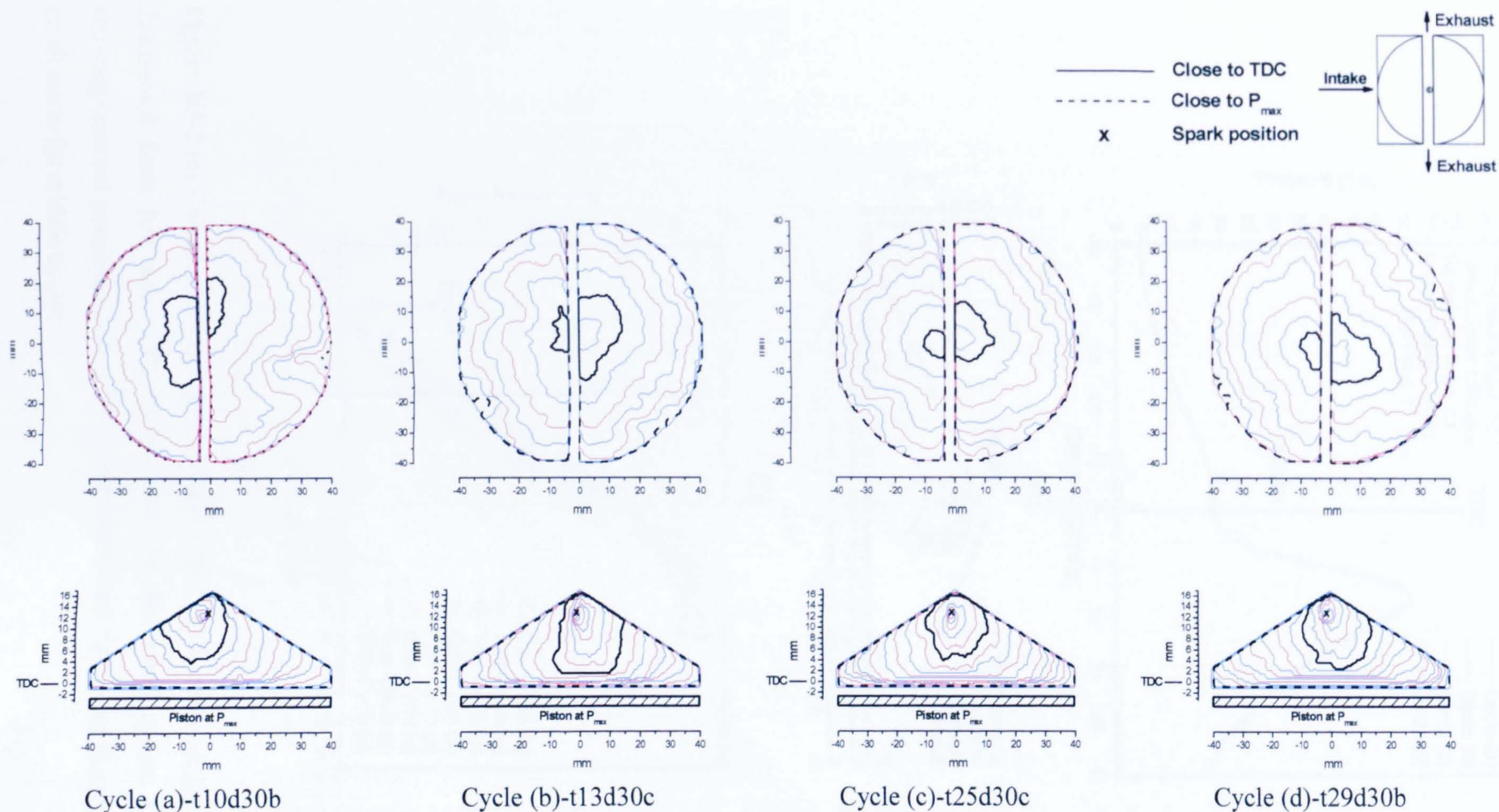
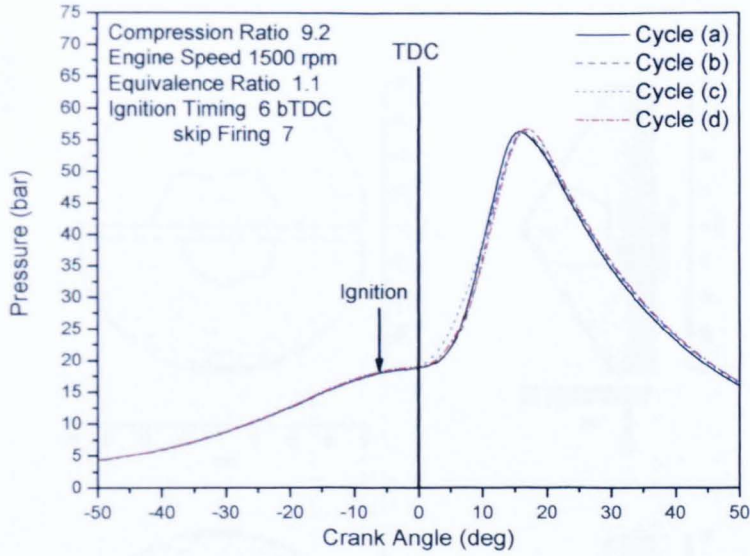
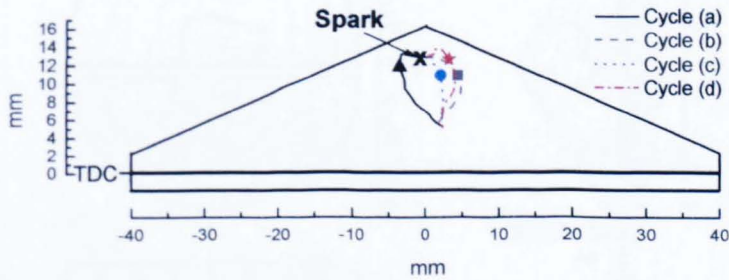


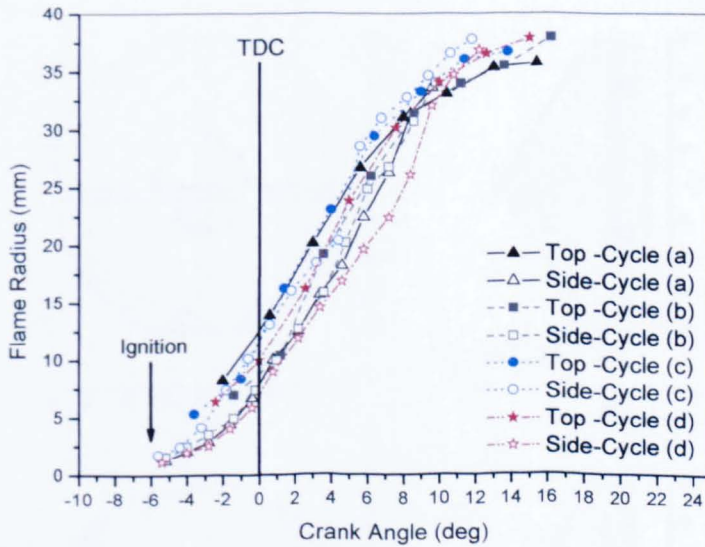
Figure B3-1 Successive flame front positions, overhead and side views, for the four selected ‘middle’ cycles for rich ($\phi = 1.1$), 1500 rpm, ignition timing 6° bTDC (with top and side contours separated by ~ 2.5 and 1.26° CA, respectively).



(a)



(b)



(c)

Figure B3-2 (a) Cylinder pressure versus crank angle, (b) flame centroid displacement determined from just side view for selected middle-filmed cycles, filled symbol showing centroid positions close to TDC and (c) top and side mean flame radius versus crank angle for middle cycles.

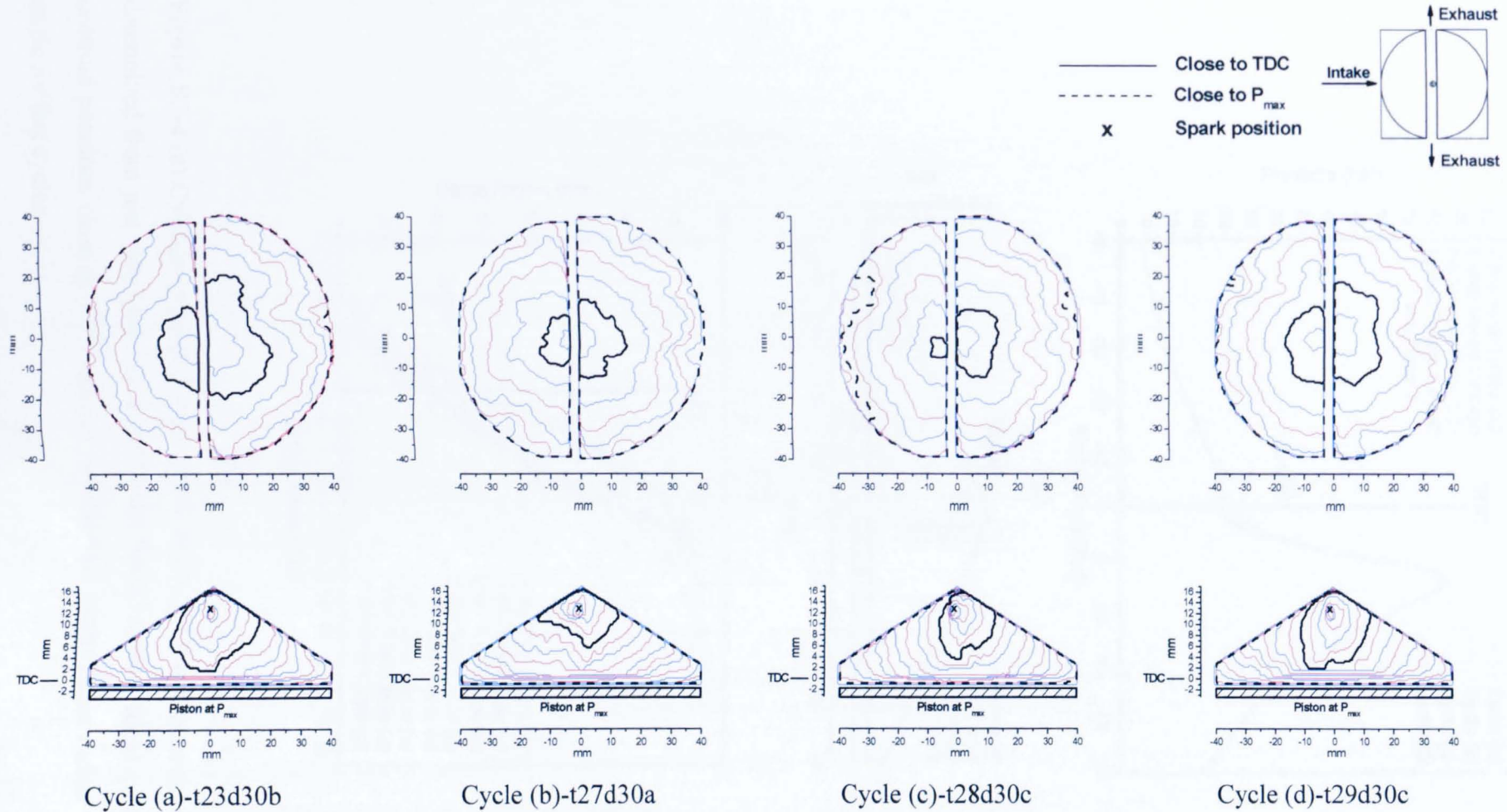
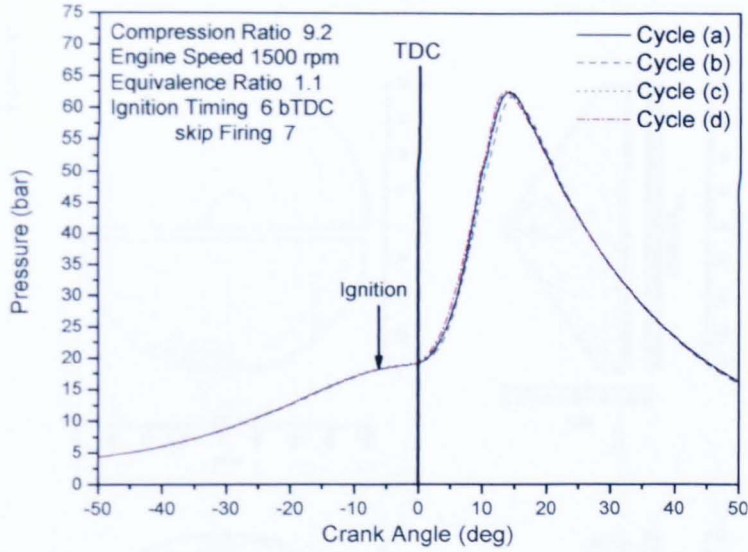
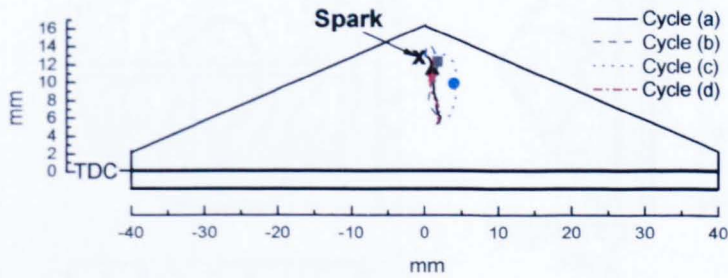


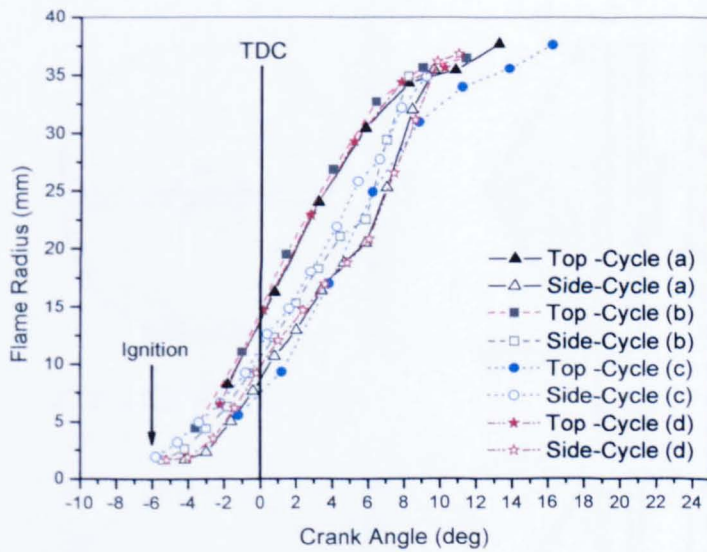
Figure B3-3 Successive flame front positions, overhead and side views, for the four selected 'fast' cycles for rich ($\phi = 1.1$), 1500 rpm, ignition timing 6° bTDC (with top and side contours separated by ~ 2.5 and 1.26° CA, respectively).



(a)



(b)



(c)

Figure B3-4 (a) Cylinder pressure versus crank angle, (b) flame centroid displacement determined from just side view for selected fast-filmed cycles, filled symbol showing centroid positions close to TDC and (c) top and side mean flame radius versus crank angle for fast cycles.

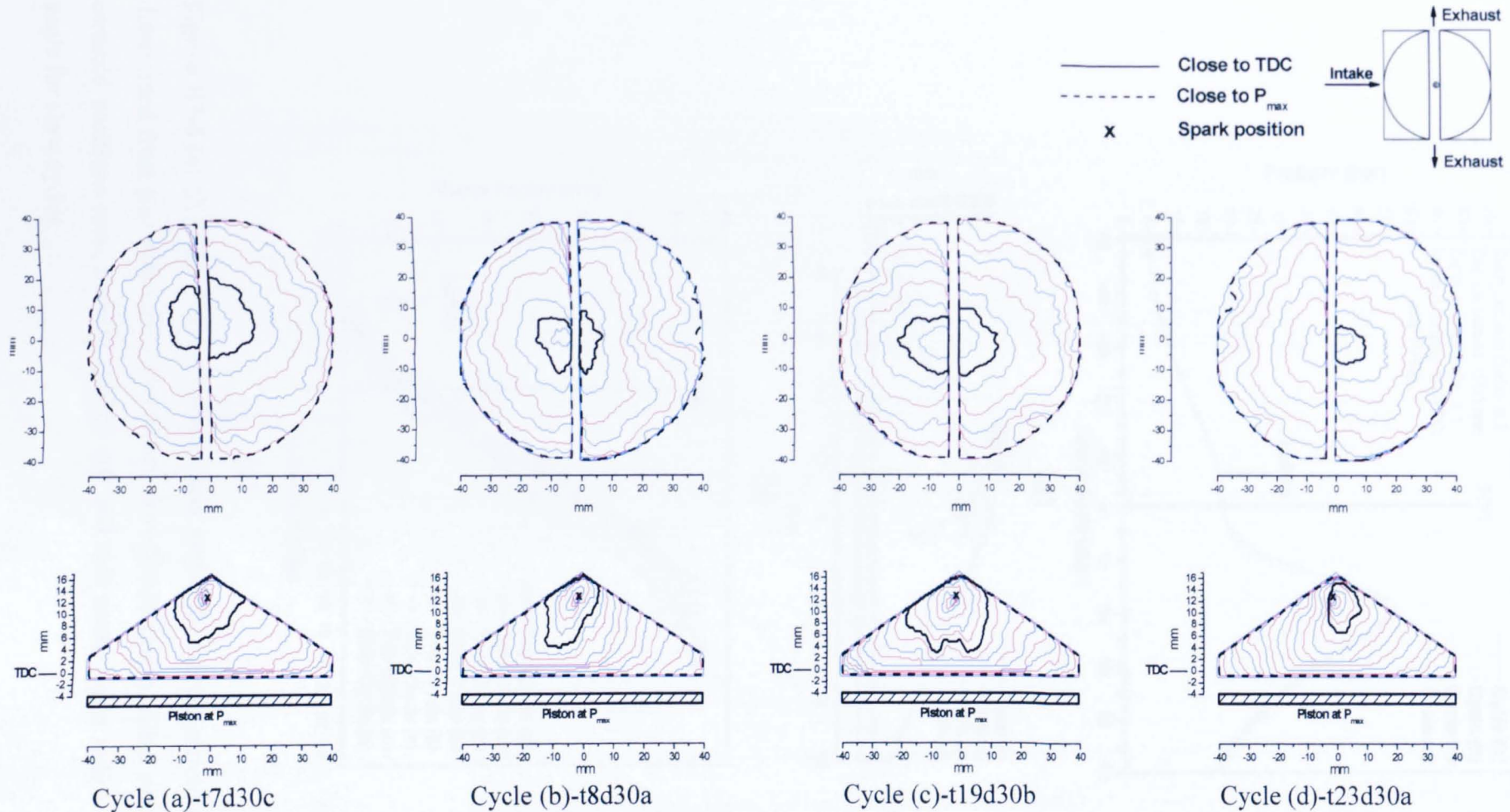
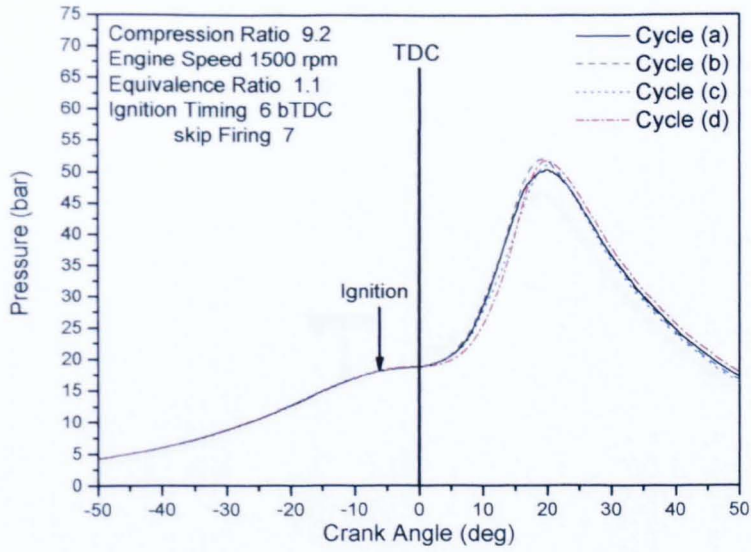
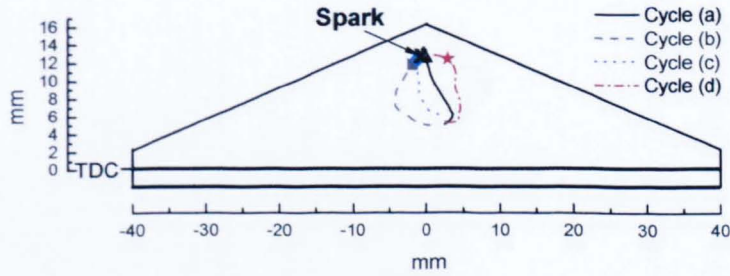


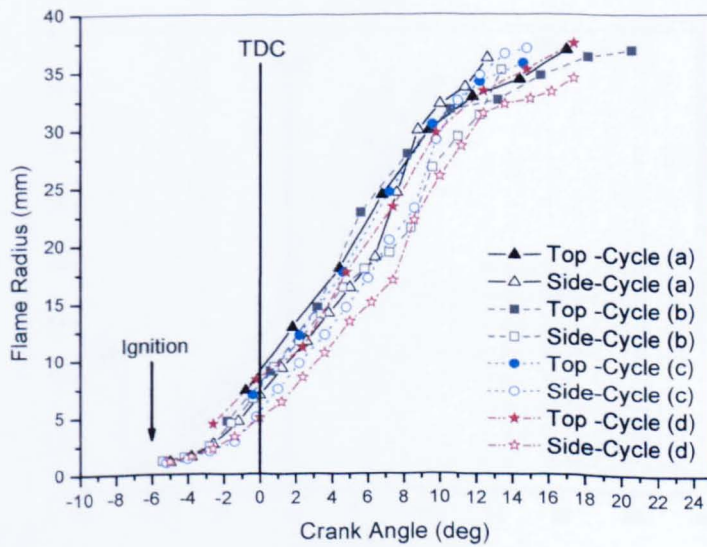
Figure B3-5 Successive flame front positions, overhead and side views, for the four selected 'slow' cycles for rich ($\phi = 1.1$), 1500 rpm, ignition timing 6° bTDC (with top and side contours separated by ~ 2.5 and 1.26° CA, respectively).



(a)

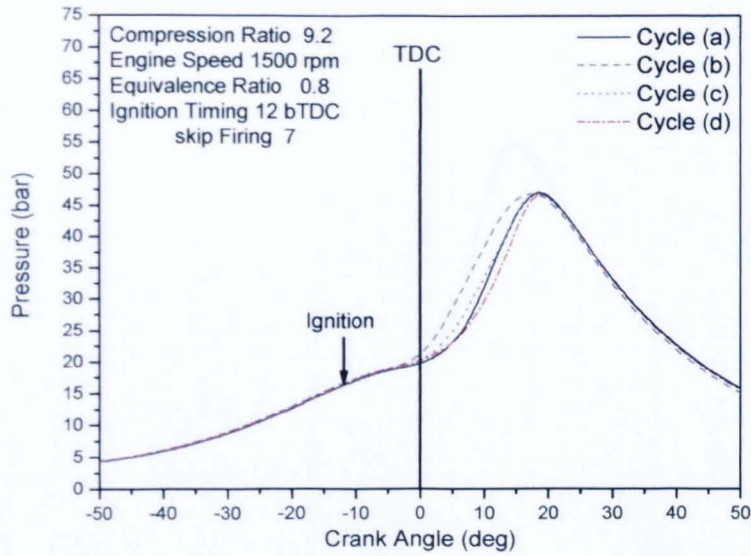


(b)

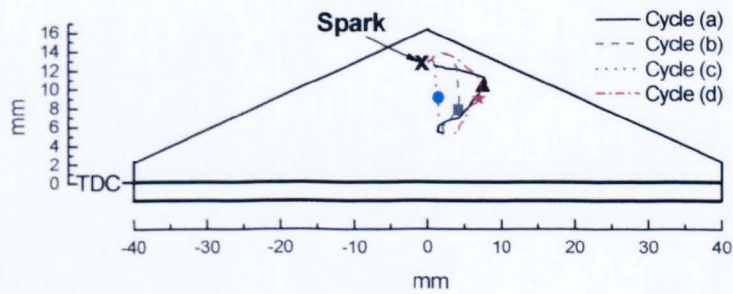


(c)

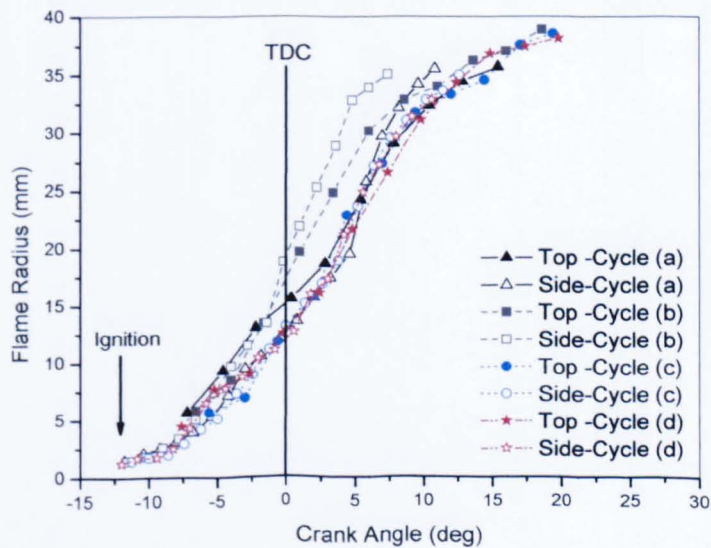
Figure B3-6 (a) Cylinder pressure versus crank angle, (b) flame centroid displacement determined from just side view for selected slow-filmed cycles, filled symbol showing centroid positions close to TDC and (c) top and side mean flame radius versus crank angle for slow cycles.



(a)

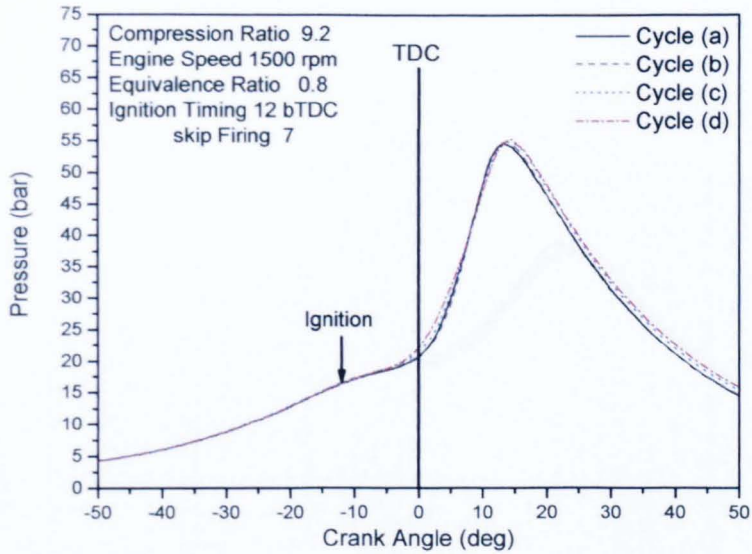


(b)

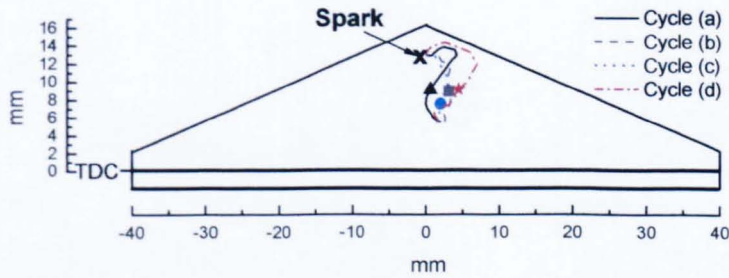


(c)

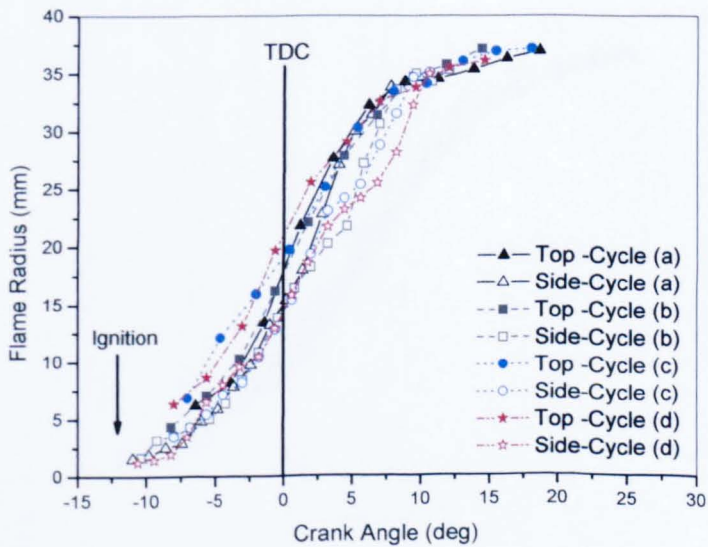
Figure B4-1 (a) Cylinder pressure versus crank angle, (b) flame centroid displacement determined from just side view for selected middle-filmed cycles, filled symbol showing centroid positions close to TDC and (c) top and side mean flame radius versus crank angle for middle cycles.



(a)

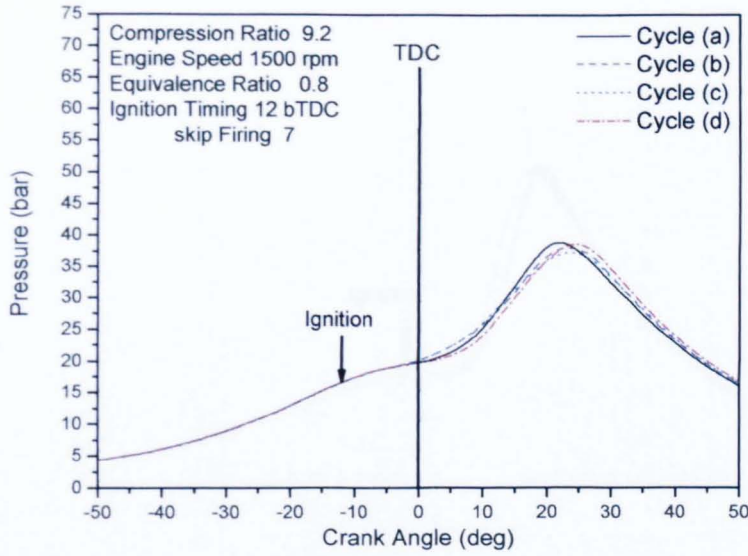


(b)

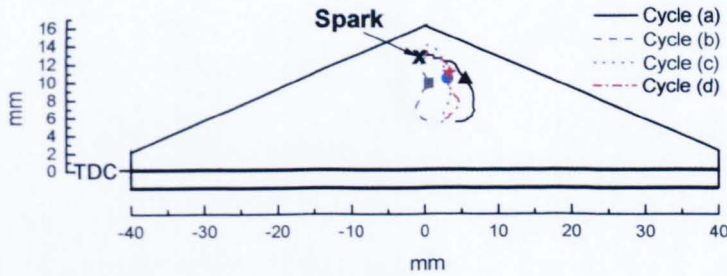


(c)

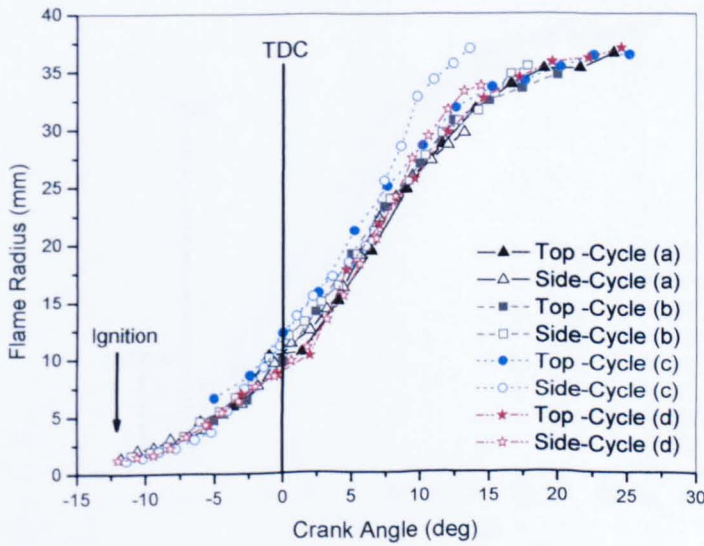
Figure B4-2 (a) Cylinder pressure versus crank angle, (b) flame centroid displacement determined from just side view for selected fast-filmed cycles, filled symbol showing centroid positions close to TDC and (c) top and side mean flame radius versus crank angle for fast cycles.



(a)

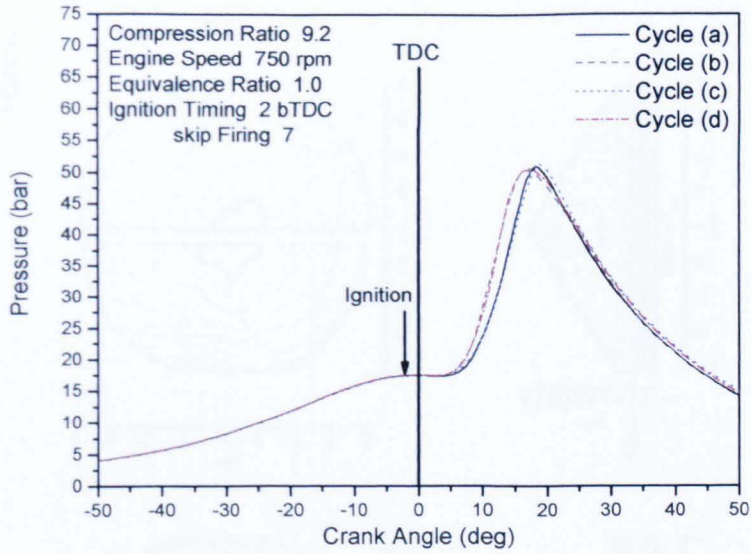


(b)

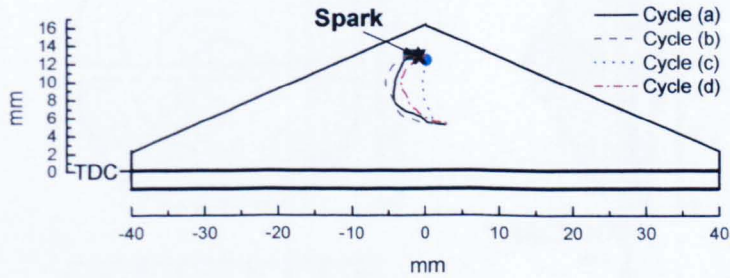


(c)

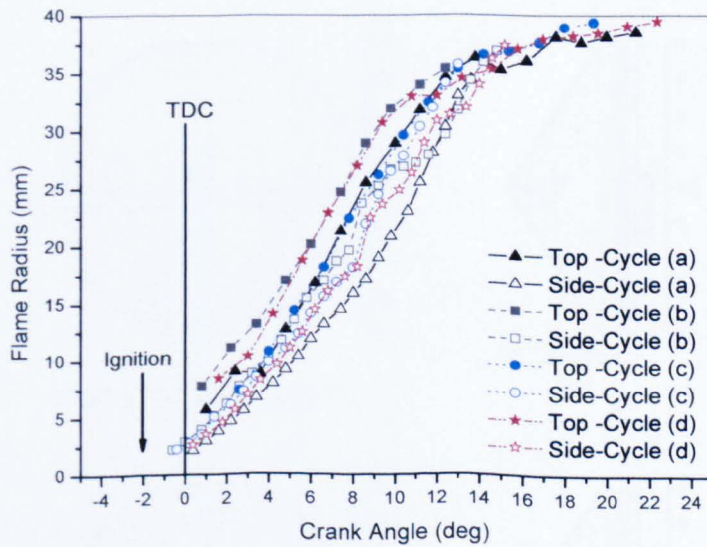
Figure B4-3 (a) Cylinder pressure versus crank angle, (b) flame centroid displacement determined from just side view for selected slow-filmed cycles, filled symbol showing centroid positions close to TDC and (c) top and side mean flame radius versus crank angle for slow cycles.



(a)



(b)



(c)

Figure B5-1 (a) Cylinder pressure versus crank angle, (b) flame centroid displacement determined from just side view for selected middle-filmed cycles, filled symbol showing centroid positions close to TDC and (c) top and side mean flame radius versus crank angle for middle cycles.

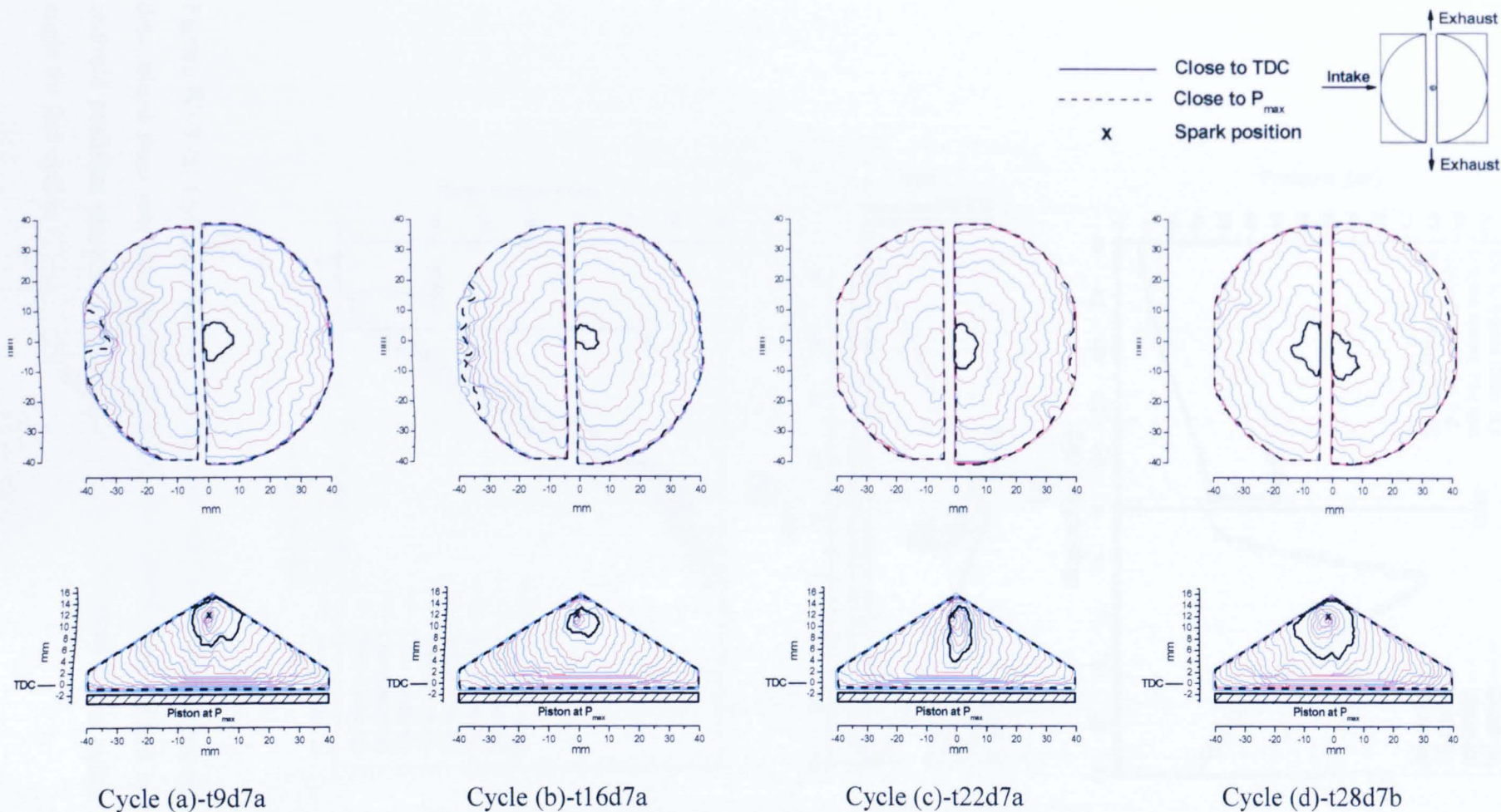
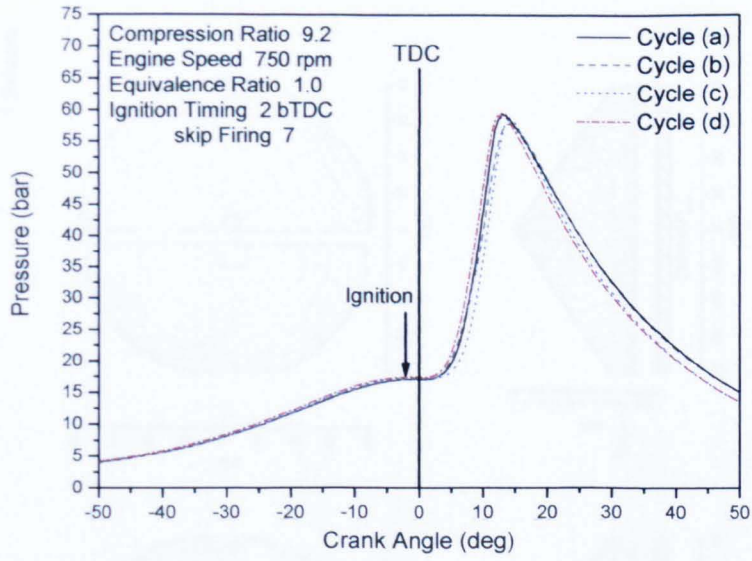
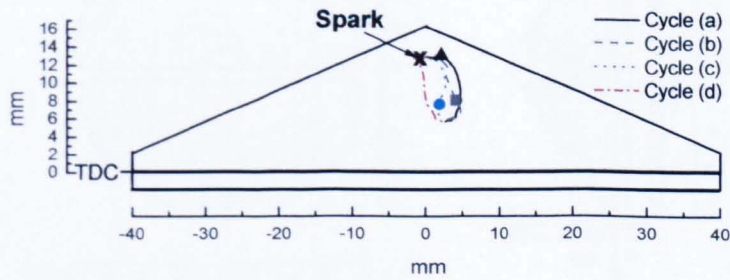


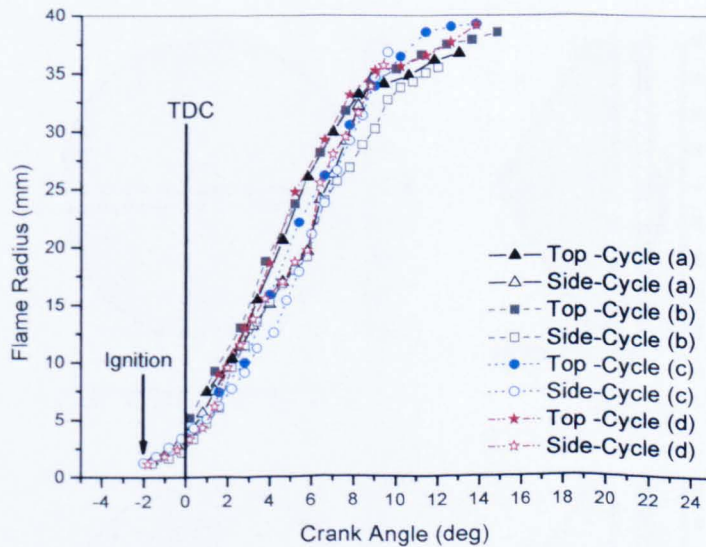
Figure B5-2 Successive flame front positions, overhead and side views, for the four selected ‘fast’ cycles for stoichiometric, 750 rpm, ignition timing 2° bTDC (with top and side contours separated by ~ 1.26 and 0.63° CA, respectively).



(a)

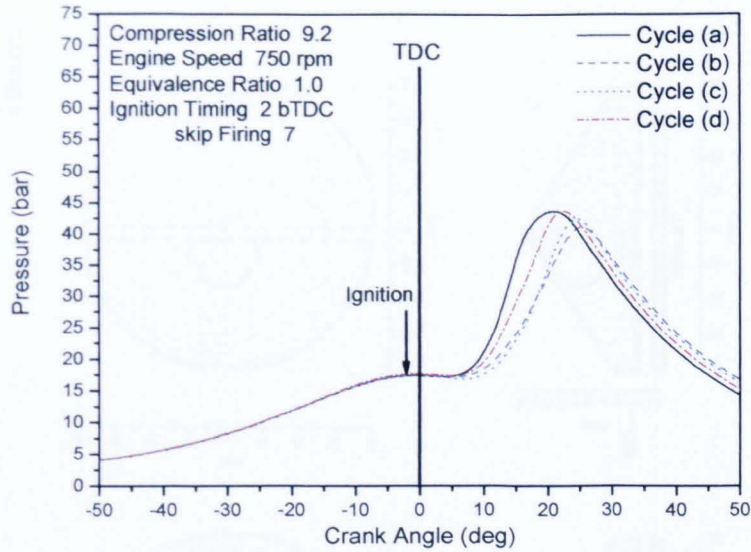


(b)

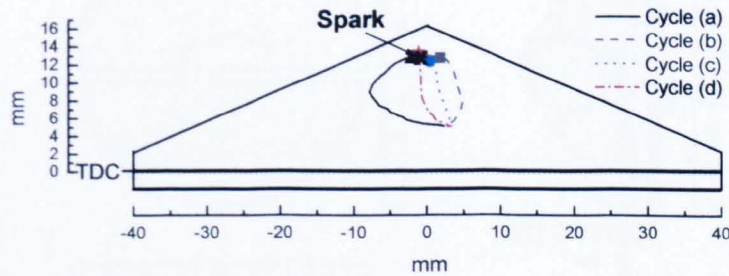


(c)

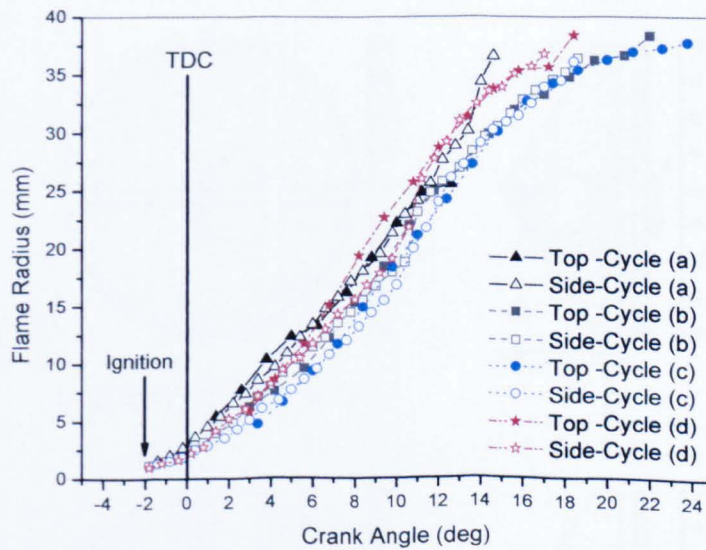
Figure B5-3 (a) Cylinder pressure versus crank angle, (b) flame centroid displacement determined from just side view for selected fast-filmed cycles, filled symbol showing centroid positions close to TDC and (c) top and side mean flame radius versus crank angle for fast cycles.



(a)



(b)



(c)

Figure B5-5 (a) Cylinder pressure versus crank angle, (b) flame centroid displacement determined from just side view for selected slow-filmed cycles, filled symbol showing centroid positions close to TDC and (c) top and side mean flame radius versus crank angle for slow cycles.

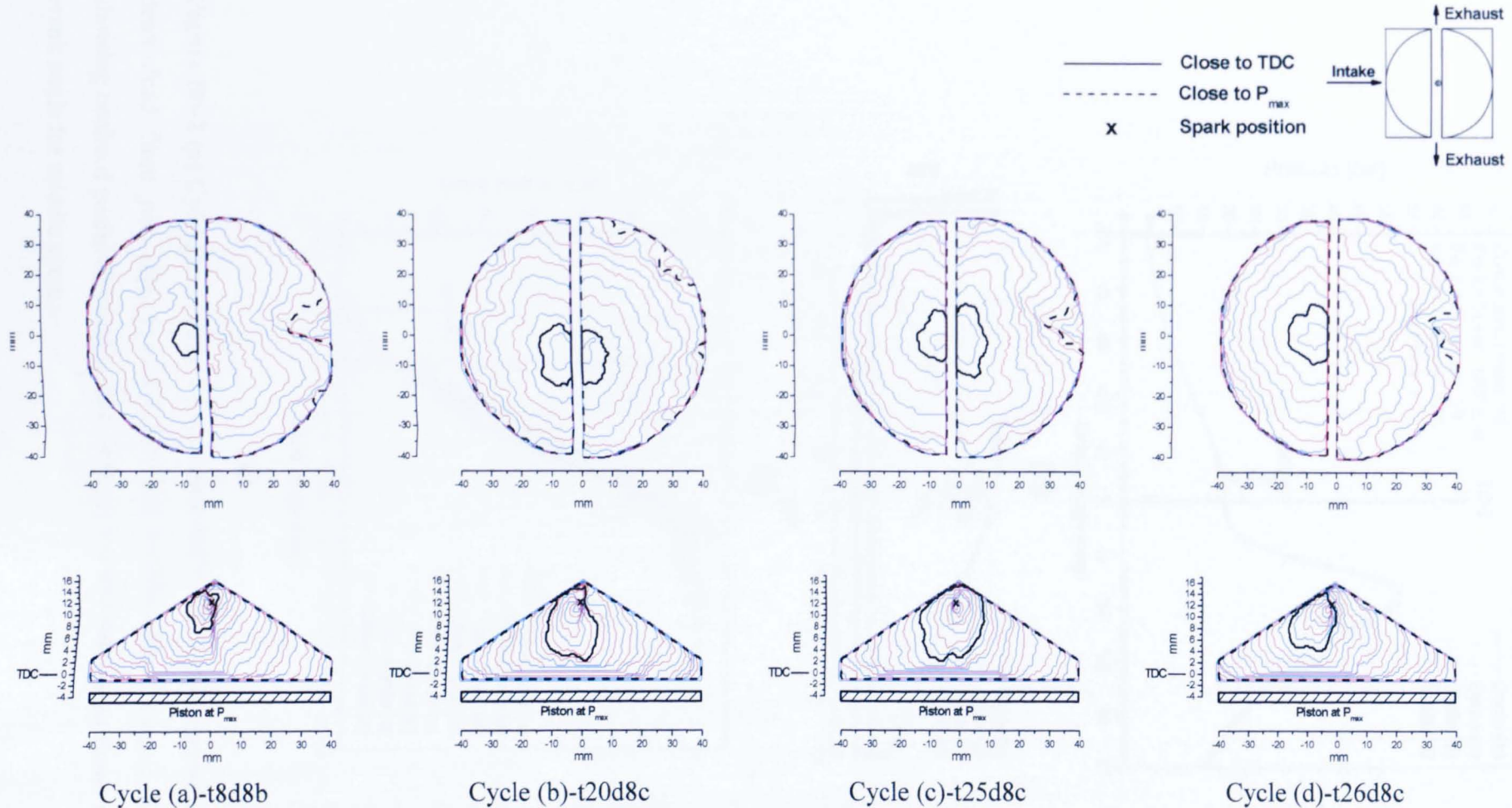
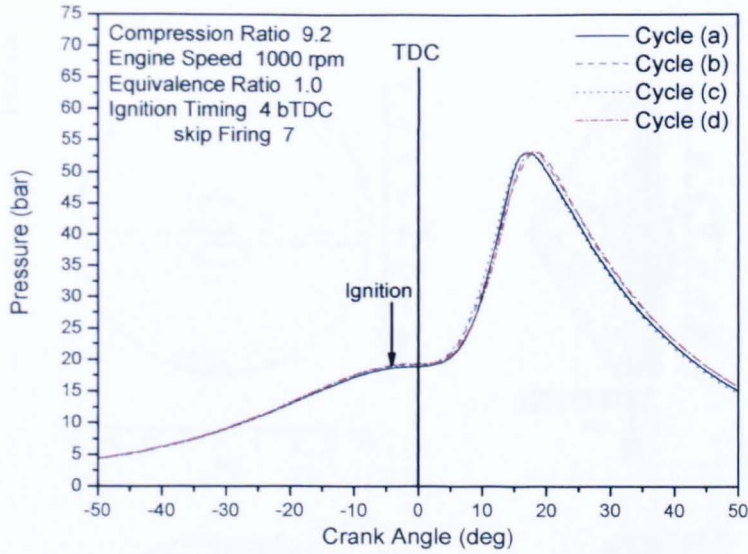
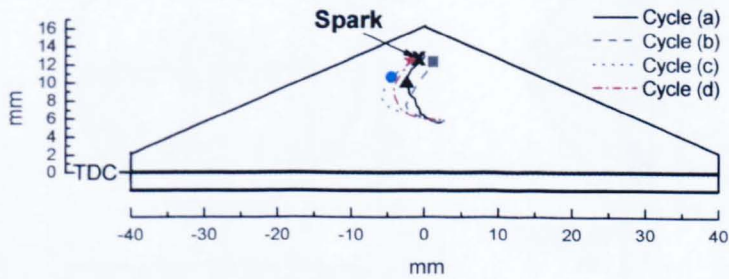


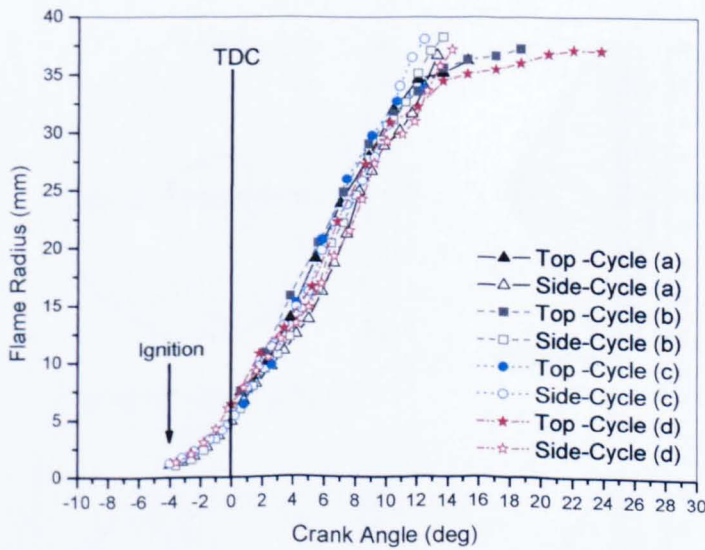
Figure B6-1 Successive flame front positions, overhead and side views, for the four selected 'middle' cycles for stoichiometric, 1000 rpm, ignition timing 4° bTDC (with top and side contours separated by ~ 1.7 and 0.84° CA, respectively).



(a)

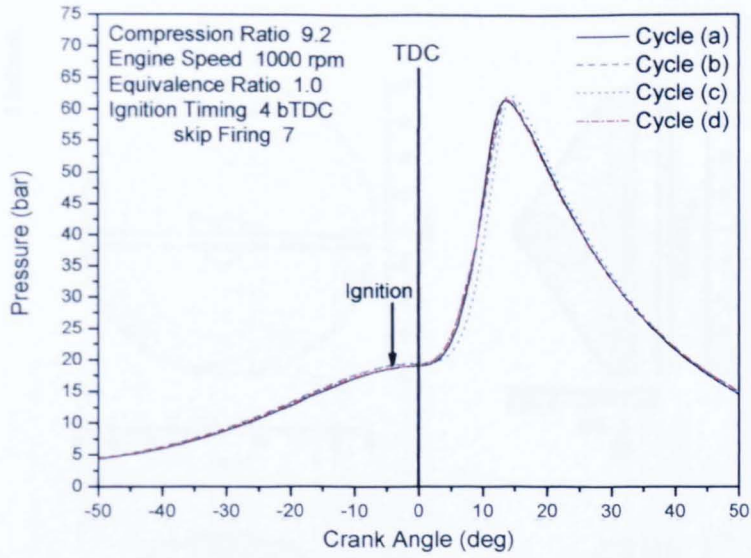


(b)

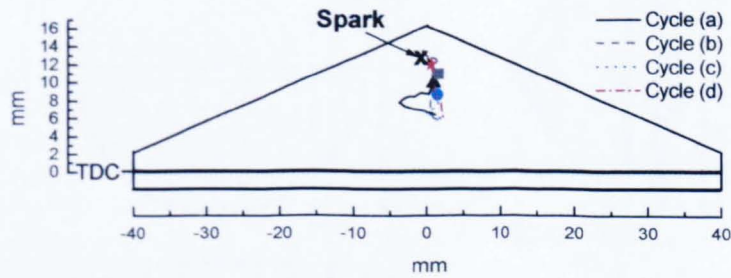


(c)

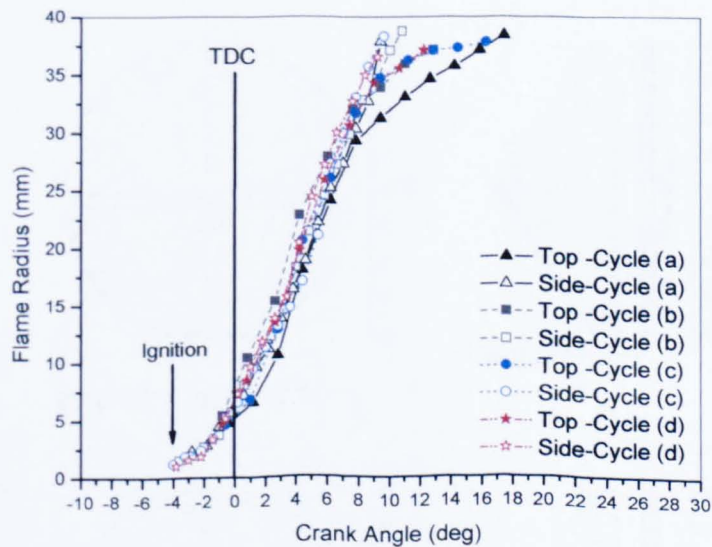
Figure B6-2 (a) Cylinder pressure versus crank angle, (b) flame centroid displacement determined from just side view for selected middle-fired cycles, filled symbol showing centroid positions close to TDC and (c) top and side mean flame radius versus crank angle for middle cycles.



(a)



(b)



(c)

Figure B6-4 (a) Cylinder pressure versus crank angle, (b) flame centroid displacement determined from just side view for selected fast-filmed cycles, filled symbol showing centroid positions close to TDC and (c) top and side mean flame radius versus crank angle for fast cycles.

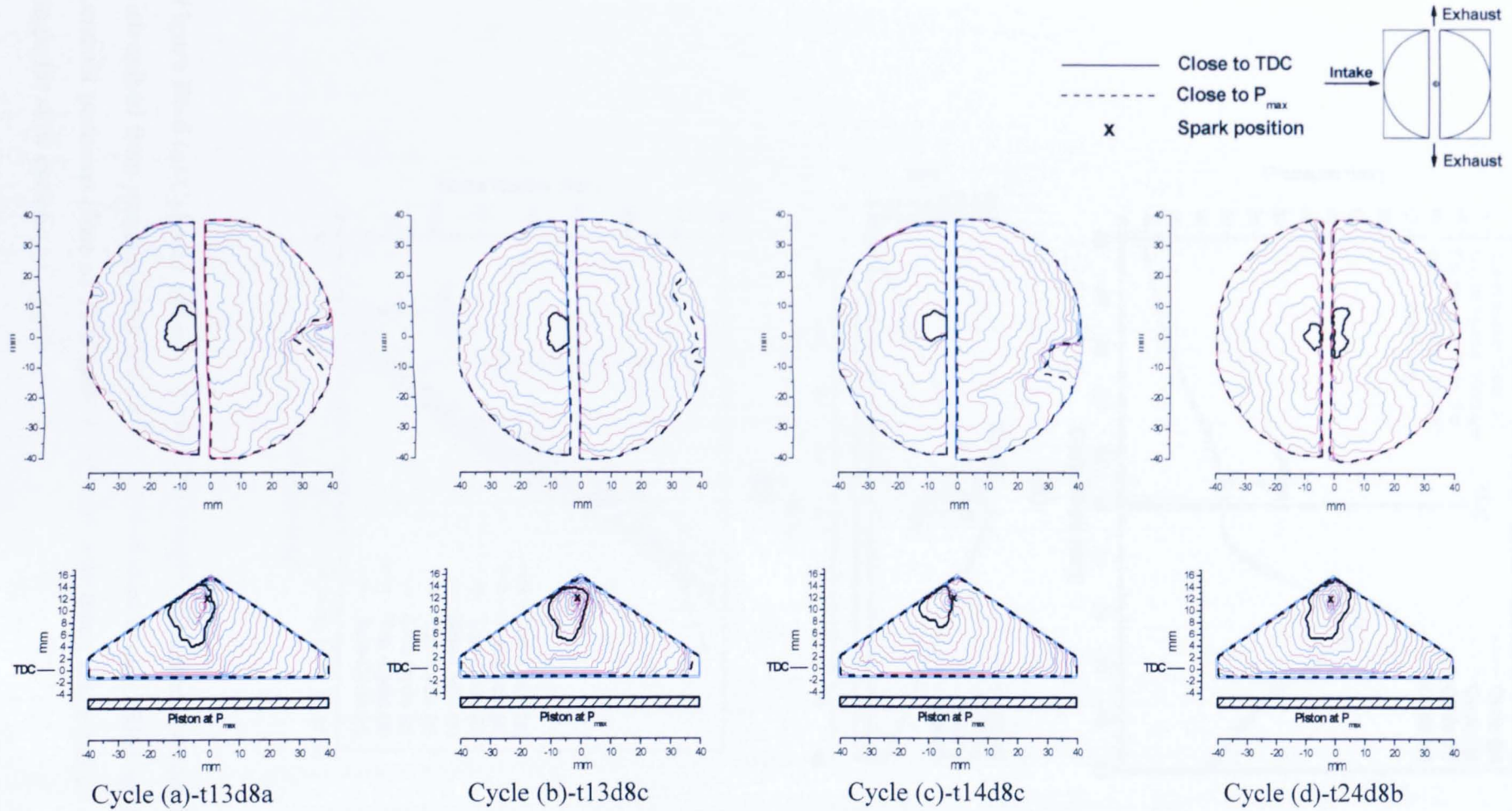
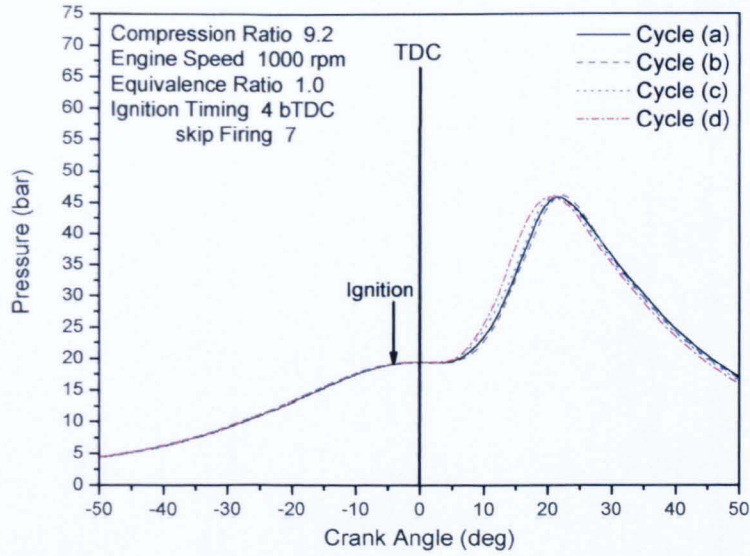
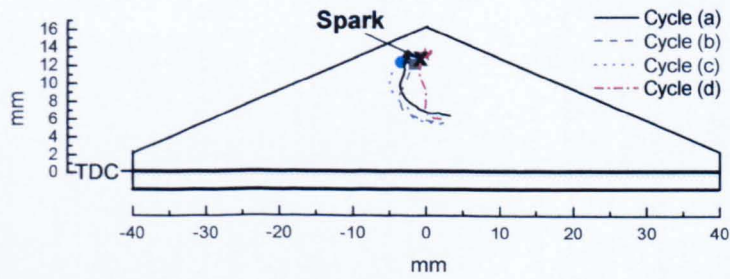


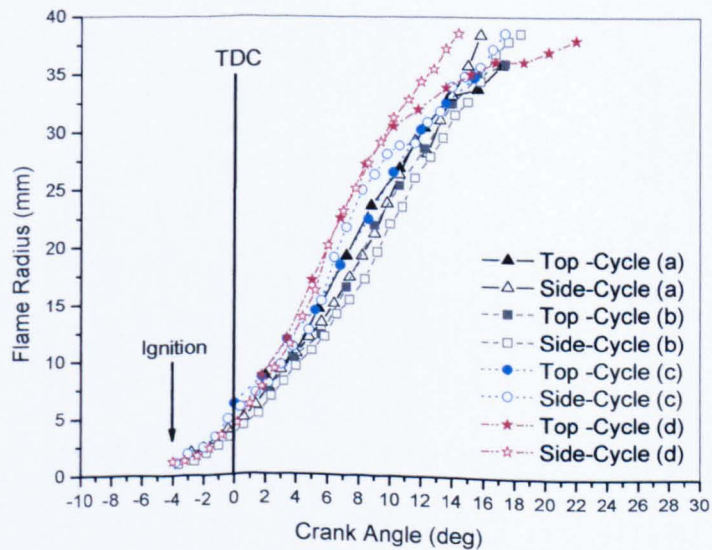
Figure B6-5 Successive flame front positions, overhead and side views, for the four selected 'slow' cycles for stoichiometric, 1000 rpm, ignition timing 4° bTDC (with top and side contours separated by ~ 1.7 and 0.84° CA, respectively).



(a)



(b)



(c)

Figure B6-6 (a) Cylinder pressure versus crank angle, (b) flame centroid displacement determined from just side view for selected slow-filmed cycles, filled symbol showing centroid positions close to TDC and (c) top and side mean flame radius versus crank angle for slow cycles.